

Johanna Kasper

Analysis of the Stochastic Electromagnetic Field Coupling to Single and Multiconductor Transmission Line Structures

This thesis is based on two major topics in electromagnetic compatibility. One topic is stochastic fields, in which neither the direction of incidence and the polarization nor the amplitude of the electrical and magnetic components are known exactly. The other topic is transmission lines, which represent an important coupling path for electromagnetic waves.

The topic of electromagnetic fields in resonators has a long history. Since more than four decades, reverberation chambers have been used in EMC tests and experiments. They can be used for both immunity and emission testing. The first reported shielding effectiveness test (a typical EMC test) within a reverberation chamber dates from 1971 and is included in the military standard MIL-STD 1377. If the data, such as geometry of the objects within the resonator, are not known exactly, the description by stochastic fields is a promising approach. During the last few years, a description by stochastic instead of deterministic methods have proven their worth in order to predict the behavior of electromagnetic fields in large and geometrically complex resonators. Complex resonators are e.g. airplanes, motor vehicles, helicopters, ships and other objects with an almost completely closed and conductive surface. Especially in the investigation of electromagnetic compatibility and wireless communication, problems must be solved whose boundary conditions are only inaccurately known.

Transmission lines such as signal lines, communication lines, power supply cables, etc. can act as parasitic antennas. Therefore, the investigation of the field coupling to e.g. power supply cables and communication lines is essential for EMC. Transmission line theory is essential in both radio frequency and microwave communications as well as in the design of fast digital circuits. This thesis combines circuit analysis with electromagnetics.
miteinander verglichen werden.

Johanna Kasper: Stochastic Field Coupling to Single and Multiconductor Transmission Lines

Analysis of the Stochastic Electromagnetic Field Coupling to Single and Multiconductor Transmission Line Structures

Dissertation

zur Erlangung des akademischen Grades

Doktoringenieur

(Dr.-Ing.)

von **M. Sc. Johanna Kasper**

geb. am 18.11.1990 in Pforzheim

genehmigt durch die Fakultät für Elektrotechnik und Informationstechnik
der Otto-von-Guericke-Universität Magdeburg

Gutachter:

Univ.-Prof. Dr.-Ing. Ralf Vick

Univ.-Prof. Dr.-Ing. Achim Enders

Promotionskolloquium am 10. November 2021

Res Electricae Magdeburgenses

Magdeburger Forum zur Elektrotechnik, Jg. 21, Band 86, 2021

<http://www.mafo.ovgu.de/>

IMPRESSUM

Herausgeber:

- Prof. Dr.-Ing. Andreas Lindemann, Lehrstuhl für Leistungselektronik, Institut für Elektrische Energiesysteme
- Prof. Dr.-Ing. habil. Martin Wolter, Lehrstuhl für Elektrische Netze und Erneuerbare Energie, Institut für Elektrische Energiesysteme
- Prof. Dr. rer. nat. Georg Rose, Lehrstuhl für Medizinische Telematik/Medizintechnik, Institut für Medizintechnik
- Prof. Dr.-Ing. Ralf Vick, Lehrstuhl für Elektromagnetische Verträglichkeit, Institut für Medizintechnik

Gründungsherausgeber:

- Prof. Dr. rer. nat. habil. Jürgen Nitsch
- Prof. Dr.-Ing. habil. Zbigniew Antoni Styczynski

alle: Otto-von-Guericke-Universität Magdeburg
Postfach 4120, 39016 Magdeburg

V. i. S. d. P.:

Dr.-Ing. Johanna Kasper

Otto-von-Guericke-Universität Magdeburg, Postfach 4120, 39016 Magdeburg

1. Auflage, Magdeburg, Otto-von-Guericke-Universität, 2021

Zugl.: Magdeburg, Univ., Diss., 2021

Auflage: 15

Redaktionsschluss: Dezember 2021

ISSN: 1612-2526

ISBN: 978-3-948749-13-2

DOI: 10.24352/UB.OVGU-2021-105

© Copyright 2021 Johanna Kasper

Bezug über die Herausgeber

Druck: docupoint GmbH

Otto-von-Guericke-Allee 14, 39179 Barleben

“If your experiment needs statistics, you ought to have done a better experiment.”

Ernest Rutherford (nobel laureate, 1871 to 1937)

Abstract

This thesis analyzes transmission lines and their behavior in a reverberation chamber. For this purpose, a time efficient closed-form solution for the coupling of stochastic electromagnetic fields to single- and multiconductor transmission line structures is presented. The simulation model is based on the Baum-Liu-Tesche (BLT) equations, but this thesis goes beyond the study of a coupling to a single plane wave and studies the excitation by a stochastic field. The transmission lines are described analytically using transmission line theory and in addition per-unit-length (p. u. l.) parameters are defined. Based on Maxwell's equations, a generalized transmission line theory is presented which, however, resembles classical transmission line theory in its structure. The classical transmission line theory is extended to include higher order modes. A high frequency (HF) model is derived for the p. u. l. parameters, in that way that the parameters become frequency dependent. The model of the frequency dependent p. u. l. parameters is deduced and validated by the method of moments and by measurements in the reverberation chamber. Different configurations of the transmission line structures are analyzed and the average magnitude of the coupled voltage at the terminals is calculated and discussed. Moreover, the influence of bending transmission lines and its influence on the field-to-wire coupling is investigated.

Kurzfassung

In dieser Dissertation werden Übertragungsleitungen und ihr Verhalten in einer Modenverwirbelungskammer analysiert. Zu diesem Zweck wird eine zeiteffiziente semianalytische Lösung zur Berechnung der Einkopplung stochastischer elektromagnetischer Felder in ein- und mehradrige Übertragungsleitungsstrukturen vorgestellt. Das Simulationsmodell basiert auf den Baum-Liu-Tesche (BLT) Gleichungen. Diese Arbeit geht über die Untersuchung der Einkopplung einer einzelnen ebenen Welle hinaus und untersucht die Anregung durch ein stochastisches Feld. Die Übertragungsleitungen werden dabei analytisch mit Hilfe der Leitungstheorie beschrieben und zusätzlich werden Leitungsbeläge definiert. Basierend auf den Maxwell-Gleichungen wird eine verallgemeinerte Leitungstheorie vorgestellt, die jedoch in ihrer Struktur der klassischen Leitungstheorie ähnelt. Für die Leitungsparameter wird ein Hochfrequenz (HF)-Modell abgeleitet, sodass die Parameter frequenzabhängig werden. Das semianalytische Modell wird mit der Momentenmethode und durch Messungen in der Modenverwirbelungskammer verglichen und validiert. Verschiedene Konfigurationen der Leitungsstrukturen werden analysiert und die eingekoppelten Spannung an den Enden der Leitungen berechnet, gemessen und diskutiert. Darüber hinaus wird der Einfluss von gebogenen und geknickten Übertragungsleitungen und der Einfluss des Knicks auf die Einkopplung untersucht.

Contents

1	Introduction	15
1.1	Reverberation Chambers	15
1.2	Transmission Lines	16
1.3	Key Questions	17
1.4	Objective and Structure of the Work	18
2	Fundamental Tools for Determining the Stochastic Field-to-Wire Coupling	19
2.1	Derivation of the Field-To-Wire Coupling Equations	19
2.1.1	Inhomogeneous Wave Equations	19
2.1.2	Field-to-Wire Coupling Equations	22
2.2	Transmission Line Theory	24
2.2.1	Arbitrary Straight Transmission Line	24
2.2.2	Per-Unit-Length Parameters	25
2.2.3	Characteristic Impedance	34
2.2.4	Reflection Coefficient	35
2.3	Stochastic Electromagnetic Fields	37
2.3.1	Occurrence and Calculation of Stochastic Electromagnetic Fields . . .	37
2.3.2	Plane Waves	38
2.3.3	Method of Moments	39
2.4	Measurements in a Reverberation Chamber	41
2.4.1	Functionality of a Reverberation Chamber	41
2.4.2	Big Reverberation Chamber at the Otto von Guericke University	42
2.4.3	Scattering Parameters	42
2.4.4	Measurement of the Coupled Current and Coupled Voltage	44
2.4.5	Measurement of the Radiation Losses	50
3	Single Conductor Transmission Line over a Conductive Ground Plane	51
3.1	Transmission Line Model	51
3.2	Field-to-Wire Coupling Equations	58
3.3	Validation of the Model	61
3.3.1	Validation Using the Method of Moments	61
3.3.2	Validation Using Measurements in the Reverberation Chamber	62

3.4	Comparison with a Double Conductor Transmission Line	64
3.4.1	Transmission Line Model	64
3.4.2	Field-to-Wire Coupling Equations	67
3.4.3	Coupled Current as a Function over the Frequency	70
3.5	Results of the Investigation of the Single and Double Conductor	71
4	Single Conductor Transmission Line with a Bend	72
4.1	Transmission Line Model	72
4.2	Field-to-Wire Coupling Equations	80
4.3	Validation of the Model	83
4.3.1	Validation Using the Method of Moments	83
4.3.2	Validation Using Measurements in the Reverberation Chamber	84
4.4	Coupled Voltage as a Function over the Frequency	85
4.4.1	Variation of the Bend Angles	85
4.4.2	Comparison of Bent and Straight Single Wires	88
4.5	Measured Radiation Losses	89
4.6	Comparison with a Single Conductor Transmission Line Network	91
4.6.1	Variation of the Line Length	92
4.6.2	Variation of the Alignment	94
4.6.3	Variation of the Termination	95
4.7	Comparison with a Curved Single Conductor Transmission Line	97
4.7.1	Measurements of the Coupled Voltage	97
4.7.2	Comparison of the Radiation Losses	100
4.7.3	Comparison of the Curved Line with Transmission Line Theory	100
5	Multiconductor Transmission Line over a Conductive Ground Plane	102
5.1	Transmission Line Model	102
5.2	Field-to-Wire-Coupling Equations	109
5.3	Validation of the Model	111
5.3.1	Validation Using the Method of Moments	111
5.3.2	Validation Using Measurements in the Reverberation Chamber	113
5.4	Coupled Voltage as a Function over the Frequency	115
5.4.1	Different Terminations	116
5.4.2	Variation of the Height	121
5.4.3	Variation of the Line Length and Position	123
5.4.4	Three-Wire Multiconductor Transmission Line	126
5.4.5	Comparison with a single conductor transmission line	127
5.5	Comparison with an Isolated Multiconductor Transmission Line	128
5.5.1	Transmission Line Model	128
5.5.2	Field-to-Wire-Coupling Equations	133

5.5.3 Coupled Voltage as Function over the Frequency	133
5.6 Comparison between the Multiconductor Structures	142
5.7 Results of the Investigation of Multiconductor Transmission Lines	143
6 Summary and Outlook	144
6.1 Important Results	144
6.2 Outlook for Future Works	145
Bibliography	146
A Calculating the Coupled Current from the Scattering Parameters	151
B Comparison of the Solutions of the Integrals of the Field-to-Wire Coupling Equations	152
C Simulation Model of the Curved Transmission Line in <i>CONCEPT-II</i>	155
D Vector Potential for the Double Line with a Bend	156
E Measurement Setup of Different Terminations of the Multiconductor Transmission Line over Ground	158
F MATLAB Program Setting for MoM Results at 0 Hz	160

Nomenclature

Number Sets

x, X	scalar, also complex-valued
\mathbf{x}, \mathbf{X}	vector, also complex-valued
$[X]$	matrix
x'	observation point
$ \mathbf{X} , X $	magnitude of a vector, magnitude of a complex quantity
$\Re \{X\}$	real part of a complex quantity
$\Im \{X\}$	imaginary part of a complex quantity
x_x, x_y, x_z	components of the vector \mathbf{x} in the direction of the unit vectors \mathbf{e}_x , \mathbf{e}_y and \mathbf{e}_z
$\langle X \rangle$	mean value of a statistical variable X
$\mathbb{1}$	identity matrix
d	differential operator
∂	partial differential operator
∇	Nabla operator

Physical Constants

e	Euler's number	
c_0	speed of light in vacuum	$299\,792\,458 \frac{\text{m}}{\text{s}}$
π	Pi	3.141
j	imaginary unit	

Symbols

a	radius	[m]
A	area	[m ²]
\mathbf{A}	vector potential	[$\frac{Vs}{m}$]
B	number of electromagnetic boundary conditions	
$\mathbf{B}(\mathbf{r})$	magnetic flux density at position \mathbf{r}	[T]
c	contour	
C^F	correction factor	
C'	per-unit-length capacitance	[$\frac{F}{m}$]
d	distance	
$[D]$	propagation matrix	
$\mathbf{D}(\mathbf{r})$	electric flux density at position \mathbf{r}	[$\frac{As}{m^2}$]
$\mathbf{e}_x, \mathbf{e}_y, \mathbf{e}_z$	unit vector in x -, y -, z -direction	
E	mean value of the electric field strength of a plane wave	[$\frac{V}{m}$]
E_0	chamber constant	[$\frac{V}{m}$]
$\mathbf{E}(\mathbf{r})$	electric field at position \mathbf{r}	[$\frac{V}{m}$]
E_{\tan}	tangential electric field	[$\frac{V}{m}$]
f	frequency	[Hz]
$g(\mathbf{r})$	Green's function at position \mathbf{r}	
G'	per-unit-length conductance	[$\frac{S}{m}$]
h	distance between a single line and a perfectly conducting plane	[m]
$\mathbf{H}(\mathbf{r})$	magnetic field at position \mathbf{r}	[$\frac{A}{m}$]
$H_0^{(2)}$	Hankel function first order second kind	
i	index variable	
I	electric current	[A]
I_L	electric current at the line ends	[A]

j	index variable	
$\mathbf{J}(\mathbf{r})$	current density at position \mathbf{r}	$[\frac{A}{m^2}]$
J_0	Bessel function first kind	
Y_0	Bessel function second kind	
\mathbf{k}, k	wave vector, wave number	
K	constant	
l	length	[m]
\mathbf{l}	vector along the line	
L'	per-unit-length inductance	$[\frac{H}{m}]$
m_1, m_2, m_3	mode indices	
n	number of wires	
\mathbf{n}	normal vector	
N	number of waves	
q	electric charge	[C]
Q	quality factor	
P	power	[W]
p	variable	
r	distance	[m]
\mathbf{r}	position vector	
R	distance between two vectors	
R'	per-unit-length resistance	$[\frac{\Omega}{m}]$
s	distance between conductors	[m]
S	source term of the incident field	
S	scattering parameter	
S_{11}	input reflection coefficient	
S_{12}	forward transmission coefficient	

S_{21}	backward transmission coefficient	
S_{22}	output reflection factor	
t	time	[s]
\mathbf{t}	tangential vector	
T	transmission coefficient	
u	auxiliary coordinate	[m]
U	electric voltage	[V]
U_L	electric voltage at the line ends	[V]
U_t	transverse voltage	[V]
v	auxiliary coordinate	[m]
V	volume	[m ³]
x, y, z	coordinates along the wire	[m]
Y	admittance	[S]
Y_c	characteristic admittance	[S]
Z	impedance	[Ω]
Z_c	characteristic impedance	[Ω]
α	polarization angle	[$^\circ$]
β	phase constant	
γ	propagation constant	
γ^+, γ^-	modified propagation constant	
γ_{EM}	Euler-Mascheroni constant	
Γ	reflection coefficient	
δ	Dirac delta function	
ε	electric permittivity of a medium	[$\frac{F}{m}$]
θ	polar angle	[$^\circ$]
Θ	Heaviside function	

List of Symbols

κ	electric conductivity	$[\frac{S}{m}]$
λ	wavelength	[m]
μ	magnetic permeability of a medium	$[\frac{H}{m}]$
ρ	charge density	$[\frac{C}{m}]$
ϕ	azimuth angle	[°]
Φ	electric potential	[V]
ω	angular frequency	$[\frac{rad}{s}]$
Ψ	magnetic flux	[Wb]

Abbreviations

A, B	inputs of the Balancing Unit
BalUn	Balancing Unit
BLT	Baum-Liu-Tesche
BTL	bent transmission line
c	characteristic
C	output of the Balancing Unit
DCL	double conductor transmission line
DUT	device under test
e	external
EUT	equipment under test
EMC	electromagnetic compatibility
F	factor
FDM	Finite Difference Method
FEM	Finite Element Method
HF	high frequency
IMTL	isolated multiconductor transmission line
In	input
l	line
L	load
LF	low frequency
LUF	lowest usable frequency
max	maximum

meas	measure
min	minimum
MTL	multiconductor transmission line
MoM	Method of Moments
o	surface
OvGU	Otto von Guericke University
P	point
r	reflected
R	reference
rad	radiation
RC	reverberation chamber
ref	reference
rx	receiving antenna
s	scattered
SCL	single conductor transmission line
SMW	Sherman–Morrison–Woodbury
t	transverse
T	termination
tan	tangential
TL	transmission line
TLM	transmission line matrix
TLT	transmission line theory
tx	transmitting antenna
VNA	vector network analyzer

List of Figures

2.1	Single wire in y -direction with the vectors \mathbf{r}' and \mathbf{r}	21
2.2	Equivalent circuit of a single line over ground or a double wire line	26
2.3	Representation of the voltage between two points	27
2.4	Representation for determining the magnetic flux	28
2.5	Illustration of the method of images	29
2.6	Setting for the exact calculation of the p. u. l. parameters for two wires	30
2.7	Comparison of the exact and approximated p. u. l. capacitance	33
2.8	Transmission line of the length l terminated with a load impedance Z_L	35
2.9	Transmission line terminated at both ends with load impedances Z_{Li}	36
2.10	Definition of the wave vector and the electric field polarization	38
2.11	Setup to define the stochastic field excitation in <i>CONCEPT-II</i>	40
2.12	Photograph of the big reverberation chamber in Magdeburg	42
2.13	Two-port network (based on [Orf08, Fig. 14.1.1])	43
2.14	Photograph of the two-port Rohde&Schwarz VNA (ZVC 20 kHz...20 GHz)	45
2.15	Schematic of the measurement using a two-port vector network analyzer	45
2.16	Quality factor of the chamber	46
2.17	Photograph of a balancing unit	47
2.18	Photograph of the four-port Rohde&Schwarz VNA (ZNB, 9 kHz to 8.5 GHz)	48
2.19	Schematic of the measurement with a four-port vector network analyzer	49
2.20	Measurement setup for measuring the radiation losses	50
3.1	Single wire and its image in y -direction	51
3.2	Classical and high frequency characteristic impedance of a single wire	56
3.3	Equivalent circuit model with frequency-dependent p. u. l. parameters	57
3.4	Geometry of a straight single line over a ground plane	58
3.5	Real- and imaginary parts of the coupled current for a single line	62
3.6	Transmission line over a conductive ground plane in the reverberation chamber	63
3.7	Measured coupled voltage at the beginning of a single wire	64
3.8	Double wire in y -direction with the length l and the radii a_0 and a_1	64
3.9	Characteristic impedance over the frequency for a double wire	68
3.10	Geometry of an arbitrarily oriented and straight double wire line	68
3.11	Comparison of the coupled current of a single and double wire	70
4.1	Schematic of a bent single conductor transmission line	73

4.2	Characteristic impedance for a single wire with different bent angles	78
4.3	Equivalent circuit of a bent transmission line	79
4.4	Bent single-wire transmission line above the x - y -plane	80
4.5	Bent single line over a conductive ground plane with a bent angle ϕ	83
4.6	Simulated coupled voltage of the bent single wire (B-60)	84
4.7	Different bend angles of the transmission line	85
4.8	Coupled voltage at the beginning of the bent single line (B-60)	85
4.9	Schematic configurations of the bent line with different angles ϕ	86
4.10	Minimum distance between the terminations of the bent transmission line . .	86
4.11	Measured coupled voltage at the beginning of the bent transmission line . . .	87
4.12	Simulated coupled voltage of the bent single wire (B-10)	88
4.13	Ratio of the measured coupled voltage of the bent to the straight line	89
4.14	Measured radiation losses for different bend angles	90
4.15	Transmission line network over the ground plane	91
4.16	Coupled voltage for the basic configuration of the network	92
4.17	Coupled voltage of the network for varying the line lengths l_3	93
4.18	Schematic configurations of the network for different angles θ	94
4.19	Coupled voltage of the network for different alignment angles θ	94
4.20	Coupled voltage of the network for different termination loads	96
4.21	Curved single conductor transmission line over a conductive ground plane . .	97
4.22	Schematic of the measured configurations of the curved line	97
4.23	Different curved transmission line in the reverberation chamber	98
4.24	Comparison of the measured and simulated results of the curved line	98
4.25	Comparison of the measured coupled voltage of the curved lines	99
4.26	Comparison of the coupled voltage of the bent and curved line	99
4.27	Measured radiation losses for the 90° curved, straight and 90° bent line . . .	100
4.28	Schematic of the 90° curved line and lines with a different bend number . . .	101
4.29	Coupled voltage of the 90° curved line and different bent transmission lines .	101
5.1	Schematic of a multiconductor transmission line over ground	102
5.2	Multiconductor transmission line over ground plane with n wires	103
5.3	Multiconductor transmission line and its image wires	104
5.4	Equivalent circuit model of a two-wire multiconductor transmission line . . .	107
5.5	Comparison of the classical and high frequency characteristic impedance . . .	109
5.6	Load impedances of the multiconductor transmission line over ground plane.	110
5.7	Geometry of a uniform two-wire line over ground	112
5.8	Real- and imaginary parts of the coupled current of the two-wire line	113
5.9	Two-wire line over a ground plane at the same height	114
5.10	Coupled voltage of the two-wire line over ground at the same height	115
5.11	Detailed view of the line terminations of the two-wire line	116

5.12	Coupled voltage of the MTL with $Z_{L1,1} = 50\Omega$ and $Z_{L2,1} = 50\Omega$	117
5.13	Coupled voltage of the MTL with $Z_{L1,1} = 50\Omega$ and $Z_{L2,1} \mapsto \infty$	119
5.14	Coupled voltage of the MTL with $Z_{L1,1} = 50\Omega$ and $Z_{L1,2} = Z_{L2,1} = Z_{L2,2} \mapsto \infty$.	120
5.15	Further investigation of the load impedance on the coupled voltage	121
5.16	Two different arrangements of the of the two-wire line with different heights	122
5.17	Detailed view of the terminations of the two-wire line	122
5.18	Coupled voltage of the two-wire line with different heights	123
5.19	Different arrangements of the two-wire line with different line lengths	124
5.20	Coupled voltage of the two-wire line for different wire arrangements	125
5.21	Schematic of the three-wire transmission line	126
5.22	Coupled voltage at the terminals of a three-wire line over ground	127
5.23	Comparison of the measured coupled voltage of SCL and MZL	127
5.24	Example of an isolated multiconductor transmission line	128
5.25	Schematic of an isolated multiconductor transmission line	128
5.26	Characteristic impedance matrix for an isolated three-wire line	132
5.27	Balancing unit for the measurements with three wires	134
5.28	Planar arrangement of the isolated three-wire line	135
5.29	Coupled voltage of the planar arrangement of the isolated three-wire line . .	136
5.30	Equilateral triangular arrangement of the isolated three-wire line	137
5.31	Coupled voltage of the triangular arrangement of the isolated three-wire line	138
5.32	Detailed view of the variation of the line terminations	139
5.33	Coupled voltage of the planar arrangement for different load resistances . . .	140
5.34	Coupled voltage over the line length of the isolated three-wire line	142
5.35	Comparison of the measured coupled voltage for different MTL structures . .	143
B.1	Comparison of the solution for the exact and approximated function	154
C.1	Simulation model of the curved transmission line in <i>CONCEPT-II</i>	155
E.1	Photographs of the termination variations of the two-wire MTL	159
F.1	Replacing the simulated values at 0 Hz with zero in <i>MATLAB</i>	160

List of Tables

4.1	Resonance frequencies for different line lengths l_3 of the network	93
4.2	Variations of the terminating resistances of the network	95
5.1	Variations of the terminating resistances of the multiconductor wire	116
5.2	Resonance frequencies for the two-wire MTL over ground	118
5.3	Terminations of the MTL given as multiples of the characteristic impedance .	120
5.4	Variations of the arrangement of the two-wire line	124
5.5	Variations of the terminating resistances of the IMTL	141
E.1	Terminating resistances of the multiconductor wire	158

1 Introduction

This thesis is based on two major topics in electromagnetic compatibility (EMC). One topic is stochastic fields, in which neither the direction of incidence and the polarization nor the amplitude of the electrical and magnetic components are known exactly. The other topic is transmission lines, which represent an important coupling path for electromagnetic waves. If the data, such as geometry of the objects within the resonator, are not known exactly, the description by stochastic fields is a promising approach. During the last few years, a description by stochastic instead of deterministic methods have proven their worth in order to predict the behavior of electromagnetic fields in large and geometrically complex resonators [Hil09]. Complex resonators are e. g. airplanes, motor vehicles, helicopters, ships and other objects with an almost completely closed and conductive surface. Especially in the investigation of electromagnetic compatibility and wireless communication, problems must be solved whose boundary conditions are only inaccurately known. Transmission line theory (TLT) is essential in both radio frequency and microwave communications as well as in the design of fast digital circuits. This thesis combines circuit analysis with electromagnetics.

1.1 Reverberation Chambers

The topic of electromagnetic fields in resonators has a long history [Ser17]. Since more than four decades, reverberation chambers (RCs) have been used in EMC tests and experiments. They can be used for both immunity and emission testing. The first reported shielding effectiveness test (a typical EMC test) within a reverberation chamber dates from 1971 and is included in the military standard MIL-STD 1377 [Uni77].

A reverberation chamber represents a screened test environment with a field that is *statistically isotropic* and has a *random polarization*. Compared to traditional semi-anechoic chamber tests, the main advantage of EMC testing in a reverberation chamber is to provide *high field strengths* with moderate *input power*. Field strengths higher than $25 \frac{\text{V}}{\text{m}}$ for an input power of around 1 W are possible for typical room-sized chambers due to the resonant environment. Moreover, there is no need for absorbers. Testing in a reverberation chamber offers the possibility to simulate a complex field in a closed environment, because the field behaves like a random arrangement of plane waves from all directions. It is not necessary to perform multiple tests with different incident angles of the source. Moreover, *wide frequency*

ranges can be tested. Under the consideration that any loading causes a reduction of the working volume, even when the equipment under test (EUT) is non-absorbing, there is still the requirement that the EUT and all supporting equipment shall not occupy more than 8 % of the total chamber volume [Int03, Clause D.1]. For emission tests the main advantage is the measured *total radiated power*. Furthermore, emission as well as immunity tests inside a reverberation chamber are not included in many current standards. The biggest challenge is the comparability with other established measurement environments, because there is no simple method to convert the measured results.

1.2 Transmission Lines

Transmission lines such as signal lines, communication lines, power supply cables, etc. can act as parasitic antennas. Therefore, the investigation of the field coupling to e. g. power supply cables and communication lines is essential for EMC.

Now the question is how to select a suitable test object to investigate the coupling of the stochastic field to the EUT. The test object should be easy to install, the measurement setup should be as uncomplicated as possible and various parameters should be quickly changeable. A test object that fulfills all these conditions is a transmission line (TL). In addition, parameter studies can easily be carried out by changing the cable length, loads, distances or similar parameters of the transmission line. The main advantage of transmission lines as EUTs is, that they can be modeled quite simple, and the per-unit-length (p.u.l.) parameters and equivalent circuit can be calculated without too much effort. Due to the well-known transmission line theory, measured and simulated effects and results can be assigned and evaluated easily.

There are different ways of modeling a transmission line. Often transmission lines are characterized by its transmission line parameters, which are also accessible via mathematical modeling. Other aspects that, apart from the type of material the transmission line is made of, influence the transmission line parameters are the operating frequency, the temperature and the length of the transmission line itself. In classical (low frequency) transmission line theory wires connect devices but are not represented in the model with any resistance. Moreover, there is no phase delay between the wires. At higher frequencies, transmission lines can behave very differently. Indeed, short-circuits can have infinite impedance and open circuits can behave like short-circuited lines. In this thesis, transmission lines without any plastic insulation are selected because such plastic insulation and its complex permeability would lead to additional uncertainties in the model.

1.3 Key Questions

The coupling of the chamber field to one-dimensional transmission lines has also been widely investigated in [MTV11], [JPD10] and [Lan10]. There is still a great need for research into three-dimensional structures, such as multiconductor transmission lines. Within this thesis a simulation model in MATLAB was developed to describe the coupling of stochastic fields into different line structures. This model should include coupling effects and crosstalk between the lines as well as effects caused by e. g. bending of the line.

The main questions are:

How does the coupled voltage to a transmission line depend on the stochastic electromagnetic field?

Can an efficient estimation of the coupled voltage be made?

Basically, existing models were used in this thesis and extended under consideration of effects like crosstalk, bending or coupling. Of particular interest is here:

How do existing models for the field coupling to single wire line structures have to be changed to apply to other transmission line structures like bent and multiconductor transmission lines?

The previous models are based on the classical transmission line theory which keeps the modeling quite simple. The main assumption is that the distance between the lines and the return path of the line (ground plane or return conductor) should be much smaller than the minimum relevant wavelength of the current in the line ($kh \ll 1$). An important question, which will be addressed in this thesis is

What happens at high frequencies and is the classical model still valid?

How must the model be modified?

This thesis is focused on these questions through the analytical description of the field-to-wire coupling. The results are compared with measurements and simulations based on the method of moments (MoM) as well as the results of an already consisting model.

1.4 Objective and Structure of the Work

In a first step, the theoretical fundamentals of transmission line theory and stochastic electromagnetic fields are introduced in Chapter 2. All necessary theoretical and mathematical descriptions for the analysis of the coupling into single and multiconductor lines as well as the occurrence and the analytical description of stochastic fields are described. Moreover, the measurements in the reverberation chamber are explained in detail, as well as the used measuring equipment and measuring procedure. The conversion of the measured parameters into the coupled voltage, which is investigated in this thesis, is also discussed. Chapter 3 deals with the coupling of stochastic fields into single lines. First a straight single line is considered and its modeling is discussed. Then the measured and simulated results are compared. Moreover, the modeling of a double conductor transmission line in free space is presented and compared to the single wire case. Chapter 4 describes how the model is extended for a bent single cable. The simulated results are compared with measurements in the reverberation chamber. Furthermore, measurements of a curved line were investigated and compared with the previous results of a straight and a bent line. In addition, Chapter 5 deals with the investigation of the coupling to multiconductor transmission lines. The transmission line modeling as well as the field-to-wire coupling are described, and the simulation and measurement results are compared to each other. The models and results for a multiconductor transmission line over a conductive ground plane and in free space are also compared.

The investigations of the different transmission line structures within this thesis are always structured in the same way. First, the line is analytically modeled and then the coupling is mathematically described. This semi-analytical model is validated by using a simulation based on the MoM. The semi-analytical simulation is then compared with real measurements in a reverberation chamber. In addition, the results of the different transmission line structures are compared with each other.

2 Fundamental Tools for Determining the Stochastic Field-to-Wire Coupling

This chapter contains the basis for the understanding of stochastic fields coupled to transmission lines in reverberation chambers. First, the theoretical modeling of transmission lines and stochastic electromagnetic fields are given followed by the measurement setup and procedure in a reverberation chamber. Finally, the necessary theories and mathematical descriptions of the coupled voltage or current and their calculation from the measured data are presented in detail.

2.1 Derivation of the Field-To-Wire Coupling Equations

This section explains the field-wire coupling equations for a general single wire over a conductive ground plane. The derivation starts from the integral form of Maxwell's equations and in a next step the equivalent circuit and the per-unit-length (p. u. l.) distributed parameters are given. This derivation will be the starting point for the theoretical modeling of a double wire, a bent single wire and a multiconductor transmission line.

2.1.1 Inhomogeneous Wave Equations

For the derivation of the transmission line equations, Maxwell's equations are provided, that describe all classical electromagnetic phenomena [Jac99, Ch. 6, Eq. (6.1)]

$$\nabla \times \mathbf{E} = -\frac{\partial \mathbf{B}}{\partial t}, \quad \text{Faraday's law of induction} \quad (2.1a)$$

$$\nabla \times \mathbf{H} - \varepsilon \frac{\partial \mathbf{E}}{\partial t} = \mathbf{J}, \quad \text{Ampere's law} \quad (2.1b)$$

$$\nabla \cdot \mathbf{E} = \frac{\rho}{\varepsilon}, \quad \text{Gauss' law} \quad (2.1c)$$

$$\nabla \cdot \mathbf{B} = 0. \quad \text{Gauss' law for magnetism} \quad (2.1d)$$

Vector quantities are represented by bold symbols and scalar quantities by italic symbols. Maxwell's equation (2.1) relates the electric field \mathbf{E} and the magnetic field intensity \mathbf{H} . The sources are the total electric charge density ρ and the total electric current density \mathbf{J} . The

universal constants of the magnetic permeability μ and the electric permittivity ε also appear in the equations. The righthand side of Eq. (2.1d) is zero because there are no magnetic monopoles. The electric and magnetic flux densities \mathbf{D} and \mathbf{B} are connected to the field strengths \mathbf{E} and \mathbf{H} via the constitutive relations. The exact form of the constitutive relations depends on the material under consideration. For a linear, isotropic and homogeneous medium the relations are given by [Hen15, p. 494]

$$\mathbf{D} = \varepsilon \cdot \mathbf{E}, \quad (2.2a)$$

$$\mathbf{B} = \mu \cdot \mathbf{H}, \quad (2.2b)$$

$$\mathbf{J} = \kappa \cdot \mathbf{E}, \quad (2.2c)$$

where κ , ε and μ do not depend on space and time. The electrical conductivity κ quantifies the ability of a material to transport electrical current. From Eq. (2.1d), it can be concluded that \mathbf{H} can be represented by the rotation of a vector potential \mathbf{A} i. e.

$$\mu \mathbf{H} = \nabla \times \mathbf{A}. \quad (2.3)$$

Inserting \mathbf{H} in Eq. (2.1a) leads to

$$\nabla \times \left(\mathbf{E} + \mu \frac{\partial \mathbf{A}}{\partial t} \right) = 0. \quad (2.4)$$

The rotation of a vanishing vector field can be expressed by a gradient of the electric potential Φ

$$\mathbf{E} + \mu \frac{\partial \mathbf{A}}{\partial t} = -\nabla \Phi. \quad (2.5)$$

Solving for \mathbf{E} results in

$$\mathbf{E} = -\nabla \Phi - \mu \frac{\partial \mathbf{A}}{\partial t}. \quad (2.6)$$

After inserting Eq. (2.3) and (2.6) in Eq. (2.1b) and (2.1c), one obtains

$$\nabla(\nabla \cdot \mathbf{A}) - \nabla^2 \mathbf{A} + \varepsilon \nabla \frac{\partial \Phi}{\partial t} + \mu \varepsilon \frac{\partial^2 \mathbf{A}}{\partial t^2} = \mu \mathbf{J}, \quad (2.7a)$$

$$\nabla^2 \Phi + \mu \frac{\partial}{\partial t} \nabla \cdot \mathbf{A} = -\frac{\rho}{\varepsilon}. \quad (2.7b)$$

Eqs. (2.7a) and (2.7b) are invariant under the following gauge transformations [Hen15, Eq. (16.7)]

$$\mathbf{A} = \mathbf{A}^* - \nabla \Psi, \quad (2.8a)$$

$$\Phi = \Phi^* + \mu \frac{\partial \Psi}{\partial t}. \quad (2.8b)$$

The magnetic flux density and the electric field are transformed as

$$\mathbf{B} = \nabla \times \mathbf{A}^* = \nabla \times (\mathbf{A} + \nabla \Psi) = \nabla \times \mathbf{A}, \quad (2.9a)$$

$$\mathbf{E} = -\nabla \Phi^* - \mu \frac{\partial \mathbf{A}^*}{\partial t} = \nabla \left(\Phi - \mu \frac{\partial \Psi}{\partial t} \right) - \mu \frac{\partial}{\partial t} (\mathbf{A} + \nabla \Psi) = -\nabla \Phi - \mu \frac{\partial \mathbf{A}}{\partial t}. \quad (2.9b)$$

The Lorenz gauge [Jac99, Ch. 6.3] condition is used to decouple Eq. (2.7)

$$\nabla \cdot \mathbf{A} = -\varepsilon \frac{\partial \Phi}{\partial t} \quad (2.10a)$$

and result in the inhomogeneous wave equations [Hen15, Eq. (16.9)]

$$\nabla^2 \mathbf{A} - \mu \varepsilon \frac{\partial^2 \mathbf{A}}{\partial t^2} = -\mathbf{J}, \quad (2.11)$$

$$\nabla^2 \Phi - \mu \varepsilon \frac{\partial^2 \Phi}{\partial t^2} = -\frac{\rho}{\varepsilon}. \quad (2.12)$$

A transformation into the frequency domain leads to

$$\nabla^2 \mathbf{A} + \omega^2 \mu \varepsilon \mathbf{A} = -\mathbf{J}, \quad (2.13a)$$

$$\nabla^2 \Phi - \omega^2 \mu \varepsilon \Phi = -\frac{\rho}{\varepsilon}, \quad (2.13b)$$

where all quantities are now complex quantities. Since the frequency domain formulation is used throughout this thesis no other notation is introduced. The solution of the inhomogeneous wave equations is similar to [Hen15, Eqs. (16.16) and (16.17)]

$$\mathbf{A}(\omega, \mathbf{r}) = \frac{1}{4\pi} \int_{V'} g(\mathbf{r}, \mathbf{r}') \mathbf{J}(\mathbf{r}') d^3 \mathbf{r}', \quad (2.14a)$$

$$\Phi(\omega, \mathbf{r}) = \frac{1}{4\pi \varepsilon} \int_{V'} g(\mathbf{r}, \mathbf{r}') \rho(\mathbf{r}') d^3 \mathbf{r}'. \quad (2.14b)$$

Here, $g(\mathbf{r}, \mathbf{r}')$ describes the Green's function [Jac99, Ch. 1.10].

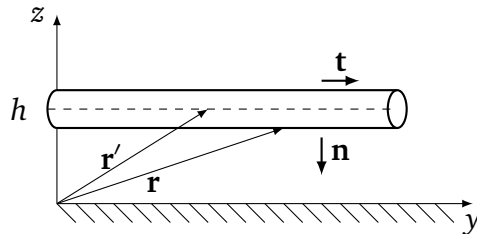


Figure 2.1: Single wire in y -direction with the vectors \mathbf{r} and \mathbf{r}' to the source and observation points on the wire

The Green's function of a wire configuration as given in Fig. 2.1 is

$$g(\mathbf{r}, \mathbf{r}') = \frac{\mu e^{-jk|\mathbf{r}-\mathbf{r}'|}}{4\pi |\mathbf{r}-\mathbf{r}'|}, \quad (2.15)$$

where \mathbf{r}' is pointing to the observation point and \mathbf{r} to the source point. The wave vector \mathbf{k} defines the polarization of the incident wave. For notational convenience ω is omitted in $\mathbf{A}(\omega, \mathbf{r})$ and $\Phi(\omega, \mathbf{r})$. The last needed equation is the continuity equation, which follows from the divergence of Eq. (2.1b) and using Eq. (2.1c)

$$\nabla \cdot (\nabla \times \mathbf{H}) = 0 = \nabla \cdot \mathbf{J} + \nabla \cdot \frac{\partial \mathbf{D}}{\partial t}, \quad (2.16a)$$

$$\nabla \cdot \mathbf{J} = -\frac{\partial}{\partial t} \nabla \cdot \mathbf{D} = -\frac{\partial \rho}{\partial t}. \quad \text{Continuity equation} \quad (2.16b)$$

Now, all the equations are known, that are needed to describe the following field-to-wire coupling in the next section.

2.1.2 Field-to-Wire Coupling Equations

Using the introduced basic theory, one can derive the general field-to-wire coupling equations. A transmission line can act like a transmitting or receiving antenna driven by an external source. The total electric field is the sum of the external source field \mathbf{E}^e and the scattered field \mathbf{E}^s . Assuming a perfectly conducting wire, the electric field has to be tangential to the surface of the conductor ([Orf08, Ch. 24])

$$\mathbf{t} \cdot \mathbf{E} = \mathbf{t} \cdot (\mathbf{E}^e + \mathbf{E}^s) = 0. \quad (2.17)$$

The scattered electric field can be expressed by the vector potential according to Eq. (2.6) in the frequency domain as

$$\mathbf{E}^s = -j\omega\mu\mathbf{A} - \nabla\Phi, \quad (2.18)$$

where (ω, \mathbf{r}) is omitted for brevity. The charge density in Eq. (2.14b) along the conductor can be described with the help of the continuity Eq. (2.16b) in frequency domain

$$\rho = -\frac{1}{j\omega} \nabla \cdot \mathbf{J}. \quad (2.19)$$

Using Eq. (2.18), for Eq. (2.17) follows

$$\mathbf{t} \cdot (\mathbf{E}^e(\mathbf{r}) - j\omega\mu\mathbf{A}(\mathbf{r}) - \nabla\Phi(\mathbf{r})) = 0. \quad (2.20)$$

Inserting Eq. (2.14a) in Eq. (2.20), the general electromagnetic field coupling equations for transmission lines are given by

$$\nabla\Phi(\mathbf{r}) + j\omega\mu \int_{V'} g(\mathbf{r}, \mathbf{r}') \mathbf{J}(\mathbf{r}') d^3\mathbf{r}' = \mathbf{t} \cdot \mathbf{E}^e(\mathbf{r}) \quad (2.21a)$$

$$\Phi(\mathbf{r}) - \int_{V'} g(\mathbf{r}, \mathbf{r}') \rho(\mathbf{r}') d^3\mathbf{r}' = 0. \quad (2.21b)$$

For the field-to-wire coupling to a single wire above ground, the scattered voltage is defined by the integral along the normal electrical field between the conductor and the conducting plane

$$U^s(\mathbf{t}) = - \int_0^h \mathbf{E}_n^s d\mathbf{n}', \quad (2.22)$$

where \mathbf{n} and \mathbf{t} are the normal and tangential vector along the line respectively. Considering in Eq. (2.18) only the normal components of the electric field

$$\mathbf{E}_n^s = -\nabla\Phi, \quad (2.23)$$

one obtains for the scattered voltage from Eq. (2.22)

$$U^s(\mathbf{t}) = \Phi(\mathbf{r}) - \Phi(\mathbf{r}_{\text{ref}}). \quad (2.24)$$

For the wire from Fig. 2.1 at the height h , the vector \mathbf{r} points to the source point on the surface of the conductor and the vector \mathbf{r}_{ref} points to the ground plane. With the boundary condition $\Phi(\mathbf{r}_{\text{ref}}) = 0$, i. e. the potential on the ground plane is zero, follows

$$U^s(\mathbf{t}) = \Phi(\mathbf{r}). \quad (2.25)$$

If Eq. (2.25) is used in Eq. (2.21a), one gets

$$\nabla U^s(\mathbf{t}) + j\omega \underbrace{\frac{\mu}{4\pi} \int_{V'} g(\mathbf{r}, \mathbf{r}') \mathbf{J}(\mathbf{r}') d^3\mathbf{r}'}_{A(\mathbf{r})} = E_{\text{tan}}^e(\mathbf{t}), \quad (2.26a)$$

$$\Phi(\mathbf{t}) = 0. \quad (2.26b)$$

Here, E_{tan}^e is the external tangential electric field. The Green's function $g(\mathbf{r}, \mathbf{r}')$ is determined by the specific transmission line configuration and geometry of the transmission lines and will be discussed in the following.

Now, the integrals of the Green's function must be solved. Depending on the transmission line arrangement and the geometry, thus the description for \mathbf{J} and the Green's function $g(\mathbf{r}, \mathbf{r}')$ change. Hence, different geometries of a transmission line are investigated in the later chapters.

2.2 Transmission Line Theory

Transmission line theory uses Maxwell's equations to determine some p. u. l. parameters of the conductor. This makes it possible to qualitatively understand the processes and wave phenomena (e. g. reflections, standing waves) that occur on transmission lines, to quantify them and to interpret them correctly for practical applications.

2.2.1 Arbitrary Straight Transmission Line

This section contains the theoretical description of the current density and vector potential of a transmission line. The current density along an arbitrary oriented straight transmission line is given by

$$\mathbf{J}(\mathbf{r}) = \begin{cases} J(p) \cdot \mathbf{t} & \begin{cases} 0 \leq p \leq l \\ \mathbf{1} \end{cases} \\ 0 & \text{else,} \end{cases} \quad (2.27)$$

where \mathbf{t} is a vector along the wire

$$\mathbf{t} = \begin{pmatrix} t_x \\ t_y \\ t_z \end{pmatrix} = \frac{1}{l} \begin{pmatrix} x_2 - x_1 \\ y_2 - y_1 \\ z_2 - z_1 \end{pmatrix}. \quad (2.28)$$

The length of the line can be determined using

$$l = \sqrt{(x_2 - x_1)^2 + (y_2 - y_1)^2 + (z_2 - z_1)^2}. \quad (2.29)$$

The start and end points of the line are (x_1, y_1, z_1) and (x_2, y_2, z_2) , respectively. The vector along the straight line in free space is given by

$$\mathbf{l} = p \cdot \frac{1}{l} \cdot \begin{pmatrix} x_2 - x_1 \\ y_2 - y_1 \\ z_2 - z_1 \end{pmatrix} + \begin{pmatrix} x_1 \\ y_1 \\ z_1 \end{pmatrix}, \quad (2.30)$$

Using Dirac deltas $\delta(x)$ and Heaviside functions $\Theta(x)$, one can write this as

$$\begin{aligned} \mathbf{J}(\mathbf{r}) = & J(p) \cdot \mathbf{t} \cdot \delta(x - (p \cdot (x_2 - x_1) + x_1)) \cdot \delta(y - (p \cdot (y_2 - y_1) + y_1)) \\ & \cdot \delta(z - (p \cdot (z_2 - z_1) + z_1)) \cdot [\Theta(p) - \Theta(p - l)]. \end{aligned} \quad (2.31)$$

Here, p is the variable to define a point on the wire and is between 0 and l . If the transmission line is composed of small pieces and these are infinite small, the current density of a straight

conductor described in Eq. (2.31) follows with

$$\mathbf{J}(\mathbf{r}) = \int_0^l J(p') \cdot \mathbf{t} \cdot \delta(x - (p' \cdot (x_2 - x_1) + x_1)) \cdot \delta(y - (p' \cdot (y_2 - y_1) + y_1)) \cdot \delta(z - (p' \cdot (z_2 - z_1) + z_1)) \cdot [\Theta(p') - \Theta(p' - l)] dp' . \quad (2.32)$$

From the Helmholtz Eq. (2.14b), for the vector potential one obtains

$$\mathbf{A}(\mathbf{r}) = \frac{\mu}{4\pi} \int_{-\infty}^{\infty} \int_{-\infty}^{\infty} \int_{-\infty}^{\infty} \int_0^l J(p') \cdot \mathbf{t} \cdot \delta(x' - (p' \cdot (x_2 - x_1) + x_1)) \cdot \delta(y' - (p' \cdot (y_2 - y_1) + y_1)) \cdot \delta(z' - (p' \cdot (z_2 - z_1) + z_1)) \cdot [\Theta(p') - \Theta(p' - l)] \cdot \frac{e^{-jkR}}{R} dx' dy' dz' dp' , \quad (2.33)$$

where R is given by

$$R = |\mathbf{r} - \mathbf{r}'| = \sqrt{(x - x')^2 + (y - y')^2 + (z - z')^2}. \quad (2.34)$$

With the position vector $\mathbf{r}' = x'\mathbf{e}_x + y'\mathbf{e}_y + z'\mathbf{e}_z$ that points to the observation point on the wire and $\mathbf{r} = x\mathbf{e}_x + y\mathbf{e}_y + z\mathbf{e}_z$ points to the source point on the wire. The remaining task is to perform the integrations along x , y , z and p which will be done in the following chapters for different transmission line structures.

2.2.2 Per-Unit-Length Parameters

Devices under test (DUTs) that are considerably larger than the wavelength are so called electrically large DUTs, which also occur in the literature as high frequency problems [Per95]. In the case of an electrically small DUT the wave propagation effects must not be taken into account and the transmission lines can be described by classical transmission line theory [TIK96], which is introduced in this chapter. With the help of classical transmission line theory, different types of lines can be investigated, where the following assumptions are made [Kin55]:

- The geometry of the line is uniform over the length of the line.
- The distance between the lines and its return path (ground plane or return conductor) is much smaller than the minimum considered wavelength of the current flowing in the line.
- The line current is balanced (sum of forward and return current is zero).

All cross-sectional dimensions of a cable, such as wire radii or conductor spacing, are summarized in the p. u. l. parameters. If the cable is uniform over its length, the electrical parameters of the cable are considered constant. To consider a transmission line as uniform, two conditions must be fulfilled [TIK96]:

- The conductors must be parallel to each other as well as to the ground plane.
- Any dielectric material around the line must be translationally symmetrical over the entire length of the line.

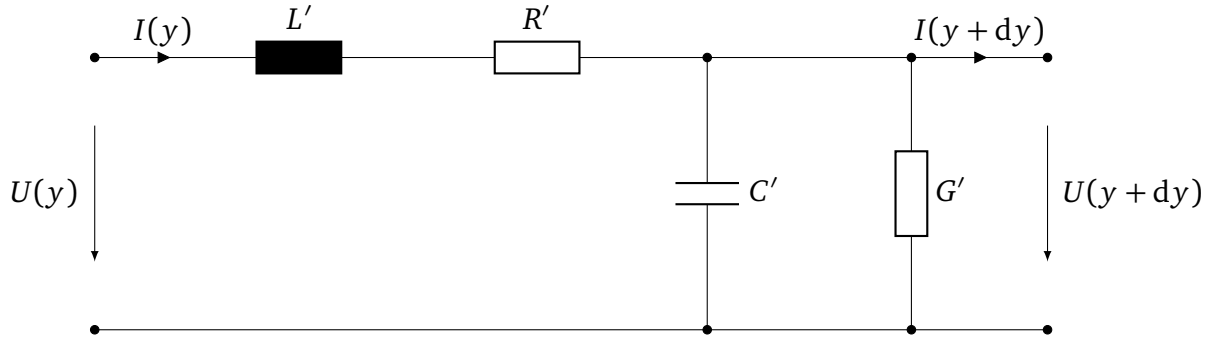


Figure 2.2: Equivalent circuit of short section of a single line over ground or a two-wire line

Using the p. u. l. parameters of a transmission line system, an equivalent circuit can be determined. The equivalent circuit of a short section of a single cable at a distance from a reference conductor or above a conductive ground plane is shown in Fig. 2.2. The simplest case of such line is called a Lecher line. It consists of two parallel wires of finite thickness which are mutually isolated. The elements contain the length-related cable parameters. Here, L' is the p. u. l. inductance, C' the p. u. l. capacitance, R' the p. u. l. resistance and G' the p. u. l. conductance ([Per95], p. 78 ff.). The line has a specific radius a and a length l .

Considering a short section of a line of Fig. 2.2 between y and $y + dy$, using the p. u. l. parameters of the line and putting them into Eq. (2.26), the so-called Telegrapher's equation [Per95, Eq.(22)] can be obtained

$$\frac{d}{dy} U^s(y) + I(y) \cdot \underbrace{(j\omega L' + R')}_Z = E_{\tan}^e, \quad (2.35a)$$

$$\frac{d}{dy} I(y) + U^s(y) \cdot \underbrace{(j\omega C' + G')}_Y = 0. \quad (2.35b)$$

The combined terms $(j\omega L' + R')$ and $(j\omega C' + G')$ are denoted as the p. u. l. line impedance Z and admittance Y , respectively.

The line parameters can be determined by measurements as well as by calculations. In the following sections, the determination of the p. u. l. parameters is done for the classical low frequency case, where the parameters only depend on the cross-sectional geometry of the line.

2.2.2.1 Fundamental Subproblems of Wires

In order to determine simple relations for the p. u. l. parameters of the wires, the following important subproblems must be discussed (as done in [Pau08]).

Voltage Between Two Points

To determine the p. u. l. capacitance, the voltage between two points must be observed. Considering a charge-carrying wire with a cylindrical radius a as shown in Fig. 2.3 and using Gauss' law (2.1c), the following applies to the electric field

$$\mathbf{E} = \frac{\rho_1}{2\pi\epsilon a}, \quad (2.36)$$

where ρ_1 is the line charge.

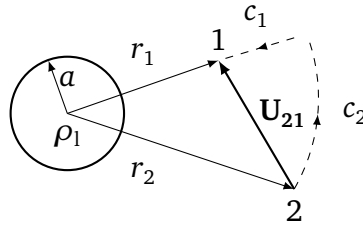


Figure 2.3: Representation of the voltage between two points

To determine the voltage between two points which have the radial distances r_1 and r_2 from the conductor (Fig. 2.3), the integral

$$\mathbf{U}_{21} = - \int_c \mathbf{E} d\mathbf{l} \quad (2.37)$$

between these two points must be evaluated respecting the condition $r_2 \geq r_1$. For symmetry reasons, the electric field is perpendicular to the contour c_2 with the distance r_2 . Thus, the second part of the integral over c_2 does not contribute and one obtains

$$\mathbf{U}_{21} = - \int_{c_1} \mathbf{E} d\mathbf{l} - \underbrace{\int_{c_2} \mathbf{E} d\mathbf{l}}_{=0}. \quad (2.38)$$

The voltage can be determined by integrating between r_2 and r_1 leading to

$$\mathbf{U}_{21} = - \int_{r_1}^{r_2} \frac{\rho_1}{2\pi\epsilon r} dr = \frac{\rho_1}{2\pi\epsilon} \ln\left(\frac{r_2}{r_1}\right). \quad (2.39)$$

Because of $r_2 > r_1$, the voltage is positive, and it is higher when getting closer to r_1 .

Magnetic Flux

In this subsection, the inductance of the transmission line is determined. Two subproblems must be considered. First, the magnetic flux Ψ which penetrates a surface A as shown in Fig. 2.4a. The surface is parallel to the wire and has a uniform cross section along the wire length. Next, the cross section as shown in Fig. 2.4b must be considered.

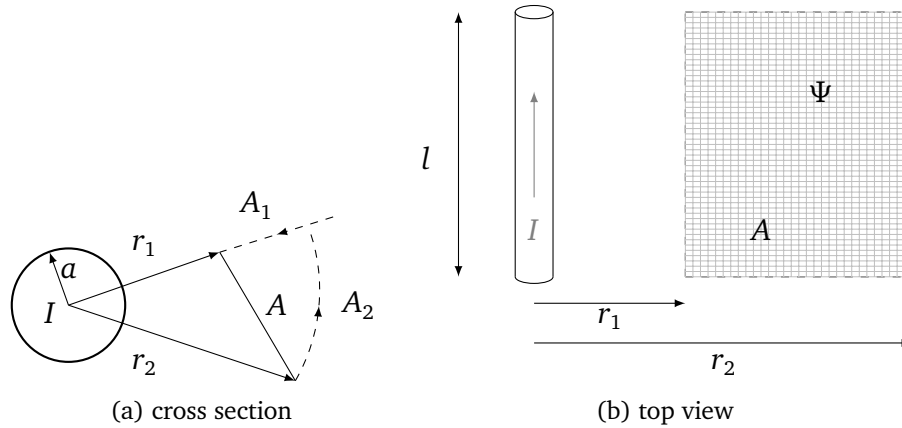


Figure 2.4: Representation for determining the magnetic flux through an area A due to a current-carrying wire

A current I through a conductor results in a magnetic field \mathbf{H} . The relationship between the magnetic flux and current is described by the law of induction

$$I = \oint \mathbf{H} d\mathbf{l}. \quad (2.40)$$

For a circular contour with the radius a it follows

$$\mathbf{B} = \frac{\mu I}{2\pi a}. \quad (2.41)$$

This surface A in Fig. 2.4b has the same length as the conductor and lies between radius r_2 and r_1 . By integrating the magnetic flux over the surface A , one obtains for $r_2 > r_1$

$$\Psi = I \int_{r_2}^{r_1} \mathbf{B} d\mathbf{r} = \frac{\mu I}{2\pi} \ln\left(\frac{r_2}{r_1}\right) \cdot l. \quad (2.42)$$

Method of Images

The method of images is a method used to solve boundary value problems [Jac99, Ch. 2.1]. This method is used, for example, to determine the behavior of a charge q that is located at h over a conductive ground or dielectric interface. The infinite plane can be replaced with an equal but negative charge $-q$ at a distance h below the plane under consideration, and the resulting electric fields will be identical to them above the surface of the plane (see Fig. 2.5). The charge $-q$ is also called a mirror charge.

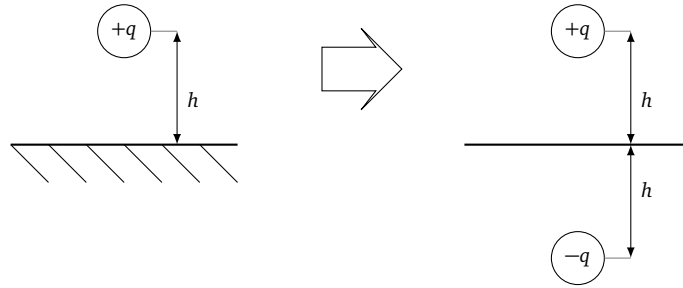


Figure 2.5: Illustration of the method of images: charge above a perfectly conducting plane

2.2.2.2 Definition of the Per-Unit-Length Inductance and Capacitance

Now, a double conductor transmission line (DCL) with the radii a_0 and a_1 and the distance s between the centers of the wires, is considered (see Fig. 2.6). To determine the p. u. l. inductance, the total flux must be considered. The total flux passing between the wires is given by

$$\Psi = \frac{\mu I}{2\pi} \ln\left(\frac{s-a_1}{a_0}\right) + \frac{\mu I}{2\pi} \ln\left(\frac{s-a_0}{a_1}\right) = \frac{\mu I}{2\pi} \ln\left(\frac{(s-a_1)(s-a_0)}{a_1 a_0}\right) \cdot l. \quad (2.43)$$

If the wires are widely separated ($a_0, a_1 \ll s$), the inductance is given by

$$L'_{\text{DCL}} = \frac{\Psi}{I} = \frac{\mu}{2\pi} \ln\left(\frac{s^2}{a_1 a_0}\right) \quad (2.44)$$

as described in [KMR08, Ch. 11.6]. If the wire radii are the same, i. e. $a_1 = a_0 = a$, the equation can be simplified to

$$L'_{\text{DCL}} = \frac{\Psi}{I} = \frac{\mu}{\pi} \ln\left(\frac{s}{a}\right). \quad (2.45)$$

The p. u. l. capacitance can be determined similarly. The voltage between two wires carrying uniformly distributed charge around each wire periphery can be obtained by superimposing the voltages

$$U = \frac{+q}{2\pi\epsilon} \ln\left(\frac{s-a_1}{a_0}\right) + \frac{-q}{2\pi\epsilon} \ln\left(\frac{s-a_0}{a_1}\right). \quad (2.46)$$

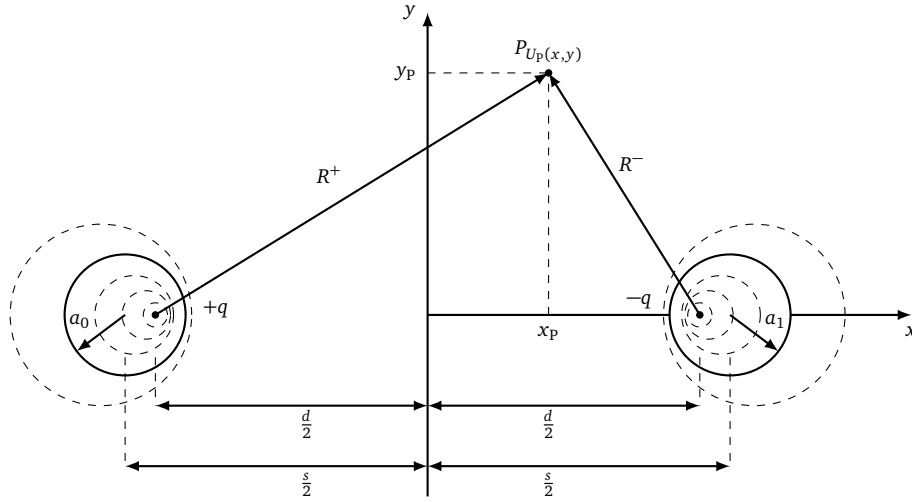


Figure 2.6: Setting for the exact calculation of the p. u. l. parameters for two wires

If both wires carrying the same charge q , Eq. (2.46) can be simplified to

$$U = \frac{q}{2\pi\epsilon} \ln\left(\frac{(s-a_1)(s-a_1)}{a_0a_1}\right). \quad (2.47)$$

Using again that the lines are far away from each other it follows

$$U = \frac{q}{2\pi\epsilon} \ln\left(\frac{s^2}{a_0a_1}\right). \quad (2.48)$$

Exploiting this result the p. u. l. capacitance is obtained [KMR08, chapter 11.6]

$$C'_{\text{DCL}} = \frac{q}{U} = \frac{2\pi\epsilon}{\ln\left(\frac{s^2}{a_0a_1}\right)}, \quad (2.49)$$

and for equal wire radii $a_1 = a_2$ this simplifies to

$$C'_{\text{DCL}} = \frac{\pi\epsilon}{\ln\left(\frac{s}{a}\right)}. \quad (2.50)$$

Exact Derivation of the Per-Unit-Length Inductance and Capacitance

In the following an exact derivation of the p. u. l. parameters analogous to [Pau08] is given. First, the p. u. l. capacitance is determined. To explain the p. u. l. capacitance one considers two wires with a p. u. l. charge $+q$ and $-q$ on its wires are assumed. The charge per unit of line length is separated by a distance d from the coordinate origin as shown in Fig. 2.6. The voltage at a point P in free space is given by

$$U_p(x, y) = -\frac{+q}{2\pi\epsilon} \ln\left(\frac{R^+}{d/2}\right) + \frac{-q}{2\pi\epsilon} \ln\left(\frac{R^-}{d/2}\right). \quad (2.51)$$

For two wires with similar p. u. l. charge q follows

$$U_p(x, y) = -\frac{+q}{2\pi\epsilon} \ln\left(\frac{R^+}{d/2}\right) + \frac{-q}{2\pi\epsilon} \ln\left(\frac{R^-}{d/2}\right) = \frac{q}{2\pi\epsilon} \ln\left(\frac{R^-}{R^+}\right). \quad (2.52)$$

Next, the equipotential contours around the charges $+q$ and $-q$ are determined, which correspond to the voltage of the wires. The equivalent distance s between the two wires carrying the same charge q . The points on the equipotential contours are selected in such a way that the ratio R^-/R^+ is constant and defined by

$$K = \frac{R^-}{R^+} = e^{\frac{2\pi\epsilon U_p}{q}}. \quad (2.53)$$

The distances R^+ and R^- can be written as

$$R^+ = \sqrt{\left(x_p + \frac{d}{2}\right)^2 + y_p^2} \quad (2.54)$$

and

$$R^- = \sqrt{\left(x_p - \frac{d}{2}\right)^2 + y_p^2}. \quad (2.55)$$

Substituting these distances in Eq. (2.53), leads to

$$\frac{\left(x_p - \frac{d}{2}\right)^2 + y_p^2}{\left(x_p + \frac{d}{2}\right)^2 + y_p^2} = K^2. \quad (2.56)$$

Rewriting the last equation results in

$$x_p^2 + x_p d \frac{K^2 + 1}{K^2 - 1} + \frac{d^2}{4} + y_p^2 = 0. \quad (2.57)$$

To determine the position of the circular equipotential surfaces that define the equivalent conductors and their radii, Eq. (2.57) is written into the equation of a circle that is located at $x_p = -\frac{s}{2}$ and has a radius of a

$$\left(x_p + \frac{s}{2}\right)^2 + y_p^2 = a^2. \quad (2.58)$$

Expanding this equation leads to

$$x_p^2 + x_p s + \left(\frac{s}{2}\right)^2 - a^2 + y_p^2 = 0. \quad (2.59)$$

Comparing Eq. (2.57) and Eq. (2.59), the following can be derived

$$\frac{s}{2} = \frac{d K^2 + 1}{2 K^2 - 1}, \quad (2.60a)$$

$$a = \frac{Kd}{K^2 - 1}. \quad (2.60b)$$

Dividing Eq. (2.60a) by Eq. (2.60b), one can write

$$K^2 - \frac{s}{a}K + 1 = 0 \quad (2.61)$$

Solving for the constant K results in

$$K = \frac{s}{2a} \pm \sqrt{\left(\frac{s}{2a}\right)^2 - 1} \quad (2.62)$$

Substitute K into Eq. (2.52), the voltage becomes

$$U_p = \frac{q}{2\pi\epsilon} \ln \left[\frac{s}{2a} \pm \sqrt{\left(\frac{s}{2a}\right)^2 - 1} \right]. \quad (2.63)$$

Considering that this is the voltage of the point with respect to the origin of the coordinate system located in the middle between the two wires, the voltage between the two wires separated by a distance s is thus

$$U = 2U_p = \frac{q}{\pi\epsilon} \ln \left[\frac{s}{2a} + \sqrt{\left(\frac{s}{2a}\right)^2 - 1} \right]. \quad (2.64)$$

Then, the p. u. l. capacitance can be defined by

$$C'_{\text{DCL}} = \frac{q}{U} = \frac{\pi\epsilon}{\ln \left[\frac{s}{2a} + \sqrt{\left(\frac{s}{2a}\right)^2 - 1} \right]}. \quad (2.65)$$

With the definition of the inverse hyperbolic cosine

$$\text{arcosh}(x) = \ln \left[x + \sqrt{x^2 - 1} \right], \quad (2.66)$$

Eq. (2.65) can be rewritten as

$$C'_{\text{DCL}} = \frac{\pi\epsilon}{\text{arcosh}\left(\frac{s}{2a}\right)}. \quad (2.67)$$

If the wire radii are not equal, the corresponding exact result for the p. u. l. capacitance becomes (derivation in [Fra77])

$$C'_{\text{DCL}} = \frac{\pi\epsilon}{\text{arcosh}\left(\frac{s^2 - a_2^2 - a_1^2}{2a_2a_1}\right)}. \quad (2.68)$$

For transmission lines in homogeneous medium the p. u. l. parameters are related as described in [Pau08]

$$L' C' = \mu \epsilon \quad (2.69)$$

and the p. u. l. inductance is given by

$$L'_{\text{DCL}} = \frac{\mu \epsilon}{C'_{\text{DCL}}} = \frac{\mu}{\pi} \operatorname{arcosh} \left(\frac{s}{2a} \right). \quad (2.70)$$

In Fig. 2.7, the comparison between the exact p. u. l. capacitance from Eq. (2.67) and the approximated p. u. l. capacitance from Eq. (2.50) p. u. l. capacitance is shown. The error for a ratio $s/a = 5$ is only 2.7 %. For smaller separations like $s/a = 4$ i. e. another wire of the same radius would just fit between the two wires, the error between the approximation and the exact solution is only 5.3 %. It can be concluded, that for practical wire separations, the wide-separation approximation as given in Eq. (2.50) is sufficient.

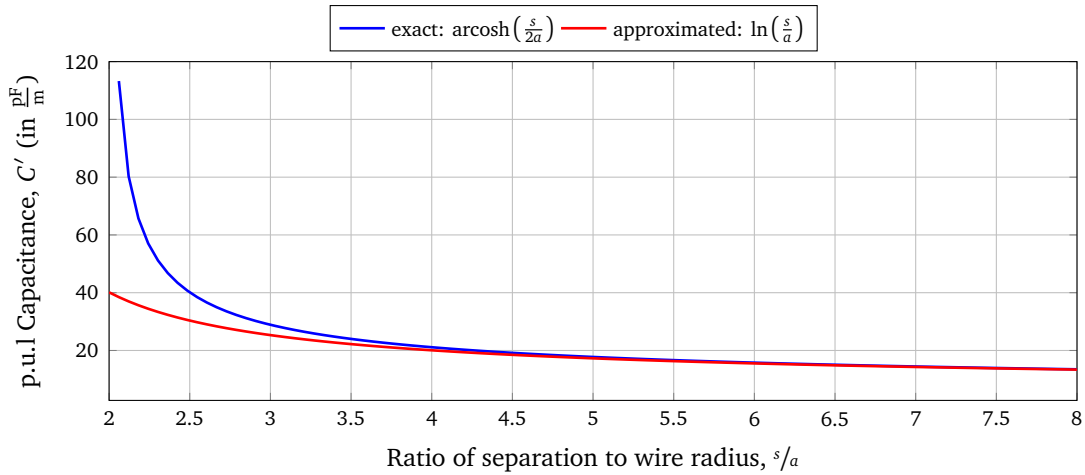


Figure 2.7: Comparison of the exact and approximated p. u. l. capacitance

Comparison of the Per-Unit-Length Parameters for Single and Double Wires

This subsection compares the single conductor transmission line (SCL) over a conductive ground plane at a height h with a double conductor transmission line (DCL) with the distance s between the two wires. For the single wire, the capacitances between the wire itself and the image wire (see method of images) to the ground plane, respectively, are connected in series and it follows from Eq. (2.67)

$$C'_{\text{SCL}} = 2C'_{\text{DCL}} \quad (2.71)$$

and the capacitance for a wire at height $h = s/2$ becomes

$$C'_{\text{SCL}} = \frac{2\pi\epsilon}{\operatorname{arcosh} \left(\frac{h}{a} \right)} \quad (2.72)$$

or, approximately for $h \gg a$

$$C'_{\text{SCL}} \cong \frac{2\pi\epsilon}{\ln\left(\frac{2h}{a}\right)}. \quad (2.73)$$

Similarly, the inductance from Eq. (2.70) becomes

$$L'_{\text{SCL}} = \frac{\mu}{2\pi} \operatorname{arcosh}\left(\frac{h}{a}\right) \cong \frac{\mu}{2\pi} \ln\left(\frac{2h}{a}\right) \quad (2.74)$$

for the single wire case. From the p. u. l. parameters, the most important parameter for any transmission line, the characteristic impedance, can be obtained.

2.2.3 Characteristic Impedance

The characteristic impedance is an important quantity in order to understand the field-to-wire coupling. This quantity describes the ratio of current and voltage waves propagating in one direction along the line

$$Z_c(\omega) = \frac{U_0^+}{I_0^+} = -\frac{U_0^-}{I_0^-} = \sqrt{\frac{Z'(\omega)}{Y'(\omega)}}, \quad (2.75)$$

where U_0^+ and U_0^- are the amplitudes of the propagating wave in positive (+ x direction) and negative ($-x$ direction). Here, Z' and Y' are the line impedance and admittance. The characteristic impedance is a function of the geometry of a conductor as well as its material. Its value is independent of the line length. It is related to the p. u. l. parameters of the wires by

$$Z_c(\omega) = \sqrt{\frac{Z}{Y}} = \sqrt{\frac{R' + j\omega L'}{G' + j\omega C'}}, \quad (2.76)$$

with the p. u. l. resistance R' , inductance L' , conductance G' and capacitance C' .

For the lossless line follows

$$Z_c(\omega) = \sqrt{\frac{L'}{C'}}. \quad (2.77)$$

Analogously, the characteristic admittance can be determined by

$$Y_c(\omega) = \frac{1}{Z_c(\omega)}. \quad (2.78)$$

The characteristic impedance and p. u. l. parameters will be given separately in the specific chapters since they depend on the number and geometry of the wires. The significance of the characteristic impedance becomes important when terminating a line. If a long line is terminated with an impedance that corresponds to the characteristic impedance of the line, then it is a matched line ($Z_L = Z_c$). Such a matched line behaves like an infinitely long line, where only one running wave exist, and no line resonances are expected. The characteristic impedance gives a specified reference impedance for the voltage and current at any point traveling along a transmission line.

2.2.4 Reflection Coefficient

Another important quantity to describe the field-to-wire coupling is the reflection coefficient. In transmission line theory, the reflection coefficient is defined as the ratio of the complex amplitude of the reflected to the incident wave. The simplest case is a finitely long line terminated with an impedance Z_L as shown in Fig. 2.8.

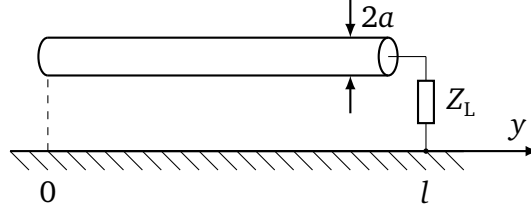


Figure 2.8: Transmission line of the length l terminated with a load impedance Z_L

This load impedance is the reason for a reflection, since the voltage U_L across and the current I_L through the impedance are defined by Ohm's law

$$\frac{U_L}{I_L} = Z_L = \frac{U_0^+(l) + U_0^-(l)}{I_0^+(l) + I_0^-(l)}. \quad (2.79)$$

The relation between the incoming and outgoing wave is given by the ratio

$$\Gamma(y) = \frac{U_0^-}{U_0^+} = -\frac{I_0^-}{I_0^+}. \quad (2.80)$$

This ratio is called the reflection coefficient [Col13] The minus in the third part of equation (2.80) means that the current is reflected opposite to the voltage. The voltage and current for any point on the line can be expressed by

$$U(y) = U_0^+ \cdot e^{\gamma y} \cdot (1 + \Gamma(y)), \quad (2.81a)$$

$$I(y) = Y_{indc} \cdot U_0^+ \cdot e^{\gamma y} \cdot (1 - \Gamma(y)), \quad (2.81b)$$

where y is a position along the wire between 0 and l and γ is the propagation constant. The ratio of voltage and current at point y is defined as input impedance directed towards the load

$$Z_{in}(y) = \frac{U(y)}{I(y)} \quad (2.82)$$

and using equations (2.81a) and (2.81b) one gets

$$Z_{in}(y) = Z_c \cdot \frac{1 + \Gamma(y)}{1 - \Gamma(y)}. \quad (2.83)$$

If the input impedance is equal to the load impedance at the end of the wire ($y = l$), then

one obtains

$$Z_{\text{in}}(l) = Z_L = Z_c \cdot \frac{1 + \Gamma(l)}{1 - \Gamma(l)}, \quad (2.84)$$

which can be solved for the reflection coefficient

$$\Gamma(l) = \frac{Z_L - Z_c}{Z_L + Z_c}. \quad (2.85)$$

In case of a matched line ($Z_L = Z_c$), it follows that $\Gamma(l) = 0$. The power of the forward and reflected waves stays the same. This means that the wave reflected by the load is zero. The reflection coefficient for an open circuit ($Z_L = \infty$) is $\Gamma(l) = 1$ implying total reflection at the open end of the line. For a short circuit ($Z_L = 0$) the reflection coefficient is $\Gamma(l) = -1$. This implies that there is total reflection with a 180° phase shift at the shorted line end.

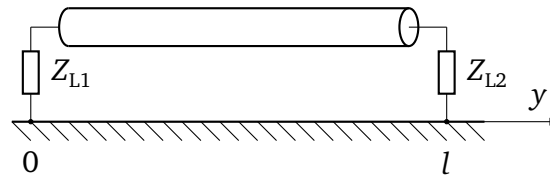


Figure 2.9: Transmission line terminated at both ends with load impedances Z_{L_i}

If a line, as shown in Fig. 2.9, is terminated with a load impedance Z_{L1} at the beginning and Z_{L2} at the end of the line, one obtains the following reflection coefficients

$$\Gamma_1 = \Gamma(0) = \frac{Z_{L1} - Z_c}{Z_{L1} + Z_c}, \quad (2.86a)$$

$$\Gamma_2 = \Gamma(l) = \frac{Z_{L2} - Z_c}{Z_{L2} + Z_c}. \quad (2.86b)$$

2.3 Stochastic Electromagnetic Fields

The transmission line theory presented above only applies to free space or half space but can also be applied to resonators if the transmission line system is a linear system. In many applications of electromagnetic interference (EMI), of EMC and wireless transmission, there is incomplete information about the cavity and its loading, e.g. in airplanes, helicopters and automobiles. If the exact geometry of large resonators and the objects inside, such as cable bundles, antennas and measuring subject, are not known, then the description by a stochastic field is appropriate [Hil09].

2.3.1 Occurrence and Calculation of Stochastic Electromagnetic Fields

Stochastic fields occur for example in metallic environments where the waves are reflected by metallic walls and/or surfaces. The reflection leads to a superposition of the waves and thus to a stochastic field. The description of stochastic fields is used wherever deterministic description is not possible or useful. A description by stochastic fields is also advantageous if the calculation of the deterministic field would become very time-consuming due to a high number of boundary conditions.

Stochastic fields can be calculated using conventional numerical field calculation methods such as the [Gus18]

- Method of Moments (MoM),
- Finite Element Method (FEM),
- Finite Difference Method (FDM) or
- Transmission Line Matrix (TLM) Method.

These methods provide approximate solutions for electromagnetic field problems. Starting point are either Maxwell's equations or mathematically equivalent formulations. In principle, any method is suitable for simulations. In practical application, however, one or the other method often has advantages and disadvantages in certain scenarios. For the simulation of stochastic fields, the above-mentioned simulation methods can be very time consuming. With the exception of the MoM, which will be discussed in more detail in Sec. 2.3.3, because there exist a special solution method for the stochastic field description and calculation.

Therefore, an analytical or better semi-analytical model is more suitable and explained in Sec. 2.3.2. For the semi-analytical model, the field can be approximated by a superposition of plane waves [Hil09, Ch. 7]. The fields can be described by statistical distributions, expectation values and variances of the field strength characteristics. In particular, the plane wave approach has been successful when applied to stochastic fields in ideal mode stirred chambers.

2.3.2 Plane Waves

A plane wave is a wave in three-dimensional space whose wave fronts (i. e. surfaces of equal phase angle) are planes which are extended perpendicular to the direction of propagation. Equivalent to this definition is that the direction of propagation of the wave is spatially constant. The term plane wave is used almost exclusively for waves which are also homogeneous and harmonic, i. e. which have a spatially constant amplitude and a sinusoidal shape with a temporally constant frequency. A successful approach for the description of stochastic fields in ideal reverberation chambers is to represent the measured field at a fixed electromagnetic boundary condition as a superposition of plane waves. Here, the directions of incidence, polarizations and phase positions of the plane wave can be statistically determined. Statistical evaluation is then performed by an ensemble of several boundary conditions. Far away from the electrically conductive walls of the chamber and other diffusers, the field is statistically homogeneous, isotropic and ergodic. Within this work, fields in reverberation chambers and in electrically large and geometrically complex resonators with variable geometry are considered as stochastic fields.

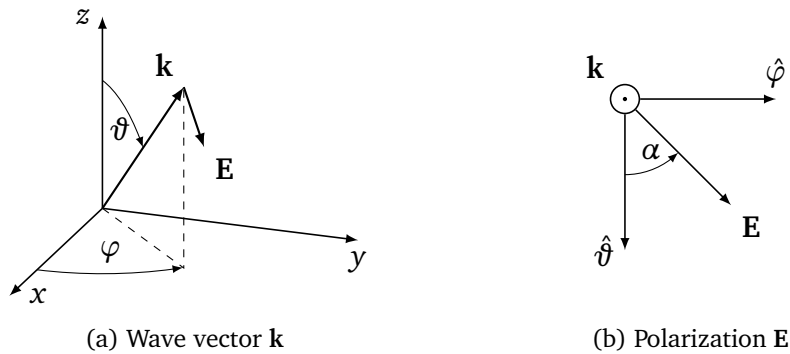


Figure 2.10: Definition of the wave vector \mathbf{k} and the electric field polarization \mathbf{E} with the polar angle ϑ , the azimuth angle φ and the polarization angle α as in [MTV11]

The analytical calculation is based on a description of the stochastic fields as a superposition of plane waves with any direction of incidence and polarization. The incident plane wave at position \mathbf{r} in space is given by (see Fig. 2.10a)

$$\mathbf{E}(\mathbf{r}) = \mathbf{e}E e^{-j(\mathbf{k}\cdot\mathbf{r}+\beta)}. \quad (2.87)$$

Here, E is the amplitude, the wave vector \mathbf{k} defines the direction of propagation and \mathbf{e} is the polarization of a wave and β describes the phase. For the superposition of many plane waves the parametrization of the wave vector \mathbf{k} in terms of φ , θ and k is useful

$$\mathbf{k} = \begin{pmatrix} k_x \\ k_y \\ k_z \end{pmatrix} = k \begin{pmatrix} \sin \vartheta \cos \varphi \\ \sin \vartheta \sin \varphi \\ \cos \vartheta \end{pmatrix}, \quad (2.88)$$

with the wave number $k = 2\pi/\lambda = \omega/c$. Similarly, the polarization is determined by (see Fig. 2.10b)

$$\mathbf{e} = \begin{pmatrix} e_x \\ e_y \\ e_z \end{pmatrix} = \begin{pmatrix} \cos \alpha \cos \vartheta \cos \varphi - \sin \alpha \sin \varphi \\ \cos \alpha \cos \vartheta \sin \varphi + \sin \alpha \cos \varphi \\ \cos \alpha \sin \vartheta \end{pmatrix}. \quad (2.89)$$

Many plane waves are superimposed to describe the stochastic field. The direction of propagation, polarization and phase angle of each plane wave are completely random. The statistical distribution of the corresponding angles is given in [MV15, Tab. 1], where all angles are uniformly distributed.

2.3.3 Method of Moments

The MoM for electromagnetic field problems was introduced by Harrington in 1967 [Har93] and has been a common tool for analyzing EMC problems ever since. It is an integral equation method that uses integral relationships to calculate the interactions between all field quantities. The space itself is considered very efficiently with an approach using Green's functions. Because only surfaces and material boundaries, but no volume areas themselves must be discretized, the number of unknowns is manageable if the structure is simple and can be described by a few surfaces. This method becomes ineffective if there are highly inhomogeneous structures with many material boundaries. The increasing number of boundaries leads to an increased workload and the method is not suitable for the MoM. Consideration of large distances between individual components is no problem for the simulation, as only the surfaces of the conductive objects have to be discretized. In addition, the method is always analyzed in frequency domain. Since the system properties within a wide frequency range are to be determined during EMC simulation, the simulation must be carried out individually for each frequency. An implementation of non-linear effects is hardly conceivable due to the evaluation in the frequency domain.

The MoM has advantages if it is used for

- structures with radiation into free space,
- models with homogeneous material (structures, with only a few material boundaries leads to a manageable number of unknowns),
- scenarios with electrically large distances between structural elements (space between the structures does not have to be discretized) or
- planar circuit structures (problem-adapted Green's function reduces the number of unknowns).

For the case of transmission lines in a resonant environment, the field equations are solved from the current distributions on the conductors also using the Green's functions. The coupling and radiation characteristics of the structure can be determined from this calculation.

CONCEPT-II is a MoM based simulation tool to model metallic and dielectric objects in frequency domain. It is possible to model structures in free space or over ideal ground. Different types of excitation are possible:

- Lumped voltage or power generators
- Impressed line currents, current generator
- Plane wave field (linear or elliptical polarization)
- Stochastic fields
- Edge generators

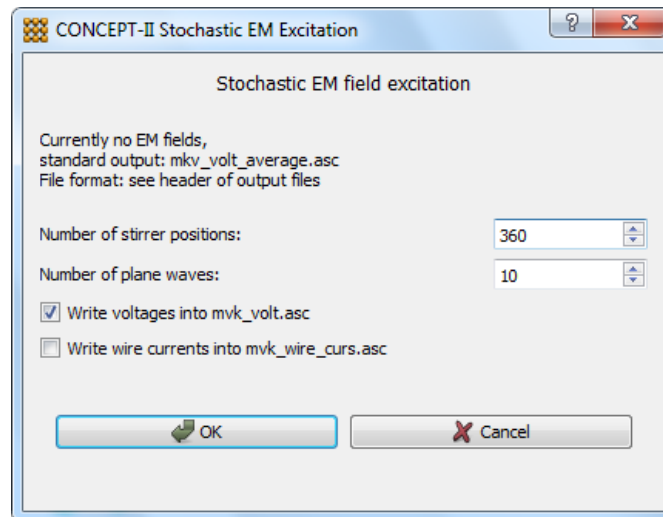


Figure 2.11: Setup to define the stochastic field excitation in *CONCEPT-II*

Full-wave solvers like the MoM can simulate more arbitrary geometries of the transmission line and the DUT itself but are very slow for stochastic simulations. Simulations of reverberation chambers are critical in terms of computing resources and stability due to their electrical size and their resonance behavior. To overcome this problem, *CONCEPT-II* contains a technique to represent the field within the chamber by field generator and to consider only the interactions of this field with the DUT. Here, the coupling to the chamber is only indirectly influenced by a change of the quality factor. These field generators e. g. superposition of several plane waves in the frequency domain, which hit the DUT from random angles and polarizations. Fig. 2.11 shows the user interface in *CONCEPT-II* to setup the number of plane waves and electromagnetic boundary conditions (stirrer positions) for the stochastic field.

2.4 Measurements in a Reverberation Chamber

A reverberation chamber is a EMC measurement and test environment according to the IEC 61000-4-21 standard [Int11] and, like an anechoic chamber, a GTEM cell or a TEM cell, it is used either to measure the radiated interference emission of an electrical or electronic device or to test the immunity of a device to electromagnetic fields. In this chapter, the reverberation chamber and its functionality will be introduced, as well as the typical measurement procedure and the measuring instruments.

2.4.1 Functionality of a Reverberation Chamber

The shape of a reverberation chamber can be quite different: circular cylindrical, spherical or rectangular to name a few. The latter is the most common form and this work is limited to rectangular chambers. To generate a stochastic field, the process of mode stirring, that means to change the electromagnetic boundary conditions, is essential for reverberation chambers. Here, different methods are possible. Changing the source point (antenna), building a cavity with flexible conducting walls as well as inserting a rotating metal paddle are some examples to stir the modes.

In this thesis the focus lies on reverberation chambers with a mechanical stirrer, which change the modal distribution within the chamber. Symmetries in the design and placement of the stirrer should be avoided to maximize the number of independent positions that the stirrer can generate. A method for evaluating the performance of the stirrer is given in [Int11, Sec. A.3)]. The homogeneous and isotropic field can only be achieved in a limited, often cuboidal working volume. This working volume has a sufficient distance to the stirrer and all walls of the chamber. It is assumed that enough stirrer positions exists, where each position results in an independent boundary condition and thus a statistically independent field distribution. During measurement, it is possible to distinguish between *mode-tuning* and *mode-stirring*. In *mode tuned* operation, the field or power is measured at different discrete frequencies for discrete positions of the tuner (Note: IEC 61000-4-21-B recommends increasing the frequency after each tuner step). The measurement is repeated for each tuner step and the measured values for each measurement frequency are averaged over all tuner positions. In *mode-stirred* operation, the stirrer is continuously rotated at constant speed. At each frequency, a series of measurements are taken and averaged. Then the system moves to a new frequency.

2.4.2 Big Reverberation Chamber at the Otto von Guericke University

The dimensions of the large reverberation chamber at the Otto von Guericke University (OvGU) in Magdeburg as shown in Fig. 2.12 are 7.9 m × 6.5 m × 3.5 m. For an ideal, lossless, empty, closed rectangular cavity of dimensions $l_{x,RC}$ (length), $l_{y,RC}$ (width), and $l_{z,RC}$ (height), the modal or resonance frequencies f_{m_1,m_2,m_3} can be calculated by [Int11, Eq. (A.2)]

$$f_{m_1,m_2,m_3} = \frac{c_0}{2} \cdot \left(\frac{m_1}{l_{x,RC}} \right)^2 + \left(\frac{m_2}{l_{y,RC}} \right)^2 + \left(\frac{m_3}{l_{z,RC}} \right)^2. \quad (2.90)$$

Here, m_1 , m_2 and m_3 are the mode indices. The first resonant frequency is at $f_{1,1,0} = 30$ MHz. The lowest usable frequency (LUF) is determined by the chamber size, quality factor and the effectiveness of the mechanical stirrer. Generally, the LUF is defined as the frequency at which the chamber meets the operational requirements. According to [Int11, Sec. (A.1.3)], this case typically occurs in practice at a frequency slightly above three times of the first chamber resonance $f_{1,1,0}$. For this chamber, the LUF is at about $f_{LUF} = 200$ MHz. Moreover, the chamber is equipped with a transmitting and receiving antenna (double logarithmic antennas, Schwarzbeck VULP 9118C) and a vertical stirrer.



Figure 2.12: Photograph of the big reverberation chamber at the at OvGU [Wik20]

2.4.3 Scattering Parameters

First, the theory of scattering parameters, short S-parameters, will be explained, because a vector network analyzer was used (VNA) during the measurements. The VNA is useful for measurements in a reverberation chamber and saves the S-parameters. Since the S-parameters determine e. g. the coupled voltage to a transmission line, first the definition of the S-parameters will be given and discussed. S-parameters are used to describe the behavior of linear electrical components and networks using wave variables. Two- and multi-port

networks can be characterized by several equivalent circuit parameters. Fig. 2.13 depicts a typical two-port network.

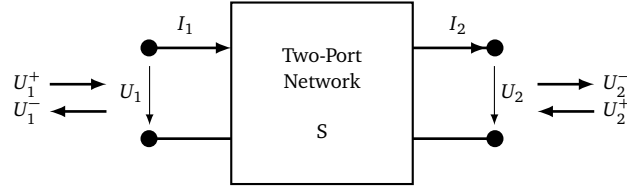


Figure 2.13: Two-port network (based on [Orf08, Fig. 14.1.1])

The S-parameters describe the response of a system for a wave U_1^- entering the gate and a wave U_1^+ reflected by the gate. The scattering matrix relates the outgoing waves U_1^- and U_2^- to the incoming waves U_1^+ and U_2^+ [Orf08, Chap. 13]

$$\begin{bmatrix} U_1^- \\ U_2^- \end{bmatrix} = \begin{bmatrix} S_{11} & S_{12} \\ S_{21} & S_{22} \end{bmatrix} \cdot \begin{bmatrix} U_1^+ \\ U_2^+ \end{bmatrix}. \quad (2.91)$$

The matrix elements are the scattering parameters or the S-parameters. Here S_{11} is the input reflection coefficient, S_{22} the output reflection coefficient, S_{21} the forward transmission and S_{12} the backward transmission coefficient. If the traveling wave variables U_1^+ , U_1^- at port 1 and U_2^+ , U_2^- at port 2 shall be defined in terms of U_1 , I_1 and U_2 , I_2 , a real-valued positive reference impedance Z_c is needed [Orf08, Eq. (13.1.4)]

$$U_1^+ = \frac{U_1 + Z_c I_1}{2\sqrt{Z_c}}, \quad (2.92a)$$

$$U_1^- = \frac{U_1 - Z_c I_1}{2\sqrt{Z_c}}, \quad (2.92b)$$

$$U_2^+ = \frac{U_2 - Z_c I_2}{2\sqrt{Z_c}}, \quad (2.92c)$$

$$U_2^- = \frac{U_2 + Z_c I_2}{2\sqrt{Z_c}}. \quad (2.92d)$$

Inverting Eq. (2.92), the voltages and currents can be expressed in terms of the wave variables

$$U_1 = \sqrt{Z_c}(U_1^+ + U_1^-), \quad (2.93a)$$

$$I_1 = \frac{1}{\sqrt{Z_c}}(U_1^+ - U_1^-), \quad (2.93b)$$

$$U_2 = \sqrt{Z_c}(U_2^+ + U_2^-), \quad (2.93c)$$

$$I_2 = \frac{1}{\sqrt{Z_c}}(U_2^- - U_2^+). \quad (2.93d)$$

The S-parameters can be measured using network analyzers as a function of frequency. They are a dimensionless complex number and known as phasors.

In practice, they have the following meaning:

- S_{11} is the input reflection coefficient and quantifies the matching of the input to a reference system. Small values indicate suppressed reflection.
- S_{21} is the forward transmission attenuation of the input signal. For a passive element it indicates the insertion loss.
- S_{12} is the backward transmission coefficient. It should correspond to S_{21} for passive bidirectional elements.
- S_{22} is the output reflection factor and quantifies the matching of the output to a reference system. Small values indicate suppressed reflection.

2.4.4 Measurement of the Coupled Current and Coupled Voltage

In order to determine the coupled voltage or the coupled current, the scattering parameters must be measured. A two-port or four-port VNA can be used for this purpose. In the following, the special aspects of the use of both measuring devices will be discussed.

Typical Measurement Procedure

Before the actual measurements could start, a calibration had to be performed to lower the systematic errors caused by e. g. the measuring cables or adapters. This calibration was carried out whenever fundamental aspects of the measurement setup changed, such as the length of the measurement cables or a measuring instrument. If only e. g. the position or the termination of the EUT was changed, no new calibration had to be performed. During the measurements, the scattering parameters were determined. For the operation mode of the stirrer, *mode-stirring* was chosen. Then, the boundary conditions had to be defined by setting the lower and upper frequency f_{\min} and f_{\max} as well as the starting position and tuning steps of the stirrer.

In the measurements of this thesis, the scattering parameters were measured at 72 equidistant stirrer positions from 0° to 355° in steps of 5° . This number of positions meets the requirements for independent stirrer positions from [Int11, Sec. A.3)]. Smaller steps are not possible in this measurement setup because the stepper motor for rotating the stirrer cannot be controlled more precisely. Nevertheless, sufficient accuracy and statistics can be achieved with this number of stirrer positions and thus fast measurement results can be obtained. The lower frequency limit was chosen at the lowest usable frequency of the chamber ($f_{\min} = 200$ MHz). At each stirrer position the frequency was swept with linearly distributed frequency steps f_{steps} from f_{\min} to f_{\max} . This number of frequency steps f_{steps} depends on the memory size of the VNA.

Two-Port Vector-Network-Analyzer

For measuring the coupled voltage with a two-port VNA the Rohde&Schwarz VNA (ZVC 20 kHz...20 GHz) as shown in Fig. 2.14 was used.

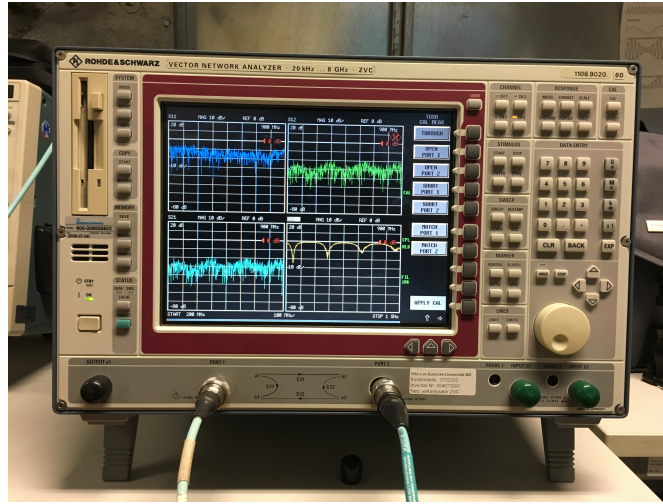


Figure 2.14: Photograph of the two-port Rohde&Schwarz VNA (ZVC 20 kHz...20 GHz)

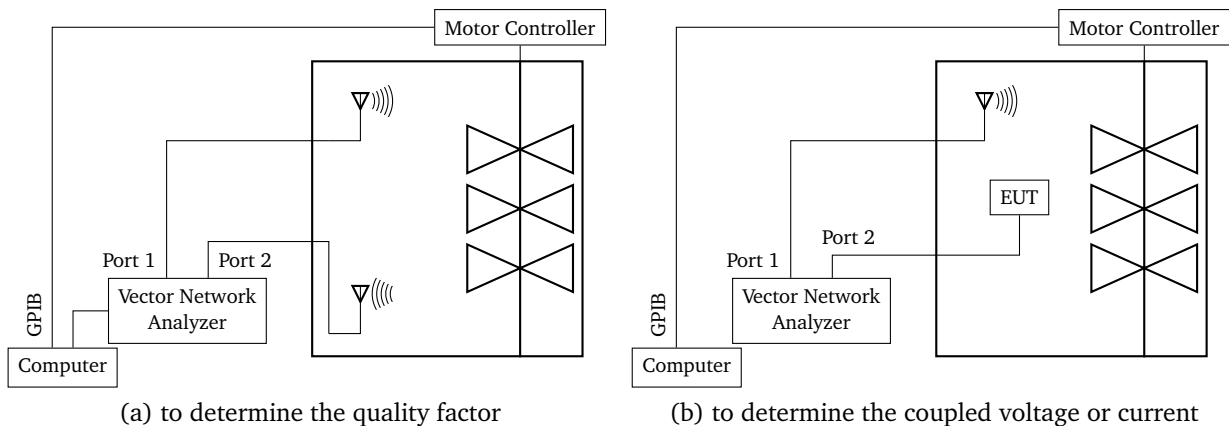


Figure 2.15: Schematic representation of the measurement within the mode stirred chamber using a two-port VNA

When using a two-port VNA the measurement was divided into two parts. First, the quality of the chamber was determined (see Fig. 2.15a). With the memory size of the two-port VNA it was possible to measure $f_{\text{steps}} = 501$ linearly spaced frequency steps. The transmitting antenna (tx) was connected to port 1 of the VNA and the receiving antenna (rx) to port 2. This measurement must be performed only once, if the quality of the chamber does not change between measurements. With the help of the quality factor of the reverberation chamber, the measured scattering parameters of the second measurement setup can be converted into the coupled voltage or current. The quality factor is calculated by the coupling of two

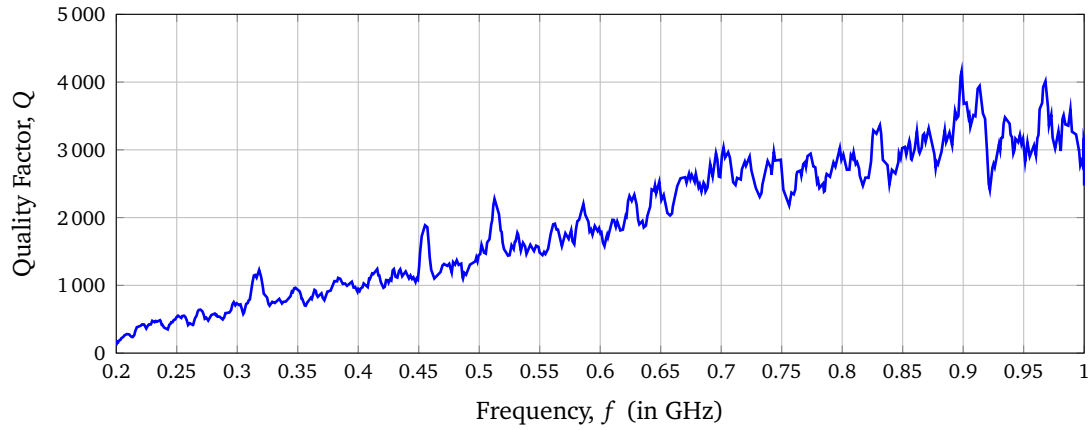


Figure 2.16: Measured quality factor over the frequency of the big reverberation chamber at the OvGU

antennas [MT96, Eq. (3)]

$$Q = 16\pi^2 \frac{V}{\lambda^3 \eta_{tx} \eta_{rx}} \left\langle \frac{|S_{21}|^2}{1 - |S_{11}|^2} \right\rangle, \quad (2.94)$$

where the efficiencies of the antennas are approximated with $\eta_{tx} = \eta_{rx} = 0.8$ and λ is the wavelength. The quality factor includes loading effects and is influenced by losses due to the finite conductivity of the chamber walls, dielectric losses such as in antenna support structures, losses due to wall coatings and leakage losses. The results are averaged $\langle \rangle$ over all stirrer positions, assuming that the stirrer positions are uncorrelated and statistically independent. The quality factor of the reverberation chamber of the OvGU is shown in Fig. 2.16 as a function of the frequency. To smooth the measured curve, a moving average over five frequencies was calculated. With increasing frequency, the quality factor also increases. There is a large fluctuation in the results when the frequency changes, which is caused by statistical uncertainties in the measurement.

In a second step the coupling to a transmission line should be determined. For this purpose, the measurement setup shown in Fig. 2.15b was used. Port 1 is connected to the transmitting antenna and port 2 to one end of the line. The coupled power P_2 at port 2 is defined by the coupled voltage U and the input impedance of the network analyzer $Z_{VNA} = 50 \Omega$

$$P_2 = \frac{|U|^2}{Z_{VNA}}. \quad (2.95)$$

The ratio between the power at port 1 and 2 can be expressed by using the quality factor from Eq. (2.94)

$$\frac{P_2}{P_1} = \frac{|S_{21}|^2}{1 - |S_{11}|^2} = \frac{|U|^2}{E_0^2} \cdot \frac{Q}{\omega \epsilon V Z_{VNA}}. \quad (2.96)$$

The so called *chamber constant* E_0 ([Hil98, eq. (23)]), puts the power P_1 at port 1, the quality

factor of the chamber Q , the chamber volume V , the dielectric constant of the medium ϵ and the angular frequency ω in a ratio

$$E_0^2 = \frac{QP_1}{\omega\epsilon V}. \quad (2.97)$$

The ratio for the coupled voltage can be determined by

$$\frac{U}{E_0 h} = \frac{S_{21}}{\sqrt{1 - |S_{11}|^2}} \cdot \frac{1}{h} \cdot \sqrt{\frac{\omega\epsilon Z_{VNA} c_0 V}{Q}} \quad (\text{SCL over Ground}), \quad (2.98)$$

where c_0 is the speed of light and h is the height of the line. By normalizing the voltage U to the chamber constant E_0 and the height h of the transmission line above ground, a dimensionless quantity is obtained for better comparison of the simulated and measured results. The coupled current can be determined analogously (see Appendix A).



Figure 2.17: Photograph of a balancing unit for the measurements of e. g. a double wire in free space

If, for example, a double line was examined, a balancing unit (BalUn) must be used to connect the balanced double line to the unsymmetrical input of the VNA, as shown in Fig. 2.17. A BalUn is used to convert balanced signals to unbalanced or vice versa at the same power. Here, at the input of the BalUn, the differential input signals are measured. This allows the measurement of the differential mode (or transmission line mode) and thus the measurement of the coupled voltage. The BalUn suppresses the common mode (or antenna mode), which also couples to the line. For the conversion of the scattering parameters to the coupled voltage, the power P_2 at port 2 and the reference impedance Z_{VNA} is needed

$$U = \frac{1}{T_{\text{BalUn}}} \cdot \sqrt{P_2 \cdot Z_{VNA}}, \quad (2.99)$$

where T_{BalUn} is the amount of the forward and backward transmission coefficients defined

by

$$T_{\text{BalUn}} = \frac{|S_{\text{AC}}| + |S_{\text{CA}}| + |S_{\text{BC}}| + |S_{\text{CB}}|}{4}. \quad (2.100)$$

Here, A and B are the inputs and C is the output. Inserting Eq. (2.97) and (2.99) in the power ratio between port 2 and 1 it follows

$$\frac{P_2}{P_1} = \frac{|S_{21}|^2}{1 - |S_{11}|^2} = \frac{|U|^2}{E_0^2} \cdot \frac{T_{\text{BalUn}}^2 Q}{\omega \varepsilon V Z_{\text{VNA}}}. \quad (2.101)$$

From the last equation, the ratio of the coupled voltage to the field strength E_0 from Eq. (2.97) and the distance s between the wires can be defined analogously to Eq. (2.98)

$$\frac{U}{E_0 s} = \frac{S_{21}}{\sqrt{1 - |S_{11}|^2}} \cdot \frac{1}{T_{\text{BalUn}} s} \cdot \sqrt{\frac{\omega \varepsilon Z_{\text{VNA}} c_0 V}{Q}} \quad (\text{DCL in free space}). \quad (2.102)$$

Four-Port Vector-Network-Analyzer

With a four-port Rohde&Schwarz VNA (ZNB, 9 kHz to 8.5 GHz) as shown in Fig. 2.18, the quality factor does not need to be determined in a separate measurement. Because it is not necessary to perform two separate measurements, statistical uncertainties between the individual measurements can be reduced. With the memory size of the four-port VNA it is possible to measure $f_{\text{steps}} = 5001$ linearly spaced frequency steps. The schematic measurement setup in the reverberation chamber is shown in Fig. 2.19.

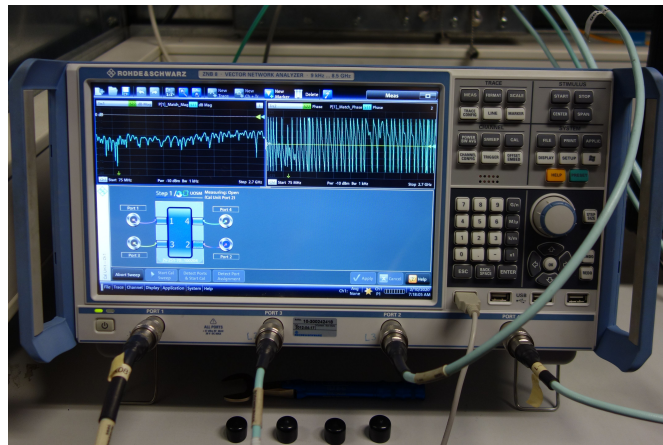


Figure 2.18: Photograph of the four-port Rohde&Schwarz VNA (ZNB, 9 kHz to 8.5 GHz)

Here port 1 is connected to the transmitting antenna, port 2 to the receiving antenna and port 3 to one end of the line. As with the two-port VNA, in order to convert the measured scattering parameters into the desired coupled voltage one uses the quality factor of the chamber given in Eq. (2.94). The difference to the two-port VNA is that here both the coupling between the antennas and the coupling between antenna and transmission line are

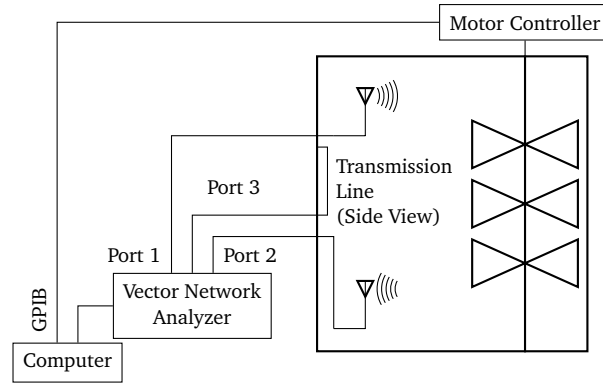


Figure 2.19: Schematic representation of the measurement within the mode stirred chamber with a four-port VNA

measured simultaneously. With the help of the coupled power

$$P_3 = \frac{|U|^2}{Z_{\text{VNA}}} \quad (2.103)$$

at port 3 and the input impedance of the network analyzer $Z_{\text{VNA}} = 50 \Omega$ the scattering parameters can be converted into the coupled voltage. Substituting Eq. (2.103) and Eq. (2.97) in the ratio between the power at ports 1 and 3, one gets

$$\frac{P_3}{P_1} = \frac{|S_{31}|^2}{1 - |S_{11}|^2} = \frac{|U|^2}{E_0^2} \cdot \frac{Q}{\omega \varepsilon V Z_{\text{VNA}}}. \quad (2.104)$$

Using (2.94) and a few simplifications, the ratio

$$U = S_{31} \cdot \lambda \cdot \sqrt{\frac{\varepsilon Z_{\text{VNA}} c_0 E_0}{8\pi \langle |S_{21}|^2 \rangle}} \quad (2.105)$$

can be calculated. Analogously to Eq.(2.98), a normalization to the chamber constant E_0 and the height h of the line to the ground plane is done to get a dimensionless quantity. It does not depend on the field strength but only on the configuration of the transmission line

$$\frac{U}{E_0 h} = S_{31} \cdot \frac{\lambda}{h} \cdot \sqrt{\frac{\varepsilon Z_{\text{VNA}} c_0}{8\pi \langle |S_{21}|^2 \rangle}} \quad (\text{SCL over ground}). \quad (2.106)$$

The same applies to the determination of the coupled voltage of a double line in the working volume

$$\frac{U}{E_0 h} = S_{31} \cdot \frac{\lambda}{T_{\text{BalUn}} s} \cdot \sqrt{\frac{\varepsilon Z_{\text{VNA}} c_0}{8\pi \langle |S_{21}|^2 \rangle}} \quad (\text{DCL in free space}). \quad (2.107)$$

2.4.5 Measurement of the Radiation Losses

A further issue in EMC that will be examined in more detail in this section is the radiation of unwanted electromagnetic waves from various electronic devices, which can lead to interference in other electrical systems. The radiation losses can be measured using the measurement setup as shown in Fig. 2.20 using a four-port VNA.

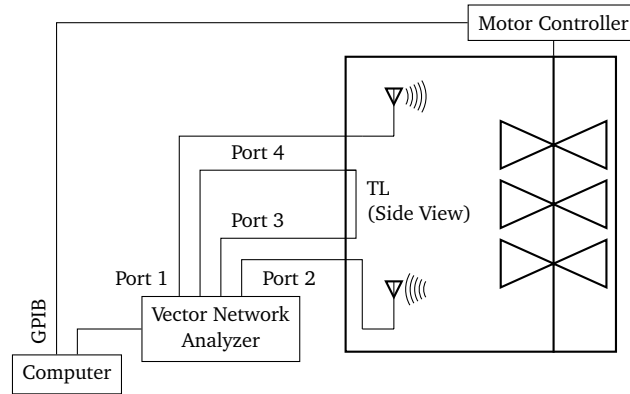


Figure 2.20: Measurement setup for measuring the scattering parameters to determine the radiation losses

The power balance for a lossy line is defined for the radiated power P_{rad} by the sum of the reflected power P_r , the transmitted power P_{trans} and the incident power P_{in} [RT08, Eq. 119]

$$P_{\text{rad}} = P_{\text{in}} - P_{\text{trans}} - P_r. \quad (2.108)$$

To analyze radiation losses, the measured scattering parameters must be converted into power. For this purpose, the definition of the scattering parameters is used, which describe the relationship between the forward and backward running voltage wave on the wire

$$[U^+] = [S] \cdot [U^-]. \quad (2.109)$$

After squaring the S-parameters it follows

$$|S_{33}|^2 = \left| \frac{U_1^+}{U_1^-} \right|^2 = \frac{P_r}{P_{\text{in}}}, \quad (2.110)$$

$$|S_{34}|^2 = \left| \frac{U_1^+}{U_2^-} \right|^2 = \frac{P_{\text{trans}}}{P_{\text{in}}}. \quad (2.111)$$

If these relations are inserted in the power balance according to Eq. (2.108), then the losses are given as

$$\frac{P_{\text{rad}}}{P_{\text{in}}} = 1 - |S_{34}|^2 - |S_{33}|^2. \quad (2.112)$$

3 Single Conductor Transmission Line over a Conductive Ground Plane

In this chapter, a straight single wire over a conductive ground plane is investigated. Based on Sec. 2.2.2, which explained the classical p. u. l. parameters, a model for frequency dependent line parameters is derived here. These parameters can be easily embedded in a program realized in *MATLAB*, which combines the stochastic field and transmission line description.

3.1 Transmission Line Model

In Section 2.2.2, the p. u. l. parameters of the single and double wire were introduced. The classical TLT and p. u. l. parameters are limited by some assumptions to which an investigated problem cannot always be limited (see Sec. 2.2.2). The main assumption is that the distance between the lines and the return path of the line (ground plane or return conductor) should be much smaller than the minimal relevant wavelength of the current within in the line. One consequence of this assumptions is that the result of the integral of the Green's function in Eq. (2.21) contains no imaginary part. This means that radiation is neglected, and the wave is considered totally guided along the wire. To include higher order modes while maintaining the simplicity of its formalism, the classical TLT is extended similar to [CBK13].

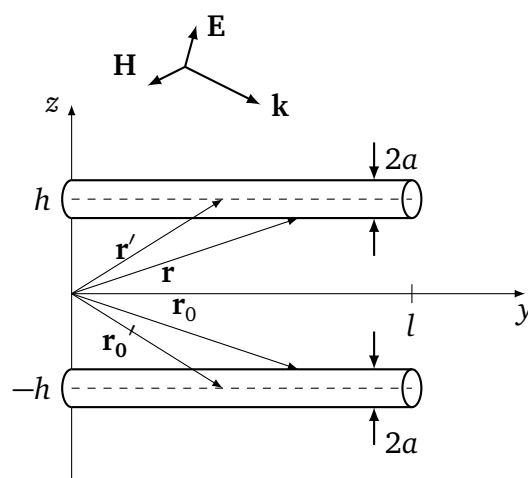


Figure 3.1: Single wire and its image in y -direction with the length l and the radius a and the vectors to the source and observation points on the wires

The investigated transmission line with the length l is shown in Fig. 3.1. The single conductor transmission line is located at a height h above the ground plane and points along the y -direction. An image wire, as explained in Sec. 2.2.2.1, is located at height $-h$. Considering a wire where the radius is much smaller than its length, the current density $\mathbf{J}(\mathbf{r})$ will be y -directed and has no transverse dimensions. According to Eq. (2.32) it becomes

$$\mathbf{J}(\mathbf{r}) = \mathbf{t} \cdot I(y')\delta(x')\delta(y'). \quad (3.1)$$

If it is a perfectly conductive transmission line, the current is essentially a surface current in radial distance a . Integrating the current density over the transverse dimensions of the wire, under the assumption of cylindrical symmetry (based on [Orf08, Eq. 14.4.2]), gives a current (see [Orf08, Ch. 14.4])

$$\int \mathbf{J}(\mathbf{r}') dx' dy' = \mathbf{t} \cdot I(y'). \quad (3.2)$$

That means that the current density is directed in the same direction as the current. Under thin wire assumption and with the help of the method of images, the vector potential becomes after performing the x' and z' integrations

$$\mathbf{A}(\mathbf{r}) = \frac{\mu}{4\pi} \int_V \mathbf{J}(\mathbf{r}') \cdot \frac{e^{-jkR_1}}{R_1} d^3\mathbf{r}' - \frac{\mu}{4\pi} \int_V \mathbf{J}(\mathbf{r}') \cdot \frac{e^{-jkR_0}}{R_0} d^3\mathbf{r}', \quad (3.3a)$$

$$= \frac{\mu}{4\pi} \int_0^l I(y') \cdot \frac{e^{-jkR_1}}{R_1} dy' - \frac{\mu}{4\pi} \int_0^l I(y') \cdot \frac{e^{-jkR_0}}{R_0} dy', \quad (3.3b)$$

where R_1 and R_0 represent the distances from the y' point on each wire to the observation point. In Fig. 3.1, the SCL and its image is shown with the vectors

$$\mathbf{r}' = y'\mathbf{e}_y + h\mathbf{e}_z, \quad (3.4a)$$

$$\mathbf{r}'_0 = y'\mathbf{e}_y + (-h)\mathbf{e}_z, \quad (3.4b)$$

that point to the observation points on the wires. The distances \mathbf{r} and \mathbf{r}_0 , that point to the source points along the wires, are defined by

$$\mathbf{r} = y\mathbf{e}_y + (h-a)\mathbf{e}_z, \quad (3.5a)$$

$$\mathbf{r}_0 = y\mathbf{e}_y + (-h-a)\mathbf{e}_z. \quad (3.5b)$$

From these definitions follow for the distances

$$R_1 = |\mathbf{r} - \mathbf{r}'| = \sqrt{(y - y')^2 + a^2}, \quad (3.6a)$$

$$R_0 = |\mathbf{r} - \mathbf{r}'_0| = \sqrt{(y - y')^2 + (2h + a)^2}. \quad (3.6b)$$

Under the assumption $a \ll h$ one can approximate

$$R_0 = \sqrt{(y - y')^2 + 4h^2}. \quad (3.7)$$

In Eq. (3.3b), the y' -integration is performed over the finite length of the line

$$A_y(y) = \frac{\mu}{4\pi} \int_0^l I(y') \frac{e^{-jkR_1}}{R_1} dy' - \frac{\mu}{4\pi} \int_0^l I(y') \cdot \frac{e^{-jkR_0}}{R_0} dy'. \quad (3.8)$$

Inserting Eq. (3.7) and (3.6a) in (3.8), the vector potential is determined by

$$A_y(y) = \frac{\mu}{4\pi} \int_0^l I(y') \cdot \frac{e^{-jk \cdot \sqrt{(y-y')^2 + a^2}}}{\sqrt{(y-y')^2 + a^2}} dy' - \frac{\mu}{4\pi} \int_0^l I(y') \cdot \frac{e^{-jk \cdot \sqrt{(y-y')^2 + 4h^2}}}{\sqrt{(y-y')^2 + 4h^2}} dy'. \quad (3.9)$$

The field-to-wire coupling equations from Eq. (2.26) can be expressed for a wire directed in y -direction with

$$\frac{d}{dy} U^s(y) + j\omega \underbrace{\frac{\mu}{4\pi} \int_0^l g(y, y') I(y') dy'}_{A_y(y)} = E_{\tan}^e, \quad (3.10a)$$

$$\frac{d}{dy} \int_0^l g(y, y') I(y') dy' + j\omega 4\pi \varepsilon U^s(y) = 0. \quad (3.10b)$$

The scattered voltage $U^s(y)$ is defined as in the classical TLT, $I(y')$ describes a current in y direction and E_{\tan}^e is the exciting tangential electric field. The Green's function for a transmission line of height h above a conductive ground plane, as determined in Eq. (3.9), is

$$g(y, y') = \frac{e^{-jk \sqrt{(y-y')^2 + a^2}}}{\sqrt{(y-y')^2 + a^2}} - \frac{e^{-jk \sqrt{(y-y')^2 + 4h^2}}}{\sqrt{(y-y')^2 + 4h^2}}, \quad (3.11)$$

where y and y' stand for the position of the observation point and the source point. This equation is similar to [RT08, Ch. 4, Eq. (7)]. Under the assumption that the current varies much slower than the Green's function ([RT08, Ch. 4, Fig. 3]) one can place the current

outside of the integral and one obtains

$$A_y(y) = \frac{\mu}{4\pi} I(y) \int_0^l \frac{e^{-jk\sqrt{(y-y')^2+a^2}}}{\sqrt{(y-y')^2+a^2}} - \frac{e^{-jk\sqrt{(y-y')^2+4h^2}}}{\sqrt{(y-y')^2+4h^2}} dy'. \quad (3.12)$$

In Appendix B, the comparison between the exact solution and the approximation that is made in Eq. (3.12) is done. The results show that this approximation is valid, especially for the use of stochastic fields. Assuming that the observation point is far enough from the end of the line and the current is locally constant, then the limits of integrations can be extended to $-\infty$ to $+\infty$ and the current distribution can be extracted from the integral. The integral is given by [PBM86]

$$\int_{-\infty}^{+\infty} g(y, y') dy' = j\pi H_0^{(2)}(-2hk) + j\pi H_0^{(2)}(-ak), \quad (3.13)$$

where $H_0^{(2)}$ describes the Hankel function of the first order of the second kind [Abr74]. The Hankel function is defined as

$$H_0^{(2)}(y) = J_0(y) - jY_0(y), \quad (3.14)$$

where $J_0(y)$ and $Y_0(y)$ are the 0-order of the Bessel function first and second kind. Using these definitions, Eq. (3.13) can be rewritten as

$$\int_{-\infty}^{+\infty} g(y, y') dy' = \pi [Y_0(2hk) - Y_0(ak)] + j\pi [J_0(2hk) - J_0(ak)]. \quad (3.15)$$

Employing the high frequency (HF) p. u. l. impedance Z_{SCL}^{HF} and admittance Y_{SCL}^{HF} and inserting them into Eq. (3.10a) and (3.10b), one obtains the following equations

$$\frac{d}{dy} U^s(y) + I(y) \cdot \underbrace{(j\omega L_{SCL}^{HF} + R_{SCL}^{HF})}_{Z_{SCL}^{HF}} = E_{\tan, SCL}^e, \quad (3.16a)$$

$$\frac{d}{dy} I(y) + U^s(y) \cdot \underbrace{(j\omega C_{SCL}^{HF} + G_{SCL}^{HF})}_{Y_{SCL}^{HF}} = 0. \quad (3.16b)$$

The p. u. l. parameters L_{SCL}^{HF} , R_{SCL}^{HF} , C_{SCL}^{HF} and G_{SCL}^{HF} also become frequency dependent. With the solution of the Green's function (3.15), the p. u. l. impedance results in

$$Z_{SCL}^{HF} = j\omega \frac{\mu}{4\pi} \left(\pi [Y_0(2hk) - Y_0(ak)] + j\pi [J_0(2hk) - J_0(ak)] \right) \quad (3.17)$$

and the admittance in

$$Y_{\text{SCL}}^{\text{HF}} = j\omega 4\pi\varepsilon \left(\pi [Y_0(2hk) - Y_0(ak)] + j\pi [J_0(2hk) - J_0(ak)] \right)^{-1}. \quad (3.18)$$

Both values $Z_{\text{SCL}}^{\text{HF}}$ and $Y_{\text{SCL}}^{\text{HF}}$ are frequency dependent. The characteristic impedance has the same frequency dependency as the p. u. l. impedance and admittance of the single wire. Using (3.17) and (3.18) in Eq. (2.76), the characteristic impedance becomes

$$Z_{\text{c,SCL}}^{\text{HF}} = \frac{1}{4\pi} \sqrt{\frac{\mu}{\varepsilon}} \left(\pi [Y_0(2hk) - Y_0(ak)] + j\pi [J_0(2hk) - J_0(ak)] \right). \quad (3.19)$$

If one is interested in the p. u. l. parameters, the series representation form of Y_0 is used as described in [Wat44, Ch. III, p. 60]

$$Y_0(y) = 2 \left[\ln \frac{y}{2} + \gamma_{\text{EM}} \right] J_0(y) - 2 \sum_{k=1}^{\infty} (-1)^k \frac{\left(\frac{y}{2}\right)^{2k}}{(k!)^2} \left(\sum_{n=1}^k \frac{1}{n} \right), \quad (3.20)$$

where γ_{EM} is the Euler-Mascheroni constant. Using this expression, the solution of the Green's integral from Eq. 3.15 follows after some rearrangement and resorting with

$$\begin{aligned} \int_{-\infty}^{+\infty} g(y, y') dy' &= 2 \ln \frac{2h}{a} \\ &+ 2 \left\{ [\ln(hk) + \gamma_{\text{EM}}] [J_0(2hk) - 1] - \left[\ln \left(\frac{ak}{2} + \gamma_{\text{EM}} \right) \right] [J_0(ak) - 1] \right\} \\ &- \left\{ \left[\sum_{k=1}^{\infty} (-1)^k \frac{(hk)^{2k}}{(k!)^2} \left(\sum_{n=1}^k \frac{1}{n} \right) \right] - \left[\sum_{k=1}^{\infty} (-1)^k \frac{\left(\frac{ak}{2}\right)^{2k}}{(k!)^2} \left(\sum_{n=1}^k \frac{1}{n} \right) \right] \right\} \\ &+ j\pi [J_0(2hk) - J_0(ak)]. \end{aligned} \quad (3.21)$$

The approximation of classical TLT keeps only the frequency independent part, which is the first term in the above expansion. The terms after the classical approximation term are referred as correction factor $C_{\text{SCL}}^{\text{F}}$

$$\begin{aligned} C_{\text{SCL}}^{\text{F}} &= 2 \left\{ [\ln(hk) + \gamma_{\text{EM}}] [J_0(2hk) - 1] - \left[\ln \left(\frac{ak}{2} + \gamma_{\text{EM}} \right) \right] [J_0(ak) - 1] \right\} \\ &- \left\{ \left[\sum_{k=1}^{\infty} (-1)^k \frac{(hk)^{2k}}{(k!)^2} \left(\sum_{n=1}^k \frac{1}{n} \right) \right] - \left[\sum_{k=1}^{\infty} (-1)^k \frac{\left(\frac{ak}{2}\right)^{2k}}{(k!)^2} \left(\sum_{n=1}^k \frac{1}{n} \right) \right] \right\} \\ &+ j\pi [J_0(2hk) - J_0(ak)]. \end{aligned} \quad (3.22)$$

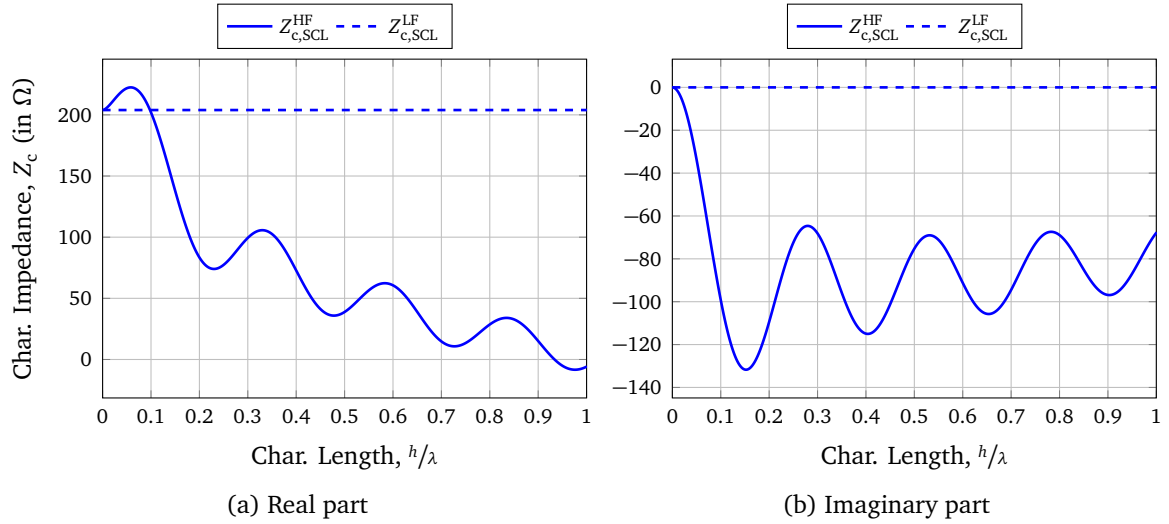


Figure 3.2: Comparison between the classical and the high frequency characteristic impedance for a single conductor transmission line with the radius $a = 1$ mm and the height $h = 1.5$ cm

The real part of the correction factor is

$$\Re \{ C_{SCL}^F \} = 2 \left\{ \left[\ln(hk) + \gamma_{EM} \right] [J_0(2hk) - 1] - \left[\ln\left(\frac{ak}{2} + \gamma_{EM}\right) \right] [J_0(ak) - 1] \right\} - \left\{ \left[\sum_{k=1}^{\infty} (-1)^k \frac{(hk)^{2k}}{(k!)^2} \left(\sum_{n=1}^k \frac{1}{n} \right) \right] - \left[\sum_{k=1}^{\infty} (-1)^k \frac{\left(\frac{ak}{2}\right)^{2k}}{(k!)^2} \left(\sum_{n=1}^k \frac{1}{n} \right) \right] \right\} \quad (3.23)$$

and the imaginary part is

$$\Im \{ C_{SCL}^F \} = j\pi [J_0(2hk) - J_0(ak)]. \quad (3.24)$$

The characteristic impedance from Eq. (3.19) can be defined by a sum of a low frequency (constant) and high frequency (frequency dependent) part. This makes the characteristic impedance complex and frequency dependent, even with a lossless transmission line. The low frequency characteristic impedance for the single line above the conductive ground plane follows with

$$Z_{c,SCL}^{LF} = \frac{1}{2\pi} \sqrt{\frac{\mu}{\epsilon}} \ln\left(\frac{2h}{a}\right). \quad (3.25)$$

In Fig. 3.2, the characteristic impedance for a single wire with the radius $a = 1$ mm, the height $h = 1.5$ cm over ground and the length $l = 1$ m is shown. The transverse dimension lead to a classical characteristic impedance of $Z_{c,SCL}^{LF} = 204 \Omega$ from Eq.(3.25). If the assumptions of the classical TLT are still fulfilled, the real elements of the HF characteristic impedance correspond to the classical ones, while the imaginary elements are zero. Furthermore, when the height of

the wires becomes significant in relation to the wavelength, both the real and imaginary parts of the characteristic impedance elements become frequency dependent and are completely different from the classical ones. This frequency dependence of the characteristic impedance has effects on the examinations in EMC. The characteristic impedance is the ratio between the forward traveling voltage and current waves or negative ratio of the backward traveling voltage and current waves (see Section 2.2.3). If Z_c has an imaginary part or a phase unequal to zero, there will be a phase between these waves. This imaginary part has an influence on the return loss and represents the loss of power in the signal reflected in a transmission line due to an impedance mismatch. As explained in Section 2.2.4, the aim is to match the line to obtain maximum signal transmission. A complex characteristic impedance makes it more difficult to find an appropriate load impedance.

Derivation of an Equivalent Circuit

The previously presented theory for transmission line can be represented by an equivalent circuit for a short section of a SCL as shown in Fig. 3.3. The equivalent circuit is similar to the classical equivalent circuit as shown in Fig. 2.2. However, the p. u. l. parameters are frequency dependent and more general compared to the classical ones. Thus, the main assumption of classical ($kh \ll 1$) TLT no longer needs to be respected. Using the definitions of the impedance and the admittance one can obtain the p. u. l. parameters from Eq. (5.4).

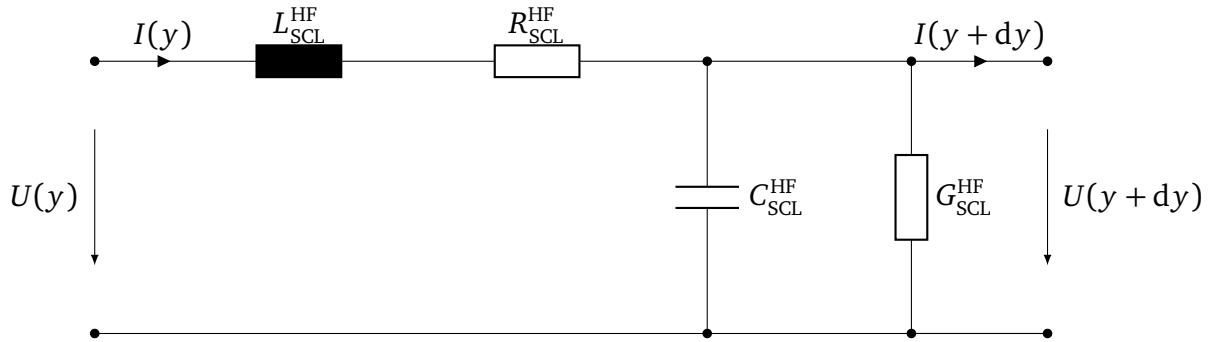


Figure 3.3: Equivalent circuit model with frequency dependent p. u. l. parameters in case for a single conductor transmission line over a ground plane

The explicit expressions of the p. u. l. parameters are given by

$$L_{SCL}^{HF} = L'_{SCL} + \frac{\mu_0}{4\pi} \Re \{ C_{SCL}^F \}, \quad (3.26a)$$

$$R_{SCL}^{HF} = -\omega \frac{\mu_0}{4\pi} \Im \{ C_{SCL}^F \}, \quad (3.26b)$$

$$C_{SCL}^{HF} = 2 \ln \left(\frac{2h}{a} \right) \frac{C'_{SCL} [2 \ln \left(\frac{2h}{a} \right) + \Re \{ C_{SCL}^F \}]}{4 \ln^2 \left(\frac{2h}{a} \right) + 4 \Re \{ C_{SCL}^F \} \ln \left(\frac{2h}{a} \right) + \Re \{ C_{SCL}^F \}^2 + \Im \{ C_{SCL}^F \}^2}, \quad (3.26c)$$

$$G_{SCL}^{HF} = 2 \ln \left(\frac{2h}{a} \right) \frac{\omega C'_{SCL} \Im \{ C_{SCL}^F \}}{4 \ln^2 \left(\frac{2h}{a} \right) + 4 \Re \{ C_{SCL}^F \} \ln \left(\frac{2h}{a} \right) + \Re \{ C_{SCL}^F \}^2 + \Im \{ C_{SCL}^F \}^2}. \quad (3.26d)$$

The classical p. u. l. parameters for a single line above a conductive plane L'_{SCL} and C'_{SCL} can be calculated using the method of images [KMR08, Ch. 11.6]. This calculation results in the same form as the classical p. u. l. parameters in Eq. (2.73) and Eq. (2.74). Furthermore, the new high frequency p. u. l. parameters are now frequency dependent and are no longer limited to the quasi static approximation. The resistance and (negative) conductivity parameters take higher order modes into account, while the frequency dependent inductance and capacitance may differ significantly from the classical parameters.

3.2 Field-to-Wire Coupling Equations

Based on the theory introduced in Sec. 2.1.2, the field-to-wire coupling for a single wire line is derived. A single line above a conductive ground plane in the x - y plane (see Fig. 3.4) is considered. The beginning of the line is defined by (x_1, y_1, z_1) and the end by (x_2, y_2, z_2) . The wire has a specific radius of a and a length l . The line represents the wire itself at the height h and its image wire at the height $-h$.

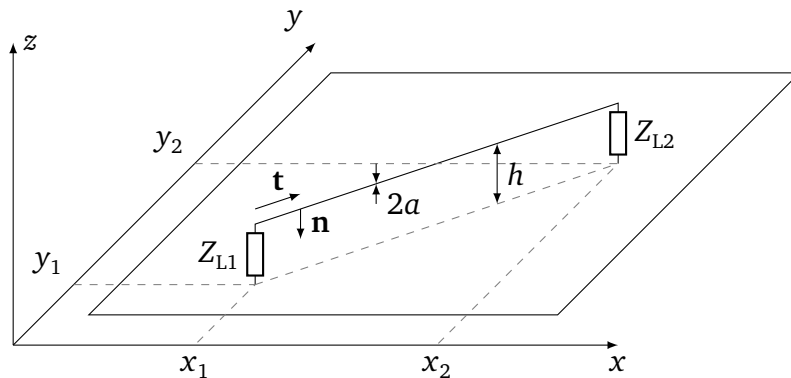


Figure 3.4: Geometry of an arbitrarily oriented and straight single line with the height h over a perfectly conductive ground plane. The line has the radius a and is terminated with load impedances Z_{L1} and Z_{L2} .

In many cases, only the coupling of the voltage and current at the ends of the wire is of interest. The BLT equations represent a very compact notation of the coupled currents and voltages at the line ends. Eqs. (2.26) can be written in a compact matrix form. The coupled currents at the line ends are given by

$$[I_{L,\text{SCL}}] = \begin{bmatrix} I_{L1,\text{SCL}} \\ I_{L2,\text{SCL}} \end{bmatrix} = Y_{c,\text{SCL}}^{\text{HF}} \cdot \begin{bmatrix} 1 - \Gamma_1 & 0 \\ 0 & 1 - \Gamma_2 \end{bmatrix} \cdot [D]^{-1} \cdot \begin{bmatrix} S_{1,\text{SCL}} \\ S_{2,\text{SCL}} \end{bmatrix}. \quad (3.27)$$

according to [TIK96]. Here, $Y_{c,\text{SCL}}$ is the characteristic admittance according to Eq. (2.78)

and together with Eq. (3.19) one obtains

$$Y_{c,SCL}^{HF} = \left(\frac{1}{4\pi} \sqrt{\frac{\mu}{\varepsilon}} \left(\pi [J_0(2hk) - J_0(ak)] + j\pi [Y_0(2hk) - Y_0(ak)] \right) \right)^{-1}. \quad (3.28)$$

Analogously to Eq. (3.27) follows for the coupled voltage

$$[U_{L,SCL}] = \begin{bmatrix} U_{L1,SCL} \\ U_{L2,SCL} \end{bmatrix} = \begin{bmatrix} 1 + \Gamma_1 & 0 \\ 0 & 1 + \Gamma_2 \end{bmatrix} \cdot [D]^{-1} \cdot [S_{SCL}]. \quad (3.29)$$

Here, $I_{L1,SCL}$ and $U_{L1,SCL}$ are the current and voltage at the beginning of the line while $I_{L2,SCL}$ and $U_{L2,SCL}$ are the current and voltage at the end of the line. The first 2×2 matrix in Eqs. (3.27) and (3.29) determines whether the current or the voltage is calculated. The reflection coefficients Γ_1 and Γ_2 are defined by Eq. (2.86). The third matrix $[D]$ is the 2×2 propagation matrix with

$$[D] = \begin{bmatrix} -\Gamma_1 & e^{\gamma l} \\ e^{\gamma l} & -\Gamma_2 \end{bmatrix}. \quad (3.30)$$

Here, γ is a propagation constant of the voltage and current waves along the wire. If it is assumed that the waves propagate equally distributed on the conductor, then it is a scalar quantity $\gamma = jk$, which depends only on the wave number k . The last matrix $[S_{SCL}]$ describes the source vectors. To simplify the source terms of the incident field ([Per95, Eq. (53)]) the formulation according to Agrawal [APG80] is used

$$S_{1,SCL} = -\frac{1}{2} \begin{cases} 0 & \text{if } \gamma_- = 0 \\ -U_{t1,SCL} \cdot (1 - e^{2\gamma l}) & \text{if } \gamma_+ = 0 \\ \left(\frac{E_{\tan,SCL}^e r_1}{\gamma_-} - U_{t1,SCL} \right) \cdot (1 - e^{\gamma l}) & \text{else,} \end{cases} \quad (3.31a)$$

$$S_{2,SCL} = -\frac{1}{2} e^{\gamma l} \begin{cases} U_{t1,SCL} \cdot (1 - e^{-2\gamma l}) & \text{if } \gamma_- = 0 \\ 0 & \text{if } \gamma_+ = 0 \\ \left(\frac{E_{\tan,SCL}^e r_1}{\gamma_+} + U_{t1,SCL} \right) \cdot (1 - e^{-\gamma l}) & \text{else.} \end{cases} \quad (3.31b)$$

Here, $r_1 = e^{-j(k_x x_1 + k_y y_1)}$ is a rotating phasor at the beginning of the conductor. For the modified propagation constants, it follows that

$$\gamma_+ = \gamma + j \cdot \mathbf{k}, \quad (3.32a)$$

$$\gamma_- = \gamma - j \cdot \mathbf{k}. \quad (3.32b)$$

In the following, the tangential electric field $E_{\tan,SCL}$ and the transverse voltage $U_{t1,SCL}$ are determined. For an excitation by a random plane wave the stochastic electric field is given by

$$E_{SCL}(\mathbf{r}) = E_{SCL} \mathbf{e} \cdot e^{-j(\mathbf{k} \cdot \mathbf{r} + \beta)}. \quad (3.33)$$

Here, E_{SCL} is the amplitude and \mathbf{k} is the wave vector. The electric field is defined as in [Mag12, Ch. 2.3]

$$E_{\text{SCL}} = \frac{E_0}{\sqrt{2N}}, \quad (3.34)$$

where N is the number of waves to be superimposed per boundary condition. The factor 2 applies if one calculates the coupling to a single line over a wall in the reverberation chamber. The exciting tangential field $E_{\text{tan,SCL}}^e$ along a single line can be described by the incident wave $E_{\text{tan,SCL}}^i$ and the reflected wave $E_{\text{tan,SCL}}^r$ by the ground plane

$$E_{\text{tan,SCL}}^e = E_{\text{tan,SCL}}^i + E_{\text{tan,SCL}}^r. \quad (3.35)$$

For the reflected wave it follows using the method of images

$$E_{\text{tan,SCL}}^r(x, y, h) = -E_{\text{tan,SCL}}^i(x, y, -h). \quad (3.36)$$

For the tangential field follows

$$E_{\text{tan,SCL}}^e(x, y, h) = E_{\text{SCL}} \mathbf{e} \cdot \mathbf{t} \cdot e^{-j(k_x \cdot x + k_y \cdot y + k_z \cdot h + \beta)} - E_{\text{SCL}} \mathbf{e} \cdot \mathbf{t} \cdot e^{-j(k_x \cdot x + k_y \cdot y - k_z \cdot h + \beta)}, \quad (3.37a)$$

$$= E_{\text{SCL}} \mathbf{e} \cdot \mathbf{t} \cdot (e^{-k_z \cdot h} - e^{k_z \cdot h}) \cdot e^{-j(k_x \cdot x + k_y \cdot y + \beta)}, \quad (3.37b)$$

$$= -2jE_{\text{SCL}} \mathbf{e} \cdot \mathbf{t} \sin k_z h \cdot e^{-j(k_x \cdot x + k_y \cdot y + \beta)}. \quad (3.37c)$$

The transverse voltage can be determined by the integration between the ground plane acting as a return conductor at $z = 0$ up to the line at $z = h$. From the transverse z -component of the incident and reflecting wave follows the transverse voltage at the beginning and end of the line (based on [TIK96, Sec. 7.2.2.2])

$$U_{t1,\text{SCL}} = \int_0^h (E_{\text{tan,SCL}}^i(x, 0, z) + E_{\text{tan,SCL}}^r(x, 0, z)) dz, \quad (3.38a)$$

$$U_{t2,\text{SCL}} = \int_0^h (E_{\text{tan,SCL}}^i(x, l, z) + E_{\text{tan,SCL}}^r(x, l, z)) dz. \quad (3.38b)$$

From Eq. (3.36) one can determine

$$U_{t1,\text{SCL}} = \int_0^h E_{\text{tan,SCL}}^i(x, 0, z) dz - \int_0^{-h} E_{\text{tan,SCL}}^i(x, 0, z) dz = \int_{-h}^h E_{\text{tan,SCL}}^i(x, 0, z) dz. \quad (3.39a)$$

Moreover, the voltage at the beginning of the line is

$$U_{t1,\text{SCL}} = 2E_{\text{SCL}} e_z e^{j\beta} r_1 \begin{cases} h & \text{if } k_z = 0 \\ \frac{\sin(k_z h)}{k_z} & \text{else.} \end{cases} \quad (3.40)$$

The same applies to the transverse voltage at the end of the line

$$U_{t2,SCL} = 2E_{SCL} e_z e^{j\beta} r_2 \begin{cases} h & \text{if } k_z = 0 \\ \frac{\sin(k_z h)}{k_z} & \text{else.} \end{cases} \quad (3.41)$$

Here, $r_2 = e^{-j(k_x x_2 + k_y y_2)}$ is a rotating phasor at the end of the line. Now, with Eqs. (3.31) to (3.40), the coupled currents and voltages at the beginning and end of the conductor can be determined.

3.3 Validation of the Model

A generic single conductor transmission line was chosen for the validation and application of the presented theory. The dimensions of this transmission line allow an experimental validation of the presented theory in a reverberation chamber. The transmission line had a specific radius of $a = 1$ mm and a length of $l = 1$ m and was placed at a height $h = 3$ cm over the conductive ground plane. A classical characteristic impedance of $Z_c = 245 \Omega$ follows from the dimensions of the transmission line. The impedances at the beginning and end of the line were $Z_{L1} = 50 \Omega$ and $Z_{L2} = 50 \Omega$.

3.3.1 Validation Using the Method of Moments

The theory presented in the previous sections is validated against the MoM. The exciting plane wave had a field strength of $E = 1 \frac{V}{m}$ and a phase angle of $\beta = 0$. The plane wave hit the transmission line slantingly from above, which means for the angles $\alpha = 315^\circ$, $\vartheta = 135^\circ$ and $\varphi = 225^\circ$ (see Fig. 2.10). The chosen angles lead to the following wave vector and electric field polarization from Eq. (2.88) and (2.89)

$$\mathbf{k} = k \cdot \begin{pmatrix} -0.5 \\ -0.5 \\ -0.7071 \end{pmatrix}, \quad \mathbf{e} = \begin{pmatrix} -0.1464 \\ 0.8536 \\ -0.5 \end{pmatrix}. \quad (3.42)$$

In order to model a plane wave, which hits the sample from in a slanted manner from above in *CONCEPT-II*, one chose the angle $\alpha = \vartheta = \varphi = 45^\circ$. Fig. 3.5 depicts the comparison between the solution based on the MoM and the solution using the BLT equation with low frequency (LF) as well as high frequency p. u. l. parameters. The real and imaginary parts of the terminal current at the end of the line is presented. The selected frequency range was 0 GHz to 4 GHz in steps of 2 MHz. At 0 MHz the result of the MoM was simply hard reset to zero as explained in Annex F. An almost excellent agreement between the simulated curves can be observed, which is also achieved for other wave incident directions. One can see that both simulation results based on TLT fit quite well up to 1 GHz to the MoM solution.

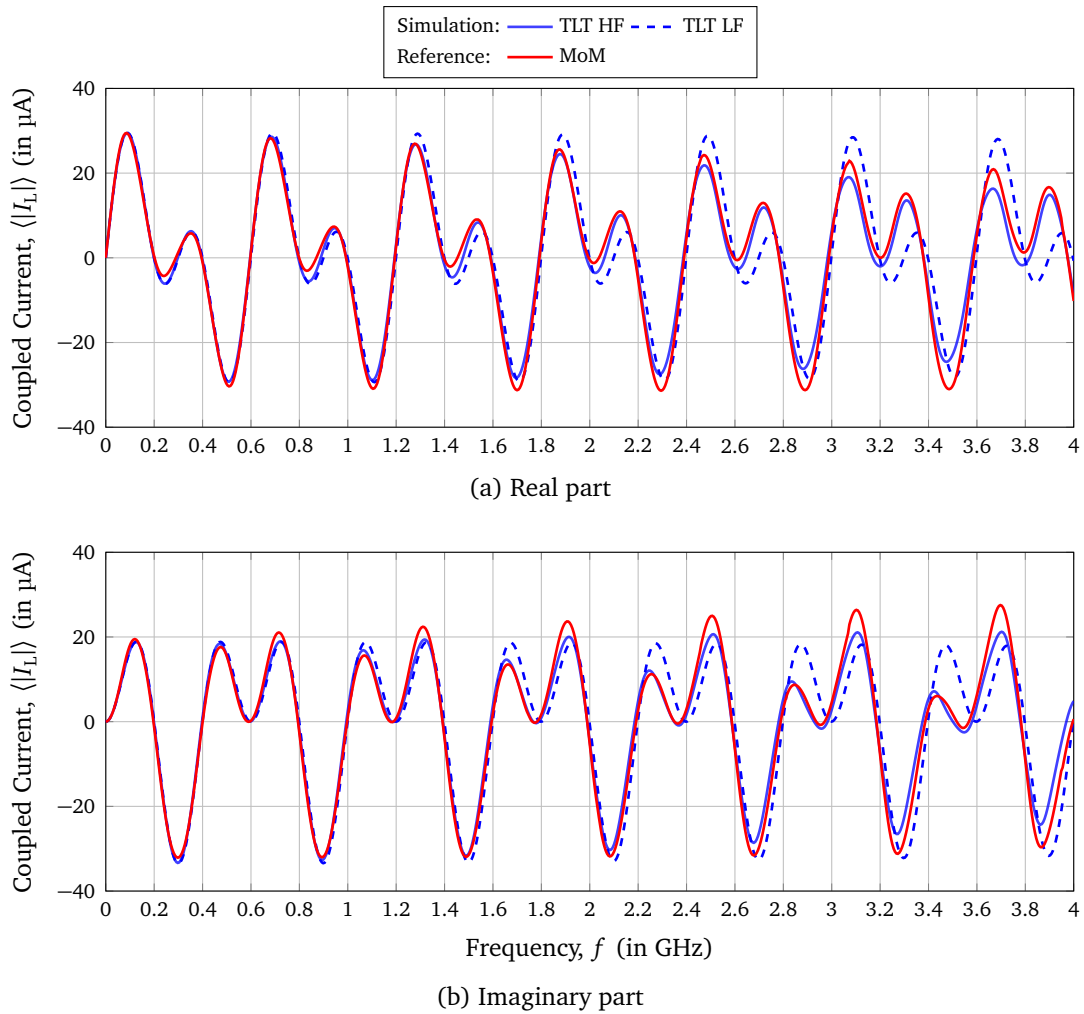


Figure 3.5: Real- and imaginary parts of the coupled current $\langle |I_{L1}| \rangle$ at the end of the line as a function of the frequency for the excitation with a single plane wave

Further, for higher frequencies over 1 GHz, the TLT solution based on HF p. u. l. parameters leads to more accurate results. Even with this correction, there are still some differences in frequency compared to the MoM results. This could be due to the monopole model used for the vertical wires and the neglected coupling effects between the horizontal and vertical wires. In general, the proposed model (TLT HF) leads to much more realistic results than the classical model (TLT LF) and generally provides a better approximation, especially for the most critical first resonances.

3.3.2 Validation Using Measurements in the Reverberation Chamber

In Fig. 5.11, the transmission line in the reverberation chamber is shown. For the transmission line, circular copper wires (see Fig. 3.6a) with a cross section of $A = 4 \text{ mm}^2$ and a line length of $l = 1 \text{ m}$ were chosen. Pins of N connectors were soldered at the ends of the wire. To connect the coaxial test cables to the ends of the wires, N feedthroughs (see Fig. 3.6b) were

mounted on the metal ground plane. These represented simultaneously a $50\ \Omega$ terminating resistance. Furthermore, the line was supported with a small styrofoam block to keep the height constant. The line was placed at $h = 3\ \text{cm}$ over the ground plane. The measurement was carried out from 200 MHz, the LUF of the chamber up to 1 GHz.

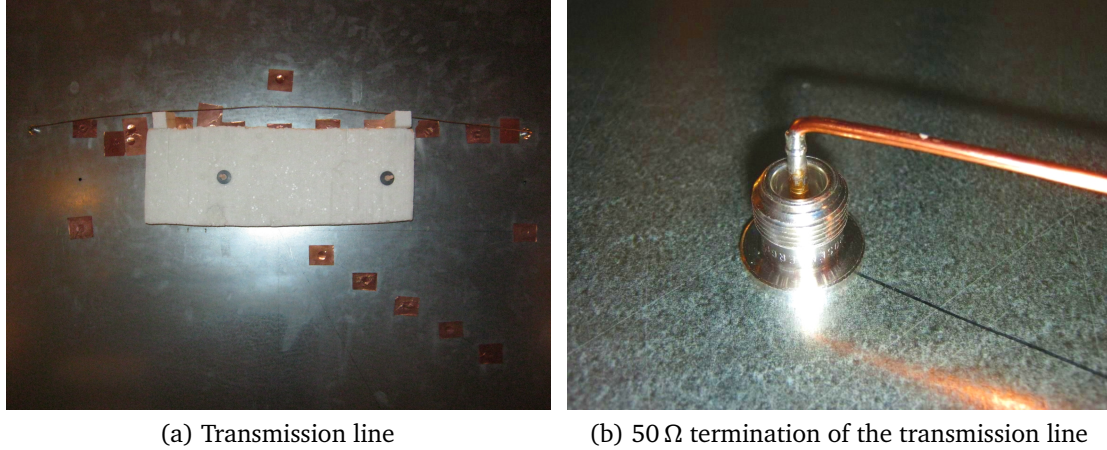


Figure 3.6: Transmission line over a conductive ground plane in the reverberation chamber

The measured scattered parameters were converted to the coupled voltage using Eq. (2.105) from Sec. 2.4.4 and the average magnitude of the coupled voltage was analyzed. A normalization to the chamber constant E_0 and to the distance h of the line to the ground plane was performed. This dimensionless quantity could be better compared to the simulation results and doesn't depend on the actual field strength and the height of the transmission line. In both transmission line models, an additional p. u. l. resistance was added, to include the effects of the vertical wires at the line ends [LMRT16, Eq. (6)]

$$R_{\text{rad}} = 160 \cdot \pi^2 \cdot \left(\frac{h}{\lambda}\right)^2 \Omega. \quad (3.43)$$

The resistance was connected in series to the loads Z_L at the beginning and the end of the line.

In Fig. 3.7, the normalized coupled voltage over the frequency is shown. A moving average over five frequencies was calculated to smooth the measured curve. For the symmetrically mismatched end of the line, strong resonances can be seen at approximately at 300 MHz, 450 MHz, 600 MHz, 750 MHz and 900 MHz. The resonances can also be expected for a symmetrically mismatched line, where resonances occur at $l = \lambda/2, \lambda, 3/2\lambda, \dots$ [MV12]. As a result, the semi-analytical simulation model could be validated using MoM simulations and measurements.

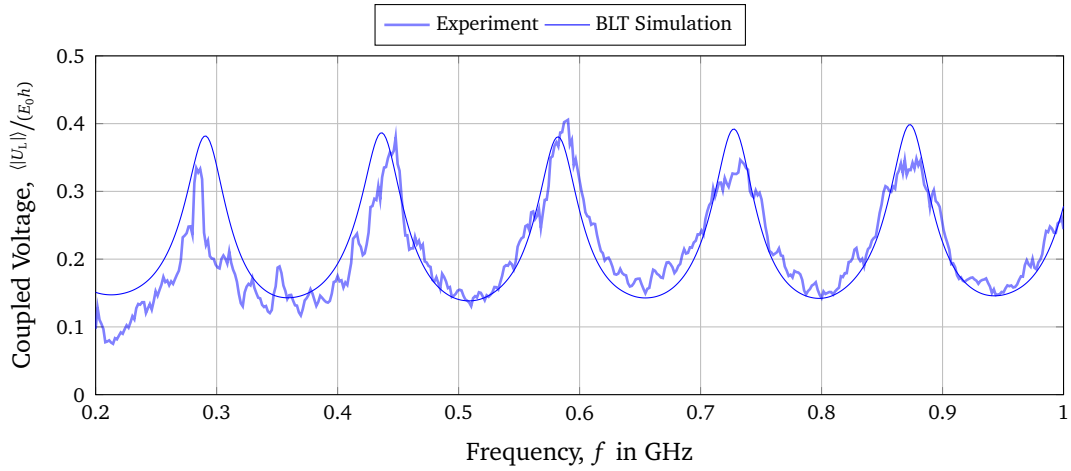


Figure 3.7: Measured mean magnitude coupled voltage $\langle |U_{L1}| \rangle$ at the beginning of a single wire over ground

3.4 Comparison with a Double Conductor Transmission Line

This section considers a double conductor transmission line as shown in Fig. 3.8. The line is directed along the y -axis and has a specific distance s between the two wires. The decisive difference to a single wire is that instead of a mirror line below the conducting plane, there is a reference conductor. In contrast to the mirror line, the reference conductor can have a different dimension than the conductor itself.

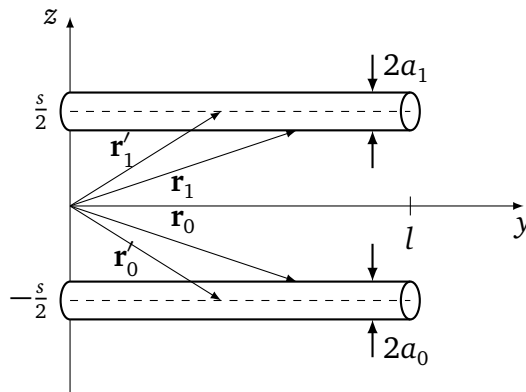


Figure 3.8: Double wire in y -direction with the length l and the radii a_0 and a_1

3.4.1 Transmission Line Model

As shown in Fig. 3.8, the wires have the radii a_0 and a_1 and are separated by a distance s from each other. Now, the Green's function $g(y, y')$ from Eq. (3.10) must be derived for this case. The observation point \mathbf{r}_1 on the surface of the conductor and \mathbf{r}_0 on the surface of the

reference conductor are defined by

$$\mathbf{r}_0 = -\frac{s}{2} \cdot \mathbf{e}_z + y \cdot \mathbf{e}_y, \quad (3.44a)$$

$$\mathbf{r}_1 = \frac{s}{2} \cdot \mathbf{e}_z + y \cdot \mathbf{e}_y. \quad (3.44b)$$

The source points \mathbf{r}'_1 and \mathbf{r}'_0 are defined with

$$\mathbf{r}'_0 = \left(-\frac{s}{2} - a_0\right) \cdot \mathbf{e}_z + y \cdot \mathbf{e}_y, \quad (3.45a)$$

$$\mathbf{r}'_1 = \left(\frac{s}{2} - a_1\right) \cdot \mathbf{e}_z + y \cdot \mathbf{e}_y. \quad (3.45b)$$

The vector potential of a double conductor transmission line is given by

$$A_y(y) = \frac{\mu}{4\pi} I(y) \int_0^l \left(\frac{e^{-jkR_{10}}}{R_{10}} + \frac{e^{-jkR_{01}}}{R_{01}} - \frac{e^{-jkR_{00}}}{R_{00}} - \frac{e^{-jkR_{11}}}{R_{11}} \right) dy'. \quad (3.46)$$

The distances between the observation and the source point are following with

$$R_{00} = |\mathbf{r}_0 - \mathbf{r}'_0| = \sqrt{a_0^2 + (y - y')^2}, \quad (3.47a)$$

$$R_{11} = |\mathbf{r}_1 - \mathbf{r}'_1| = \sqrt{a_1^2 + (y - y')^2}, \quad (3.47b)$$

$$R_{01} = |\mathbf{r}_0 - \mathbf{r}'_1| = \sqrt{(-s - a_1)^2 + (y - y')^2}, \quad (3.47c)$$

$$R_{10} = |\mathbf{r}_1 - \mathbf{r}'_0| = \sqrt{(s + a_0)^2 + (y - y')^2}. \quad (3.47d)$$

Assuming $a_1, a_0 \ll s$ one can approximate

$$R_{01} = |\mathbf{r}_0 - \mathbf{r}'_1| = \sqrt{s^2 + (y - y')^2}, \quad (3.48a)$$

$$R_{10} = |\mathbf{r}_1 - \mathbf{r}'_0| = \sqrt{s^2 + (y - y')^2}. \quad (3.48b)$$

For an observation point far enough away from the ends of the wires, the limits of integration can be extended to $-\infty$ to ∞ . Under assistance of some Hankel functions $H_0^{(2)}$, the solution of the Green's function integral becomes

$$\int_{-\infty}^{\infty} g(y, y') dy' = j\pi H_0^{(2)}(-ks) + j\pi H_0^{(2)}(-ks) - j\pi H_0^{(2)}(-ka_0) - j\pi H_0^{(2)}(-ka_1). \quad (3.49)$$

With the relationship between the Hankel function and some 0th-order Bessel function [Jac99], the final solution of the Green's function integral is

$$\int_{-\infty}^{\infty} g(y, y') dy' = \pi [2Y_0(sk) - Y_0(a_0k) - Y_0(a_1k)] + j\pi [2J_0(sk) - J_0(a_0k) - J_0(a_1k)]. \quad (3.50)$$

Here, the series expansion of Y_0 from Eq. (3.20) is used. After rearranging of terms, Eq. (3.49) can be rewritten as

$$\int_{-\infty}^{+\infty} g(y_i - y_j') dy' = 2 \ln \left(\frac{s^2}{a_0 a_1} \right) + C_{\text{DCL}}^{\text{F}}, \quad (3.51)$$

where all frequency dependent terms are summarized in the correction factor

$$\begin{aligned} C_{\text{DCL}}^{\text{F}} = & 2 \left\{ 2 \left[\ln \left(\frac{s}{2} k \right) + \gamma \right] [J_0(sk) - 1] - \left[\ln \left(\frac{a_0}{2} k \right) + \gamma \right] [J_0(a_0k) - 1] \right. \\ & \left. - \left[\ln \left(\frac{a_1}{2} k \right) + \gamma \right] [J_0(a_1k) - 1] \right\} - 2 \left\{ 2 \left(\sum_{k=1}^{\infty} (-1)^k \frac{\left(\frac{s}{2}\right)^{2k}}{(k!)^2} \left(\sum_{n=1}^k \frac{1}{n} \right) \right) \right. \\ & \left. - \left[\sum_{k=1}^{\infty} (-1)^k \frac{\left(\frac{a_0}{2}\right)^{2k}}{(k!)^2} \left(\sum_{n=1}^k \frac{1}{n} \right) \right] - \left[\sum_{k=1}^{\infty} (-1)^k \frac{\left(\frac{a_1}{2}\right)^{2k}}{(k!)^2} \left(\sum_{n=1}^k \frac{1}{n} \right) \right] \right\} \\ & + j\pi [J_0(sk) + J_0(sk) - J_0(a_0k) - J_0(a_1k)]. \end{aligned} \quad (3.52)$$

In classical TLT, one neglects the contribution of $C_{\text{DCL}}^{\text{F}}$. The explicit forms of the p. u. l. parameters are given by

$$L_{\text{DCL}}^{\text{HF}} = L'_{\text{DCL}} + \frac{\mu_0}{4\pi} \Re \{ C_{\text{DCL}}^{\text{F}} \}, \quad (3.53a)$$

$$R_{\text{DCL}}^{\text{HF}} = -\omega \frac{\mu_0}{4\pi} \Im \{ C_{\text{DCL}}^{\text{F}} \}, \quad (3.53b)$$

$$C_{\text{DCL}}^{\text{HF}} = 2 \ln \left(\frac{s^2}{a_0 a_1} \right) \frac{C'_{\text{DCL}} \left[2 \ln \left(\frac{s^2}{a_0 a_1} \right) + \Re \{ C_{\text{DCL}}^{\text{F}} \} \right]}{4 \ln^2 \left(\frac{s^2}{a_0 a_1} \right) + 4 \Re \{ C_{\text{DCL}}^{\text{F}} \} \ln \left(\frac{s^2}{a_0 a_1} \right) + \Re \{ C_{\text{DCL}}^{\text{F}} \}^2 + \Im \{ C_{\text{DCL}}^{\text{F}} \}^2}, \quad (3.53c)$$

$$G_{\text{DCL}}^{\text{HF}} = 2 \ln \left(\frac{s^2}{a_0 a_1} \right) \frac{\omega C'_{\text{DCL}} \Im \{ C_{\text{DCL}}^{\text{F}} \}}{4 \ln^2 \left(\frac{s^2}{a_0 a_1} \right) + 4 \Re \{ C_{\text{DCL}}^{\text{F}} \} \ln \left(\frac{s^2}{a_0 a_1} \right) + \Re \{ C_{\text{DCL}}^{\text{F}} \}^2 + \Im \{ C_{\text{DCL}}^{\text{F}} \}^2}. \quad (3.53d)$$

Here, L'_{DCL} and C'_{DCL} are the classical transmission line p. u. l. parameters for a double conductor transmission line as defined in (2.44) and (2.49). Eqs. (3.16a) and (3.16b) have the same form for the double wire case and result in an impedance of

$$Z_{\text{DCL}}^{\text{HF}} = \frac{j\omega\mu}{4\pi} \left(\pi [2Y_0(sk) - Y_0(a_0k) - Y_0(a_1k)] + j\pi [2J_0(sk) - J_0(a_0k) - J_0(a_1k)] \right) \quad (3.54)$$

and an admittance of

$$Y_{\text{DCL}}^{\text{HF}} = j\omega 4\pi\epsilon (\pi [2Y_0(sk) - Y_0(a_0k) - Y_0(a_1k)] + j\pi [2J_0(sk) - J_0(a_0k) - J_0(a_1k)])^{-1}. \quad (3.55)$$

If the impedance and the admittance of the double wire are frequency dependent, the characteristic impedance has the same frequency dependence. Using (3.54) and (3.55), the characteristic impedance becomes

$$Z_{\text{c,DCL}}^{\text{HF}} = \frac{1}{4\pi} \sqrt{\frac{\mu}{\epsilon}} \left(\pi [2Y_0(sk) - Y_0(a_0k) - Y_0(a_1k)] + j\pi [2J_0(sk) - J_0(a_0k) - J_0(a_1k)] \right). \quad (3.56)$$

The characteristic impedance can be represented by the sum of a low frequency part, that is known from the classical transmission line theory and the frequency dependent correction factor

$$Z_{\text{c,DCL}} = \underbrace{\frac{1}{2\pi} \sqrt{\frac{\mu}{\epsilon}} \ln\left(\frac{s^2}{a_0 a_1}\right)}_{Z_{\text{c,DCL}}^{\text{LF}}} + C_{\text{DCL}}^{\text{F}}. \quad (3.57)$$

In Fig. 3.9, the characteristic impedance for a double wire with the radius $a_1 = a_0 = 1$ mm, the distance $s = 3$ cm and the length $l = 1$ m is shown. From the transverse dimensions of the DCL follows a classical characteristic impedance of $Z_{\text{c,DCL}}^{\text{LF}} = 408 \Omega$. Additionally, the characteristic impedance for a single wire with the same dimensions ($s = 2h = 3$ cm, $a = a_0 = 1$ mm) is shown. The characteristic impedance elements for both cases become frequency dependent and qualitatively different from the classical ones.

Note, if the wires have the following dimensions $s = 2h$ and $a_0 = a_1 = a$, the characteristic impedance for the SCL and the DCL have the following dependence

$$Z_{\text{c,SCL}}^{\text{LF}} = \frac{Z_{\text{c,DCL}}^{\text{LF}}}{2}. \quad (3.58)$$

3.4.2 Field-to-Wire Coupling Equations

The previously presented theory handled a single wire above a conductive ground plane and is now extended to a double wire. A schematic of a double wire is shown in Fig. 3.10. A system of a uniform double conductor transmission line excited by an external electromagnetic field is considered. The double wire can be constructed from a single-wire line with the start and end coordinates of each line $(x_{1,1}, y_{1,1}, z_{1,1})$ and $(x_{2,1}, y_{2,1}, z_{2,1})$ as well as a reference conductor with the coordinates $(x_{1,0}, y_{1,0}, z_{1,0})$ at the beginning and $(x_{2,0}, y_{2,0}, z_{2,0})$ at the

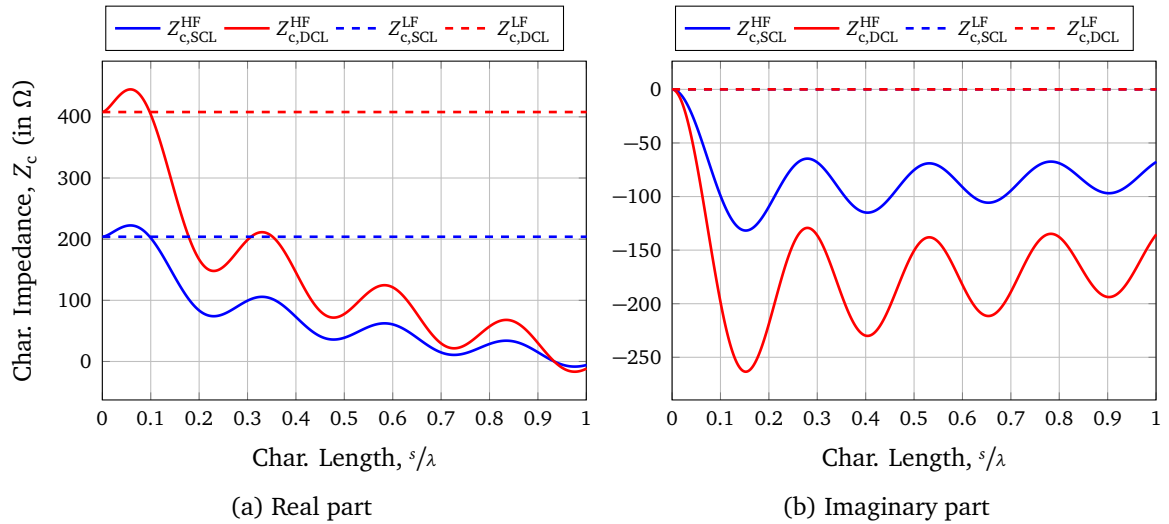


Figure 3.9: Comparison between the classical and the HF characteristic impedance as a function of the frequency of a double wire with the radius $a_0 = a_1 = 1$ mm and the distance $s = 3$ cm with the classical and the HF characteristic impedance of a single wire with the same radius ($s = h$)

end of the line. The first index 1 stands for the beginning of the line and index 2 for the end point of the line. The wires have a specific radius a_1 and the reference conductor a_0 .

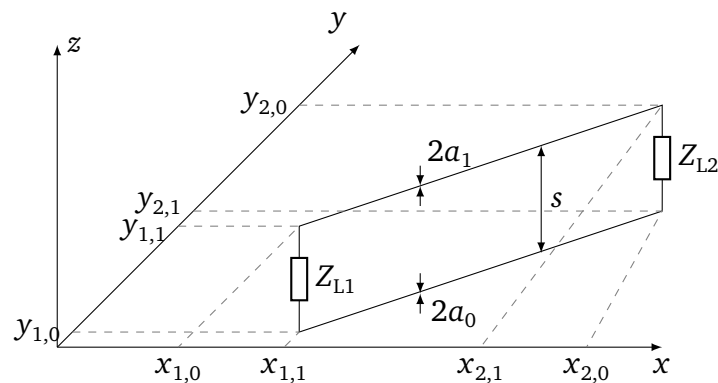


Figure 3.10: Geometry of an arbitrarily oriented and straight double wire line with the distance s . The lines have the radius a_0 and a_1 and are terminated with load impedances Z_{L1} and Z_{L2} .

The scattered voltage is described similar to Eq. (2.22) as integral over the normal electrical field between the reference conductor and the conductor. For the scattered voltage from Eq. (2.22) follows with the boundary conditions of the double wire case

$$U^s(\mathbf{t}) = \phi(\mathbf{r}_1) - \phi(\mathbf{r}_0). \quad (3.59)$$

The observation point \mathbf{r}_1 on the surface of the conductor and \mathbf{r}_0 on the surface of the reference conductor are already defined in Eq. (3.44). With the boundary condition $\phi(\mathbf{r}_0) = 0$ follows

$$U^s(\mathbf{t}) = \phi(\mathbf{r}_1). \quad (3.60)$$

Under these boundary conditions, the field-to-wire coupling equations are the same as in Eq. 2.26, with the difference that the tangential field $E_{\text{tan,DCL}}$ must be determined from the geometry. The BLT equations have the same form as in Eq. (3.29) and (3.27)

$$[U_{L,\text{DCL}}] = \begin{bmatrix} U_{L1,\text{DCL}} \\ U_{L2,\text{DCL}} \end{bmatrix} = \begin{bmatrix} 1 + \Gamma_1 & 0 \\ 0 & 1 + \Gamma_2 \end{bmatrix} \cdot [D]^{-1} \cdot \begin{bmatrix} S_{1,\text{DCL}} \\ S_{2,\text{DCL}} \end{bmatrix}. \quad (3.61)$$

Now, the source vector changes due to the different geometry to

$$S_{1,\text{DCL}} = -\frac{1}{2} \begin{cases} 0 & \text{if } \gamma_- = 0 \\ -U_{t1} \cdot (1 - e^{2\gamma l}) & \text{if } \gamma_+ = 0 \\ \left(\frac{E_{\text{tan,DCL}}^e r_1}{\gamma_-} - U_{t1,\text{DCL}} \right) \cdot (1 - e^{\gamma l}) & \text{else,} \end{cases} \quad (3.62a)$$

$$S_{1,\text{DCL}} = -\frac{1}{2} e^{\gamma l} \begin{cases} U_{t1,\text{DCL}} \cdot (1 - e^{-2\gamma l}) & \text{if } \gamma_- = 0 \\ 0 & \text{if } \gamma_+ = 0 \\ \left(\frac{E_{\text{tan,DCL}}^e r_1}{\gamma_+} + U_{t1,\text{DCL}} \right) \cdot (1 - e^{-\gamma l}) & \text{else.} \end{cases} \quad (3.62b)$$

The excitation by a random plane wave from Eq. (3.34) changes for the double wire case to

$$E_{\text{DCL}}(\mathbf{r}) = E_{\text{DCL}} \mathbf{e} \cdot e^{-j(\mathbf{k}\cdot\mathbf{r}+\beta)}, \quad (3.63)$$

with

$$E_{\text{DCL}} = \frac{E_0}{\sqrt{N}}, \quad (3.64)$$

when the line is not placed above a wall in the reverberation chamber as in Eq. (3.34). The exciting tangential field along the double wire has the same form as in Eq. (3.35)

$$E_{\text{tan,DCL}}^e(x, y, \frac{s}{2}) = E_{\text{tan,DCL}}^i(x, y, \frac{s}{2}) - E_{\text{tan,DCL}}^i(x, y, -\frac{s}{2}), \quad (3.65)$$

with the incident wave $E_{\text{tan,DCL}}^i$ and the reflected wave $E_{\text{tan,DCL}}^r$. For the tangential field at \mathbf{r} follows as in Eq. (3.37c)

$$E_{\text{tan,DCL}}^e(x, y, \frac{s}{2}) = -2jE_{\text{DCL}} \mathbf{e} \cdot \mathbf{t} \sin(k_z \frac{s}{2}) \cdot e^{-j(k_x \cdot x + k_y \cdot y + \beta)}. \quad (3.66a)$$

Furthermore, the tangential voltage is

$$U_{t1,\text{DCL}} = 2E_{\text{DCL}} e_z e^{j\beta} r_1 \begin{cases} \frac{s}{2} & \text{if } k_z = 0 \\ \frac{\sin(k_z \frac{s}{2})}{k_z} & \text{else,} \end{cases} \quad (3.67a)$$

$$U_{t2,\text{DCL}} = 2E_{\text{DCL}} e_z e^{j\beta} r_2 \begin{cases} \frac{s}{2} & \text{if } k_z = 0 \\ \frac{\sin(k_z \frac{s}{2})}{k_z} & \text{else.} \end{cases} \quad (3.67b)$$

With the last two expressions all necessary equations are given to determine the field-to-wire coupling.

3.4.3 Coupled Current as a Function over the Frequency

Now, the theory of the double line is compared with the previous theory of the single line. For the analysis of the stochastic field coupling the same transmission line structure and the same frequency range was used ($l = 1$ m, $s = 2h = 2$ cm and $a_1 = a_0 = 1$ mm, $f_{\min} = 0$ Hz, $f_{\max} = 1$ GHz). From the transverse dimensions, a LF characteristic impedance for the SCL follows from Eq. (3.19) with $Z_{c,SCL} = 204 \Omega$. For the DCL, Eq. (5.59) leads to a characteristic impedance of $Z_{c,DCL} = 408 \Omega$. The characteristic impedance of the single wire case is one-half of the double wire case. If the termination impedances of the SCL were one-half of the DCL case, the value of the reflection coefficient Γ become the same for both problems. The load impedances of the SCL were $Z_{L,SCL1} = 50 \Omega$ and $Z_{L,SCL2} = 50 \Omega$ and for the DCL $Z_{L,DCL1} = 100 \Omega$ and $Z_{L,DCL2} = 100 \Omega$. The transmission line propagation γ remains unchanged for both cases, because the p. u. l. inductance was two times smaller than the corresponding inductance for the SCL and the p. u. l. capacitance became two times larger than the SCL capacitance. For the simulation $B = 360$ electromagnetic boundary conditions were chosen. This number represents the number of stirrer positions. Each boundary condition consisted of $N = 10$ plane waves. For the chamber constant a value of $E_0 = 1 \frac{V}{m}$ was used. Again, a p. u. l. resistance to the DCL transmission model in order to include the effects of the vertical wires at the line ends (similar to Eq. (3.43)) was added in series to the loads Z_L at the beginning and the end of the line

$$R_{\text{rad}} = 160 \cdot \pi^2 \cdot \left(\frac{s}{2\lambda} \right)^2 \Omega. \quad (3.68)$$

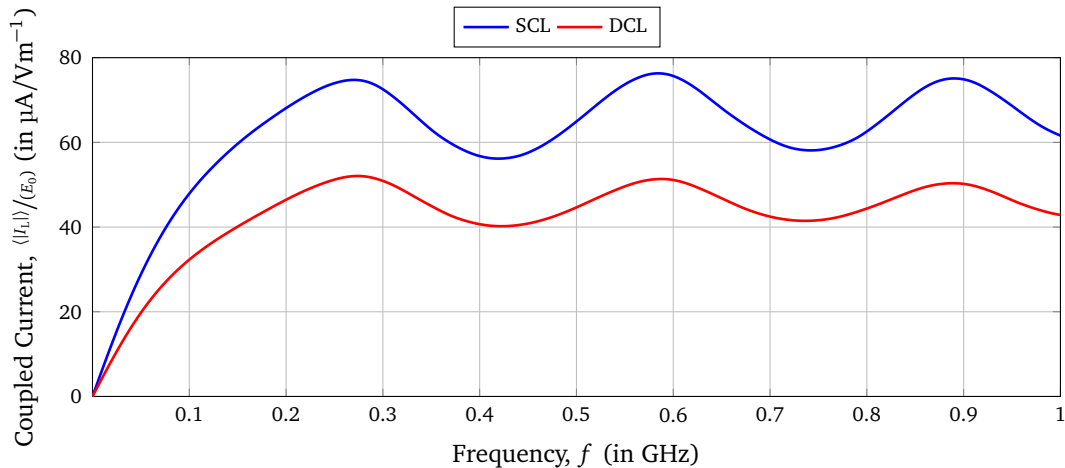


Figure 3.11: Comparison of the simulated average magnitude of the coupled current $\langle |I_{L1}| \rangle$ at the beginning of a single line over ground and the double line in free space

In Fig. 3.11, the comparison between the coupled current of the single and the double wire calculated using Eq. (3.27) is shown. Here, $\langle |I_L| \rangle$ is the average magnitude of the electric current over the boundary conditions. Because of the same lengths of the lines, the resonances occur at the same frequencies ($l = \lambda/2, \lambda, 3/2\lambda, \dots$). The expected value of the magnitude of the coupled current for a single wire is a factor two larger than for the

corresponding double line with the same transverse dimensions of the wires. Summarizing these observations, the line-to-line voltage of the DCL is the same as the line-to-ground voltage of the SCL.

3.5 Results of the Investigation of the Single and Double Conductor

Within this chapter one-dimensional structures such as single and double wires were investigated. Some complex and frequency dependent p. u. l. parameters were derived for the SCL and DCL case. For both investigated cases the used transmission line model could be validated. Here, the already widely used BLT equations could be combined with a stochastic field excitation and with frequency dependent transmission line parameters. For the mismatched line one could observe all resonances, which are expected from transmission line theory. Furthermore, the results of the single wire line were compared with those of the double wire line. As expected from the theory, the coupled current of the DCL and the SCL with the same dimensions results in a current for the single wire twice as high as for the double wire case. These equivalences are only valid for a perfectly conducting ground plane. Hence, the observations within this work are limited to perfectly conducting grounds.

These results form the basis for further investigations within this thesis, in which more complex and three-dimensional structures are examined. Of particular interest is here the investigation of bends in the line and the influence when the single line is extended to a multiconductor line.

4 Single Conductor Transmission Line with a Bend

Classical TLT does not consider variations in the parameters of the line and the coupling near a terminating resistor or near another change in its uniform properties. If the uniformity of a transmission line is disturbed, radiation effects appear. A bend could be such disturbance of the uniformity. For the field of electromagnetic compatibility it is an important problem and has been subject of many recent publications [PXPk06, Tom50, KT49].

4.1 Transmission Line Model

In this section, the modeling of a bent line will be discussed. First, a bent line consisting of two segments is considered. Then the model is extended for a bent transmission line (BTL) with n bends. In Fig. 4.1a, a bent transmission line consisting of two single wires with the radius a and with an arc θ between x -axis and conductor and the angle ϕ between the two conductors is shown. For the mathematical description it is also useful to define the angle $\theta = 180^\circ - \phi$, which is dependent on the bending angle ϕ . The bend is in the middle of the line, whereby the individual lines 1 and 2 have a length of l_1 and l_2 respectively. The distance between the conductive plane and the bent line is constant over the length at h . For the mathematical description of the conductors the coordinates w and u are introduced, which have their origin in the bend and are directed away from it. In order to define an equation for the vector potential, the distances R_1 , R_{01} , R_{12} and R_{012} from Fig. 4.1b must be defined. The distances for the first line are

$$R_1 = \sqrt{(w - w')^2 + a^2}, \quad (4.1a)$$

$$R_{01} = \sqrt{(w - w')^2 + (2h + a)^2}, \quad (4.1b)$$

where the variable w stands for the position of the observation point and w' for the position of the source point of wire 1. Again, under the assumption $a \ll h$ one can approximate

$$R_{01} = \sqrt{(w - w')^2 + 4h^2}. \quad (4.2a)$$

For the coupling between wire 1 and 2 the distances are given

$$R_{12} = \sqrt{(w + u' \cos \theta)^2 + (u' \sin \theta)^2 + a^2}, \quad (4.3a)$$

$$R_{012} = \sqrt{(w + u' \cos \theta)^2 + (u' \sin \theta)^2 + 4h^2}. \quad (4.3b)$$

The variables u and u' define the position of the observation and the source point of wire 2. In case of $\theta = 0^\circ$, R_{12} and R_{012} correspond to the single wire case. The currents are continuous at the line-load junction so that

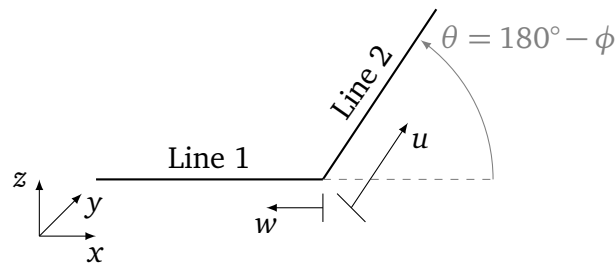
$$I_{x1}(w' \mapsto 0) = I_{u2}(u' \mapsto 0). \quad (4.4)$$

If $I_{u1}(u')$ is the total axial current at u' in the termination, then the current on wire 2 can be expressed by angular relations between the wires

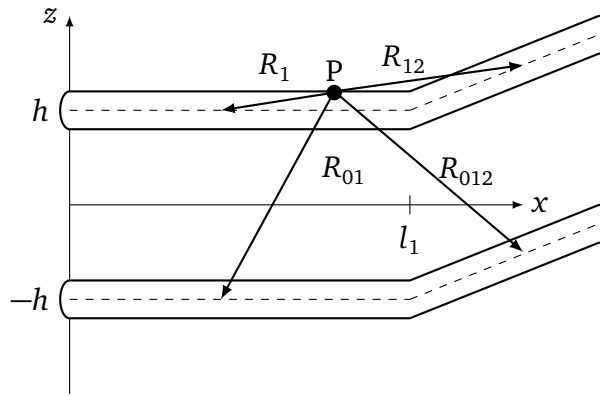
$$I_{x2}(u') = I_{u2}(u') \cdot \cos(\theta), \quad (4.5a)$$

$$I_{y2}(u') = I_{u2}(u') \cdot \sin(\theta), \quad (4.5b)$$

with the angle θ between the direction of the current at u' and the x -axis.



(a) Top view of a bent single wire



(b) Bent single conductor and its image wire

Figure 4.1: Schematic of a bent single conductor transmission line with the length l_1 and l_2 and the radius a

The field-to-wire coupling equations from Eq. (2.21) shall now be solved for the bent wire. In a first step, only wire 1 is considered and its coupling effect to wire 2. Later in this section, wire 2 is also considered. With the distances from Eq. (3.47d) and the definition of the

currents from Eqs. (4.5) the vector potential becomes

$$A_x(x) = \frac{\mu}{4\pi} \int_0^{l_1} I_{x1}(w') g_1(w, w') dw' + \frac{\mu}{4\pi} \int_0^{l_2} I_{x2}(u') g_{12}(u, u') du', \quad (4.6a)$$

$$A_y(y) = \frac{\mu}{4\pi} \int_0^{l_2} I_{y2}(u') g_{12}(u, u') du'. \quad (4.6b)$$

From the relations of Eq. (4.4) and under the condition, that the current is locally constant, the current can be put in front of the integral (assumption similar to Eq. (3.12))

$$A_x(x) = \frac{\mu}{4\pi} I_{x1} \int_0^{l_1} g_1(w, w') dw' + \frac{\mu}{4\pi} \cos(\theta) \cdot I_{x1} \int_0^{l_2} g_{12}(u, u') du', \quad (4.7a)$$

$$A_y(y) = \frac{\mu}{4\pi} \sin(\theta) \cdot I_{x1} \int_0^{l_2} g_{12}(u, u') du'. \quad (4.7b)$$

The field-to-wire coupling equations from Eq. (5.2) can be put in a matrix notation

$$\frac{d}{dw} \begin{bmatrix} U_1^s(w) \\ U_2^s(w) \end{bmatrix} + j\omega \underbrace{\frac{\mu}{4\pi} \begin{bmatrix} G_{BTL,1} & G_{BTL,12} \\ G_{BTL,12} & G_{BTL,2} \end{bmatrix}}_{[Z_{BTL}^{HF}]} \begin{bmatrix} I_1(w) \\ I_2(w) \end{bmatrix} = [E_{\tan, BTL}^e], \quad (4.8a)$$

$$\frac{d}{dw} \begin{bmatrix} I_1(w) \\ I_2(w) \end{bmatrix} + j\omega 4\pi\epsilon \underbrace{\begin{bmatrix} G_{BTL,1} & G_{BTL,12} \\ G_{BTL,12} & G_{BTL,2} \end{bmatrix}^{-1}}_{[Y_{BTL}^{HF}]} \begin{bmatrix} U_1(w) \\ U_2(w) \end{bmatrix} = 0, \quad (4.8b)$$

where, the matrix $[G_{BTL}]$ is an $n \times n$ matrix with the integrals of the Green's function on its matrix entries. The Green's functions g_1 represents the influence of the wire itself and g_{12} the influence of the bend (B). The matrix entry $G_{BTL,1}$ is given by

$$G_{BTL,1} = \int_0^{l_1} g_1(w, w') du' + \cos(\theta) \int_0^{l_2} g_{12}(u, u') du' \quad (4.9)$$

and $G_{BTL,12}$ by

$$G_{BTL,12} = \sin(\theta) \int_0^{l_2} g_{12}(u, u') du'. \quad (4.10)$$

Here, g_1 and g_{12} are defined as

$$g_1(w, w') = \frac{e^{-jkR_1}}{R_1} - \frac{e^{-jkR_{01}}}{R_{01}} \quad (4.11)$$

and

$$g_{12}(u, u') = \frac{e^{-jkR_{12}}}{R_{12}} - \frac{e^{-jkR_{012}}}{R_{012}}. \quad (4.12)$$

The integral of the Green's function g_1 can be solved directly like in Eq. (3.15) for the SCL

$$\int_0^{l_1} g_1(w, w') dw' = \pi [J_0(2hk) - J_0(ak)] + j\pi [Y_0(2hk) - Y_0(ak)]. \quad (4.13)$$

To solve the integral of the Green's function g_{12} , first some mathematical rearrangements of Eqs. (4.3a) and (4.3b) are necessary

$$R_{12} = \sqrt{(u' - u_0)^2 + d_{11}^2}, \quad (4.14a)$$

$$R_{012} = \sqrt{(u' - u_0)^2 + d_{10}^2}. \quad (4.14b)$$

Here, d_{11} and d_{10} are defined as follows

$$d_{11}^2 = w^2 + a^2 - w \cos \theta, \quad (4.15a)$$

$$d_{10}^2 = w^2 + 4h^2 - w \cos \theta, \quad (4.15b)$$

$$u_0 = -w \cos \theta. \quad (4.15c)$$

The solution of the integral of the Green's function g_{12} becomes

$$\int_0^{l_2} g_{12}(u, u') du' = \pi [J_0(d_{10}k) - J_0(d_{11}k)] + j\pi [Y_0(d_{10}k) - Y_0(d_{11}k)]. \quad (4.16)$$

In order to determine the vector potential of the second line, the coordinate system has to be adjusted in a way that w is directed towards line 2 and u towards line 1. Then, the vector potential can be set up analogous to Eq. (4.7)

$$A_x(x) = \frac{\mu}{4\pi} I_{x1} \int_0^{l_2} g_2(w, w') dw' + \frac{\mu}{4\pi} \cos(\theta) \cdot I_{x1} \int_0^{l_1} g_{12}(u, u') du', \quad (4.17a)$$

$$A_y(y) = \frac{\mu}{4\pi} \sin(\theta) \cdot I_{x2} \int_0^{l_1} g_{12}(u, u') du', \quad (4.17b)$$

where g_2 is determined by

$$G_{\text{BTL},2} = \int_0^{l_2} g_2(w, w') dw' = \int_0^{l_2} \left(\frac{e^{-jkR_{12}}}{R_2} - \frac{e^{-jkR_{02}}}{R_{02}} \right) dw' + \cos(\theta) \int_0^{l_1} g_{12}(u, u') du'. \quad (4.18)$$

The distances are defined analogous to Eq. (4.1) with

$$R_2 = \sqrt{(w - w')^2 + a^2}, \quad (4.19a)$$

$$R_{02} = \sqrt{(w - w')^2 + 4h^2}. \quad (4.19b)$$

Again, the integral of the Green's function g_2 can be solved like in Eq. (3.15)

$$\int_0^{l_2} g_2(w, w') dw' = \pi [J_0(2hk) - J_0(ak)] + j\pi [Y_0(2hk) - Y_0(ak)]. \quad (4.20)$$

The matrix of the Green's function integrals can also be written as

$$[G_{\text{BTL}}] = [G_{\text{BTL}}^{\text{LF}}] + [C_{\text{BTL}}^{\text{F}}], \quad (4.21)$$

where $[G_{\text{BTL}}]^{\text{LF}}$ is the classical low frequency solution of the Green's function integral and $[C_{\text{BTL}}^{\text{F}}]$ describes the high frequency correction matrix.

Impedance and Admittance Matrix

From Eqs. (4.8) and (4.21), the high frequency impedance matrix follows with

$$[Z_{\text{BTL}}^{\text{HF}}] = j\omega \frac{\mu}{4\pi} [G_{\text{BTL}}]. \quad (4.22)$$

The impedance matrix can also be written as

$$[Z_{\text{BTL}}^{\text{HF}}] = j\omega \frac{\mu}{4\pi} ([G_{\text{BTL}}^{\text{LF}}] + \Re \{ [C_{\text{BTL}}^{\text{F}}] \} + j\Im \{ [C_{\text{BTL}}^{\text{F}}] \}). \quad (4.23)$$

The impedance matrix is also defined as the sum of the high frequency p. u. l. inductance and resistance

$$[Z_{\text{BTL}}^{\text{HF}}] = [R_{\text{BTL}}^{\text{HF}}] + j\omega [L_{\text{BTL}}^{\text{HF}}], \quad (4.24)$$

where the p. u. l. inductance is given by

$$[L_{\text{BTL}}^{\text{HF}}] = [L'_{\text{BTL}}] + \frac{\mu_0}{4\pi} \Re \{ [C_{\text{BTL}}^{\text{F}}] \}, \quad (4.25)$$

and the p. u. l. resistance is given by

$$[R_{\text{BTL}}^{\text{HF}}] = -\omega \frac{\mu_0}{4\pi} \Im \{ [C_{\text{BTL}}^{\text{F}}] \}. \quad (4.26)$$

For the LF p. u. l. inductance for the i th wire follows

$$[L'_{\text{BTL}}] = \frac{\mu}{4\pi} [G_{\text{BTL}}^{\text{LF}}]. \quad (4.27)$$

From Eq. (4.35), the high frequency admittance matrix follows with

$$[Y_{\text{BTL}}^{\text{HF}}] = j\omega 4\pi\epsilon [G_{\text{BTL}}^{\text{HF}}]^{-1} \quad (4.28a)$$

$$= j\omega 4\pi\epsilon \left([G_{\text{BTL}}^{\text{LF}}] + \Re \{ [C_{\text{BTL}}^{\text{F}}] \} + j\Im \{ [C_{\text{BTL}}^{\text{F}}] \} \right)^{-1}. \quad (4.28b)$$

Characteristic Impedance Matrix

A frequency dependent characteristic impedance can be obtained

$$[Z_{\text{c,BTL}}^{\text{HF}}] = \left([Z_{\text{BTL}}^{\text{HF}}] [Y_{\text{BTL}}^{\text{HF}}]^{-1} \right)^{\frac{1}{2}}. \quad (4.29)$$

It is defined by a sum of the classical characteristic impedance matrix $[Z_{\text{c,BTL}}^{\text{LF}}]$ and the correction factor

$$[Z_{\text{c,BTL}}^{\text{HF}}] = [Z_{\text{c,BTL}}^{\text{LF}}] + [C_{\text{BTL}}^{\text{F}}]. \quad (4.30)$$

For a bent wire with two segments the characteristic impedance has the following matrix form

$$Z_{\text{c,BTL}}^{\text{HF}} = \begin{bmatrix} Z_{\text{c,BTL},1}^{\text{HF}} & Z_{\text{c,BTL},12}^{\text{HF}} \\ Z_{\text{c,BTL},12}^{\text{HF}} & Z_{\text{c,BTL},2}^{\text{HF}} \end{bmatrix} \quad (4.31)$$

The difference to the single wire case in Eq. (5.4) is that the characteristic impedance for the whole bent line is the sum of a part which represents the wire itself and a part representing the influence of the bend. The characteristic impedance for wire 1 can be determined by

$$Z_{\text{c,BTL},1}^{\text{HF}} = \frac{1}{4\pi} \sqrt{\frac{\mu}{\epsilon}} \left(\pi [J_0(2hk) - J_0(ak)] + j\pi [Y_0(2hk) - Y_0(ak)] \right) \quad (4.32a)$$

$$+ \frac{1}{4\pi} \sqrt{\frac{\mu}{\epsilon}} \cos(\theta) \left(\pi [J_0(d_{10}k) - J_0(d_{11}k)] + j\pi [Y_0(d_{10}k) - Y_0(d_{11}k)] \right). \quad (4.32b)$$

This characteristic impedance is dependent of the position w on the wire. It follows a low frequency characteristic impedance for the bent single line above the conductive ground

plane with

$$Z_{c,BTL,1}^{LF} = Z_{c,BTL,2}^{LF} = \frac{1}{4\pi} \sqrt{\frac{\mu}{\varepsilon}} \ln\left(\frac{2h}{a}\right) + \frac{1}{4\pi} \sqrt{\frac{\mu}{\varepsilon}} \cos\theta \ln\left(\frac{d_{10}}{d_{11}}\right), \quad (4.33a)$$

$$Z_{c,BTL,12}^{LF} = \frac{1}{4\pi} \sqrt{\frac{\mu}{\varepsilon}} \sin\theta \ln\left(\frac{d_{10}}{d_{11}}\right). \quad (4.33b)$$

As long as the line is symmetrical and both lines have the same transverse dimensions, the characteristic impedances for wire 1 and 2 are the same and $Z_{c,BTL,1}^{HF} = Z_{c,BTL,2}^{HF}$. Now, a characteristic impedance for the solution of Eq. (4.18) for the coupling of the lines follows with

$$Z_{c,BTL,12}^{HF} = \frac{1}{4\pi} \sqrt{\frac{\mu}{\varepsilon}} \sin(\theta) \left(\pi [J_0(d_{10}k) - J_0(d_{11}k)] + j\pi [Y_0(d_{10}k) - Y_0(d_{11}k)] \right). \quad (4.34)$$

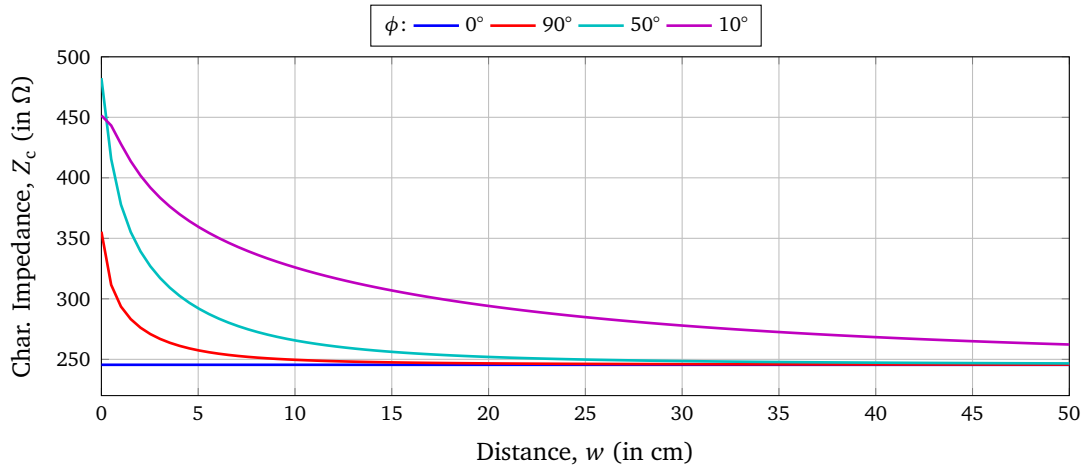


Figure 4.2: Low frequency characteristic impedance element $Z_{c,BTL,1}^{LF}$ depending on the distance w from the bend. Investigation of different bent angles ϕ and wire dimensions of $l_1 = l_2 = 50$ cm, $a = 1$ mm and $h = 3$ cm.

In the following, a bent single wire consisting of two segments with the dimensions $l_1 = 50$ cm, $l_2 = 50$ cm, $a = 1$ mm and $h = 3$ cm was investigated. In Fig. 4.2, the low frequency characteristic impedance element $Z_{c,BTL,1}^{LF}$ over the distance w is shown, which is the distance from the bend along wire 1. As expected, the influence of the bend and thus $Z_{c,BTL,1}^{LF}$ is greatest near the bend and decreases with increasing distance w . The smaller the bending angle gets, the greater the coupling between the conductors. Without any bending, the coupling element of the Green's function g_{12} approach to zero. That means, far enough away from the bend ($w \gg 2h$), the effect of the bend is negligible and the characteristic impedance correspond to the case of a single conductor transmission line from Eq. (3.25) and has no coupling elements. For the individual single wires 1 and 2 follow from the dimensions a characteristic impedance of $Z_{c,BTL,1}^{LF} = Z_{c,BTL,2}^{LF} = 245.5 \Omega$ far away from the bend.

Derivation of an Equivalent Circuit

The solution of the characteristic impedance can now be used to derive an equivalent circuit and some p. u. l. parameters for the bent cable. In Fig. 4.3, an equivalent circuit of the first two segments of a bent single wire is shown.

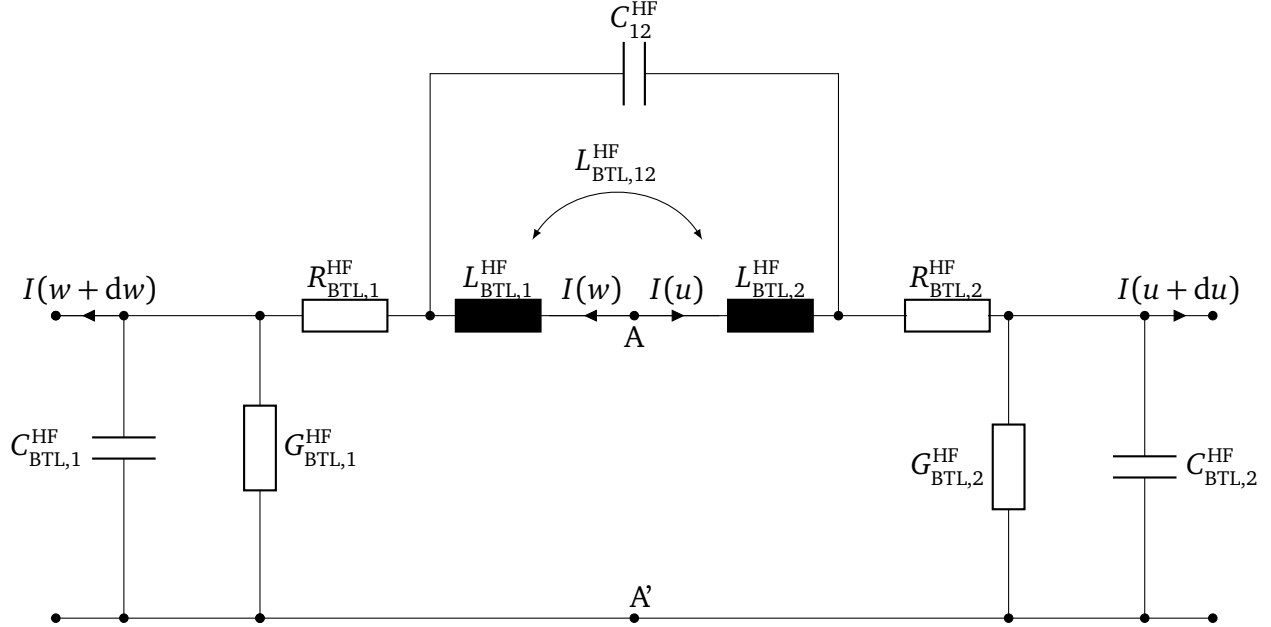


Figure 4.3: Equivalent circuit of the first two segments of a bent single wire at the position A of the bend

The p. u. l. parameters consist of a part, that defines the influence of the single line and a part describing the influence of the bend and the coupling to the second line. The low frequency part of the p. u. l. inductance of the wire itself can be determined by $L_{BTL,1}^{HF}$ and $L_{BTL,1}^{HF}$ using the theory from Sec. 3.1 described by Eq.(3.26a) for the p. u. l. inductance L_{SCL}^{HF} . Analogously, the p. u. l. capacitance $C_{BTL,1}^{HF}$ and $C_{BTL,2}^{HF}$ can be described by corresponding to the classic C_{SCL}^{HF} from Eq.(3.26c). The circuit elements $L_{BTL,12}^{HF}$ and $C_{BTL,12}^{HF}$ of the equivalent circuit describing the influence of the bend and the coupling between the elements are defined as the sum of a constant LF and frequency dependent HF part.

Extension to Any Number of Wires and Bends

The solution for a wire consisting of two segments can be extended to any number of bends. In this case, a line i exist which is connected to its neighbor line j at the bend. The field-to-wire coupling equations become

$$\frac{d}{dw} [U_i^s(w)] + j\omega \frac{\mu}{4\pi} [G_{BTL}] [I(w)] = [E_{\tan,BTL}^e], \quad (4.35)$$

$$\frac{d}{dw} [I(w)] + j\omega 4\pi\epsilon [G_{BTL}]^{-1} [U(w)] = 0. \quad (4.36)$$

The vector potential for the i th line follows with

$$A_x(x) = \frac{\mu}{4\pi} I_{xi} \int_0^{l_i} g_i(w, w') dw' + \frac{\mu}{4\pi} \cos(\theta) I_{xi}(u) \int_0^{l_j} g_{ij}(u, u') du', \quad (4.37a)$$

$$A_y(y) = \frac{\mu}{4\pi} \sin(\theta) I_{xi} \int_0^{l_j} g_{ij}(u, u') du', \quad (4.37b)$$

where i and j are the number of wires. Then, an $n \times n$ matrix for $Z_{c,BTL}^{HF}$ can be obtained from Eq. (4.34). The matrix consist of the characteristic impedances $Z_{c,BTL,i}^{HF}$ of the wire itself on the main diagonal elements and the coupling characteristic impedances $Z_{c,BTL,ij}^{HF}$ on the secondary elements of the matrix.

4.2 Field-to-Wire Coupling Equations

To determine the coupled voltage and to take into account the position dependency of the characteristic impedance, the matrix form of the BLT equations must be used . The field-to-wire coupling to a bent wire, with n nodes is explained. A bent wire with one node and $n = 2$ segments is shown Fig. 4.4. The lines are denoted with bold numbers and the nodes with italic numbers. The lines are terminated with load impedances $Z_{L1,i}$ at the beginning and $Z_{L2,i}$ at the end of the i th line.

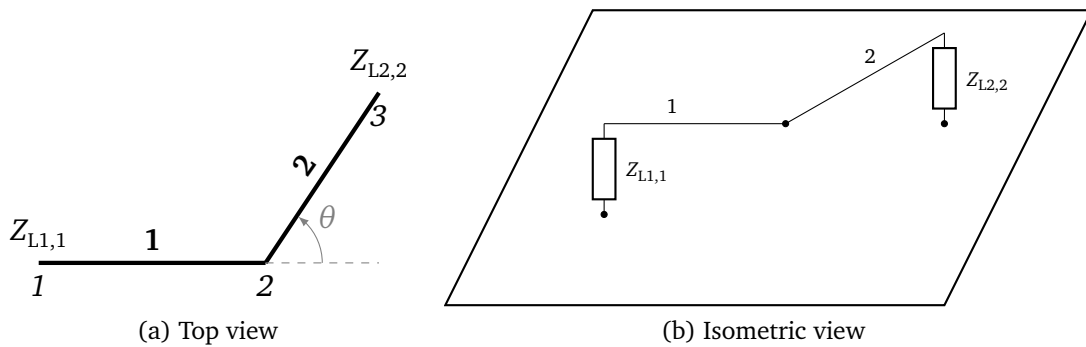


Figure 4.4: Bent single wire transmission line above the x - y -plane

The coupled voltage at the beginning and at the end of the bent line can be calculated using the very compact BLT equations

$$[U_{L,BTL}] = \begin{bmatrix} [U_{L1,BTL}] \\ [U_{L2,BTL}] \end{bmatrix} = \left[[1] + [\Gamma_{BTL}] \right] \cdot [D_{BTL}]^{-1} \cdot \begin{bmatrix} [S_{1,BTL,i}] \\ [S_{2,BTL,i}] \end{bmatrix}. \quad (4.38)$$

They are valid under the assumption that the wires are parallel to the ground. Here, the

vector $[U_{L,BTL}]$ contains the terminal voltages $[U_{L1,BTL}]$ at the beginnings and $[U_{L2,BTL}]$ at the ends of the lines. The vector $[U_{L,BTL}]$ has the dimension $2n \times 1$, and each vector $[U_{L1,BTL}]$ and $[U_{L2,BTL}]$ the dimension $n \times 1$, where n is the number of conductors. The matrix $[\mathbb{1}]$ is the $2n \times 2n$ identity matrix and the reflection matrix $[\Gamma_{BTL}]$ is defined by

$$[\Gamma_{BTL}] = \begin{bmatrix} [\Gamma_{BTL,1}] & [0] \\ [0] & [\Gamma_{BTL,2}] \end{bmatrix}, \quad (4.39)$$

where $[\Gamma_{BTL,1}]$ and $[\Gamma_{BTL,2}]$ are the $n \times n$ reflection coefficient matrices for the beginnings and the ends of the lines

$$[\Gamma_{BTL,1}] = ([Z_{L1}] - [Z_{c,BTL}^{HF}]) \cdot ([Z_{L1}] + [Z_{c,BTL}^{HF}])^{-1}, \quad (4.40a)$$

$$[\Gamma_{BTL,2}] = ([Z_{L2}] - [Z_{c,BTL}^{HF}]) \cdot ([Z_{L2}] + [Z_{c,BTL}^{HF}])^{-1}. \quad (4.40b)$$

Assuming that the bent line is only terminated with a resistance at the beginning and at the end as shown in Fig. 4.4b, the load resistances are

$$[Z_{L1}] = \begin{bmatrix} Z_{L1,1} & \infty \\ \infty & \infty \end{bmatrix}, \quad [Z_{L2}] = \begin{bmatrix} \infty & \infty \\ \infty & Z_{L2,2} \end{bmatrix} \quad (4.41)$$

on the diagonal elements. The matrix $[Z_c^{HF}]$ is the $n \times n$ characteristic impedance matrix of the bent transmission line from the previous Sec. 4.1. In Eq. (4.40), the main diagonal elements of the respective reflection coefficient matrix can be determined by

$$\Gamma_{BTLn,n} = \begin{cases} 1 & \text{if node: } Z_L \mapsto \infty, \\ \frac{Z_L - Z_{c,BTL,i}^{HF}}{Z_L + Z_{c,BTL,i}^{HF}} & \text{else.} \end{cases} \quad (4.42)$$

This means, that at a node the voltage wave is fully reflected and at the beginning or end of the line there is the individual reflection with the load impedance $Z_{L,i}$.

The matrix term $[D]$ in Eq. (4.38) contains the $2n \times 2n$ propagation matrix

$$[D_{BTL}] = \begin{bmatrix} -[\Gamma_{BTL,1}] & e^{\gamma l_i} [\mathbb{1}] \\ e^{\gamma l_i} [\mathbb{1}] & -[\Gamma_{BTL,2}] \end{bmatrix}. \quad (4.43)$$

Here, $e^{\gamma l_i} [\mathbb{1}]$ is a diagonal matrix with the corresponding elements on the main diagonal, where i is the number of the segment. Finally, the sources for distributed field excitation must be defined for this case. The individual elements for the i th line of the $2n \times 1$ supervector

are given by

$$[S_{1,BTL,i}] = -\frac{1}{2} \begin{cases} 0 & \text{if } \gamma_{-,i} = 0 \\ -U_{t1,i} \cdot (1 - e^{2\gamma l_i}) & \text{if } \gamma_{+,i} = 0 \\ \left(\frac{E_{\tan,i}^e r_{1,i}}{\gamma_-} - U_{t1,i} \right) (1 - e^{-\gamma_{-,i} l_i}) & \text{else,} \end{cases} \quad (4.44a)$$

$$[S_{2,BTL,i}] = -\frac{1}{2} e^{\gamma l_i} \begin{cases} U_{t1,i} \cdot (1 - e^{-2\gamma l_i}) & \text{if } \gamma_{-,i} = 0 \\ 0 & \text{if } \gamma_{+,i} = 0 \\ \left(\frac{E_{\tan,BTL,i}^e r_{1,i}}{\gamma_+} + U_{t1,i} \right) (1 - e^{-\gamma_{+,i} l_i}) & \text{else.} \end{cases} \quad (4.44b)$$

The modified propagation constants for the i th line are equal to Eq. (3.32)

$$\gamma_{+,i} = \gamma + \mathbf{jk} \cdot \mathbf{t}_i, \quad (4.45a)$$

$$\gamma_{-,i} = \gamma - \mathbf{jk} \cdot \mathbf{t}_i. \quad (4.45b)$$

The unit tangential vector along the line is

$$\mathbf{t}_i = \begin{pmatrix} t_{x,i} \\ t_{y,i} \\ t_{z,i} \end{pmatrix} = \frac{1}{l_i} \begin{pmatrix} x_{2,i} - x_{1,i} \\ y_{2,i} - y_{1,i} \\ 0 \end{pmatrix} \quad (4.46)$$

with the line length of the i th wire

$$l = \sqrt{(x_{2,i} - x_{1,i})^2 + (y_{2,i} - y_{1,i})^2}. \quad (4.47)$$

In Eq. (3.31) the exciting tangential electric field vector along the i th line is determined by the incident and reflected wave, while the angle β represents the phase of the plane wave

$$E_{\tan,BTL,i}^e = -2jE e^{j\beta} \mathbf{e} \cdot \mathbf{t}_i \sin(k_z h_i). \quad (4.48)$$

Here, h_i is the height of the uniform i th line and \mathbf{e} is the electric field vector as defined in Eq. (2.89). Analogous to the single wire case in Eq.(3.40), the transverse electric field between the conducting plane and the i -th wire must be integrated to obtain the transverse voltage

$$U_{t1,BTL,i} = 2E e_z e^{j\beta} r_{1,i} \begin{cases} h_i & \text{if } k_z = 0 \\ \frac{\sin(k_z h_i)}{k_z} & \text{else.} \end{cases} \quad (4.49)$$

Using Eq. (4.38) to (4.49) and $[Z_c^{\text{HF}}]$ the coupled terminal voltages for a bent transmission line with an arbitrary start and end point can be easily calculated.

4.3 Validation of the Model

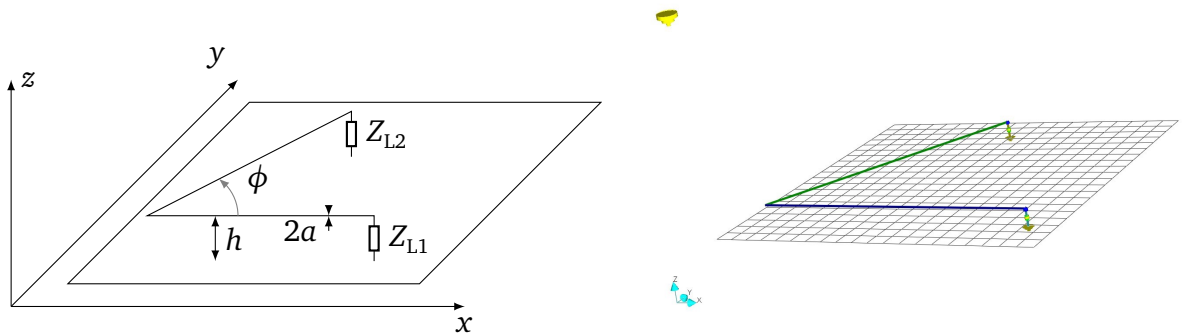
For validation, a bent wire consisting of two segments as shown in Fig. 4.5 was chosen. The length of the line was $l = l_1 + l_2 = 1$ m ($l_1 = l_2 = 50$ cm), had a radius of $a = 1.8$ mm and was located at a height of $h = 3$ cm over a conductive ground plane. The line was bent in the middle at 50 cm.

4.3.1 Validation Using the Method of Moments

From Fig. 4.5, the following terminations can be derived

$$[Z_{L1}] = \begin{bmatrix} 50\Omega & \infty \\ \infty & \infty \end{bmatrix}, \quad [Z_{L2}] = \begin{bmatrix} \infty & \infty \\ \infty & 50\Omega \end{bmatrix}. \quad (4.50)$$

The load impedances correspond to the N feedthroughs with 50Ω to connect the wires with the coaxial measurement cables. In Fig. 4.5b, the simulation model in *CONCEPT-II* is shown.



(a) Schematic of the single conductor transmission line at a height h , with a specific radius $2a$ (b) Screenshot of the simulation model of the bent transmission line in *CONCEPT-II* [Tec]

Figure 4.5: Bent single line over a conductive ground plane with a bent angle ϕ

In Fig. 4.6, the comparison between the solution in *CONCEPT-II* and the solution in MATLAB according to the BLT equations according to Eq. (4.38) for two different bend angles is shown. Both simulations are performed for a stochastic field with $B = 360$ electromagnetic boundary conditions (stirrer positions). Here, the mean magnitude of the coupled voltage $\langle |U_{L1}| \rangle$ is shown over the frequency. The averaging was done over all electromagnetic boundary conditions B . Additionally, a model for transmission line networks based on [MV15] is shown, where the coupling between the lines was not included. An almost excellent agreement can be observed for the 60° bend angle in Fig. 4.6. Resonances can be expected from theory at approximately 282 MHz, 424 MHz, 566 MHz, 707 MHz, 849 MHz and 990 MHz for a symmetrically mismatched 1.06 m long line ($l + 2h$). Both BLT simulation models based on

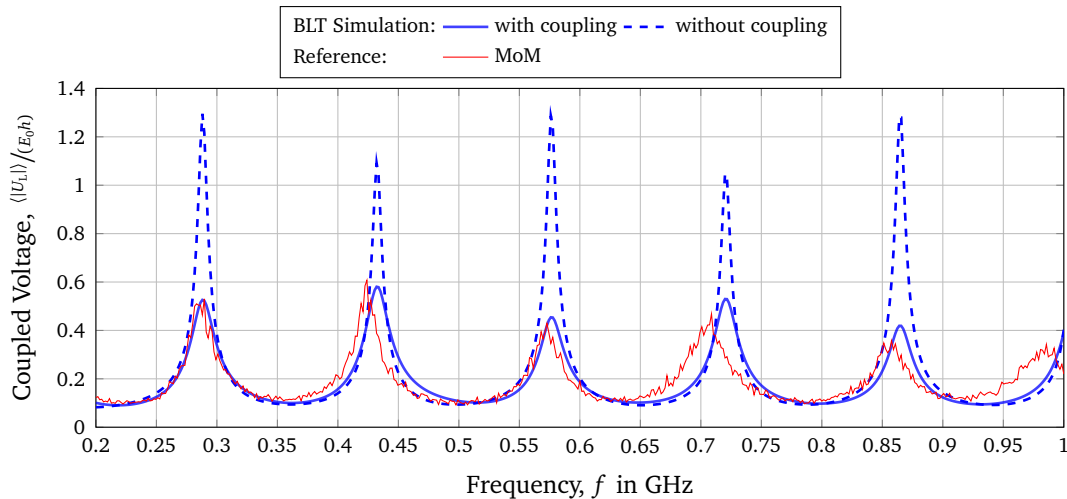


Figure 4.6: Coupled voltage $\langle |U_{L1}| \rangle$ at the beginning of a 60° bent line (B-60) simulated using the BLT equations with the presented parameters, simulation results in *CONCEPT-II* and a simulation model for transmission line networks, not including the coupling between the lines [MV15]

classical transmission line theory lead to good results. The resonant frequencies correspond exactly to those simulated in *CONCEPT-II*. The simulation model that takes the coupling into account leads to more precise solutions with respect to the amplitude of the resonances.

For smaller angles, the MoM simulation does not show accurate solutions. Errors occur during the simulation because the lines are too close together near the bend. Therefore, the investigation of smaller angles with the help of the MoM simulation was not carried out. The model will be further validated by measurements in the reverberation chamber.

4.3.2 Validation Using Measurements in the Reverberation Chamber

Fig. 4.7 depicts two configurations of the bent line in the reverberation chamber. The line was located over a conductive ideal ground plane and was terminated with the load impedances $Z_{L1} = 50 \Omega$ and $Z_{L2} = 50 \Omega$. Again, the length of the line was $l = l_1 + l_2 = 1$ m ($l_1 = l_2 = 50$ cm). The investigated transmission lines consisted of a single copper wire with a cross section of 4 mm^2 . The radius of the wire was much smaller than the wavelength ($a = \lambda/230$ at 1 GHz).

In Fig. 4.8, the normalized coupled voltage over the frequency is shown. A moving average over five frequencies was calculated to smooth the measured curve. As for the straight single wire and a symmetrically mismatched line, strong resonances can be seen at approximately 300 MHz, 450 MHz, 600 MHz, 750 MHz and 900 MHz. The experimental and semi-analytical results show a good agreement. In conclusion the semi-analytical simulation model could be validated by measurements in the reverberation chamber as well as by simulations in

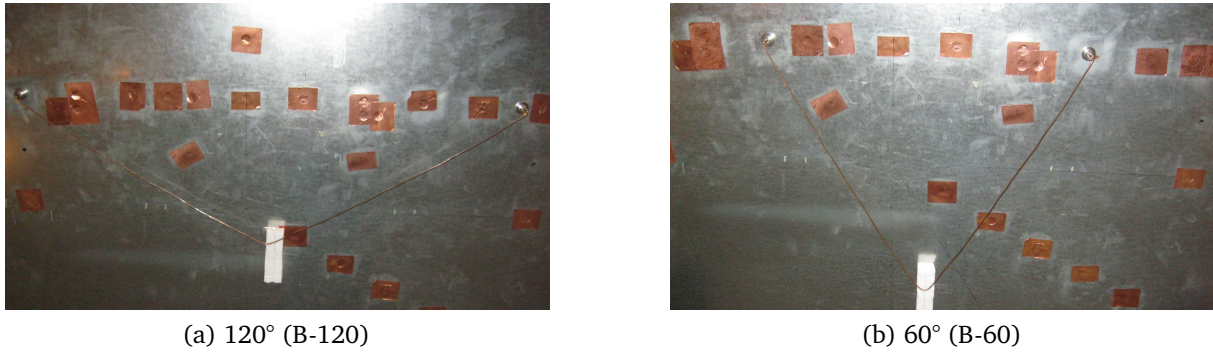


Figure 4.7: Different bend angles of the transmission line

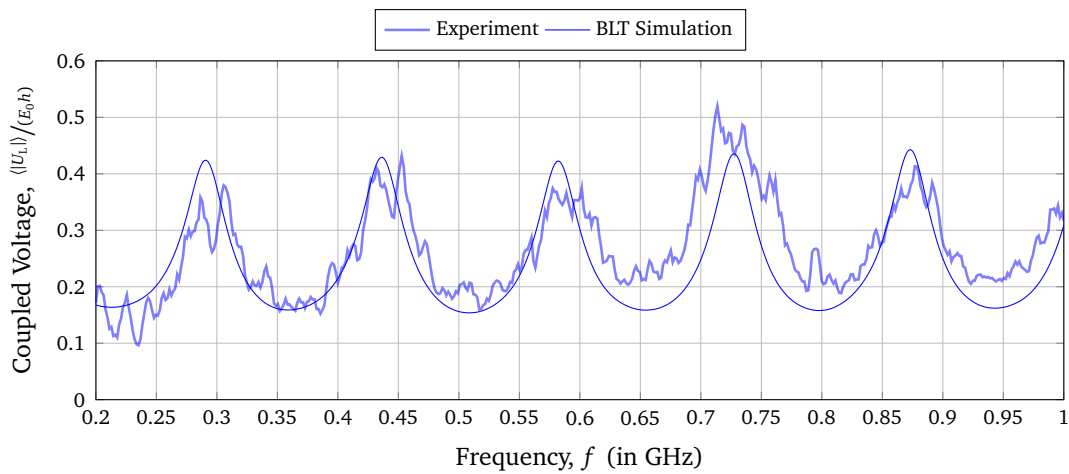


Figure 4.8: Coupled voltage $\langle |U_{L1}| \rangle$ at the beginning of the 60° bent line simulated using the BLT equations and measured in the reverberation chamber

CONCEPT-II in Section 4.3.1. Now, some parameter studies are to be carried out to investigate the behavior of the bent transmission line within the reverberation chamber.

4.4 Coupled Voltage as a Function over the Frequency

Within this section, different bend angles of the bent line are to be examined. First, the focus lies on measurements performed in the reverberation chamber. To investigate the influence of different parameters of the bent line on the coupled voltage, the configuration of the transmission line was changed in the following measurements with respect to its geometry. During all measurements, the line length of 1 m of the transmission line was kept constant.

4.4.1 Variation of the Bend Angles

Fig. 4.9 depicts the bend angles, which are experimentally investigated and their respective naming. The line was successively bent from 180° (B-180) to nearly 0° in 30° steps. The

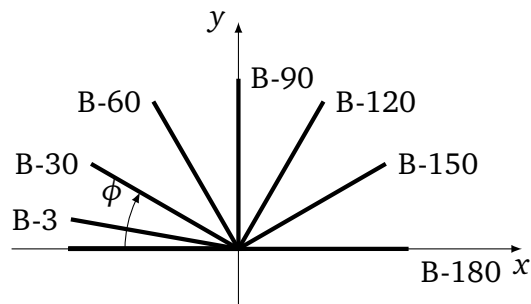


Figure 4.9: Schematic configurations of the bent line with different angles ϕ

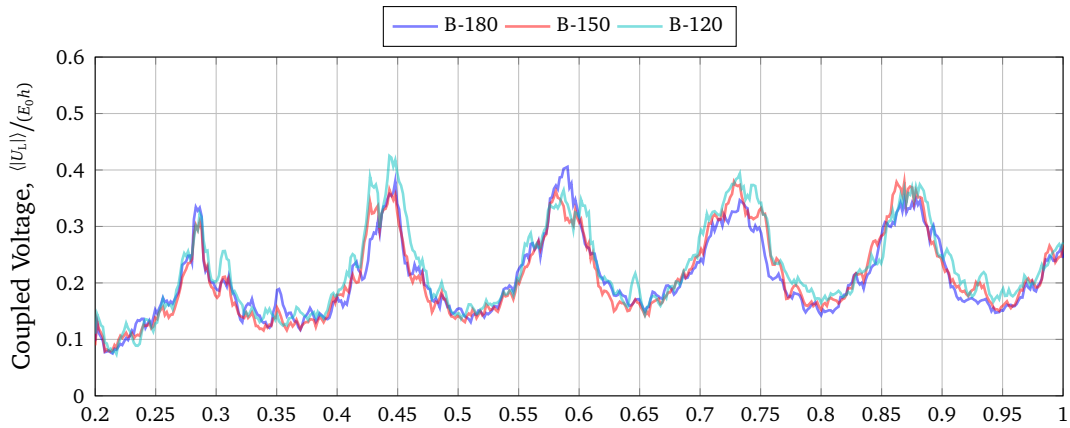
smallest bend angle of 3° (B-3) of the transmission line followed from the minimum distance between the N feedthroughs at the end of the line (see Fig. 4.10).



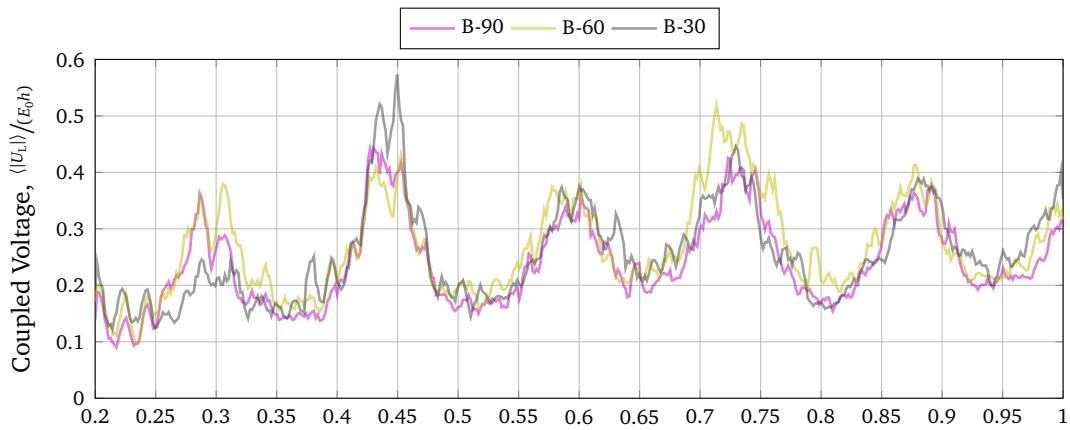
Figure 4.10: Minimum distance between the terminations of the bent transmission line

The coupled terminal voltage over the frequency was investigated. In Fig. 4.11, the coupled voltage at the beginning of the line for different bend angles is shown. For a symmetrically mismatched 1 m long line the expected resonance frequencies occur at 300 MHz, 450 MHz, 600 MHz, 750 MHz, 900 MHz and 1000 MHz ($l = \frac{\lambda}{2}, \lambda, \frac{3}{2}\lambda, \dots$ [MV12]). All these resonances can be seen for a bend angle of 30° . Resonances are shifted to lower frequencies because of the influence of the vertical risers. As the bending angle decreases smaller than 30° , some resonances disappear at about 300 MHz, 600 MHz and 900 MHz. At a bend of 3° these resonances have completely disappeared. This transmission line (B-3) acts like a 0.5 m long line with an open line end, where resonances occur at about 450 MHz, 750 MHz and 1000 MHz (asymmetric mismatched line $l = \frac{\lambda}{4}, \frac{3}{4}\lambda, \dots$ [MV12]). Asymmetric, because the small bend angle causes that all waves along the transmission line are fully reflected at the bend so that the line acts like a 0.5 m long line with $Z_{L1} = 50 \Omega$ and an open line end.

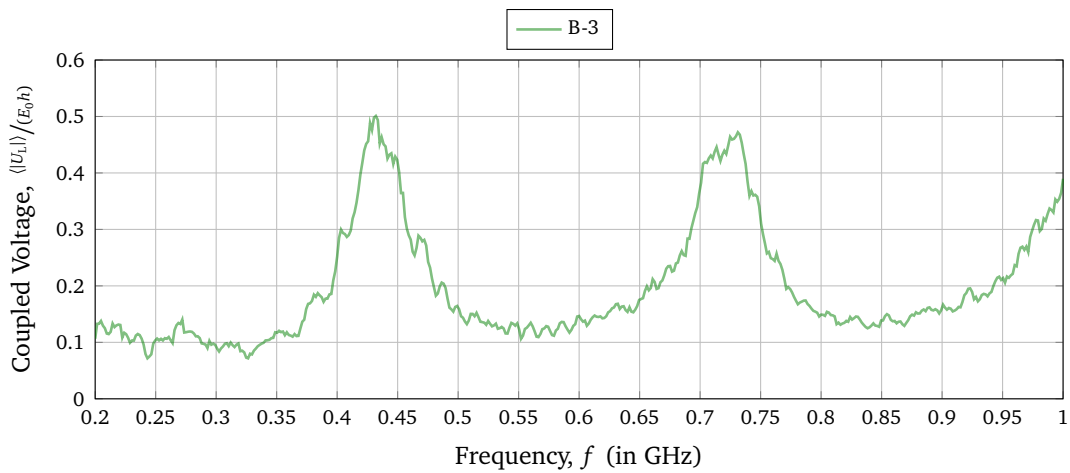
4.4 Coupled Voltage as a Function over the Frequency



(a) 180°, 150° and 120°



(b) 90°, 60° and 30°



(c) 3°

Figure 4.11: Measured average magnitude of the coupled voltage $\langle |U_{L1}| \rangle$ at the beginning of the bent transmission line for different bend angles (schematic shown in Fig. 4.9)

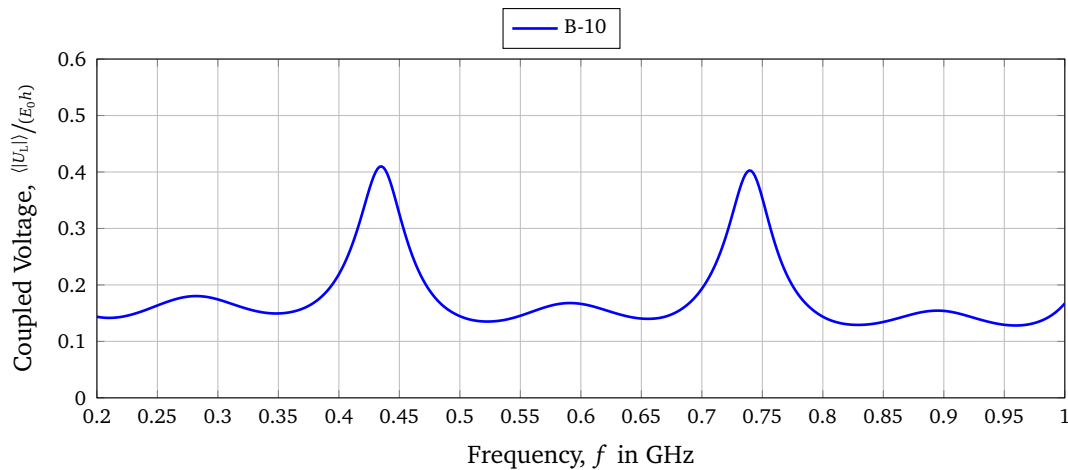


Figure 4.12: Coupled voltage $\langle |U_{L1}| \rangle$ at the beginning of a 10° bent line (B-10) simulated using the BLT equations with the presented parameters

Because of the shown measured results for the 3° bent line some further simulation was performed. In Fig. 4.12, the coupled voltage for a bend angle of 10° is shown. The simulations were performed with $B = 360$ electromagnetic boundary conditions and $N = 10$ plane waves. As shown in Sec. 4.1, the characteristic impedance depends on the variable w . In the simulation model, wire 1 was divided into 10 pieces to get satisfactory results. A higher number would only increase the computing time, but not the accuracy. As expected, the coupled voltage does not change abruptly, but every second resonance (300 MHz, 600 MHz and 900 MHz) decreases with the decreasing bending angle.

4.4.2 Comparison of Bent and Straight Single Wires

In Fig. 4.13, the ratios of the measured coupled voltage of the bent lines to the straight line (B-180) are shown. In order to smooth the curves and thus to be able to compare them better, a running average over further ten frequencies was performed. The 150° bent line acts similar to the straight line. There are almost no differences in the curves. In contrast, at bending angles smaller than 120° the coupled voltage increases, especially in the resonances. For the results for bending angles smaller than 120° and larger than 3° it is interesting to observe that at frequencies of 600 MHz and 900 MHz the deviation to the straight line decreases and is close to one.

In general, it can be said that the lowest field-to-wire coupling occurs with the straight line (B-180). The smaller the bending angle becomes, the greater the coupled voltage. For smaller bending angles the coupled voltage in the resonances increases, which is caused by the greater coupling of the conductors as well as larger reflections at the bend could also be a reason for this. In addition, it can be seen that the voltage coupled into a bent line with a bending angle of 90° (B-90) is about 0.25 % greater than that of a straight line (B-180), but smaller than the smaller bending angles.

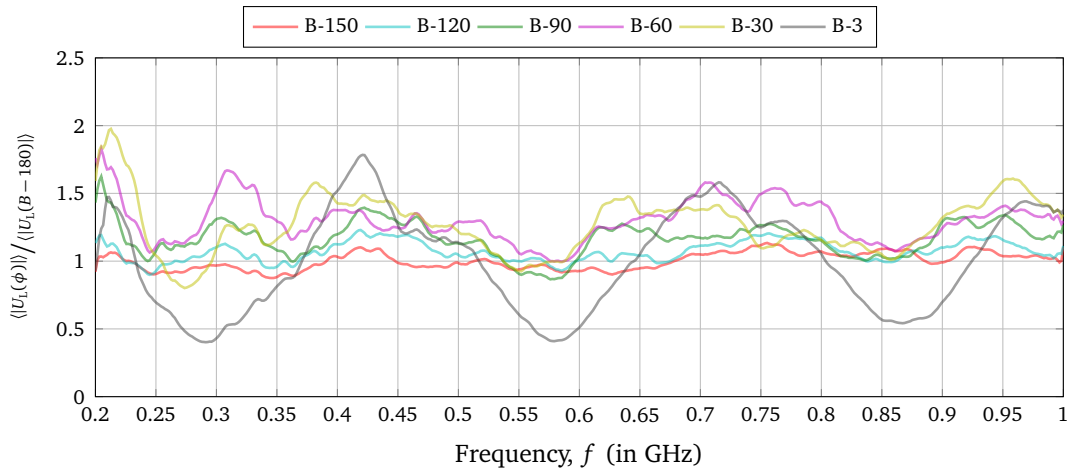


Figure 4.13: Ratio of the measured coupled voltage of the bent line $\langle |U_L| \rangle (\phi)$ to the straight line $\langle |U_L| \rangle (B - 180)$

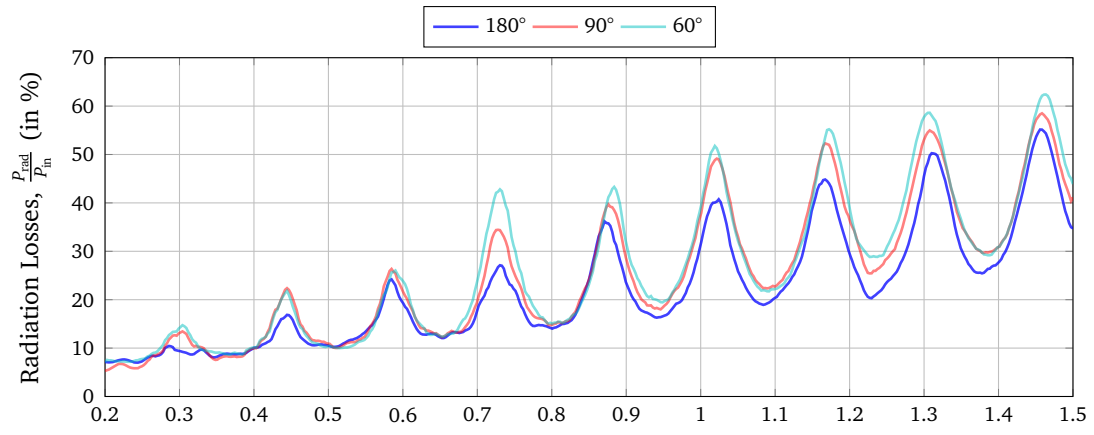
The comparison of the bent and straight single wire shows that any kind of bending have an influence on the field-to-wire coupling. It can be said for the EMC of a system that if possible, any kind of bends in a line should be avoided. If a bend is unavoidable, it should be greater than 90° if possible.

4.5 Measured Radiation Losses

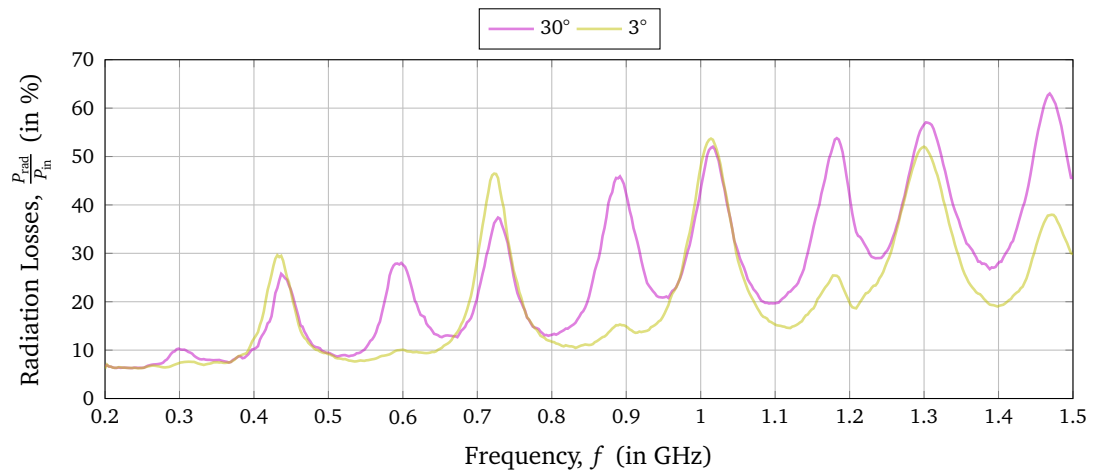
Based on the results of the coupling to the bend line, the next step was to investigate the radiation losses. The radiation phenomenon can be regarded as the opposite of the field-to-wire coupling phenomenon.

In Fig. 4.14, the measured radiation losses calculated by Eq. (2.112) over the frequency for different bent angles of the line is shown. The frequency range for the measurement of the radiation loss was from 200 MHz up to 1.5 GHz. The expected resonance frequencies for a symmetrically mismatched 1 m long line, occur at 300 MHz, 450 MHz, 600 MHz, 750 MHz and 900 MHz ($l = \frac{\lambda}{2}, \lambda, \frac{3}{2}\lambda, \dots$ [MV12]). All these resonances are found in the diagram for a bending angle between 180° and 30° . With a bending angle of 3° the main resonances can be seen at 450 MHz, 750 MHz and 900 MHz. The results are consistent with those of the previous studies. As the bending angle decreases, the losses grow, especially at lower frequencies.

The results show that the radiation of the line is not negligible. The radiation of unwanted electromagnetic waves from a bend wire can cause interference in other electrical systems.



(a) 180°, 90° and 60°



(b) 30° and 3°

Figure 4.14: Measured radiation losses for different bend angles

4.6 Comparison with a Single Conductor Transmission Line Network

The presented model for the investigation of a line consisting of one node and two lines can easily be extended to any number of nodes or lines. If the examined line consists of more than two lines, it is called a transmission line network. Again, one has to calculate the vector potential for the transmission line network using Eq. (4.37a). The coupled voltage can be calculated analogously to Sec. 4.2

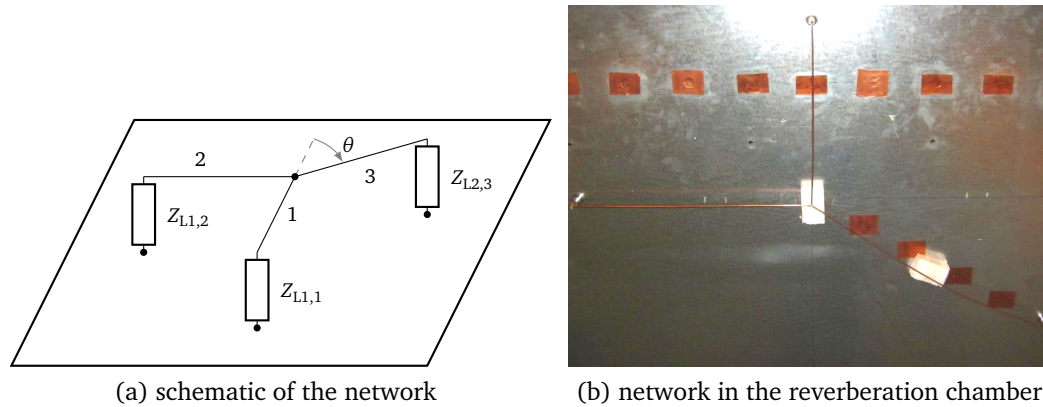


Figure 4.15: Transmission line network over the ground plane

For further investigations, a network of three single wire conductor transmission line was investigated. A schematic of the examined network is shown in Fig. 4.15a. Fig. 4.15b shows the network inside the reverberation chamber. The several small pieces of conductive copper tape are used to cover holes in the ground plate from previous measurements. The several lines of the network had a length of $l_1 = 40$ cm, $l_2 = 30$ cm and $l_3 = 50$ cm, respectively. Line one and two are perpendicular to each other. The angle of the third line in relation to the imaginary extension of the first line is $\theta = 30^\circ$. The heights h of the lines and the ground plane was 3 cm. From the transverse dimensions of the line and Eq. (3.19), a characteristic impedance of about $Z_{cLF} = 238 \Omega$ can be obtained for the low frequency case.

In Fig. 4.16, the comparison of the measured and the simulated results performed in MATLAB are shown. Here, the average magnitude of the coupled voltage at all three terminals is presented. Again, a moving average over five frequencies was performed to minimize random noise. The measured line resonances correspond to the expected resonance frequencies of the several line lengths of the network ($l = \lambda/2$). The following resonance frequencies are expected for the several lines:

30 cm: at 500 MHz and 1000 MHz

40 cm: at 375 MHz, 750 MHz and 1125 MHz

50 cm: at 300 MHz, 600 MHz and 900 MHz

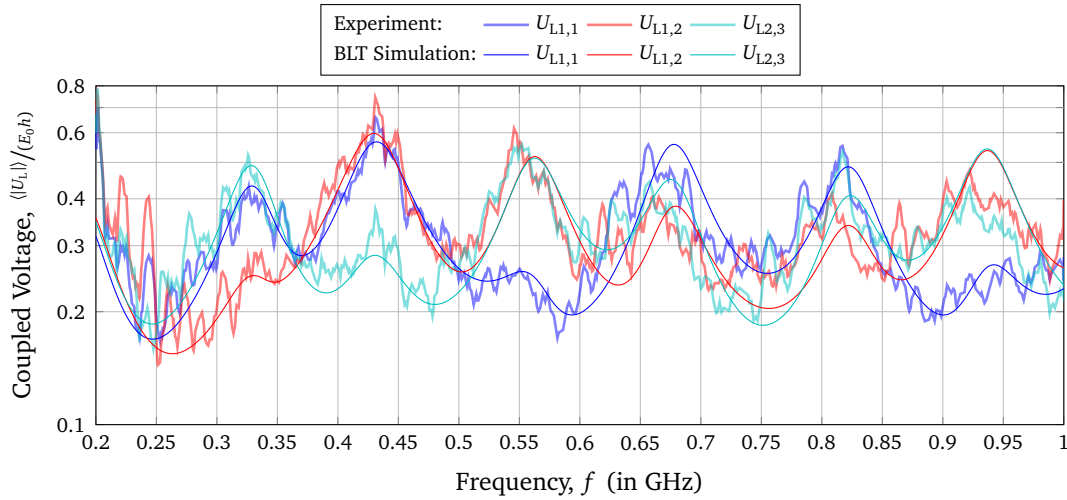


Figure 4.16: Average magnitude of the coupled voltage $\langle |U_L| \rangle$ at the three line ends for the basic configuration of the network

Additionally, resonances from the combination of the lines occur. The following resonances are possible ($l = \lambda/4$):

$l_1 + l_2 = 70$ cm: at 214 MHz, 428 MHz, 642 MHz and 857 MHz

$l_2 + l_3 = 80$ cm: at 188 MHz, 375 MHz, 563 MHz, 750 MHz and 938 MHz

All these resonances are visible in Fig. 4.16. The resonance for $l_1 + l_3 = 90$ cm is with 1666 MHz outside the measuring range.

4.6.1 Variation of the Line Length

In this part the line length l_3 was varied. The results of the coupled voltage at the end of the third line are presented in Fig. 4.17. The simulated and measured results are in a good match. The expected resonances are summarized in Tab. 4.1, where they are analyzed for different lengths of l_3 . Again, resonance frequencies of the individual line 3 can be observed, which would still be expected at multiples of $\lambda/2$. Also resonance frequencies of the connection of line 2 and line 3 at multiples of $\lambda/4$ are to be expected. The measured line resonances correspond to the expected resonance frequencies of the network.

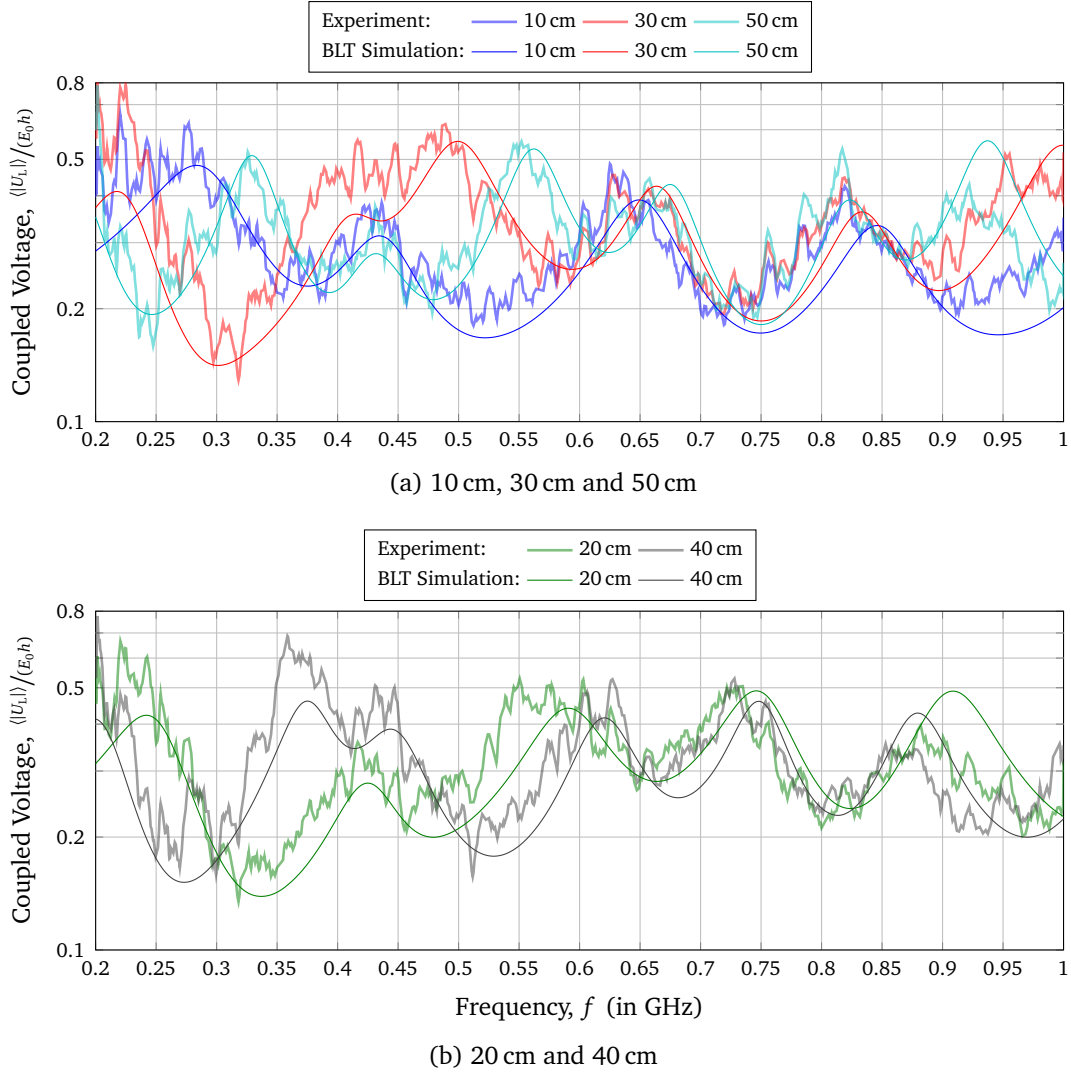


Figure 4.17: Average magnitude of the coupled voltage $\langle |U_{L,3}| \rangle$ at the end of the third line for varying the line lengths l_3

Table 4.1: Resonance frequencies for different line lengths l_3 of the third line of the network

l_3 [cm]	Resonances [MHz]	$l_3 + l_2$ [cm]	Resonances [MHz]
10	300, 450, 600, 750, 900	40	187, 562
20	750	50	150, 450, 750
30	500, 1000	60	125, 375, 625, 875
40	375, 750	70	107, 321, 535, 750, 963
50	300, 600, 900	80	94, 281, 468, 655, 843

4.6.2 Variation of the Alignment

Finally, the angle of the third line was varied. Fig. 4.18 depicts a schematic drawing of the investigated angles of the third line of the network. The angle ϑ is defined from the x -axis counterclockwise.

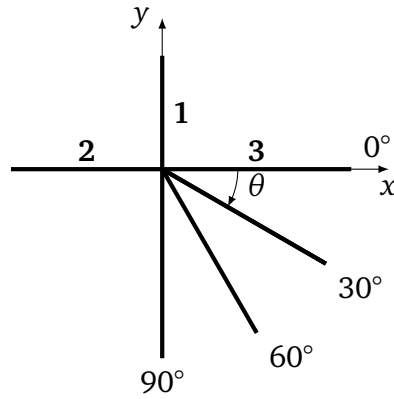


Figure 4.18: Schematic configurations of the network for different angles θ

The simulation and measurement results in Fig. 4.19 are almost coincide. This is due to three facts. First, the line length was kept constant and therefore the resonance frequencies remain the same. Second, the bend angle ϑ was minimum 30°, so that no coupling effects occurred between the lines. Third, all lines are symmetrically terminated with 50Ω and there are no large line resonances.

Summarizing these results, when excited with a stochastic field the exact orientation of the network does not matter as long as the angle is not too small and coupling effects between the conductors occur, as shown in section 4.4.2. In this network there were already influences when the bending angle was reduced to $\theta = 60^\circ$.

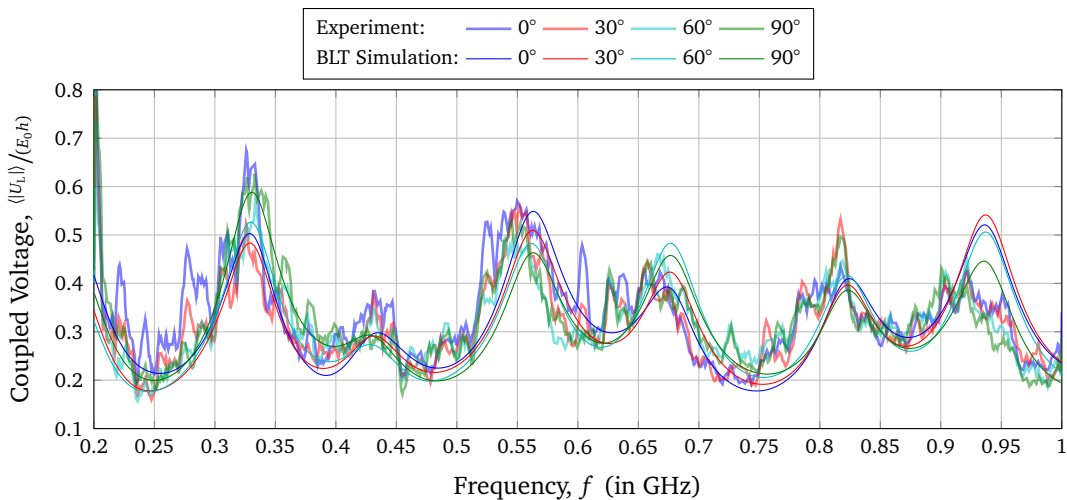


Figure 4.19: Average magnitude of the coupled voltage $\langle |U_{L,3}| \rangle$ at the end of the third line of the transmission line network for different alignment angles θ

4.6.3 Variation of the Termination

In addition, the terminations at the beginning of the first and second line were varied, as summarized in Tab. 4.2. The corresponding results are shown in Fig. 4.20. Due to the bigger mismatch, the resonances are much more peaked, and a logarithmic scaling of the y -axis was chosen, to be able to represent large variations in the voltages better. In order to illustrate how important it is to take coupling into account during modeling, the results from [MV15], where coupling effects are neglected, are also shown here. The larger mismatch also leads to higher coupled voltages and thus to a larger influence of the voltages on the other conductors. The comparison of the two simulation models shows that a consideration of the coupling between the wires in case of a large mismatch is indispensable even for quite large bending angles.

Table 4.2: Variations of the terminating resistances at the line ends of the network for the results shown in Fig. 4.20

Name	$Z_{L1,1}$	$Z_{L1,2}$	$Z_{L2,3}$	Curve
Open-Short	∞	0	$50\ \Omega$	—
Short-Open	0	∞	$50\ \Omega$	—
Open-Open	∞	∞	$50\ \Omega$	—
Short-Short	0	0	$50\ \Omega$	—

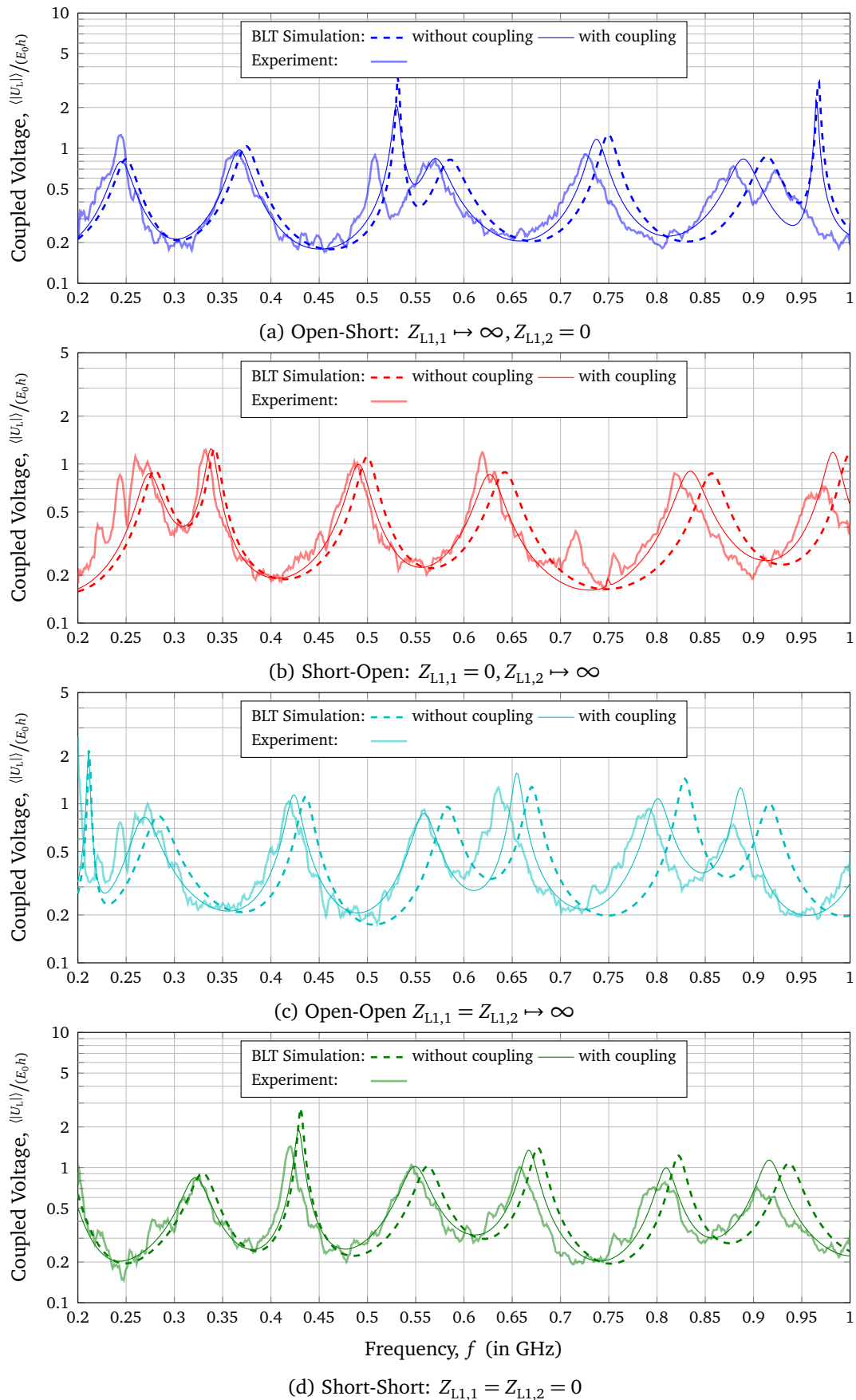


Figure 4.20: Average magnitude of the coupled voltage $\langle |U_{L,3}| \rangle$ at the end of the third line of the network for different configurations of the termination loads at line 1 and 2

4.7 Comparison with a Curved Single Conductor Transmission Line

Transmission lines often do not run straight but have to follow other shapes due to external boundary conditions of the surrounding. In addition to the possibility of a bent from the previous section, a line can also be curved. In this Section, the influence of the curving of a transmission line to the coupled voltage is investigated experimentally in the reverberation chamber and by simulations using the MoM. Here, the effects on the coupled voltage and on the radiation losses and differences between bending and curving of a transmission line are investigated and discussed. A schematic of the curved transmission line is shown in Fig. 4.21.

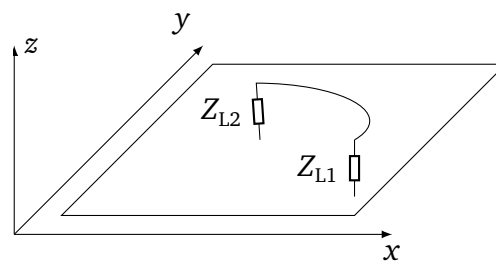


Figure 4.21: Curved single conductor transmission line over a conductive ground plane

4.7.1 Measurements of the Coupled Voltage

During measurements, the curved transmission line had a length of $l = 1$ m, was located at a height of $h = 3$ cm over the conductive x - y ground plane. The line ends were terminated with Z_{L1} and Z_{L2} . A schematic of the different curving angles is shown in Fig. 4.22. Because the line length was kept constant, the radius of the circle segment was decreasing.

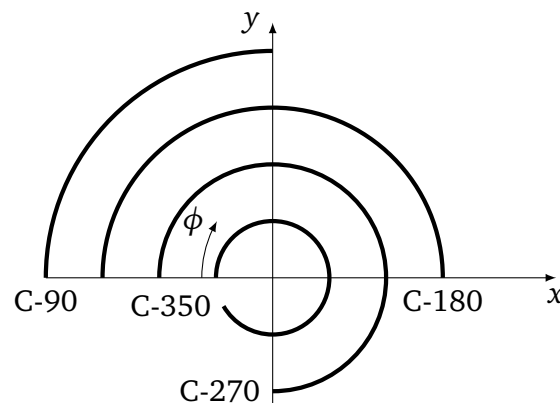


Figure 4.22: Schematic of the measured configurations of the curved line with different angles ϕ

In Fig. 4.23, photos of the 180° (C-180) and 350° (C-350) curved line in the reverberation chamber are shown. Due to the minimum distance of 2.5 cm between the N feedthroughs the maximum angle of the circle segment was again 350°.

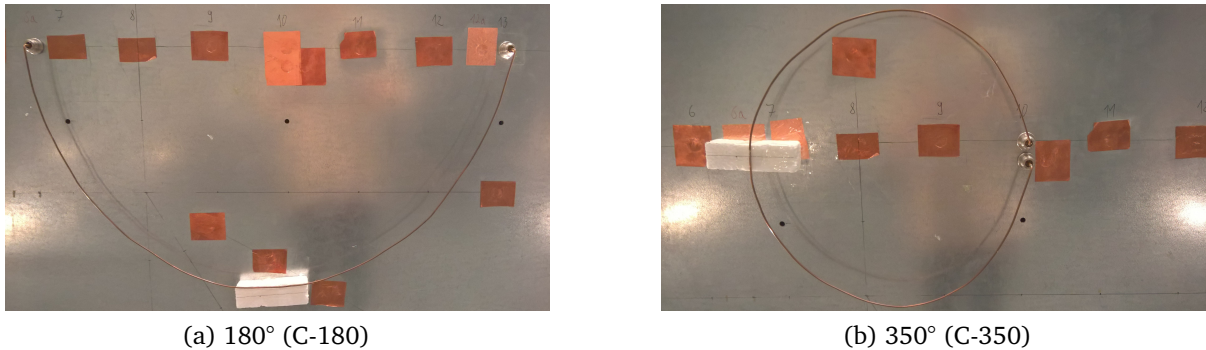


Figure 4.23: Different curved transmission line in the reverberation chamber

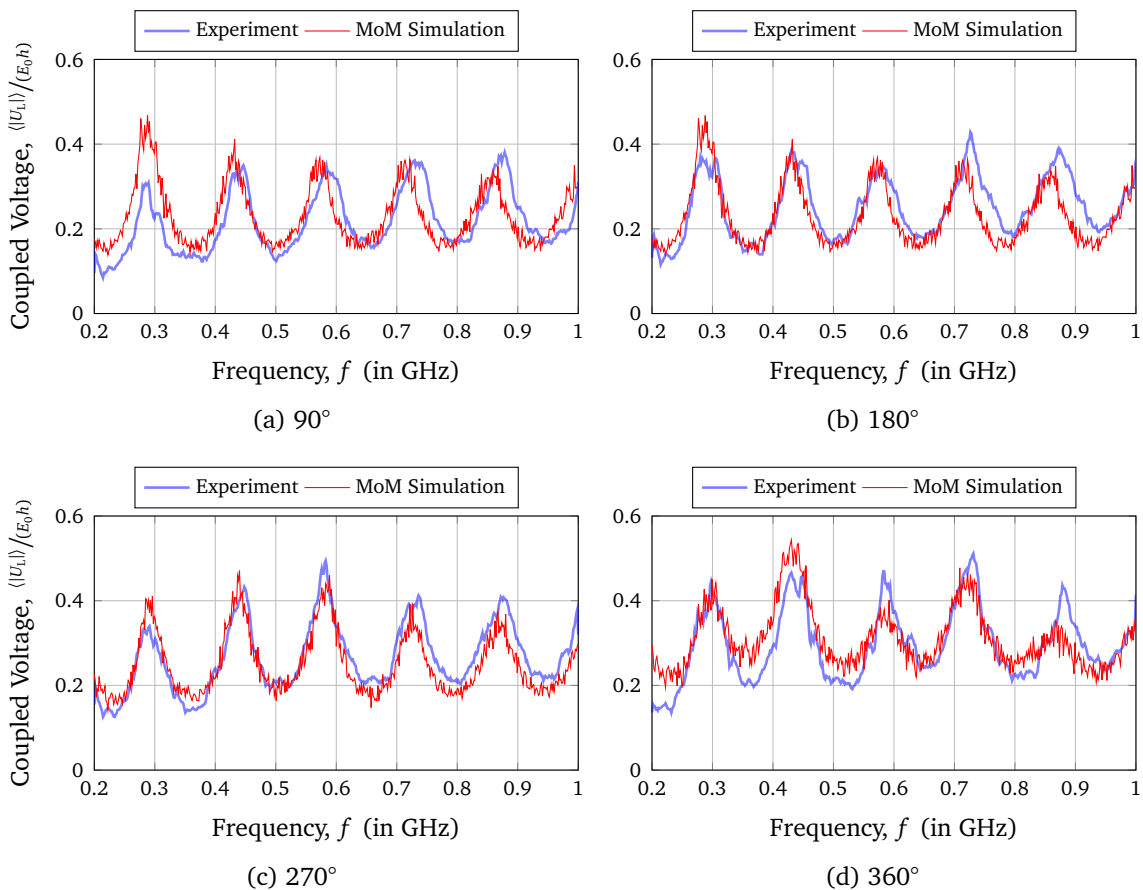


Figure 4.24: Comparison of the measured and simulated results of the average magnitude of the coupled voltage $\langle |U_{L1}| \rangle$ at the beginning of the curved transmission line over ground

In Fig. 4.24, the measured and simulated (*CONCEPT-II*) normalized coupled voltage at the beginning of the curved line for different curve angles over the frequency is shown. The screenshots of the simulation f models for the different geometries of the curved transmission

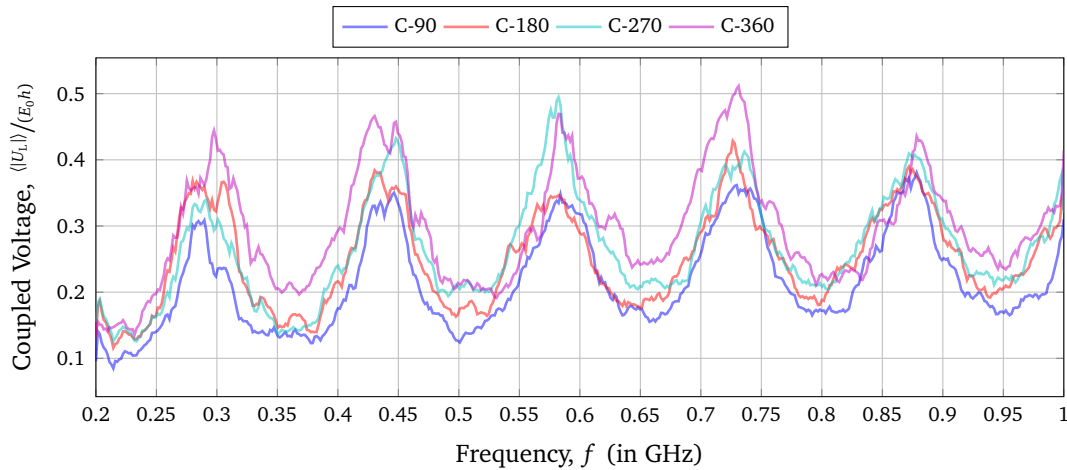


Figure 4.25: Comparison of the measured coupled voltage of the curved lines C-90 to C-360

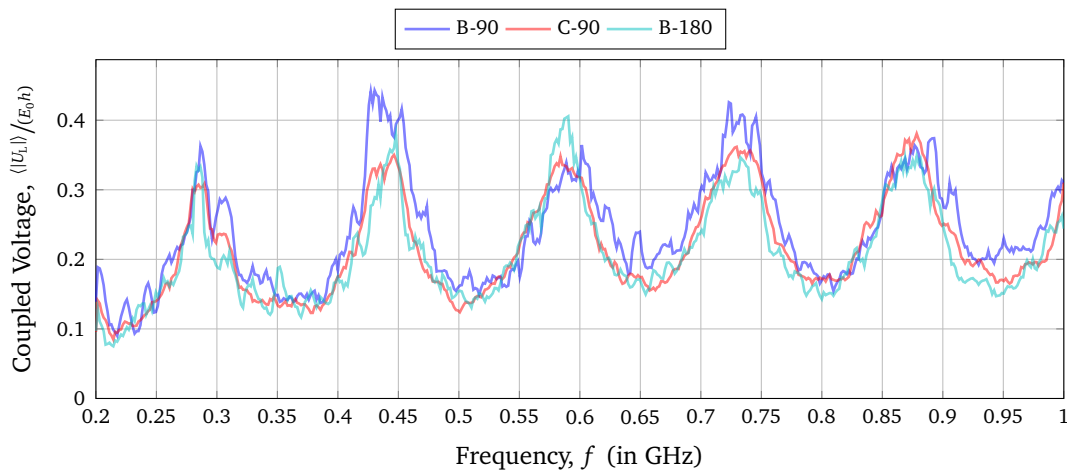


Figure 4.26: Comparison of the coupled voltage of the bent and curved line

line in *CONCEPT-II* can be found in Appendix C. For all lines, resonances occur at about 300 MHz, 450 MHz, 600 MHz, 750 MHz and 900 MHz, which fits to the theoretical expected resonances for a symmetrically mismatched 1 m long line ($l = \frac{\lambda}{2}, \lambda, \frac{3}{2}\lambda, \dots$ [MV12]). The simulated and measured results fit quite well. There are some small deviations which can be caused by the stochastics.

In Fig. 4.25, all measured results of the coupled voltage are shown to see a better comparison. It can be seen, that for the angles of 270° and 360° there are higher amplitudes in some resonances. It can be said that the extension of the fixed radius segment of the circle results in higher coupled voltage, as the line gets closer together, which can cause coupling effects.

In Fig. 4.26 the result of the 90° curved line (C-90) and the 90° bent line (B-90) is directly compared to the straight line (B-180). The coupled voltage of the straight, the bent and the curved lines show the same behavior and similar resonances at 450 MHz, 750 MHz and 900 MHz because all lines are 1 m long. If one compares the results, one can see that the curving has no great influence on the coupled voltage.

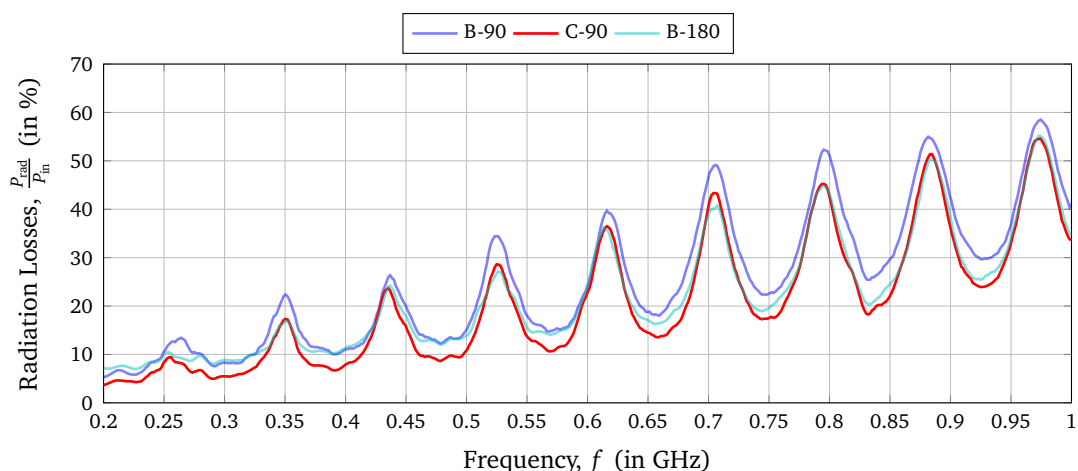


Figure 4.27: Measured radiation losses for the 90° curved line in comparison to the straight (B-180) and 90° bent line

4.7.2 Comparison of the Radiation Losses

In Fig. 4.27, the radiation losses calculated by Eq. (2.112) over the frequency for the 90° curved line (C-90) in comparison to the straight line (B-180) and the 90° bent line (B-90) is shown. The experiment on the radiation loss for the curved line was performed similar to the bent line in Section 4.5. The losses are almost the same for the straight and the 90° curved line. Comparing the results to the 90° bent line, the losses are about 5 % smaller for the curved line, especially at the resonances.

However, Fig. 4.27 gives a lot of useful information about the radiation of curved lines. The radiation loss of a 90° curved line is comparable to the losses of a straight line. At lower frequencies there are even lower losses, away from the resonant frequencies. The results show that the radiation of the curved line cannot be neglected nor the bent line (Section 4.5). It can be concluded that right angle curving is most strongly recommended to minimize radiation losses, which is also the easiest.

4.7.3 Comparison of the Curved Line with Transmission Line Theory

Now, the solutions of the curved line are compared to the transmission line theory of the bent wire. For this purpose, a 90° curved wire is constructed from various numbers of individual straight transmission line sections.

Fig. 4.28 illustrates models of transmission lines with bends, in order to make a comparison of different types of bent lines. Here, $n = 2$ indicates a bend with a right angle, $n = 3$ corresponds to the case of two corners and $n = 5$ to the case of four corners. To make the results comparable, the line length of the curved and the bent lines must be equal to 1 m.

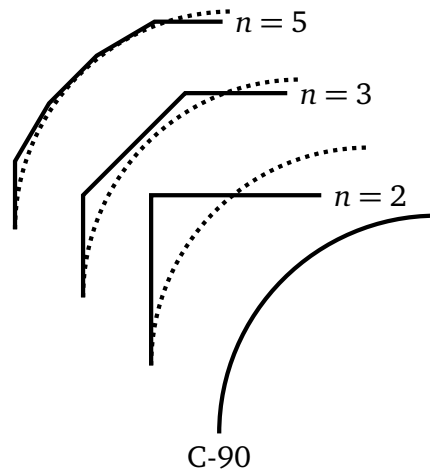


Figure 4.28: Schematic for the comparison of the 90° curved line with transmission lines with different numbers of segments

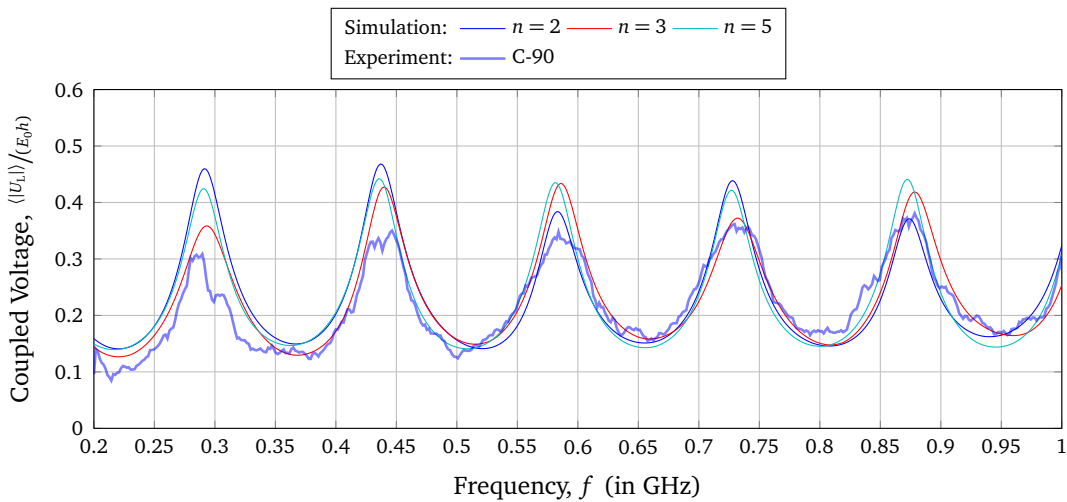


Figure 4.29: Comparison of the measured coupled voltage $\langle |U_{L1}| \rangle$ of the 90° curved line and the simulated results for transmission lines with a different number of bends (schematic shown in Fig. 4.28)

The coupled voltage for each shape of the transmission line models are shown in Fig. 4.29. Here, the measured results for the 90° curved line are compared to the simulation results with a different number of bends. Because of the constant line length, the resonance frequencies remain the same, but the amplitude differs. The coupling to a curved line is lower than the coupling to the transmission lines with different numbers of bends. It can be concluded that the curving is much better for the field-to-wire coupling than to a line with several bends.

5 Multiconductor Transmission Line over a Conductive Ground Plane

The influence of a stochastic electric field coupling to a single wire above a conductive ground plane was considered at the previous chapters. Now another three-dimensional transmission line structure is to be investigated. Such single wire system can be extended to the case of a multiconductor transmission line (MTL). A general MTL consists of n conductors with a reference conductor (see Section 5.5) or a ground plane acting as a return conductor. In this chapter, the second case is considered. The n -conductor system plus an additional ground return (Reference) is illustrated in Fig. 5.1. All lines are terminated with some terminations at the beginning (load 1) and at the end of the lines (load 2). Typical examples are cables that have a metallic structure as return conductor or high-voltage lines for power distribution. The aim is to investigate the influence of the number of wires and various parameters of the wires of such multiconductor transmission lines. The multiconductor line over ground can be used for modeling a bundle of telecommunication wires in a non-shielded cable [Per95].

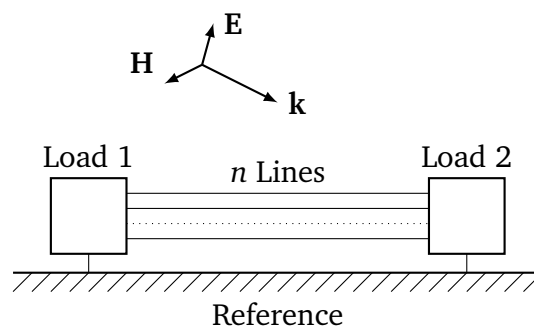


Figure 5.1: Schematic of a multiconductor transmission line over a ground plane

5.1 Transmission Line Model

Now, the distributed transmission line parameters of the MTL were determined. For high frequencies, the coupling among several conductors must be taken into account. Because of the limitation of classical transmission line theory, the theory proposed by [CBK17] is used, to contain high frequency effects in the model. For a system of n lines over ground, the p. u. l. parameters are written as $n \times n$ matrix. The multiconductor transmission line can be

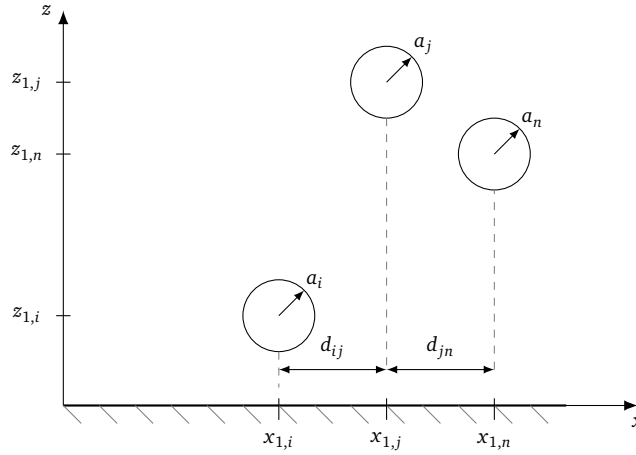


Figure 5.2: Multiconductor transmission line over a conducting ground plane with n wires

constructed from several single wire lines with the start and end coordinates of $(x_{1,i}, y_{1,i}, z_{1,i})$ and $(x_{2,i}, y_{2,i}, z_{2,i})$. Here, i is the line number (see Fig. 5.2). Every wire has a specific radius a_i , is located at a height h_i above the ground plane and is separated from another wire j by a distance d_{ij} . All the notations, conventions and assumptions that were made for the single-wire case in Chapter 3 are retained for the multi-wire configuration.

By adapting the equation for the vector potential from Eq. (3.8) from the case of a single wire to the general case of n wires, the vector potential for the i th wire becomes

$$\mathbf{A}(\mathbf{r}) = \sum_{j=1}^n \int_0^l J_j(y') \cdot \mathbf{t} \cdot g(y_i - y'_j) dy'. \quad (5.1)$$

Since the wire is oriented in y direction, the Green's function $g(y_i, y'_j)$ also depends only on the y components. Here y_i describes the position of the observation point on wire i and y'_j the position of the source point on wire j .

The field-to-wire coupling to a MTL is described by the following set of equations

$$\frac{dU_i^s(y)}{dy} + j\omega \frac{\mu}{4\pi} \sum_{j=1}^n I_j(y) \int_0^l g(y_i - y'_j) dy' = E_{\text{tan,MTL}}^e(z_i, y), \quad (5.2a)$$

$$\frac{d}{dy} \sum_{j=1}^n I_j(y) \int_0^l g(y_i - y'_j) dy' + j\omega 4\pi \varepsilon U_i^s(y) = 0. \quad (5.2b)$$

Here, $I_j(y)$ and $U_i^s(y)$ are the current and the voltage related to the scattered electric field, $E_{\text{tan,MTL}}^e(z_i, y)$ is the incident tangential electric field. In this case, the Green's function is

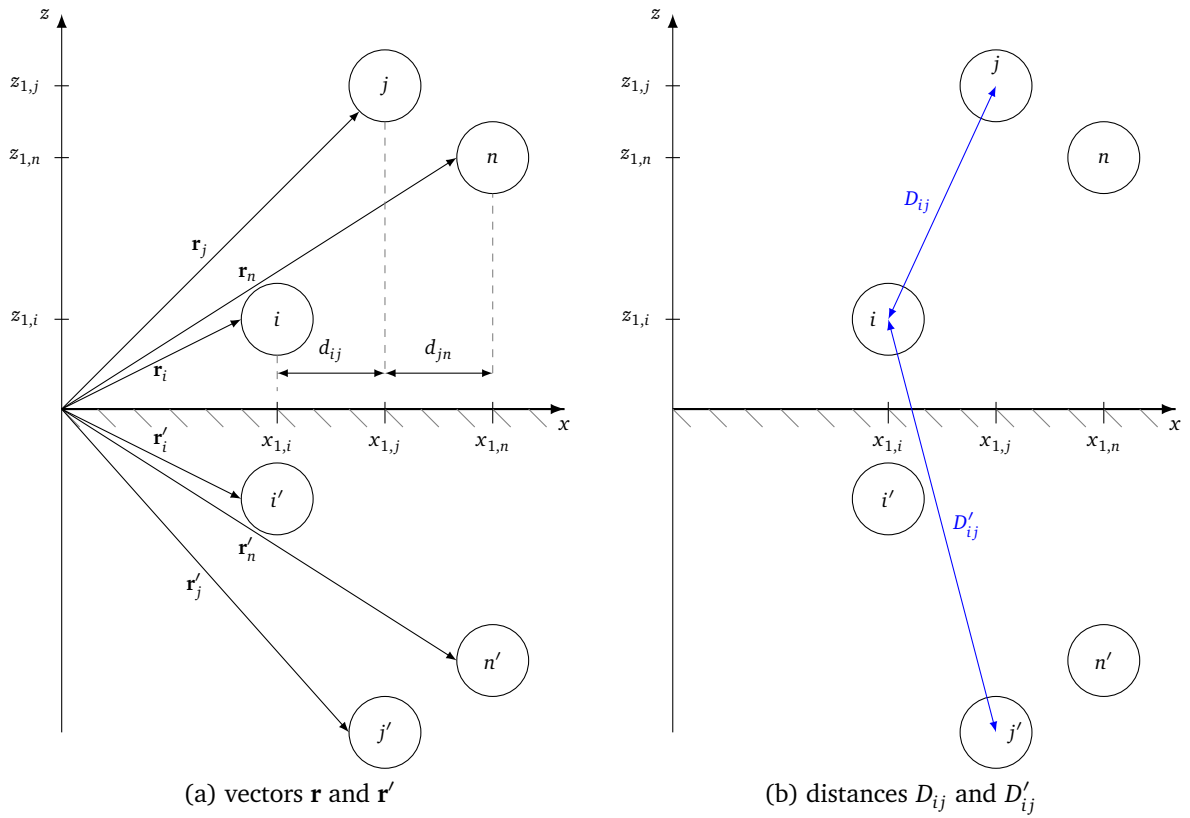


Figure 5.3: Multiconductor transmission line over a conducting ground plane with n wires and its image wires

defined by

$$g(y_i - y'_j) = \frac{e^{-jk|\mathbf{r}_i - \mathbf{r}'_j|}}{|\mathbf{r}_i - \mathbf{r}'_j|}. \quad (5.3)$$

The vectors \mathbf{r}_i and \mathbf{r}'_j can be taken from Fig. 5.3a. In order to evaluate the integral two cases are distinguished:

1. $i = j$: The effect of the wire itself is considered and the Green's function represents the self-induced voltages of wire i . This case is similar to a single wire line over ground.
2. $i \neq j$: The coupling between the wires is considered and the Green's function represents the mutual coupling between wire i and j .

However, both integrals are calculated in the same way, since only the arguments of the Green's functions change.

The field-to-wire coupling equations (5.2) can be put in a matrix notation

$$\frac{d}{dy} [U_i^s(y)] + j\omega \frac{\mu}{4\pi} [G_{\text{MTL}}] [I(y)] = [E_{\text{tan,MTL}}^e], \quad (5.4a)$$

$$\frac{d}{dy} [I(y)] + j\omega 4\pi\epsilon [G_{\text{MTL}}]^{-1} [U(y)] = 0. \quad (5.4b)$$

Here, the matrix $[G_{\text{MTL}}]$ is an $n \times n$ matrix, where the main diagonal elements describe the effect of the wire itself and the side diagonal elements describe the mutual coupling between the wires. The quantities $[U_i^s(y)]$, $[I(y)]$ as well as $[E_{\text{tan,MTL}}^e]$ are vectors of the size $n \times 1$. To solve the Green's function integral as done in Eq. (3.12) to (3.15), a generalization can be made for the multiconductor case.

Interaction of the Wire with Itself

The solution of the Green's function for the interaction of the wire with itself ($i = j$) follows similar to Eq. (3.15) for the i th wire

$$G_{\text{MTL},ii} = \int_{-\infty}^{+\infty} g(y_i, y_i') dy' = \pi [Y_0(2h_i k) - Y_0(a_i k)] + j\pi [J_0(2h_i k) - J_0(a_i k)]. \quad (5.5)$$

The solution is identical to the single conductor case and it can be separated in a frequency independent part $G_{\text{MTL},ii}^{\text{LF}}$, that is equal to the low frequency solution and frequency dependent part $C_{\text{MTL},ii}^{\text{F}}$, that is called the correction factor

$$G_{\text{MTL},ii} = G_{\text{MTL},ii}^{\text{LF}} + C_{\text{MTL},ii}^{\text{F}}. \quad (5.6)$$

The low frequency approximation is given by

$$G_{\text{MTL}}^{\text{LF}} = 2 \ln \left(\frac{2h_i}{a_i} \right). \quad (5.7)$$

The correction factor $C_{\text{MTL},ii}^{\text{F}}$ is separated into a real part

$$\begin{aligned} \Re \{ C_{\text{MTL},ii}^{\text{F}} \} = & 2 \left\{ [\ln(h_i k) + \gamma_{\text{EM}}] [J_0(2h_i k) - 1] - \left[\ln \left(\frac{a_i k}{2} + \gamma_{\text{EM}} \right) \right] [J_0(a_i k) - 1] \right\} \\ & - \left\{ \left[\sum_{k=1}^{\infty} (-1)^k \frac{(h_i k)^{2k}}{(k!)^2} \left(\sum_{m=1}^k \frac{1}{m} \right) \right] - \left[\sum_{k=1}^{\infty} (-1)^k \frac{\left(\frac{a_i k}{2} \right)^{2k}}{(k!)^2} \left(\sum_{m=1}^k \frac{1}{m} \right) \right] \right\} \end{aligned} \quad (5.8)$$

and an imaginary part

$$\Im \{ C_{\text{MTL},ii}^{\text{F}} \} = j\pi [J_0(2h_i k) - J_0(a_i k)]. \quad (5.9)$$

Interaction between the Wires

If current carrying conductors are close to each other, there are coupling effects between them. There exist a capacitive and inductive coupling between the wires. These types of coupling can be prevented by, for example, shielding [TIK96, Ch. 9], increasing the distance or twisting [Per95, Ch. 2, Sec. 2.4]. Without these preventive methods, and since such couplings are possible anyway, they will be considered here. Considering the mutual coupling between wire i and j , the calculation of the Green's function integral leads to an expression similar to Eq. (5.5)

$$G_{\text{MTL},ij} = \int_{-\infty}^{+\infty} g(y_i, y'_i) dy' = \pi [Y_0(D_{ij}k) - Y_0(D'_{ij}k)] + j\pi [J_0(D_{ij}k) - J_0(D'_{ij}k)], \quad (5.10)$$

where the distances D_{ij} and D'_{ij} are defined by

$$D_{ij} = \sqrt{(h_i + h_j)^2 + d_{ij}^2}, \quad (5.11)$$

$$D'_{ij} = \sqrt{(h_i - h_j)^2 + d_{ij}^2}, \quad (5.12)$$

as shown in Fig. 5.3b. Again, the solution can be separated in a low frequency solution and frequency dependent correction factor $C_{\text{MTL},ij}^{\text{F}}$

$$G_{\text{MTL},ij} = G_{\text{MTL},ij}^{\text{LF}} + C_{\text{MTL},ij}^{\text{F}}. \quad (5.13)$$

Here, the transmission line approximation of the Green's function integral is

$$G_{\text{MTL},ij}^{\text{LF}} = 2 \ln \left(\frac{D_{ij}}{D'_{ij}} \right). \quad (5.14)$$

Derivation of an Equivalent Circuit

In contrast to a single line above ground, the p. u. l. parameters and the resulting characteristic impedance describing multiconductor transmission lines are not scalar quantities but matrices. Eqs. (5.6) and (5.13) can be put in a general matrix

$$[G_{\text{MTL}}] = [G_{\text{MTL}}^{\text{LF}}] + [C_{\text{MTL}}^{\text{F}}], \quad (5.15)$$

where $[G_{\text{MTL}}^{\text{LF}}]$ is the classical low frequency solution of the Green's function integral and $[C_{\text{MTL}}^{\text{F}}]$ describes the high frequency correction matrix. Solving the Green's matrix elements the p. u. l. parameters can be determined. The equivalent circuit of the multiconductor transmission line over a conductive ground plane is shown in Fig. 5.4. The difference to the case of a single wire is in the coupling elements between the conductors. Eq. (5.4) can be

expressed in matrix form

$$\frac{d}{dy} [U^s(y)] + [I(y)] \underbrace{(j\omega [L_{\text{MTL}}^{\text{HF}}] + [R_{\text{MTL}}^{\text{HF}}])}_{[Z_{\text{MTL}}^{\text{HF}}]} dy' = [E_{\text{tan,MTL}}^e], \quad (5.16a)$$

$$\frac{d}{dy} [I(y)] + [U^s(y)] \underbrace{(j\omega [C_{\text{MTL}}^{\text{HF}}] + [G_{\text{MTL}}^{\text{HF}}])}_{[Y_{\text{MTL}}^{\text{HF}}]} = [0]. \quad (5.16b)$$

The high frequency impedance matrix is defined as

$$[Z_{\text{MTL}}^{\text{HF}}] = [R_{\text{MTL}}^{\text{HF}}] + j\omega [L_{\text{MTL}}^{\text{HF}}]. \quad (5.17)$$

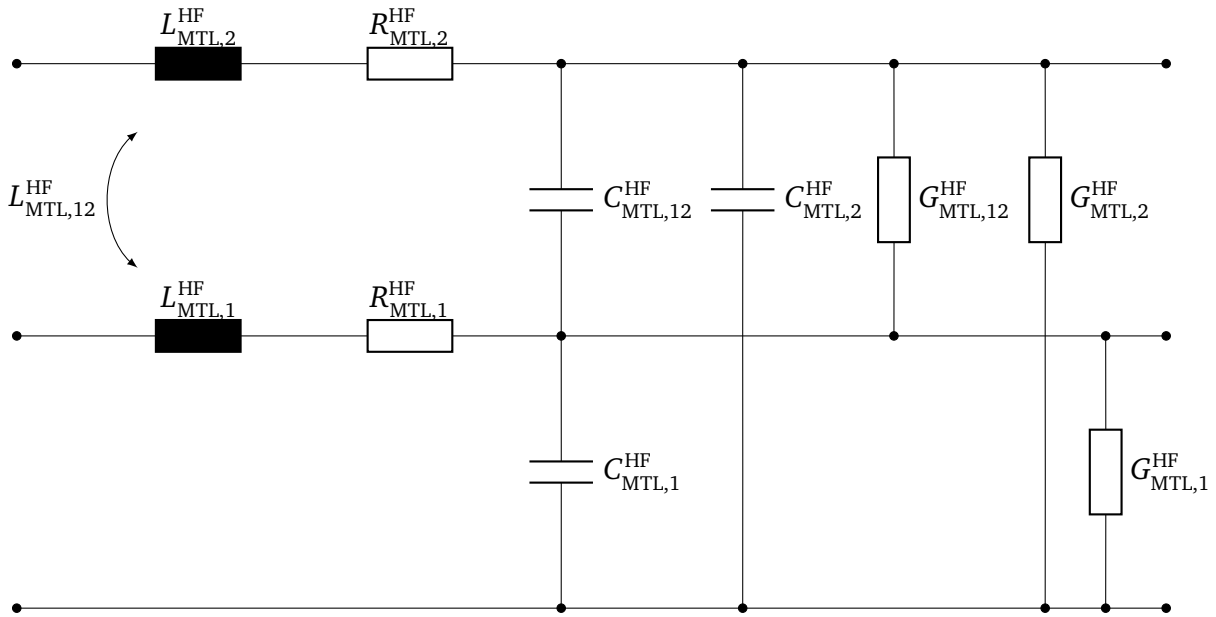


Figure 5.4: Equivalent circuit model of a short segment of a two-wire multiconductor transmission line

In Eq. (5.17), the high frequency p. u. l. inductance and resistance are defined by

$$[L_{\text{MTL}}^{\text{HF}}] = [L'_{\text{MTL}}] + \frac{\mu_0}{4\pi} \Re \{ [C_{\text{MTL}}^{\text{F}}] \}, \quad (5.18)$$

and

$$[R_{\text{MTL}}^{\text{HF}}] = -\omega \frac{\mu_0}{4\pi} \Im \{ [C_{\text{MTL}}^{\text{F}}] \}. \quad (5.19)$$

For the p. u. l. inductance for the i th wire follows

$$[L'_{\text{MTL}}] = \frac{\mu}{4\pi} [G_{\text{MTL}}^{\text{LF}}]. \quad (5.20)$$

The high frequency admittance matrix follows with

$$[Y_{\text{MTL}}^{\text{HF}}] = [G_{\text{MTL}}^{\text{HF}}] + j\omega [C_{\text{MTL}}^{\text{HF}}]. \quad (5.21)$$

From Eq. (5.4b), the high frequency admittance can also be written as

$$[Y_{\text{MTL}}^{\text{HF}}] = j\omega\pi\epsilon \left([G_{\text{MTL}}^{\text{LF}}] + \Re \{ [C_{\text{MTL}}^{\text{F}}] \} + j\Im \{ [C_{\text{MTL}}^{\text{F}}] \} \right)^{-1}. \quad (5.22)$$

The classical transmission line p. u. l. capacity can be determined for the i th wire as

$$[C'_{\text{MTL}}] = 4\pi\epsilon [G_{\text{MTL}}^{\text{LF}}]^{-1}. \quad (5.23)$$

Hence, the high frequency impedance and admittance are expressed as a combination of a classical part (quasi static) and a high frequency correction. In the following, the effects of these frequency p. u. l. parameters on the characteristic impedance matrix of the multiconductor line is shown.

Characteristic Impedance Matrix

The characteristic impedance matrix has the same dependency as the p. u. l. parameters and is denoted as

$$[Z_{\text{c,MTL}}^{\text{HF}}] = \left([Z_{\text{MTL}}^{\text{HF}}] [Y_{\text{MTL}}^{\text{HF}}]^{-1} \right)^{\frac{1}{2}}. \quad (5.24)$$

With Eqs. (5.17) and (5.21) follows

$$[Z_{\text{c,MTL}}^{\text{HF}}] = [Z_{\text{c,MTL}}^{\text{LF}}] + [C_{\text{MTL}}^{\text{F}}], \quad (5.25)$$

where $[Z_{\text{c,MTL}}^{\text{LF}}]$ is the classical characteristic impedance matrix given by

$$[Z_{\text{c,MTL}}^{\text{LF}}] = \frac{1}{4\pi} \sqrt{\frac{\mu}{\epsilon}} [G_{\text{MTL}}^{\text{LF}}]. \quad (5.26)$$

In Fig. 5.5, the elements of the real and imaginary part of the characteristic impedance matrix are shown, which were calculated using the classical as well as the HF p. u. l. parameters. Both wires of the multiconductor transmission line had a radius of $a = 1$ mm, the height $h = 3$ cm over ground and the length $l = 1$ m is shown. The distance between the wires was $s = 2.5$ cm. With the help of Eq. (5.26) the classical characteristic impedance matrix can be calculated from the transverse dimensions of the line

$$[Z_{\text{c,MTL}}^{\text{LF}}] = \begin{bmatrix} 245.5 \Omega & 108.3 \Omega \\ 108.3 \Omega & 245.5 \Omega \end{bmatrix} \quad (5.27)$$

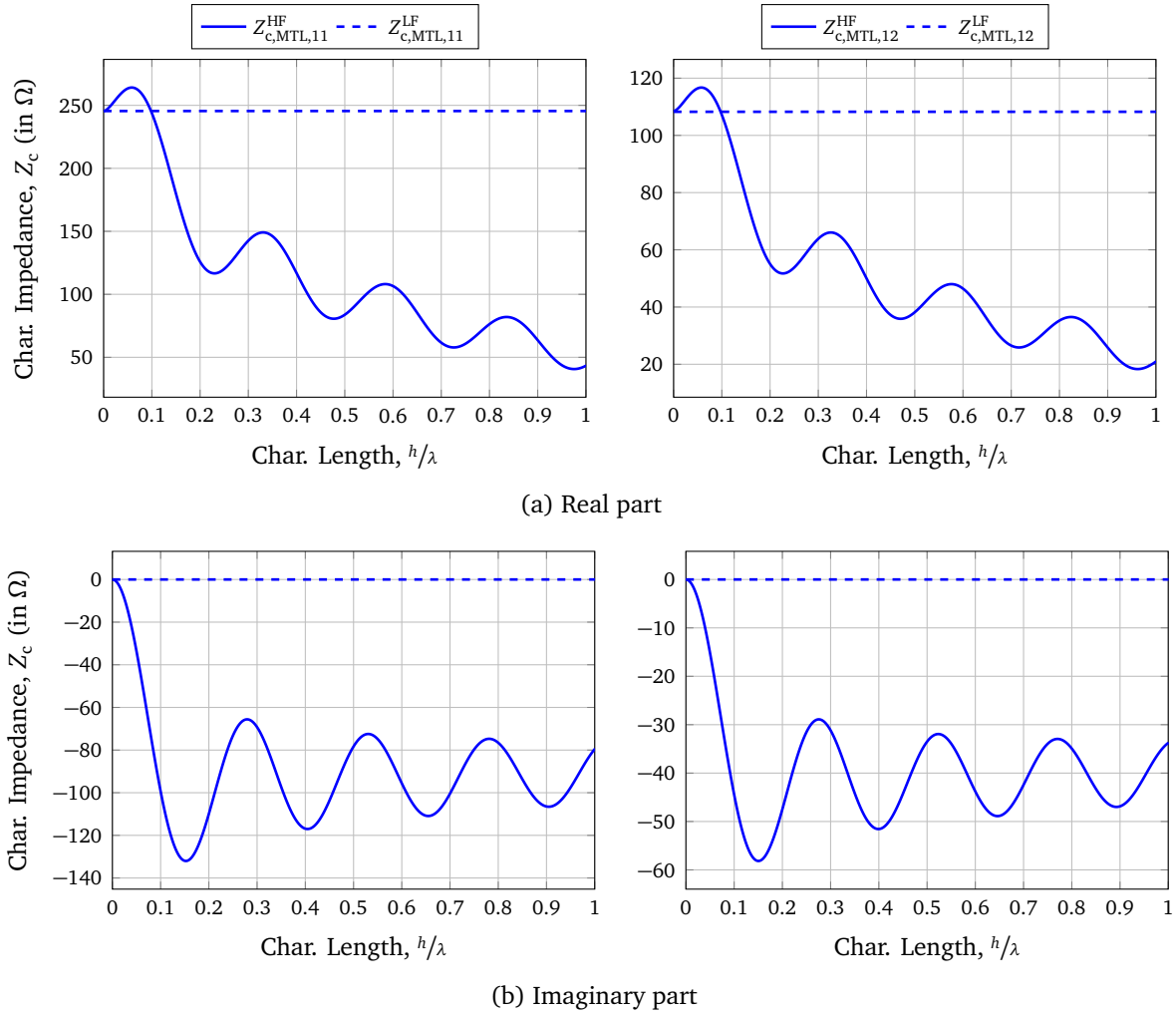


Figure 5.5: Comparison between the classical (LF) and high frequency (HF) characteristic impedance matrix elements for a multiconductor transmission line over a conductive ground plane

can be obtained. The matrix elements $Z_{c,MTL,22}^{LF}$ and $Z_{c,MTL,21}^{LF}$ are analogous to those of $Z_{c,MTL,11}^{LF}$ and $Z_{c,MTL,12}^{LF}$ because of the symmetric arrangement of the two wires.

5.2 Field-to-Wire-Coupling Equations

The BLT equations to calculate the coupled voltage

$$[U_{L,MTL}] = \begin{bmatrix} [U_{L1,MTL}] \\ [U_{L2,MTL}] \end{bmatrix} = \left[[1] + [\Gamma_{MTL}] \right] \cdot [D_{MTL}]^{-1} \cdot \begin{bmatrix} [S_{1,MTL,i}] \\ [S_{2,MTL,i}] \end{bmatrix} \quad (5.28)$$

are of the same form as for the bent wire (Eq. (4.38)). The formulas for the source term $[S]$ from Eq. (4.44) remain the same for the multiconductor case. Here, the tangential electric field can be determined using Eq. (4.48) and the transverse voltage is defined analogously

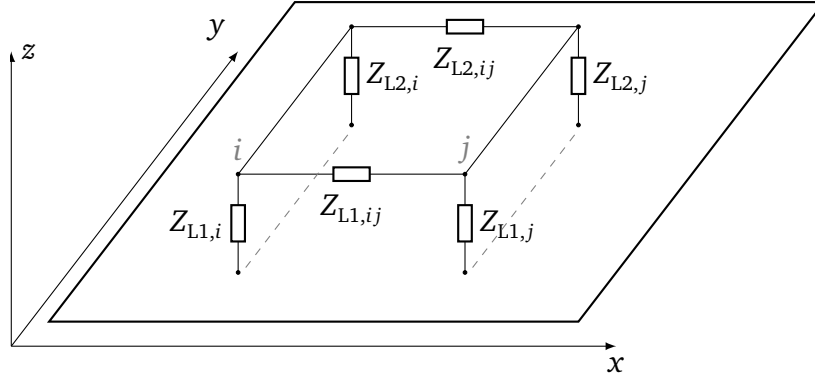


Figure 5.6: Definition of the load impedances of the multiconductor transmission line over ground plane. The lines are terminated with $Z_{L1,i}$ and $Z_{L1,j}$ at the beginning and with $Z_{L2,i}$ and $Z_{L2,j}$ at the end.

to Eq. (4.49). In Eq. (5.60), the $n \times n$ reflection matrix $[\Gamma_{\text{MTL}}]$ is defined equal to Eq. (4.39) and is repeated for clarity here

$$[\Gamma_{\text{MTL}}] = \begin{bmatrix} [\Gamma_{\text{MTL},1}] & [0] \\ [0] & [\Gamma_{\text{MTL},2}] \end{bmatrix}, \quad (5.29)$$

where $[\Gamma_{\text{MTL},1}]$ and $[\Gamma_{\text{MTL},2}]$ are the $n \times n$ reflection coefficient matrices for the beginnings and the ends of the lines

$$[\Gamma_{\text{MTL},1}] = ([Z_{L1}] - [Z_{\text{c,MTL}}^{\text{HF}}]) \cdot ([Z_{L1}] + [Z_{\text{c,MTL}}^{\text{HF}}])^{-1}, \quad (5.30a)$$

$$[\Gamma_{\text{MTL},2}] = ([Z_{L2}] - [Z_{\text{c,MTL}}^{\text{HF}}]) \cdot ([Z_{L2}] + [Z_{\text{c,MTL}}^{\text{HF}}])^{-1}. \quad (5.30b)$$

The matrix for the load impedances $[Z_{L1}]$ and $[Z_{L2}]$ at the beginning and the end of the lines, respectively, can be a full matrix. Here, e. g. $Z_{L1,1}$ means the load from the beginning of wire 1 to the conductive ground plane and $Z_{L2,1}$ is the load resistance between the end of conductor 1 and ground. Further, $Z_{L1,12}$ is the load between the beginnings of wire 1 and 2. The matrix $[Z_{\text{c,MTL}}^{\text{HF}}]$ is the $n \times n$ characteristic impedance matrix of the multiconductor transmission line from Eq. (5.25). The limiting case of sending $Z_{L1,1}$, $Z_{L1,2}$, $Z_{L2,1}$ and $Z_{L2,2}$,

separately to infinity leads to the following 2×2 matrices

$$\lim_{Z_{L1,1} \rightarrow \infty} [\Gamma_{\text{MTL},1}] = \begin{bmatrix} 1 & -\frac{2Z_{c,\text{MTL}1,2}^{\text{HF}}}{Z_{L2,2} + Z_{c,\text{MTL}2,2}} \\ 0 & \frac{Z_{L2,2} - Z_{c,\text{MTL}2,2}^{\text{HF}}}{Z_{L2,2} + Z_{c,\text{MTL}2,2}^{\text{HF}}} \end{bmatrix}, \quad (5.31a)$$

$$\lim_{Z_{L1,2} \rightarrow \infty} [\Gamma_{\text{MTL},1}] = \begin{bmatrix} 1 & -\frac{2Z_{c,\text{MTL}1,1}^{\text{HF}}}{Z_{L2,1} + Z_{c,\text{MTL}2,1}^{\text{HF}}} \\ 0 & \frac{Z_{L2,1} - Z_{c,\text{MTL}2,1}^{\text{HF}}}{Z_{L2,1} + Z_{c,\text{MTL}2,1}^{\text{HF}}} \end{bmatrix}, \quad (5.31b)$$

$$\lim_{Z_{L2,1} \rightarrow \infty} [\Gamma_{\text{MTL},1}] = \begin{bmatrix} \frac{Z_{L1,2} - Z_{c,\text{MTL}1,2}^{\text{HF}}}{Z_{L1,2} + Z_{c,\text{MTL}1,2}^{\text{HF}}} & 0 \\ -\frac{2Z_{c,\text{MTL}2,2}^{\text{HF}}}{Z_{L1,2} + Z_{c,\text{MTL}1,2}^{\text{HF}}} & 1 \end{bmatrix}, \quad (5.31c)$$

$$\lim_{Z_{L2,2} \rightarrow \infty} [\Gamma_{\text{MTL},1}] = \begin{bmatrix} \frac{Z_{L1,1} - Z_{c,\text{MTL}1,1}^{\text{HF}}}{Z_{L1,1} + Z_{c,\text{MTL}1,1}^{\text{HF}}} & 0 \\ -\frac{2Z_{c,\text{MTL}2,1}^{\text{HF}}}{Z_{L1,1} + Z_{c,\text{MTL}1,1}^{\text{HF}}} & 1 \end{bmatrix}. \quad (5.31d)$$

The $2n \times 2n$ propagation matrix $[D_{\text{MTL}}]$ is given equal to Eq. (4.43).

$$[D_{\text{MTL}}] = \begin{bmatrix} -[\Gamma_{\text{MTL},1}] & e^{\gamma l_i} [\mathbb{1}] \\ e^{\gamma l_i} [\mathbb{1}] & -[\Gamma_{\text{MTL},2}] \end{bmatrix}. \quad (5.32)$$

In Eq. (5.29), the main diagonal elements of the respective reflection coefficient matrix can be determined by

$$\Gamma_{n,n} = \begin{cases} 1 & \text{if node: } Z_L \mapsto \infty, \\ \frac{Z_L - Z_{c,\text{MTL},i}^{\text{HF}}}{Z_L + Z_{c,\text{MTL},i}^{\text{HF}}} & \text{else.} \end{cases} \quad (5.33)$$

This means, that at a node the voltage wave is fully reflected and at the beginning or end of the line there is the individual reflection with the load impedance $Z_{L,i}$.

5.3 Validation of the Model

To validate the model, the results are first compared with simulations of the MoM and then with measurements inside the reverberation chamber. A multiconductor transmission line consisting of two wires above a conductive ground plane as shown in Fig. 5.7 was chosen. The length of the line were 50 cm and both wires were located at a height of $h = 3$ cm over the conductive ground plane.

5.3.1 Validation Using the Method of Moments

First, a multiconductor transmission line as explained in the previous section was simulated with the MoM. The dimensions of the two-wire multiconductor transmission line as shown

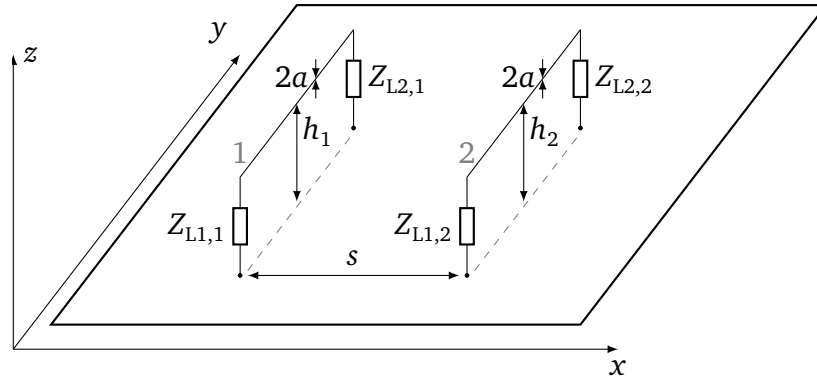


Figure 5.7: Geometry of a uniform two-wire transmission line at the height h over a perfectly conductive ground plane. The lines are terminated with the termination impedances at the beginning with $Z_{L1,1}$ and $Z_{L1,2}$ and at the end with $Z_{L2,1}$ and $Z_{L2,2}$.

in Fig. 5.7 were as follows

$$\begin{aligned} [x_1] &= [x_2] = \begin{bmatrix} 0 \text{ cm} & 1 \text{ cm} \end{bmatrix}, \\ [y_1] &= \begin{bmatrix} 0 \text{ cm} & 0 \text{ cm} \end{bmatrix}, \\ [y_2] &= \begin{bmatrix} 50 \text{ cm} & 50 \text{ cm} \end{bmatrix}, \\ [z_1] &= [z_2] = \begin{bmatrix} 1 \text{ cm} & 1 \text{ cm} \end{bmatrix}. \end{aligned} \quad (5.34)$$

The load resistances for the beginning and end of the lines were chosen as multiples of the characteristic impedances of the two wires

$$[Z_{L1}] = \begin{bmatrix} Z_{c,MTL,1}^{LF} & \infty \\ \infty & 2Z_{c,MTL,2}^{LF} \end{bmatrix} \quad \text{and} \quad [Z_{L2}] = \begin{bmatrix} 0.5Z_{c,MTL,1}^{LF} & \infty \\ \infty & 1.5Z_{c,MTL,2}^{LF} \end{bmatrix}. \quad (5.35)$$

With the exception of the beginning of line 1, the line ends were terminated with a mismatched impedance, which leads to resonances of the transmission line. The elements $Z_{L1,12}$ and $Z_{L1,21}$ as well as $Z_{L2,12}$ and $Z_{L2,21}$ describe here the load impedances between conductors 1 and 2. Because there was no resistance between the two conductors ∞ was chosen for the coupling elements on the minor diagonal in the simulation.

The field strength of the exciting plane wave was set to $E = 1 \frac{\text{V}}{\text{m}}$. The frequency was swept from 0 GHz to 5 GHz in steps of 2 MHz. The exciting plane wave hit the multiconductor transmission line slantingly from above, what means for the phase angle $\beta = 0^\circ$, $\alpha = 315^\circ$, $\vartheta = 135^\circ$, and $\varphi = 225^\circ$ ($\alpha = \vartheta = \varphi = 45^\circ$ in *CONCEPT-II*). The solution simulated by the MoM and the solution derived from the BLT equations (5.28) using the HF p. u. l. parameters is shown in Figure 5.8. Here, the real and imaginary part of the coupled current at the end of the second line $I_{L2,2}$ is displayed. Both simulation results agree considerably well up to 3 GHz. At frequencies above this, there are slight differences between the two simulation results.

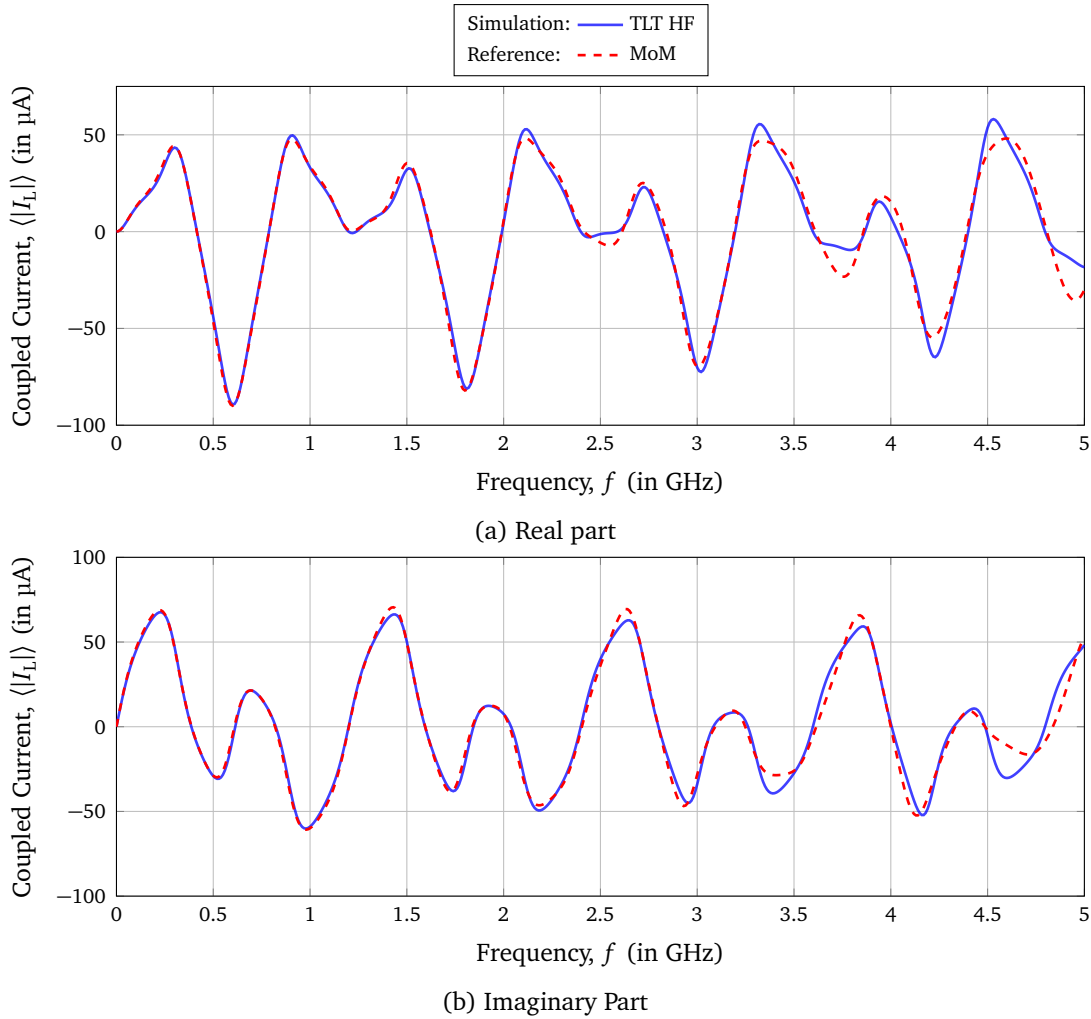


Figure 5.8: Real- and imaginary parts of the coupled current $\langle |I_{L,2}| \rangle$ at the end of the second line of the two-wire multiconductor transmission line over ground as a function of the frequency for the excitation with a single plane wave

The analytical model does not take into account the vertical risers at the beginning and end of the lines, thus the radiation losses and couplings between the vertical and horizontal components are neglected. This simplification can be used to explain differences between the numerical and analytical results. The results for the other terminals and other directions of incidence of the wave also provide an equally good agreement.

5.3.2 Validation Using Measurements in the Reverberation Chamber

For the experimental validation of the presented theory, some measurements were performed in a reverberation chamber. The following measurements were used to determine the influence of the geometry, height of the two lines, terminating resistors and the number of wires of the MTL to the coupled voltage. Again, to reduce the statistical uncertainty, a running average over five adjacent frequencies was calculated for all the following measurement

results. The measurements were done with 72 stirrer positions. In simulations, a higher number of $B = 360$ electromagnetic boundary conditions were chosen, to get simulation results with a lower statistical uncertainty. Each boundary condition consisted of $N = 10$ plane waves.

First, a configuration of the multiconductor transmission line was examined as shown in Fig. 5.9a. The distance s between the two lines of the multiconductor transmission line was 2.5 cm and the heights were $h_1 = h_2 = h = 3$ cm above the ground plane. The heights of the lines were kept constant with small styrofoam blocks. Both lines of the multiconductor wire have the same lengths of $l_1 = l_2 = l = 50$ cm.

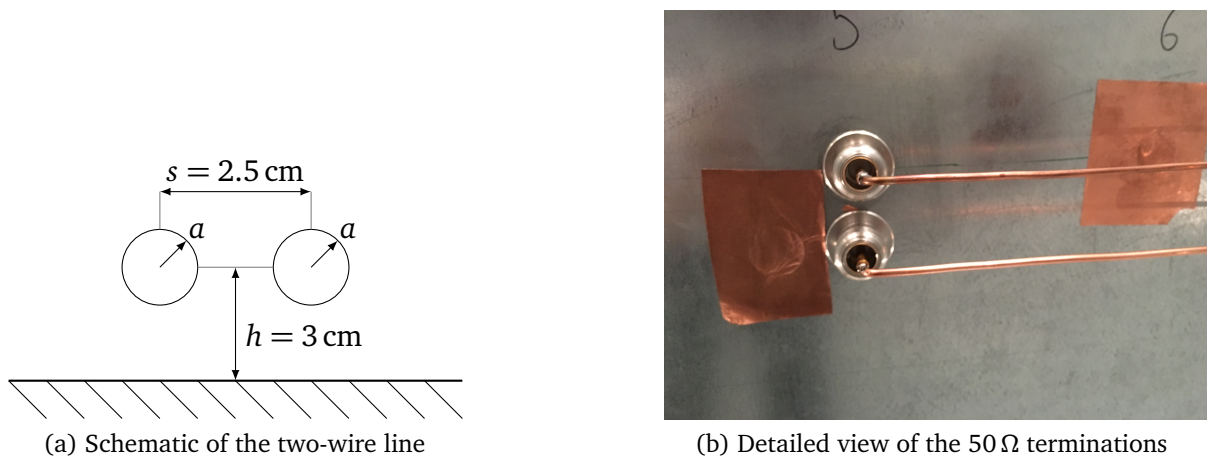


Figure 5.9: Two-wire multiconductor transmission line over a ground plane at the same height of $h_1 = h_2 = h = 3$ cm, $s = 2.5$ cm and a similar radius of $a = 1.12$ mm

As used in Section 3.3.2, plain circular copper wires with a cross section of 4 mm^2 were chosen. In Fig. 5.9b, the closest distance between the two conductors are shown, due to the N feedthroughs that were mounted on the ground plane to connect the coaxial test cables to the ends of the wires. The feedthroughs represent simultaneously a 50Ω -terminating resistance. Thus, the terminating impedances at the beginnings and ends were

$$[Z_{L1}] = \begin{bmatrix} 50 \Omega & \infty \\ \infty & 50 \Omega \end{bmatrix}, \quad [Z_{L2}] = \begin{bmatrix} 50 \Omega & \infty \\ \infty & 50 \Omega \end{bmatrix}. \quad (5.36)$$

These N feedthroughs defined the closest distance d between the lines as shown in Fig. 5.9b.

In Fig. 5.10, the normalized average magnitude of the coupled voltage at the beginnings of the MTL is shown. The normalization to the field strength E_0 and the height h of the lines was done to get a dimensionless quantity, which can be better compared to the simulation results. Due to the same transverse geometry and the same length of the lines, the coupled voltages of both lines show the same characteristics. The measured and simulated curves show good agreement. From transmission line theory resonance frequencies were expected at 300 MHz, 600 MHz and 900 MHz for a 50 cm long line. In Fig. 5.10, the measured resonances have a

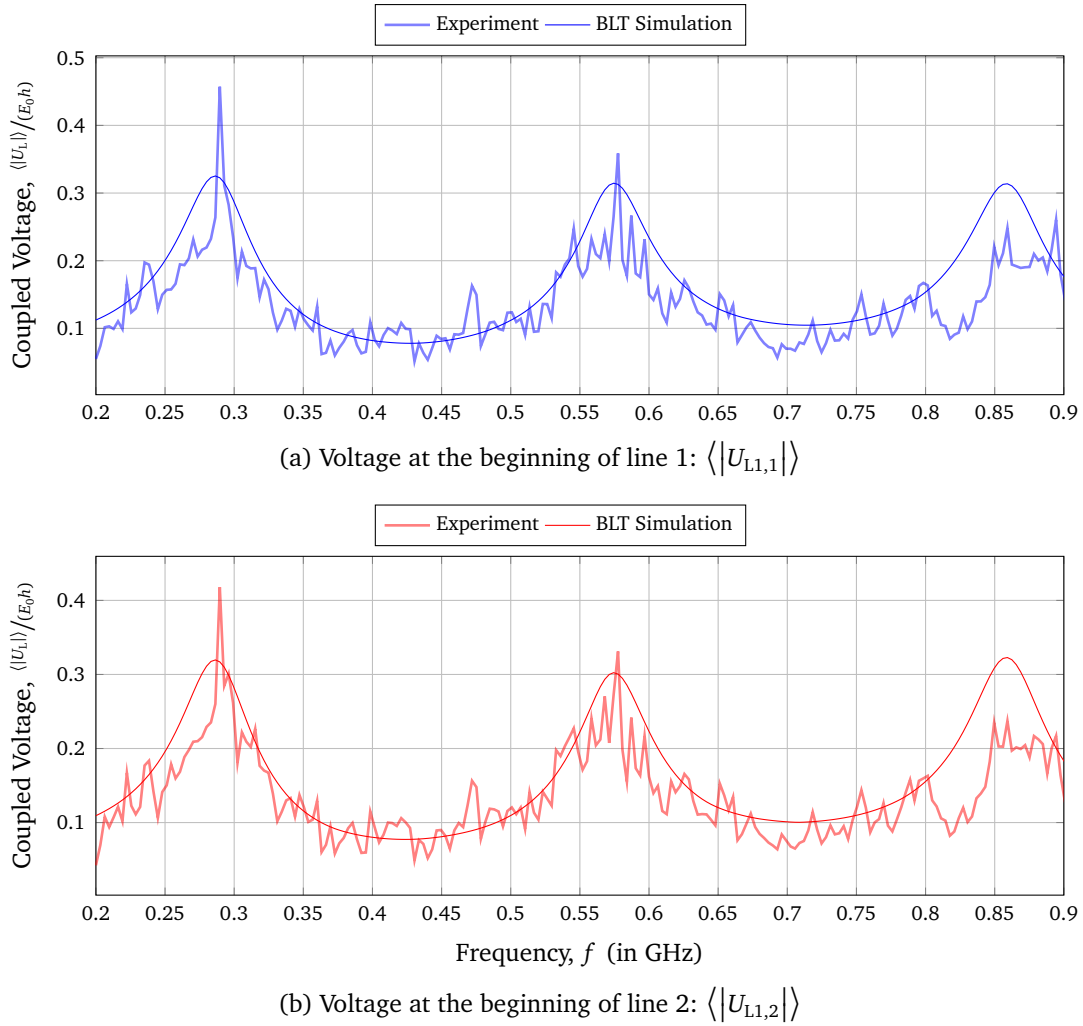


Figure 5.10: Average magnitude of the coupled voltage at the terminals of the two-wire multiconductor transmission line over ground at the same height

little shift and are at about 285 MHz, 570 MHz and 855 MHz. Due to the resonances, the line lengths of the MTL must be adapted in the simulation model to $l = 53$ cm.

5.4 Coupled Voltage as a Function over the Frequency

In the following section, the results of the presented multiconductor transmission line model and the measurements are examined and discussed. The mean magnitude of the coupled terminal voltages of the multiconductor transmission line were investigated. In addition, the configuration of the multiconductor transmission line was changed with respect to its geometry, load resistances and number of wires. In the simulations, the line lengths were set to $l_1 = l_2 = l = l_{\text{meas}} + 2h$, where h is the height of the line, to include the length of the vertical risers.

5.4.1 Different Terminations

In a next step, the influence of the load impedance on the coupled voltage was investigated. For this purpose, an open and short-circuited line end was chosen as a variant in addition to the $50\ \Omega$ termination.

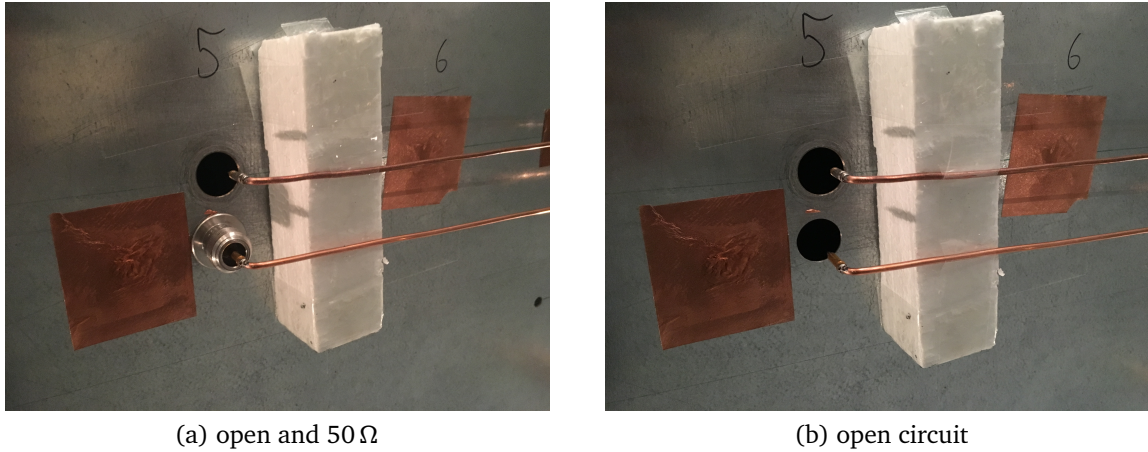


Figure 5.11: Detailed view of the line terminations of the two-wire line

Table 5.1: Variations of the terminating resistances of the multiconductor transmission line while the load impedance $Z_{L1,1}$ is always $50\ \Omega$

$Z_{L2,1}$	$Z_{L1,2}$	$Z_{L2,2}$	Figure	Curve
$50\ \Omega$	$50\ \Omega$	∞	5.12a	—
	∞	$50\ \Omega$	5.12b	—
	∞	∞	5.12c	—
∞	$50\ \Omega$	$50\ \Omega$	5.13	—
	$50\ \Omega$	∞		—
	∞	$50\ \Omega$		—
∞	∞	∞	5.14	—

Because a matched line end cannot be realized over a wide frequency range, a major mismatch was chosen here. Moreover, an open and short-circuited line end was easy to realize in the measurement setup. To create an open circuit, the end of the line was insulated from the ground plane and fixed with a styrofoam block (see Fig. 5.11b). In case of the significant mismatch, strong line resonances are expected. Tab. 5.1 summarizes the different terminating resistor configurations. Photographs of the different configurations are attached in Appendix E. The corresponding results are shown in the following diagrams.

Fig. 5.12 represents the results when the first line had a $50\ \Omega$ termination at the beginning and at the end while the terminations of the second line were varied. The measurement

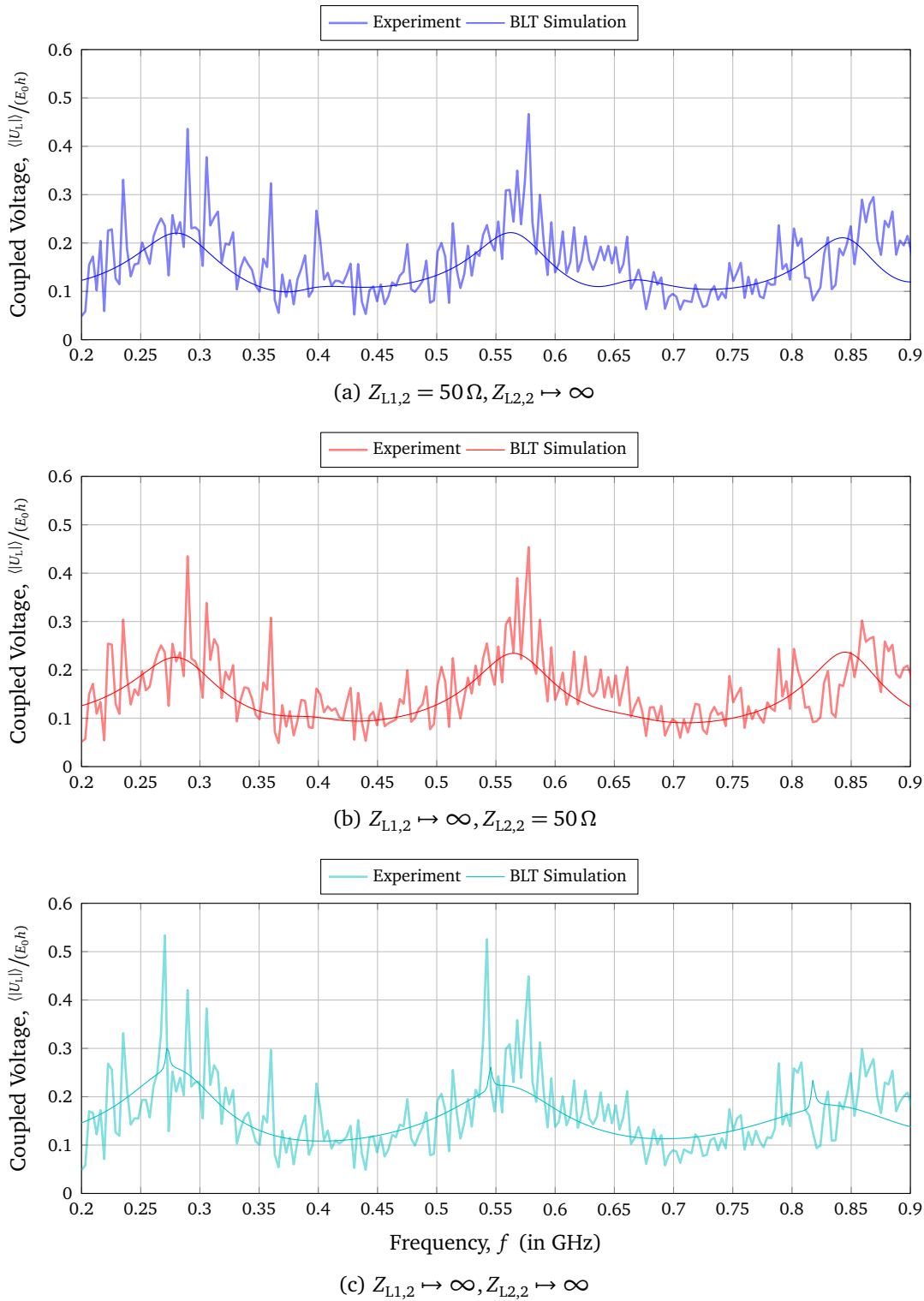


Figure 5.12: Average magnitude of the coupled voltage $\langle |U_{L1,1}| \rangle$ at the beginning of the first line of the two-wire multiconductor transmission line for different terminal configurations, when $Z_{L1,1} = 50 \Omega$ and $Z_{L2,1} = 50 \Omega$

and simulation results show a similar characteristic. In all three cases, strong resonances are visible at approximately 285 MHz, 570 MHz and 855 MHz ($l = \frac{\lambda}{2}, \frac{3}{2}\lambda, \dots$ [MV12]) for the 50Ω terminated end of line 1. These resonances fit to a line length of $l = 53$ cm. In Fig. 5.12a and 5.12b, due to the normalization, the small resonances at about 420 MHz and 690 MHz are not clearly visible. These frequencies depend on an asymmetrically mismatched second line, where the first resonance frequency occurs at $\frac{\lambda}{4}$. The different resonances could be caused by different line lengths in the measurement setup. It seems that in the measuring arrangement the two lines do not have the same length and do not have the same resonance frequencies. Due to the coupling the resonance frequencies of line 2 can be seen on line 1. In the simulations, the second line was adapted to a line length of $l_2 = 58$ cm. In Fig. 5.12c, the second line is kept open at the beginning as well as at the end of the line. Strong peaks occur at about 270 MHz and 540 MHz, which fit to the resonance frequencies of the open circuited second line that are much more peaked because of the completely open line. These frequencies depend on a symmetrically mismatched line, where the first resonance frequency occur at $\frac{\lambda}{2}$. The resulting resonance frequencies for the different line length for an asymmetrical and symmetrical mismatched line are summarized in Tab. 5.2.

Table 5.2: Resonance frequencies for the two-wire multiconductor transmission line over ground for an asymmetrical and symmetrical load mismatch

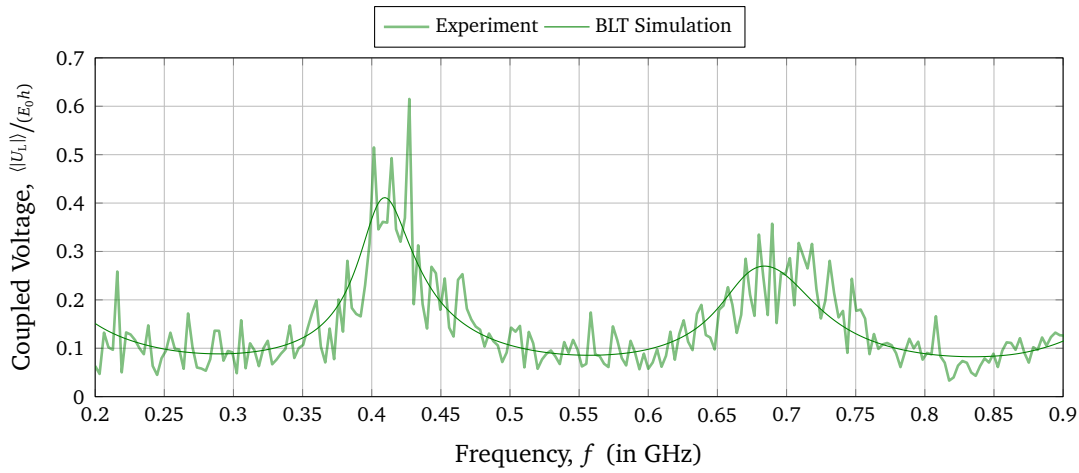
line length	asymmetrical $\frac{\lambda}{4}$	symmetrical $\frac{\lambda}{2}$
53 cm	420 MHz and 690 MHz	285 MHz, 570 MHz and 855 MHz
58 cm	390 MHz and 650 MHz	270 MHz, 540 MHz and 810 MHz

In Fig. 5.13, the coupled voltage at the end of the first line was investigated for different variations of the second line, while $Z_{L2,1} \mapsto \infty$. Resonance frequencies occur at about 420 MHz and 690 MHz for an open end of line 1 (asymmetrically mismatched line, $l = \frac{\lambda}{4}$).

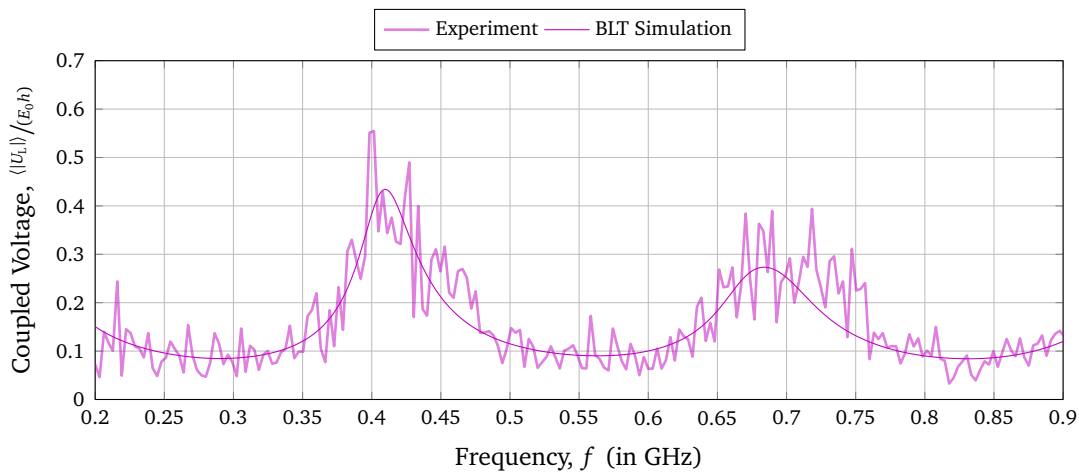
In Fig. 5.14 the results of the coupled voltage for the termination, when except of the beginning of line 1 all line ends are open circuited ($Z_{L1,1} = 50\Omega$ and $Z_{L1,2} = Z_{L2,1} = Z_{L2,2} \mapsto \infty$) are shown. The main resonances occur at about 420 MHz and 690 MHz for an open end of line 1. Additional resonance peaks can be seen at about 270 MHz, 540 MHz and 810 MHz, which fit to the resonance frequencies of the open circuited second line with 58 cm that occur at multiple of $\frac{\lambda}{4}$. This means that only the presence of a wire changes already the field-to-wire coupling behavior. Again, in measurements the additional resonances are much more peaked than in the simulation.

Further Investigations on the Termination Impedances

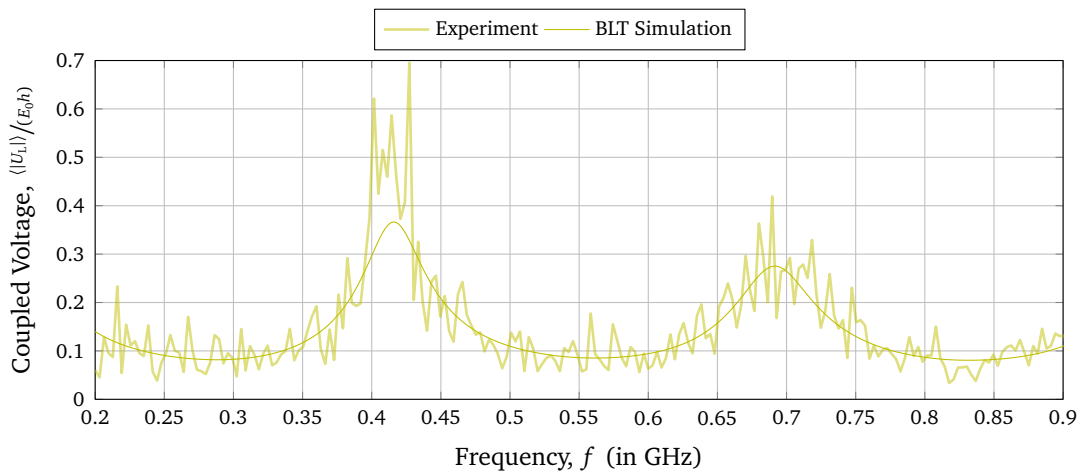
In a next step, further investigations of the load impedances will be carried out using simulations. Here, the same configuration of the multiconductor line was chosen as before. Different configurations for the terminations Z_{L2} at the end of the line were investigated.



(a) $Z_{L1,2} = 50 \Omega, Z_{L2,2} = 50 \Omega$



(b) $Z_{L1,2} = 50 \Omega, Z_{L2,2} \mapsto \infty$



(c) $Z_{L1,2} \mapsto \infty, Z_{L2,2} \mapsto \infty$

Figure 5.13: Average magnitude of the coupled voltage $\langle |U_{L,1}| \rangle$ at the beginning of the first line of the two-wire multiconductor transmission line for different terminal configurations, when $Z_{L1,1} = 50 \Omega$ and $Z_{L2,1} \mapsto \infty$

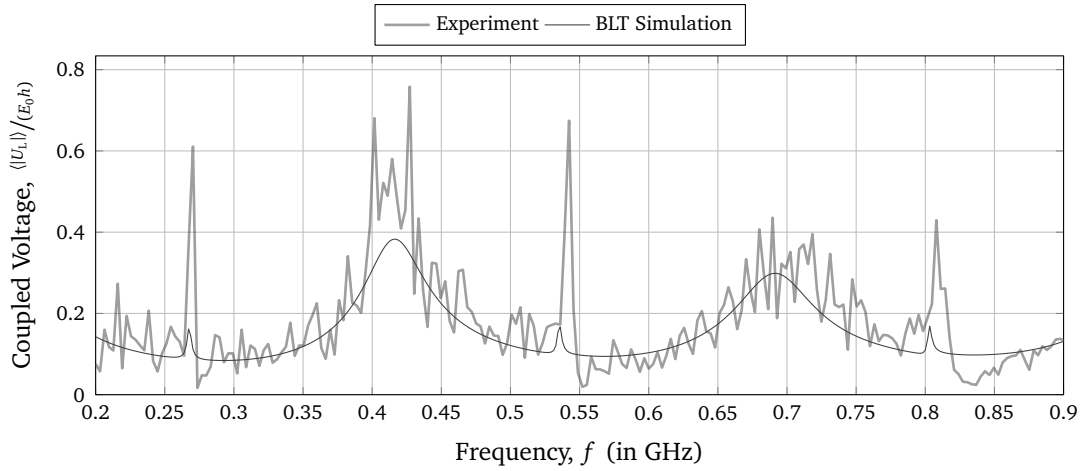


Figure 5.14: Average magnitude of the coupled voltage $\langle |U_{L1,1}| \rangle$ at the beginning of the first line of the two-wire multiconductor transmission line with the terminal impedances of $Z_{L1,1} = 50 \Omega$ and $Z_{L1,2} = Z_{L2,1} = Z_{L2,2} \mapsto \infty$

The load impedance matrix at the beginning of the line was set as follows

$$[Z_{L1}] = \begin{bmatrix} 1 & 1 \\ 1 & 1 \end{bmatrix} \cdot [Z_{c,MTL,1}^{LF}]. \quad (5.37)$$

The loads at the line end are varied as summarized in Tab. 5.3.

Table 5.3: Variations of the terminating resistances of the multiconductor transmission line, which are given as multiples of the characteristic impedance $[Z_{c,MTL,2}^{LF}]$ of the line

Termination Variation	$[Z_{L2}]$	Curve
T-1	$\begin{bmatrix} 1 & 1 \\ 1 & 1 \end{bmatrix} \cdot [Z_{c,MTL,2}^{LF}]$	—
T-2	$\begin{bmatrix} 10 & 10 \\ 10 & 10 \end{bmatrix} \cdot [Z_{c,MTL,2}^{LF}]$	—
T-3	$\begin{bmatrix} \frac{1}{10} & 1 \\ 1 & \frac{1}{10} \end{bmatrix} \cdot [Z_{c,MTL,2}^{LF}]$	—
T-4	$\begin{bmatrix} 1 & \infty \\ \infty & 1 \end{bmatrix} \cdot [Z_{c,MTL,2}^{LF}]$	—

In Fig. 5.15, the normalized coupled voltages at the beginning for the first line for the termination variations according to Tab. 5.3 are shown. It can be observed that a higher

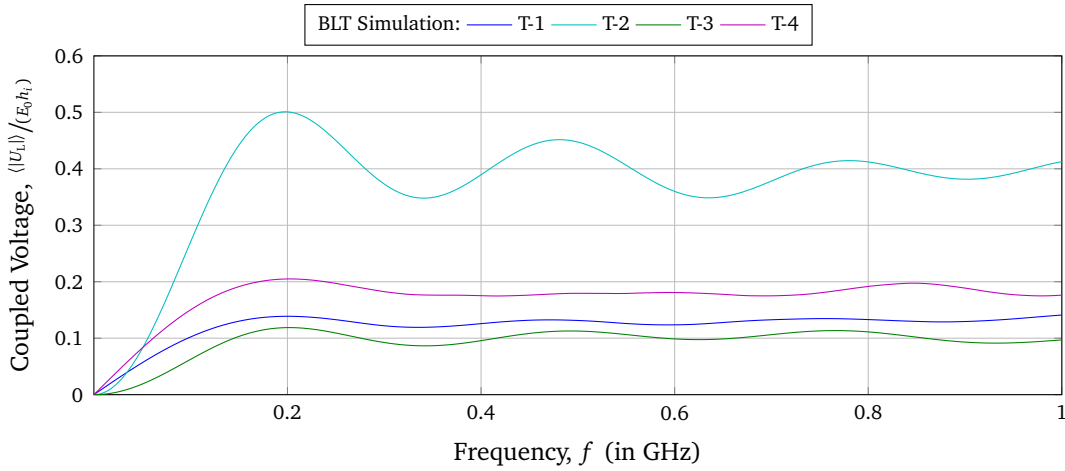


Figure 5.15: Average magnitude of the simulated coupled voltage $\langle |U_{L1,1}| \rangle$ at the beginning of the first line of the two-wire multiconductor transmission line for different terminal configurations given as multiples of Z_c according to Tab 5.3

mismatch leads to more distinct transmission line resonances (T-2). For the matched line (T-1), almost no resonances are visible. This can also be seen from Eq. (5.30b) it should be noted that to eliminate all reflections from the load, the line must be terminated with its characteristic impedance matrix, $[Z_L] = [Z_{c,MTL}^{LF}]$. This is the meaning of a matched line in the multiconductor case. It is not sufficient to place impedances only between each line and the reference conductor. Instead, the impedances must be placed between all pairs of the n lines. The coupled voltage of the two resistance configurations T-1 and T-4 have a similar form. The coupled voltage for the configuration T-4 is higher than for the matched line T-1. This is because in T-4 the conductors are terminated with their characteristic impedance between the conductors and ground and not between the wires.

5.4.2 Variation of the Height

Now, the height of the second line was increased to $h_2 = 5$ cm. Line 1 was still at $h_1 = 3$ cm. Furthermore, the coupling between the lines was investigated by changing the position of the two lines as shown in Fig. 5.16a and 5.16b.

Line 1 was still 50 cm long. Because line 2 was also connected to the N feedthroughs on the ground plane it had to be a little longer $l_2 = 55$ cm (see Fig. 5.17). Each line end was terminated with a load impedance of 50Ω .

The measured and simulated coupled voltages at the beginnings of the lines $\langle |U_{L1,1}| \rangle$ and $\langle |U_{L1,2}| \rangle$ for the MTL with different heights are shown in Fig. 5.18. The measured and simulated curves are in a good match for both configurations, for the wires on top of each other as shown in in Fig. 5.18a as well as the wires next to each other as shown in Fig. 5.18b. In the simulation, the line lengths of the upper wire had to be adjusted to 59 cm because

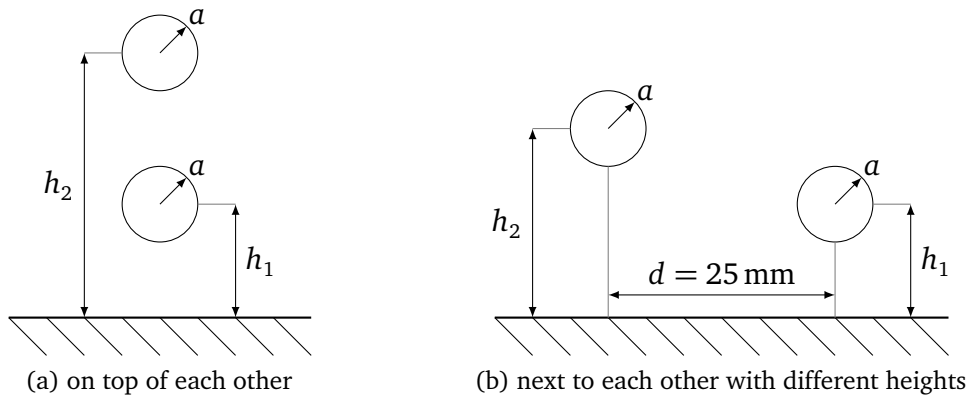


Figure 5.16: Two different arrangements of the of the two-conductor transmission line over a ground plane with different heights of $h_1 = 30$ mm and $h_2 = 50$ mm

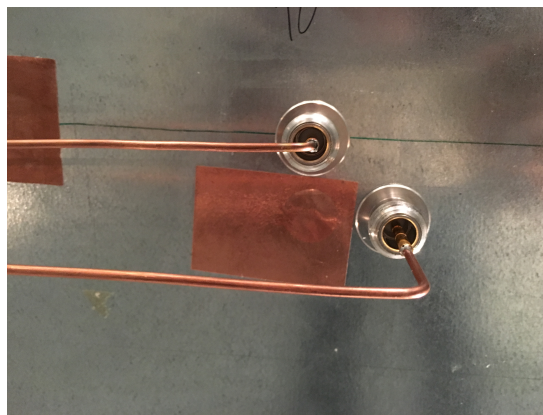


Figure 5.17: Detailed view of the terminations of the measurement setup of the multiconductor transmission line with different heights

the electrical and physical line lengths did not fit. The resonance frequencies of the 59 cm long line expected from transmission line theory are 250 MHz, 500 MHz and 750 MHz. Again, for the 53 cm long line 1, the resonances occur at 285 MHz, 570 MHz and 855 MHz. The advantage of the different line lengths was that both lines show different resonance frequencies and thus the coupling can be seen more clearly. The coupling of the two lines can be recognized by the fact that resonances of line 2 are also found on line 1. Thus, for example, the superposition of the resonances at 500 MHz and 570 MHz is clearly visible in the blue curve. The coupled voltage depends strongly on the height of the lines. Because of the normalization to the height h , the coupled voltages on the individual lines have the same order of magnitude. The green curve essentially shows only the resonance frequencies of the upper line 2, since the coupled voltage and thus the coupling depends significantly on the height. The field-to-wire coupling is higher to the upper line and thus, the coupling from the upper line to the lower line is higher than vice versa.

Comparing the coupled voltage of the two configurations, they are almost identical. Generally, it can be said that the position in z - and x -direction of the wires to each other has no big

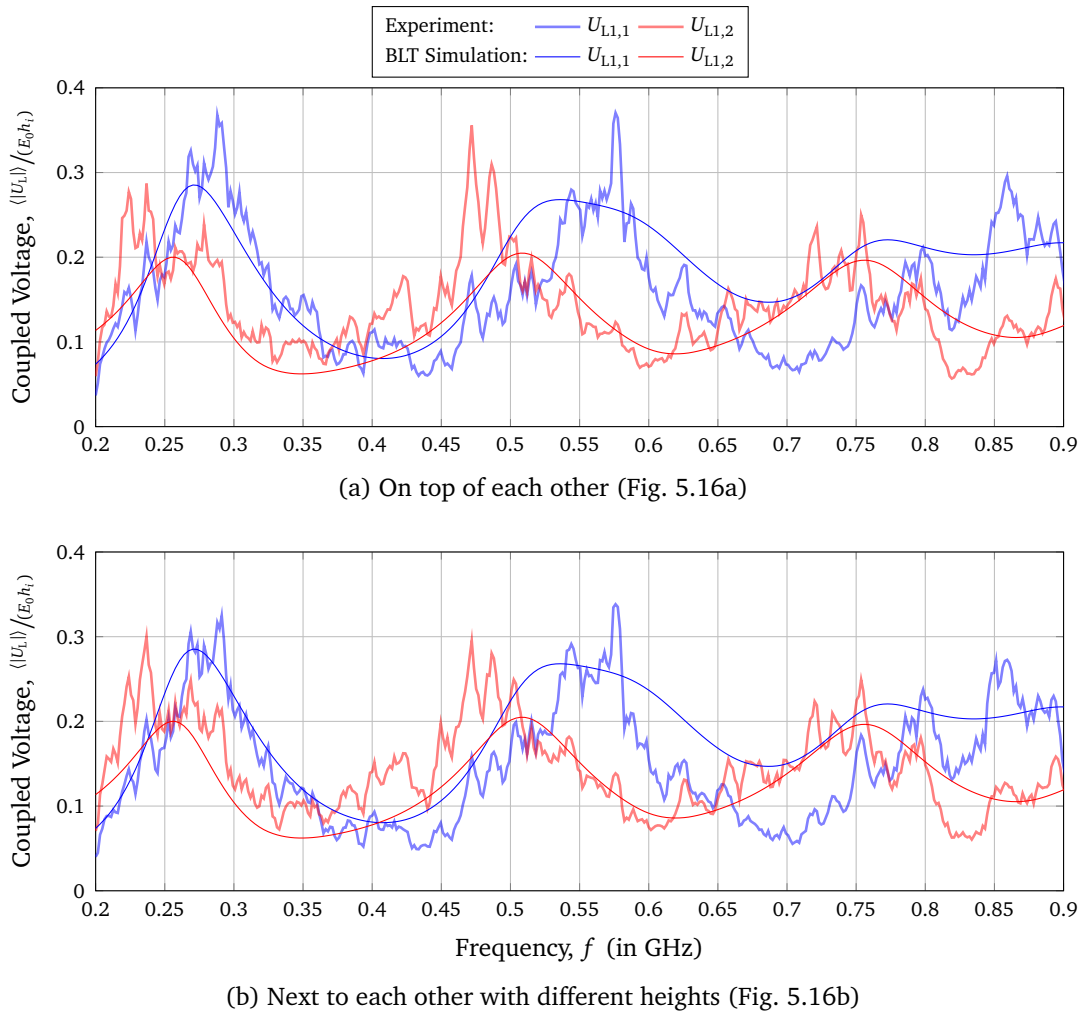


Figure 5.18: Average magnitude of the coupled voltage $\langle |U_{L1}| \rangle$ at the beginnings of the two-conductor multiconductor transmission line with different heights

influence on the coupled voltage, as long as the distance between the lines and to the ground plane remain the same. The distance between the wires and the height above the ground mainly influences the coupled voltage. With a smaller distance between the conductors the coupling would increase.

5.4.3 Variation of the Line Length and Position

For further investigations of the coupling between the lines, the line length and position were varied. These investigations were carried out purely by measurement. Here, three different arrangements as shown in Fig. 5.20 were investigated. Both lines had a distance of 2.5 cm to each other. The line length were kept constant at $l_1 = 70$ cm and $l_2 = 50$ cm. Tab. 5.4 summarizes the different arrangements of the lines.

In Fig. 5.20a, the coupled voltages at the beginnings and at the ends of the lines are shown for arrangement 1 (A-1). From transmission line theory, resonance frequencies were expected

Table 5.4: Variations of the arrangement of the two-wire multiconductor transmission line

Arrangement	$[y_1]$	$[y_2]$	Figure
A-1	[0 cm, 0 cm]	[70 cm, 50 cm]	5.20a
A-2	[0 cm, 10 cm]	[70 cm, 60 cm]	5.20b
A-3	[0 cm, -10 cm]	[70 cm, 40 cm]	5.20c

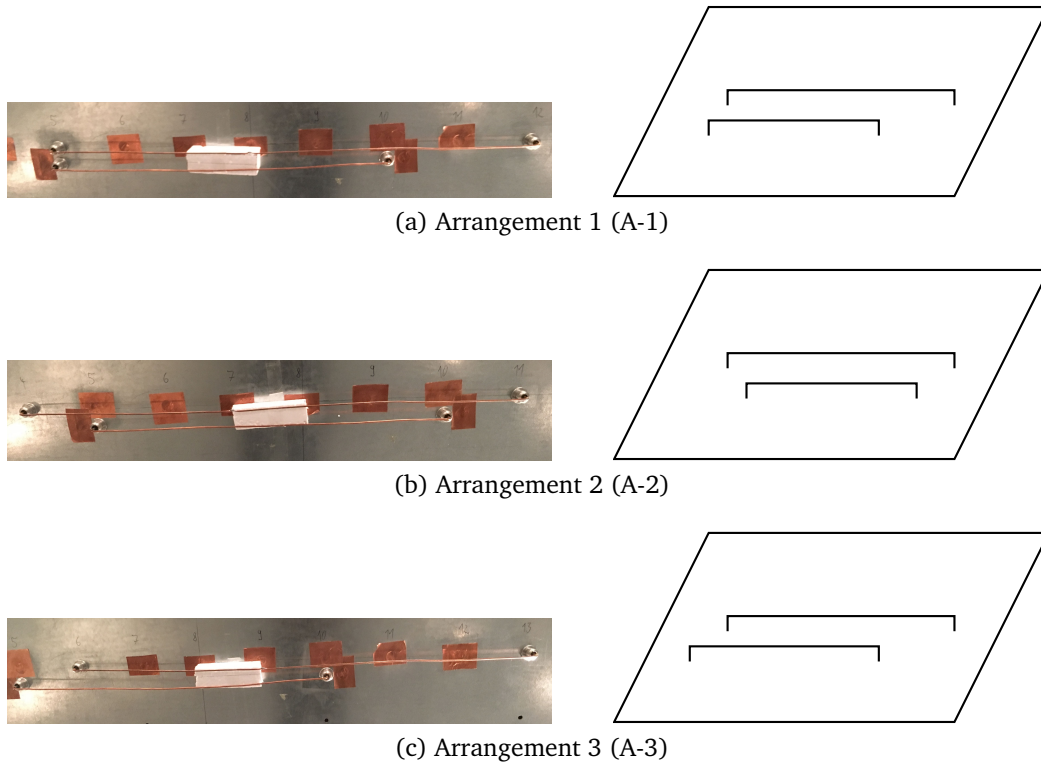
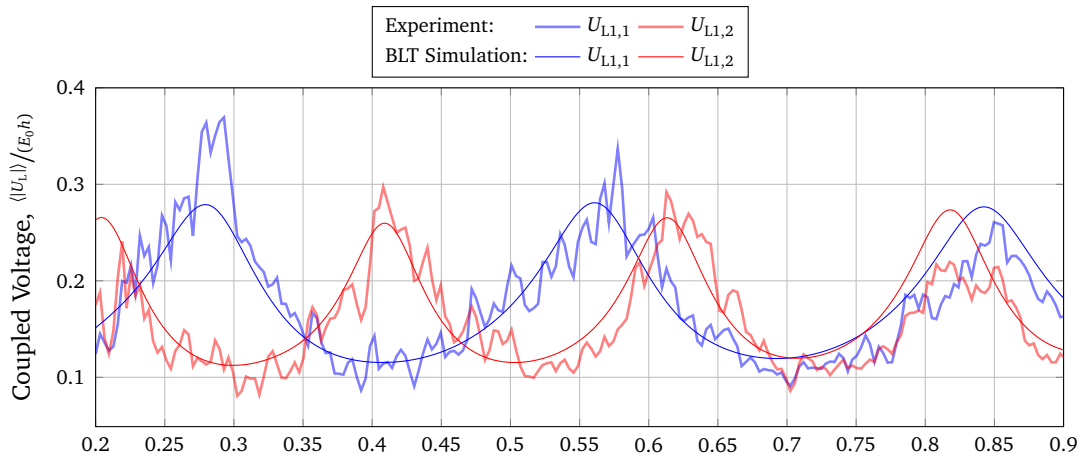


Figure 5.19: Different arrangements of the two-wire multiconductor transmission line with different line lengths of $l_1 = 70$ cm and $l_2 = 50$ cm

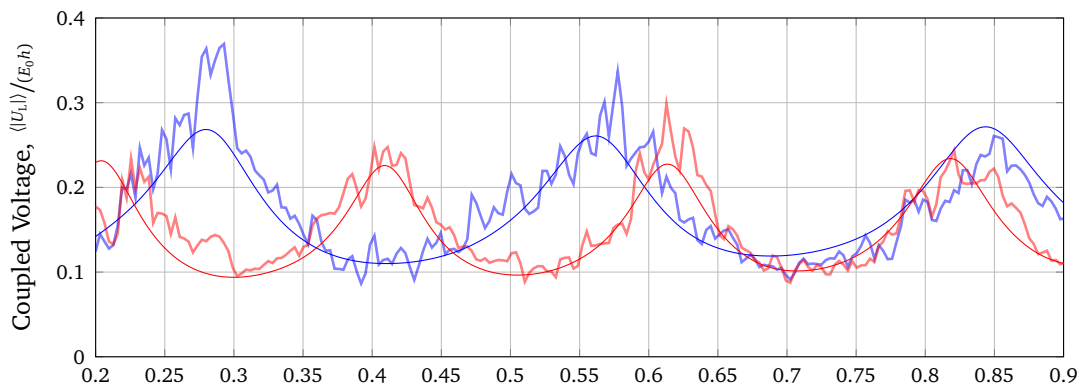
at about 214 MHz, 428 MHz, 624 MHz and 856 MHz for the 70 cm long line and at about 300 MHz, 600 MHz and 900 MHz for the 50 cm long line. One can see resonances at about 283 MHz, 566 MHz and 850 MHz (blue curve). That means that the electrical line length in simulation had to be adapted to 53 cm.

Now, the second line was shifted to the middle of the first line and the lines are arranged symmetrically. The beginning and end of the lines had the same distance from each other. In Fig. 5.20b, the same characteristics like in Fig. 5.20a can be seen. The same resonance frequencies occur. From this investigation it can be concluded that the transverse location of the two line has no influence on the resonance frequencies.

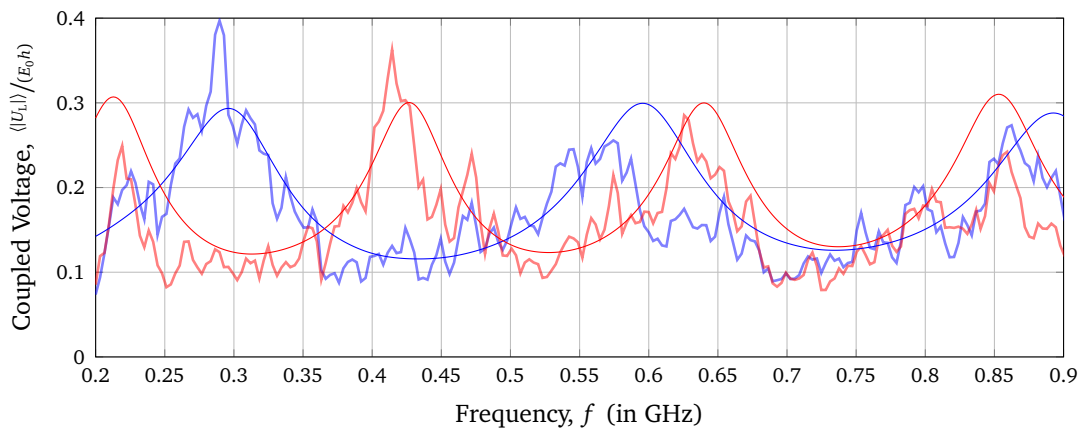
In the first two cases, the starting point of the second line was at the level of the first line. Now the question arises whether the results will change if the start of the second line was outside of the first line. Therefore, as shown in Fig. 5.19c, the start of the second line was now moved. The curves show the same characteristics as the two cases before. Nevertheless, the amplitudes in the resonances for arrangement A-3 are the highest compared to A-1 and



(a) Arrangement 1 (Fig. 5.19a)



(b) Arrangement 2 (Fig. 5.19b)



(c) Arrangement 3 (Fig. 5.19c)

Figure 5.20: Average magnitude of the coupled voltage $\langle |U_{L1}| \rangle$ at the beginnings of the two-conductor transmission line for different wire arrangements (Fig. 5.20)

A-2. Although only minimal, a difference can be noticed. Especially $\langle |U_{L1,2}| \rangle$ shows higher values compared to arrangements A-2 and A-3. In the third measurement setup A-3, the overlapping of the lines is the smallest, which means that the shielding effect against each other is the lowest and therefore the coupling is the strongest.

5.4.4 Three-Wire Multiconductor Transmission Line

In the next experimental setup, it was investigated how the number of wires influences the coupled voltage. Therefore, a three-wire transmission line was set up as shown in Fig. 5.21. The three lines were arranged in an isosceles triangle over the ground plane with the heights $h_1 = h_2 = 3$ cm and $h_3 = 5.5$ cm. The lines had a line length of $l_1 = 50$ cm, $l_2 = 50$ cm and $l_3 = 55$ cm and a radius of each line of $a = 1.12$ mm. As previously in Sec. 5.4.2, the top line was longer than the bottom lines. All wire beginnings and ends were terminated with a 50Ω resistance.

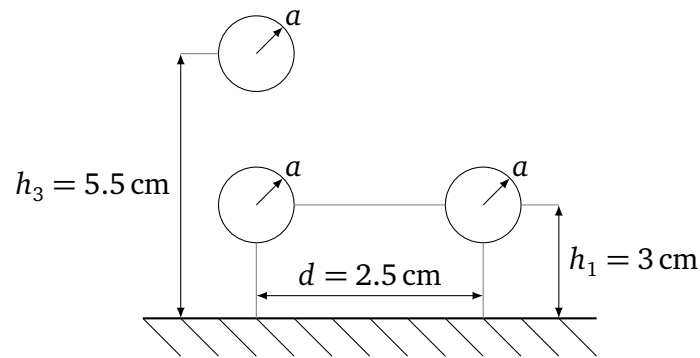


Figure 5.21: Schematic of the three-wire transmission line arranged in an isosceles triangle over a ground plane

In Fig. 5.22, the simulated and measured mean magnitude of the coupled voltage at each beginning of the three lines $\langle |U_{L1,1}| \rangle$, $\langle |U_{L1,2}| \rangle$ and $\langle |U_{L1,3}| \rangle$ are presented. Except for the first resonance of line 1 and 2 the measured and simulated results show a good agreement. The expected resonances for line 1 and 2 for the 53 cm long line occur at about 283 MHz, 566 MHz and 850 MHz. Both measured curves show a similar behavior. In the simulation results, there are small differences between line 1 and 2. The 59 cm long third line showed resonances at about 250 MHz, 500 MHz and 750 MHz. Due to the coupling the resonances of the third line can also be seen on the coupled voltage of line 1 and 2. The simulation model predict a higher coupling especially for the first resonance frequency. It is interesting that the third line seems to influence the coupled voltage in line 1 and line 2 equally. Although there is 2.5 cm distance between lines 2 and 3 and 3.5 cm distance between lines 1 and 3. The difference of 1 cm seems marginal in this measurement setup.

By extending the measurement to a three-wire line, the model could also be validated for

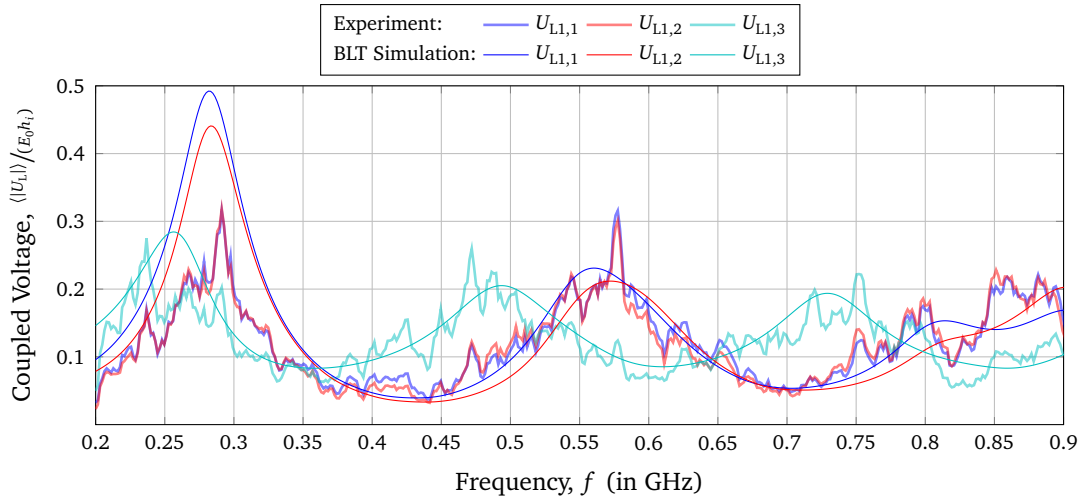


Figure 5.22: Average magnitude of the coupled voltage $\langle |U_{L1}| \rangle$ at the terminals of a three-wire multiconductor transmission line over a conductive ground plane

this configuration. It can be concluded that the simulation model can be applied to any number of wires above the ground plane.

5.4.5 Comparison with a single conductor transmission line

Comparing the field-to-wire coupling between single and multiconductor transmission line structures over ground in Fig. 5.23 shows that if the structures have the same transverse dimensions and load impedances, the amplitude of the coupled voltage are similar. The reason for the different resonance frequencies is that the single wire is twice as long as the multiconductor line. This applies if all lines of the multiconductor line have the same termination and the same length. If these factors are changed, couplings between the conductors can occur even in quite simple structures such as those investigated in this thesis.

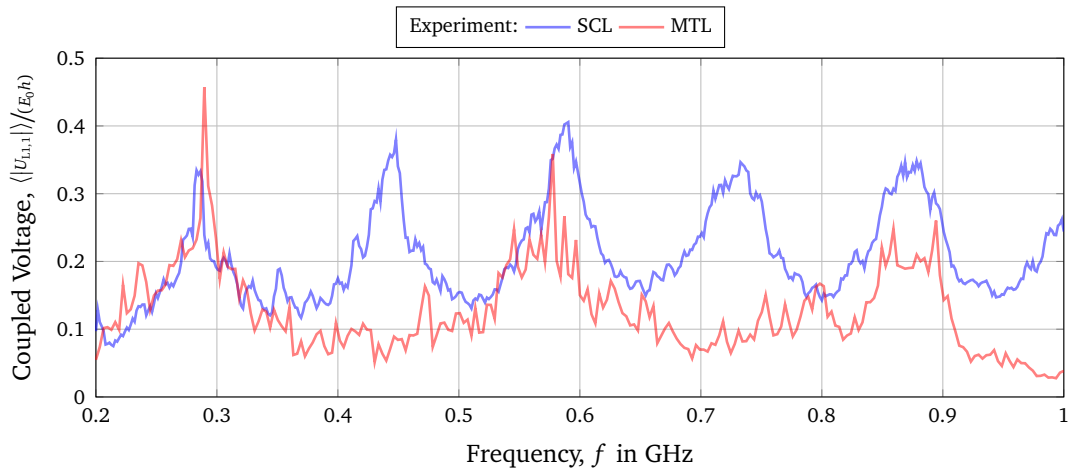


Figure 5.23: Comparison of the average magnitude of the simulated coupled voltage of the 1 m single conductor transmission line (SCL) and the 50 cm multiconductor transmission line over ground (MTL)

5.5 Comparison with an Isolated Multiconductor Transmission Line

In the next step, the previous results for a MTL above a conductive ground are to be compared with the results of an isolated multiconductor transmission line (IMTL). In particular, the multiconductor transmission line is far away from a conducting wall or earth. Fig. 5.24 depicts an isolated multiconductor transmission line structure. Such cable generally consists of n conductors and a reference conductor. Isolated multiconductor structures have practical relevance and such a representation is used to model e. g. cable bundles or ribbon cables.

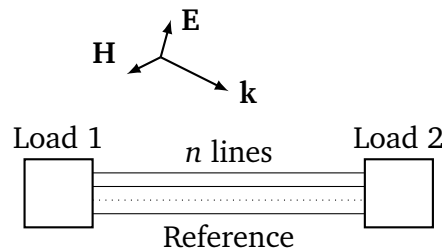


Figure 5.24: Example of an isolated multiconductor transmission line with $n + 1$ wires

5.5.1 Transmission Line Model

To consider an isolated multiconductor transmission line excited by an external electromagnetic field, a system of $n + 1$ uniform wires must be modeled. This multiconductor structure can be made from several single wire lines as shown in Fig. 5.25. The beginning and end coordinates of each line are at $(x_{1,i}, y_{1,i}, z_{1,i})$ and $(x_{2,i}, y_{2,i}, z_{2,i})$ and each wire has a radius of a_i . Again, i represents the line number. The reference conductor has the number $i = 0$. Fig. 5.25a shows the isometric perspective of the three-wire transmission line with their line terminations $[Z_{L1}]$ at the beginnings and $[Z_{L2}]$ at the ends.

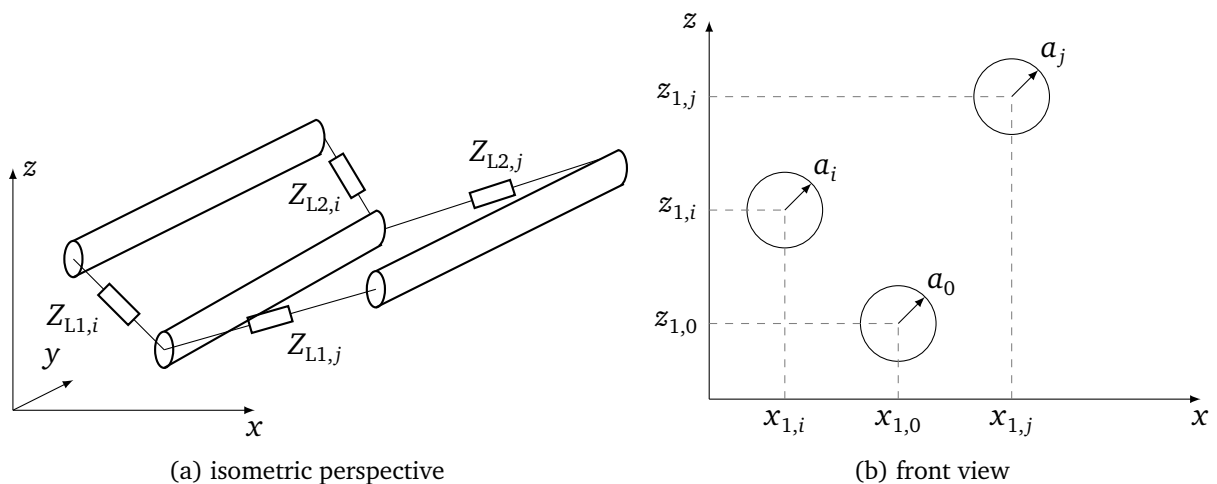


Figure 5.25: Schematic of an isolated multiconductor transmission line with $n + 1$ conductors

For the determination of the p. u. l. parameters of the multiconductor transmission line, it is assumed that the lines are directed in y direction. As introduced in Section 5.1, the field-to-wire coupling equations become the same form as in Eq. (5.2)

$$\frac{dU_i^s(y)}{dy} + j\omega \frac{\mu}{4\pi} \sum_{j=1}^n I_j(y) \int_0^l g(y_i - y'_j) dy' = E_{\tan, \text{IMTL}}^e(z_i, y), \quad (5.38a)$$

$$\frac{d}{dy} \sum_{j=1}^n I_j(y) \int_0^l g(y_i - y'_j) dy' + j\omega 4\pi\epsilon U_i^s(y) = 0. \quad (5.38b)$$

Again, the field-to-wire coupling equations from Eq. (5.38) can be put in a matrix notation

$$\frac{d}{dy} [U_i^s(y)] + j\omega \frac{\mu}{4\pi} [G_{\text{IMTL}}][I(y)] = [E_{\tan, \text{IMTL}}^e], \quad (5.39a)$$

$$\frac{d}{dy} [I(y)] + j\omega 4\pi\epsilon [G_{\text{MTL}}]^{-1} [U(y)] = 0. \quad (5.39b)$$

Similar to the multiconductor transmission line over ground, in order to evaluate the integral of the Green's function, two cases are distinguished:

1. $i = j$: The effect of the wire itself is considered and the Green function represents the self-induced voltages of wire i . This case is similar to a double wire line.
2. $i \neq j$: The coupling between the wires is considered and the Green function represents the mutual coupling between wire i and j .

For an isolated multiconductor transmission line as shown in Fig. 5.25b, the scalar Green's function becomes

$$g(y_i - y'_j) = \frac{e^{-jk|\mathbf{r} - \mathbf{r}'_0|}}{|\mathbf{r} - \mathbf{r}'_0|} + \frac{e^{-jk|\mathbf{r}_i - \mathbf{r}'_j|}}{|\mathbf{r}_i - \mathbf{r}'_j|} - \frac{e^{-jk|\mathbf{r} - \mathbf{r}'_j|}}{|\mathbf{r} - \mathbf{r}'_j|} - \frac{e^{-jk|\mathbf{r} - \mathbf{r}'_i|}}{|\mathbf{r} - \mathbf{r}'_i|} \quad (5.40)$$

Inserting the distances results in

$$\begin{aligned} g(y_i - y'_j) = & \frac{e^{-jk\sqrt{(z-z'_0)^2+(y-y'_0)^2+(x-x'_0)^2}}}{\sqrt{(z-z'_0)^2+(y-y'_0)^2+(x-x'_0)^2}} \\ & + \frac{e^{-jk\sqrt{(z_i-z'_j)^2+(y_i-y'_j)^2+(x_i-x'_j)^2}}}{\sqrt{(z_i-z'_j)^2+(y_i-y'_j)^2+(x_i-x'_j)^2}} \\ & - \frac{e^{-jk\sqrt{(z-z'_i)^2+(y-y'_i)^2+(x-x'_i)^2}}}{\sqrt{(z-z'_i)^2+(y-y'_i)^2+(x-x'_i)^2}} \\ & - \frac{e^{-jk\sqrt{(z-z'_j)^2+(y-y'_j)^2+(x-x'_j)^2}}}{\sqrt{(z-z'_j)^2+(y-y'_j)^2+(x-x'_j)^2}}. \end{aligned} \quad (5.41)$$

For a simplified and shorter representation some variables s_i , s_j and s_{ij} are introduced

$$g(y_i - y_j) = \frac{e^{-jk\sqrt{a_0^2 + (y - y_0')^2}}}{\sqrt{a_0^2 + (y - y_0')^2}} + \frac{e^{-jk\sqrt{s_{ij}^2 + (y_i - y_j')^2}}}{\sqrt{s_{ij}^2 + (y_i - y_j')^2}} - \frac{e^{-jk\sqrt{s_i^2 + (y - y_i')^2}}}{\sqrt{s_i^2 + (y - y_i')^2}} - \frac{e^{-jk\sqrt{s_j^2 + (y - y_j')^2}}}{\sqrt{s_j^2 + (y - y_j')^2}}. \quad (5.42)$$

Again, the assumptions are made that the observation point is far enough away from the ends of the wires and the current is locally constant. Thus, the limits of integration can be extended to $-\infty$ to $+\infty$ and the current can be put in front of the integral. With [RT08] and [NT04], the integrals can be solved

$$\int_{-\infty}^{+\infty} g(y_j - y_j') dy' = j\pi H_0^{(2)}(-ka_0) + j\pi H_0^{(2)}(-ks_{ij}) - j\pi H_0^{(2)}(-ks_i) - j\pi H_0^{(2)}(-ks_j). \quad (5.43)$$

By the use Eq. (3.14), Eq (5.43) can be rewritten as

$$\int_{-\infty}^{+\infty} g(y_i - y_j') dy' = \pi [J_0(s_i k) + J_0(s_j k) - J_0(a_0 k) - J_0(s_{ij} k)] \quad (5.44)$$

$$+ j\pi [Y_0(s_i k) + Y_0(s_j k) - Y_0(a_0 k) - Y_0(s_{ij} k)]. \quad (5.45)$$

If the expansion form of the Bessel function of J_0 as described in Eq. (3.20) is used, then after some mathematical rearrangements Eq. (5.43) can be rewritten as follows

$$\int_{-\infty}^{+\infty} g(y_i - y_j') dy' = 2 \ln \left(\frac{s_i s_j}{s_{ij} a_0} \right) + C_{\text{IMTL}}^F. \quad (5.46)$$

All frequency dependent terms are summarized to a correction factor C_{IMTL}^F .

Interaction between the Wire and the Reference Conductor

The calculation of the integral of the Green's function for the interaction between a wire i and the reference conductor yields to

$$G_{\text{IMTL},ii} = G_{\text{IMTL},ii}^{\text{LF}} + C_{\text{IMTL},ii}^F, \quad (5.47)$$

where $C_{\text{IMTL},ii}^F$ is the correction factor and $G_{\text{IMTL},ii}^{\text{LF}}$ is the classical transmission line approximation given by

$$G_{\text{IMTL},ii}^{\text{LF}} = 2 \ln \left(\frac{s_i^2}{a_0 a_i} \right). \quad (5.48)$$

Here,

$$s_i = \sqrt{(z_0 - z_i)^2 + (x_0 - x_i)^2} \quad (5.49)$$

is the distance between the i th line and the reference wire. The correction factor $C_{\text{IMTL},ii}^{\text{F}}$ is determined by substituting s_j with s_i and s_{ij} with a_i in Eq. (5.46).

Interaction between the Wires

The solution of the Green function integral for the interaction between wire i and j gives an expression similar to Eq. (5.47)

$$G_{\text{IMTL}ij} = G_{\text{IMTL},ij}^{\text{LF}} + C_{\text{IMTL},ij}^{\text{F}}, \quad (5.50)$$

where $C_{\text{IMTL},ij}^{\text{F}}$ is the correction factor and the expression

$$G_{\text{IMTL},ij}^{\text{LF}} = 2 \ln \left(\frac{s_i s_j}{a_0 s_{ij}} \right) \quad (5.51)$$

is the low frequency approximation of the Green's function integral as used in classical transmission line theory. Here, s_j is the distance from the j th wire to the reference conductor

$$s_j = \sqrt{(z_0 - z_{1,j})^2 + (x_0 - x_{1,j})^2} \quad (5.52)$$

and s_{ij} describes the distance between the two wires

$$s_{ij} = \sqrt{(z_{1,i} - z_{1,j})^2 + (x_{1,i} - x_{1,j})^2}. \quad (5.53)$$

The correction factor $C_{\text{IMTL}ij}^{\text{F}}$ can be obtained by substituting s_i , s_j , a_0 and s_{ij} .

Impedance and Admittance Matrix

The Green's function matrix $[G_{\text{IMTL}}]$ in Eq. (5.39) can be inserted in a general matrix

$$[G_{\text{IMTL}}] = [G_{\text{IMTL}}^{\text{LF}}] + [C_{\text{IMTL}}^{\text{F}}], \quad (5.54)$$

where $[G_{\text{IMTL}}^{\text{LF}}]$ describe the classical Green function integral and $[C_{\text{IMTL}}^{\text{F}}]$ the high frequency correction factor. The high frequency impedance matrix can be written from Eqs. (5.39) and (5.54) as follows

$$[Z_{\text{IMTL}}^{\text{HF}}] = j\omega \frac{\mu}{4\pi} ([G_{\text{IMTL}}^{\text{LF}}] + [C_{\text{IMTL}}^{\text{F}}]). \quad (5.55)$$

From Eqs. (5.4b) and (5.54) follow the high frequency admittance matrix with

$$[Y_{\text{IMTL}}^{\text{HF}}] = j\omega 4\pi\epsilon ([G_{\text{IMTL}}^{\text{LF}}] + [C_{\text{IMTL}}^{\text{F}}])^{-1}. \quad (5.56)$$

Characteristic Impedance Matrix

The characteristic impedance matrix has the same frequency dependency as the p. u. l. parameters and is referred as in Eq. (5.25). Using Eqs. (3.54) and (3.55) results in

$$\left[Z_{c,IMTL}^{HF} \right] = \left[Z_{c,IMTL}^{LF} \right] + \left[C_{IMTL}^F \right], \quad (5.57)$$

with $\left[Z_{c,IMTL}^{LF} \right]$ as classical characteristic impedance matrix given by

$$\left[Z_{c,IMTL}^{LF} \right] = \frac{1}{4\pi} \sqrt{\frac{\mu}{\epsilon}} \left[G_{IMTL}^{LF} \right]. \quad (5.58)$$

In Fig. 5.26, the comparison of the high frequency characteristic impedance matrix elements to the classical ones for an isolated three-wire multiconductor transmission line (IMTL) are shown.

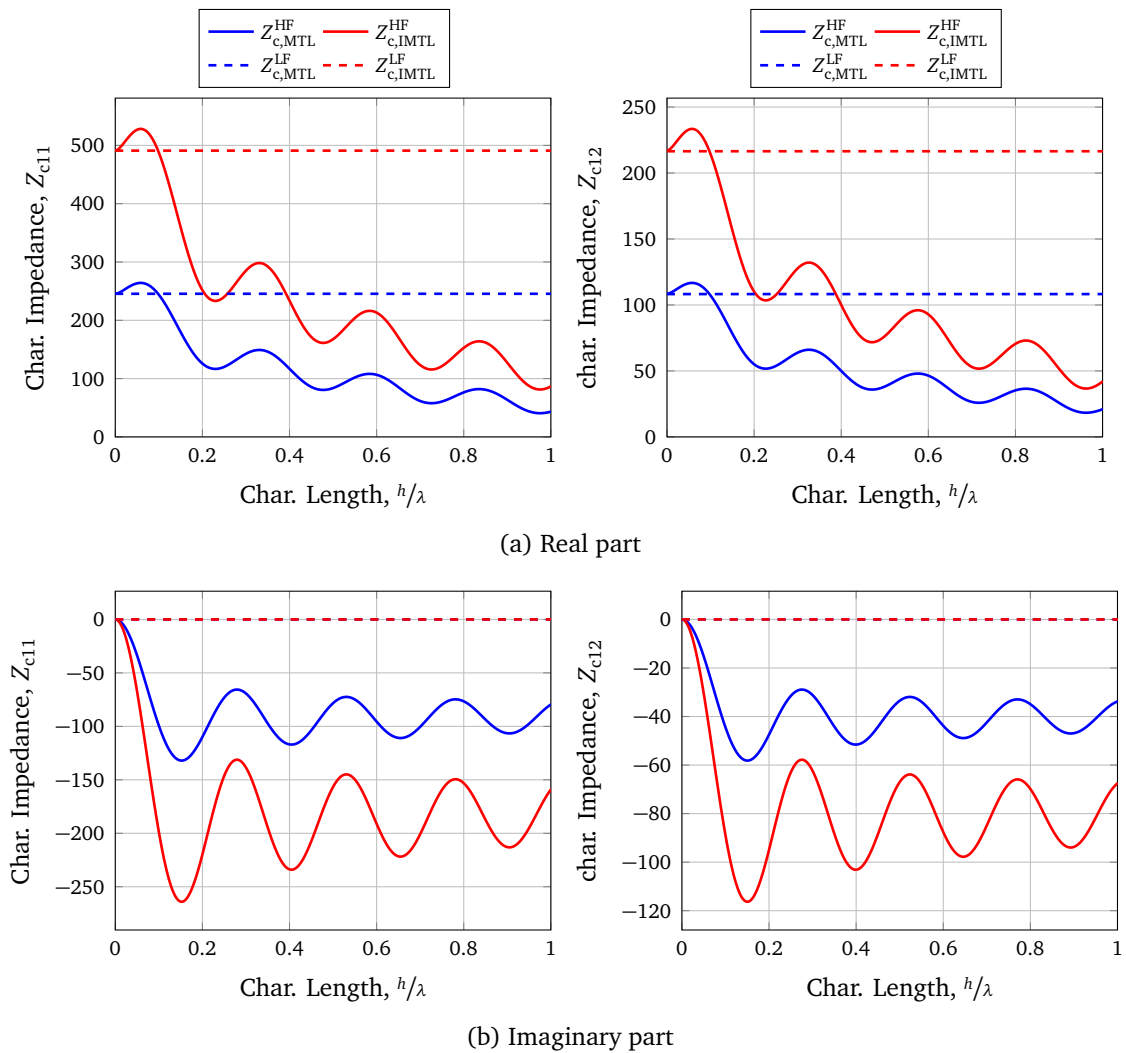


Figure 5.26: Comparison between the classical (LF) and high frequency (HF) characteristic impedance matrix elements for an isolated three-wire multiconductor transmission line

For the investigation of the characteristic impedance, an isolated multiconductor transmission line consisting of three conductors was examined. These conductors formed an equilateral triangle. The distances between the wires and the reference conductor were $s_1 = s_2 = 6$ cm and between the conductors $s_{12} = 6$ cm. The wire radii were 1 mm for each line. Additionally, the results of a multiconductor transmission line over ground (MTL) with the same dimensions are shown in Fig. 5.26. The multiconductor wire over ground had the following dimensions. A height $h_1 = h_2 = \frac{s_1}{2} = 3$ cm, a wire separation of $s = \frac{s_{12}}{2} = 3$ cm and the wires had a radius of $a_1 = a_2 = a = 1$ mm. For these dimensions, the characteristic impedance for the MTL and the IMTL have the following dependence

$$[Z_{c,MTL}^{HF}] = \frac{1}{2} [Z_{c,IMTL}^{HF}]. \quad (5.59)$$

5.5.2 Field-to-Wire-Coupling Equations

Using the frequency dependent characteristic impedance $[Z_{c,IMTL}^{HF}]$ from Eq. (5.57), the stochastic field coupling to an isolated multiconductor transmission line can be examined. The BLT equations to calculate the coupled voltage is here repeated for convenience

$$[U_{L,IMTL}] = \begin{bmatrix} [U_{L1,IMTL}] \\ [U_{L2,IMTL}] \end{bmatrix} = [[\mathbb{1}] + [\Gamma_{IMTL}]] \cdot [D_{IMTL}]^{-1} \cdot \begin{bmatrix} [S_{1,IMTL,i}] \\ [S_{2,IMTL,i}] \end{bmatrix}, \quad (5.60)$$

and are of the same form as for the multiconductor transmission line over ground Eq. (5.28) or the bent wire Eq. (4.38). The formulas for the tangential electric field and the transverse voltage differ from the multiconductor case over a ground plane. The tangential electric field is

$$E_{\tan,IMTL,i}^e = -2jE_{IMTL} e^{j\beta} \mathbf{e} \cdot \mathbf{t}_i \sin\left(k_z \frac{s_i}{2}\right), \quad (5.61)$$

with $E_{IMTL} = E_0/\sqrt{N}$ from Section 3.4.2. The definition of $[\Gamma_{IMTL}]$, $[D_{IMTL}]$ and $[S_{IMTL}]$ are similar to the case of the multiconductor over ground. The transverse voltage is needed to determine $[S_{IMTL}]$. It follows with

$$U_{t1,IMTL,i} = 2E e_z e^{j\beta} r_{1,i} \begin{cases} \frac{s_i}{2} & \text{if } k_z = 0 \\ \frac{\sin(k_z \frac{s_i}{2})}{k_z} & \text{else.} \end{cases} \quad (5.62)$$

5.5.3 Coupled Voltage as Function over the Frequency

Now, the results for an isolated multiconductor transmission line were compared to measurement results in the reverberation chamber. Again, the mean magnitude of the coupled terminal voltages of the multiconductor transmission line were investigated. In addition, the

configuration of the isolated multiconductor transmission line was changed with respect to its geometry, load resistances and line lengths. The investigated multiconductor transmission line consisted of two $l_1 = l_2 = 76$ cm long transmission lines and a reference conductor with the same line length $l_0 = 76$ cm. The wires were unshielded and made from copper with a radius of 0.41 mm. To connect the multiconductor transmission line with the measuring cables a BalUn was used as shown in Fig. 5.27 . It had two terminals with a 50Ω impedance on each terminal. For the three-wire system, the two conductors were connected to the BalUn and the wires were connected to the reference wire.



Figure 5.27: Balancing unit for the measurements with three wires

To include the vertical risers in the simulation, the line lengths were set to $l = l_{\text{meas}} + s$. As in the investigations before, a running average over five adjacent frequencies was performed. The measurements were performed with 72 stirrer positions. For the analytical and *CONCEPT-II* simulation a number of $B = 360$ electromagnetic boundary conditions, each consisting of $N = 10$ plane waves were chosen. The chamber constant was set to $E_0 = 1 \frac{\text{V}}{\text{m}}$.

5.5.3.1 Planar Arrangement

First a planar arrangement of the multiconductor transmission line was examined as shown in Fig. 5.28. To ensure mechanical stability and the distances between the conductors, a metal plate as shown in Fig. 5.28b was used. This plate was used as an adapter for connecting the three-wire system to the BalUn. For this purpose, the two conductors were connected to the terminals of the BalUn and each was terminated with a resistor to the reference conductor. Several holes were provided in the plate to allow different distances of the three-wire system. In this first measurement setup, the distance between the individual lines was $s = 3.2$ cm. This distance was chosen based on the dimensions of the BalUn input ports. The x - and z -coordinates of the line start and end were specified by

$$\begin{aligned} [x_1] = [x_2] &= [0 \text{ mm} \quad 32 \text{ mm} \quad 64 \text{ mm}], \\ [z_1] = [z_2] &= [0 \text{ mm} \quad 0 \text{ mm} \quad 0 \text{ mm}]. \end{aligned} \quad (5.63)$$

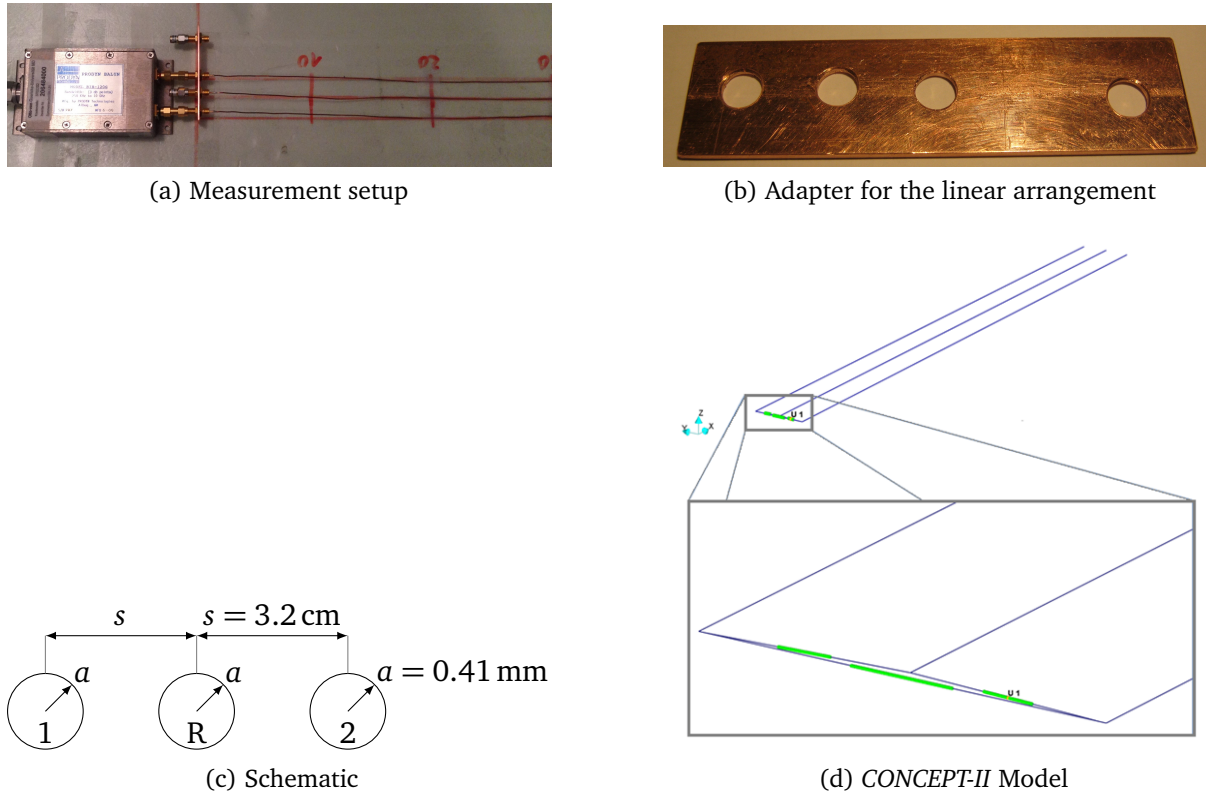


Figure 5.28: Planar arrangement of the isolated three-wire line

To determine the load resistances at the beginning of the line $[Z_{L1}]$, these were determined using a multimeter

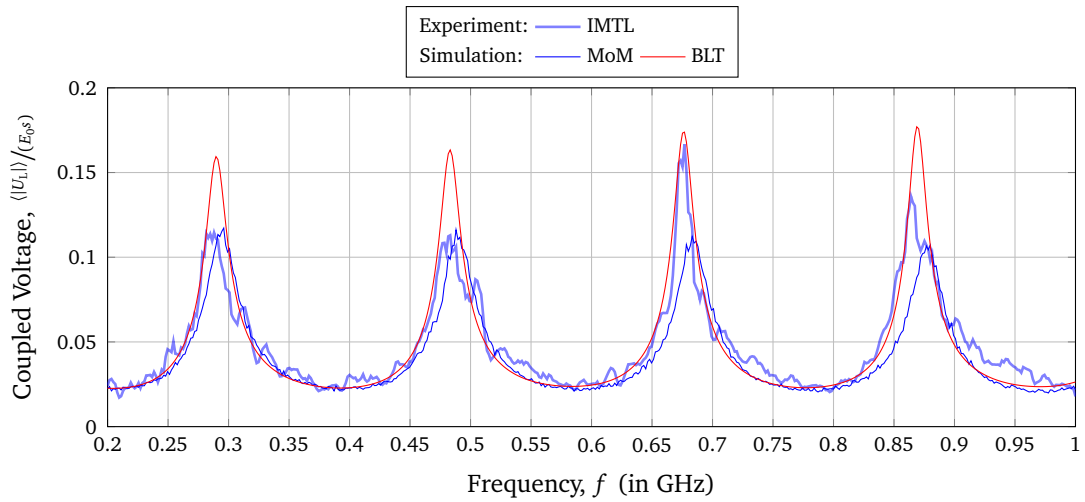
$$[Z_{L1}] = \begin{bmatrix} 34 \Omega & 84.5 \Omega \\ 84.5 \Omega & 34 \Omega \end{bmatrix}. \quad (5.64)$$

The line ends $[Z_{L2}]$ were kept open

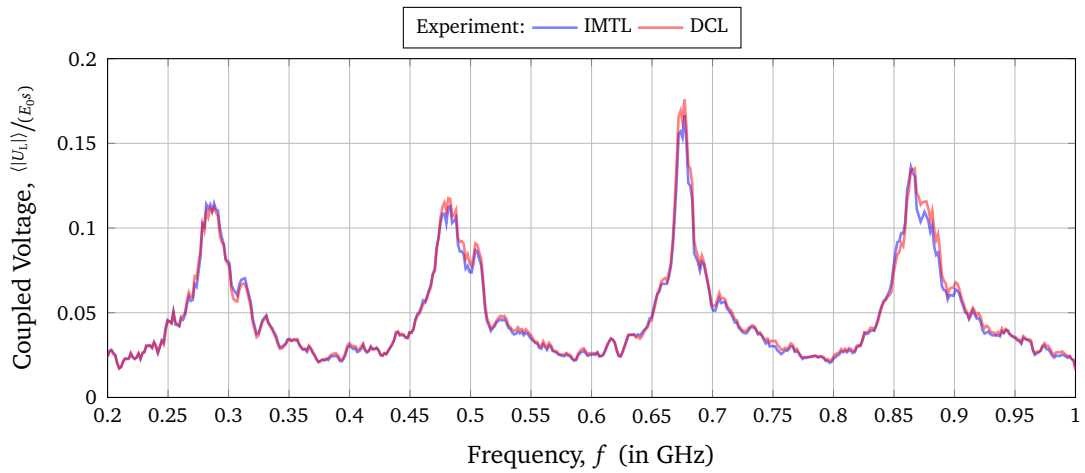
$$Z_{L2} = \begin{bmatrix} \infty & \infty \\ \infty & \infty \end{bmatrix}. \quad (5.65)$$

Here, the diagonal elements of the matrices represent the impedances between the individual wire and the reference conductor, and the non-diagonal elements represent the coupled impedances between the wires.

In Fig. 5.29a, the normalized average magnitude of the coupled voltage at the beginning of the first line $\langle |U_{L1,1}| \rangle$ as function of the frequency is shown. As in the chapters before, to obtain a dimensionless quantity for better comparison of the simulated and measured results, the coupled voltage was normalized to the field chamber constant E_0 and the distance s between the lines. Resonances can be found at about 290 MHz, 490 MHz, 690 MHz and 890 MHz, which fit to the asymmetric load mismatch of the lines ($l = \lambda/4, 3/4\lambda, 5/4\lambda, \dots$ [MV12]). In addition, the experimental results for a double line are shown in Fig. 5.29b, where the measurements were performed without the third line. The curves for the double conductor



(a) simulation and measurement results of the planar IMTL



(b) comparison of the DCL and the planar IMTL

Figure 5.29: Average magnitude of the coupled voltage $\langle |U_{L,1}| \rangle$ at the beginning of the first line of the planar arrangement (schematic shown in Fig. 5.28)

line and the multiconductor transmission line are nearly identical. From this fact it can be concluded that in this planar arrangement the third line has no influence on the coupled voltage on the first line. Generally, the simulations and the measurements show a good agreement. The analytical solution of the coupled voltage shows a slightly higher amplitude in the resonances than in the measurements. This could be due to losses that are not taken into account. The solution in *CONCEPT-II* shows some deviations in the third resonance and the analytical solution lies exactly on the measurement curve.

5.5.3.2 Triangular Arrangement

To model typical three-phase transmission lines, a triangular arrangement was chosen as shown in Fig. 5.30. Again, to connect the two terminals of the BalUn to the lines, a triangular metal plate from Fig. 5.30b was constructed.

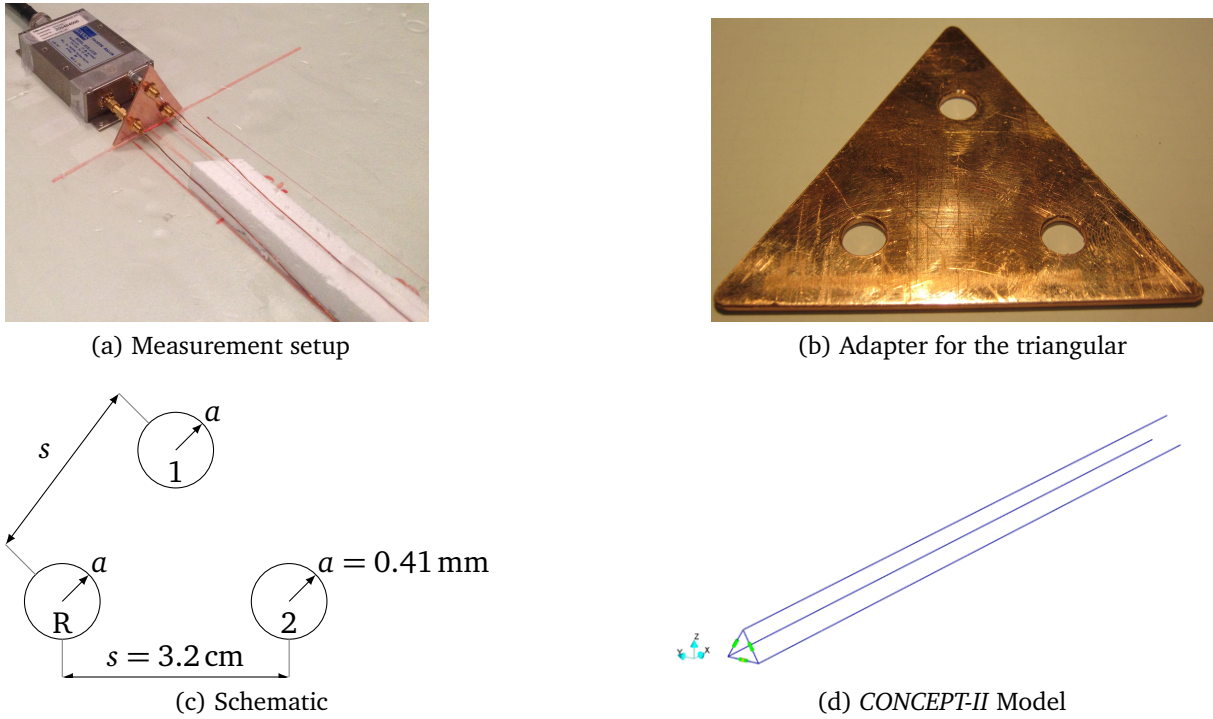


Figure 5.30: Equilateral triangular arrangement of the isolated three-wire multiconductor transmission line

The distance between all three conductors were $s = 32$ mm, the length of each line was 76 cm and the wire radii were $a = 0.41$ mm. The x - and z -coordinates of the line beginnings and ends were given by

$$\begin{aligned} [x_1] = [x_2] &= \begin{bmatrix} 0 \text{ mm} & 16 \text{ mm} & 32 \text{ mm} \end{bmatrix}, \\ [z_1] = [z_2] &= \begin{bmatrix} 0 \text{ mm} & 27.7 \text{ mm} & 0 \text{ mm} \end{bmatrix}. \end{aligned} \quad (5.66)$$

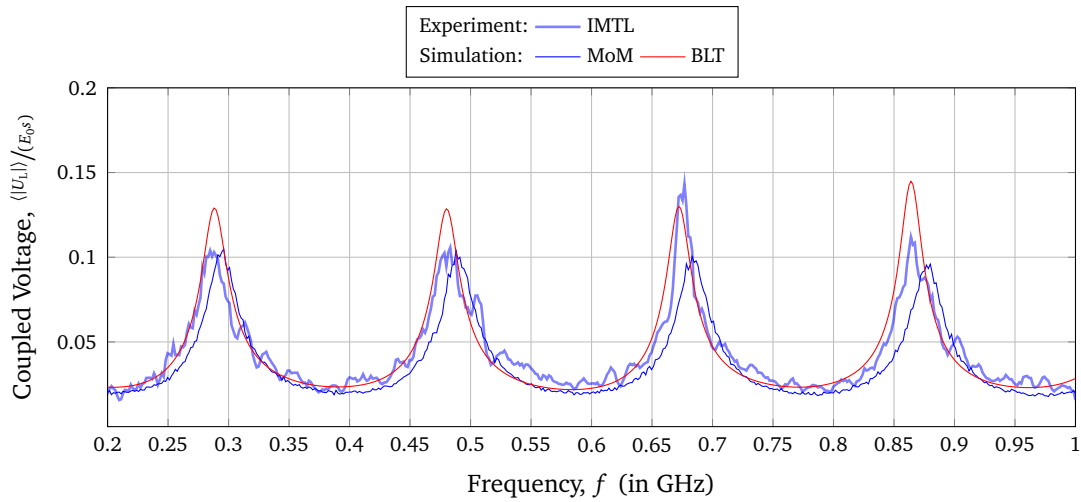
Again, in order to determine the load resistances at the beginning of the line, these were measured using a multimeter between the wires and the reference conductor (on-diagonal elements) as well as the impedances between the wires (off-diagonal elements)

$$Z_{L1} = \begin{bmatrix} 34 \Omega & 84.5 \Omega \\ 84.5 \Omega & 34 \Omega \end{bmatrix}. \quad (5.67)$$

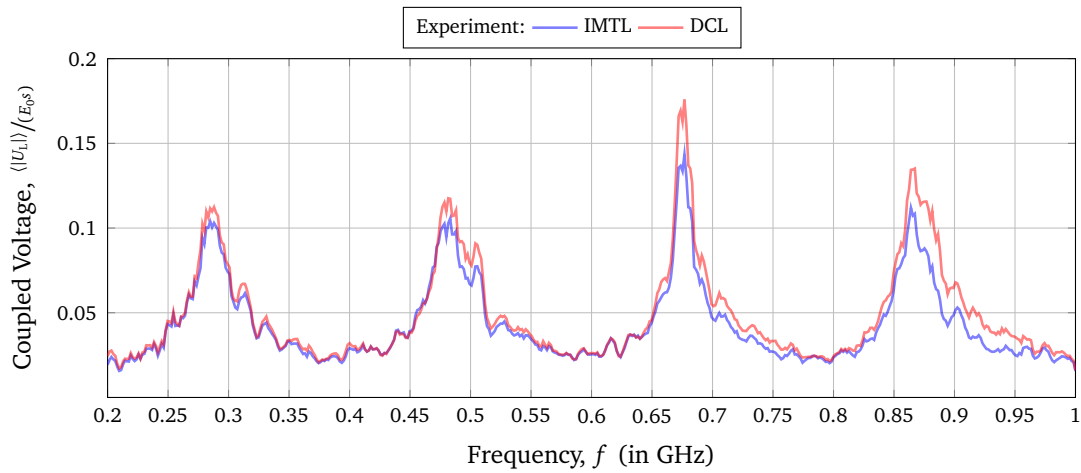
The line ends were kept open

$$Z_{L2} = \begin{bmatrix} \infty & \infty \\ \infty & \infty \end{bmatrix}. \quad (5.68)$$

The normalized mean magnitude of the coupled voltage at the beginning of the first line is shown in Fig. 5.31a. Again, resonances can be found at 290 MHz, 490 MHz, 690 MHz and 890 MHz because the line length remained the same ($l = \lambda/4, 3/4\lambda, 5/4\lambda, \dots$). In addition, the measured and simulated curves of the triangle arrangement are again compared with the



(a) simulation and measurement results of the triangular IMTL



(b) comparison of the DCL and the triangular IMTL

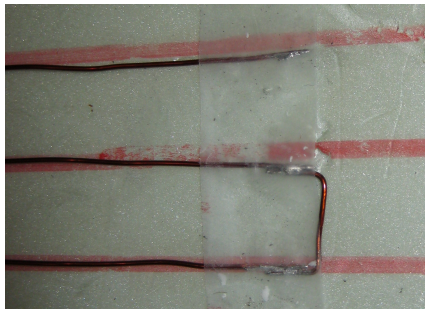
Figure 5.31: Average magnitude of the coupled voltage $\langle |U_{L,1}| \rangle$ at the beginning of the first line for the triangular arrangement (schematic shown in Fig. 5.30)

double wire case in Fig. 5.31b. As in the planar arrangement, there are no major differences between the measured curves. The small variations between the measured results can be explained by the reverberation chamber statistics and are negligible.

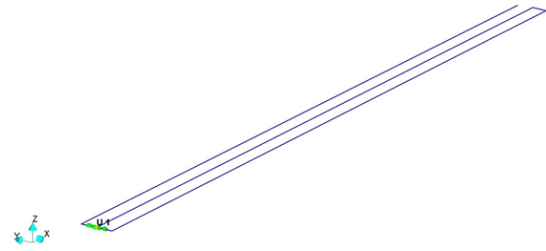
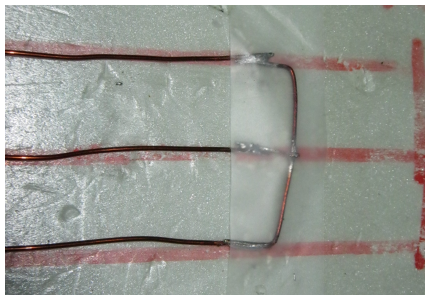
Comparing the coupled voltage of the planar and triangle arrangement with the double wire case in Fig. 5.29 and Fig. 5.31, no big differences can be seen between the different wire arrangements. It can be said that the arrangement of the conductors is not relevant for these particular configurations. Only the distance and the conductor dimensions, such as radius and length, are decisive for the coupled voltage. Since the lines are all the same length and terminated with the same load, no coupling effects were seen between the lines. Therefore, further investigations were carried out and the load impedances were varied.

5.5.3.3 Different Termination Resistances

In a next step, the terminating resistors at the ends of the wires were changed. Due to the large mismatch in the case of a short-circuited line end, strong line resonances were expected. Fig. 5.32 depicts the end of the lines in the measurement setup and the corresponding realization in *CONCEPT-II*. Tab. 5.5 lists the investigated termination resistance configurations.



(a) Variation 1: measurement setup

(b) Variation 1: *CONCEPT-II* model

(c) Variation 3: measurement setup

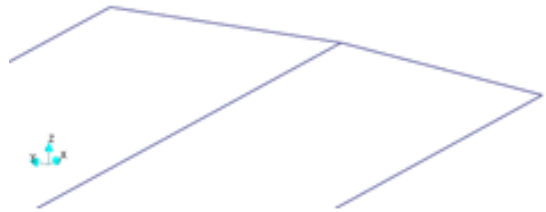
(d) Variation 3: *CONCEPT-II* model

Figure 5.32: Detailed view of the variation of the line terminations

The mean magnitude of the coupled voltage over the frequency is shown in Fig. 5.33. In general, the simulation results show a good agreement with the measurements. The resonance frequencies for variation 1 and 2 (Figs. 5.33a and 5.33b) are found at about 390 MHz, 590 MHz, 790 MHz and 990 MHz (symmetric mismatch, $l = \lambda/2, \lambda, 3/2\lambda, \dots$: 395 MHz, 592 MHz, 789 MHz and 986 MHz). For variation 3 and 4 (Figs. 5.33c and 5.33d), big resonances can be seen at about 300 MHz, 500 MHz, 700 MHz and 900 MHz (asymmetrical mismatched lines, $l = \lambda/4, 3\lambda/4, 5\lambda/4, \dots$: 296 MHz, 493 MHz, 691 MHz and 888 MHz). In addition, at 400 MHz, 600 MHz, 790 MHz and 990 MHz resonances can be found that belong to line 3 with a symmetric mismatch. The TLT-based simulation results show better results for variations 2 and 3 and the additional resonances. In general, the BLT simulation curves show a very good agreement to the measurements. The MoM simulations show higher peaks at the resonance frequencies. Using the MoM simulation, errors in the calculation can occur because the wires are very close together at the line ends for some termination variations.

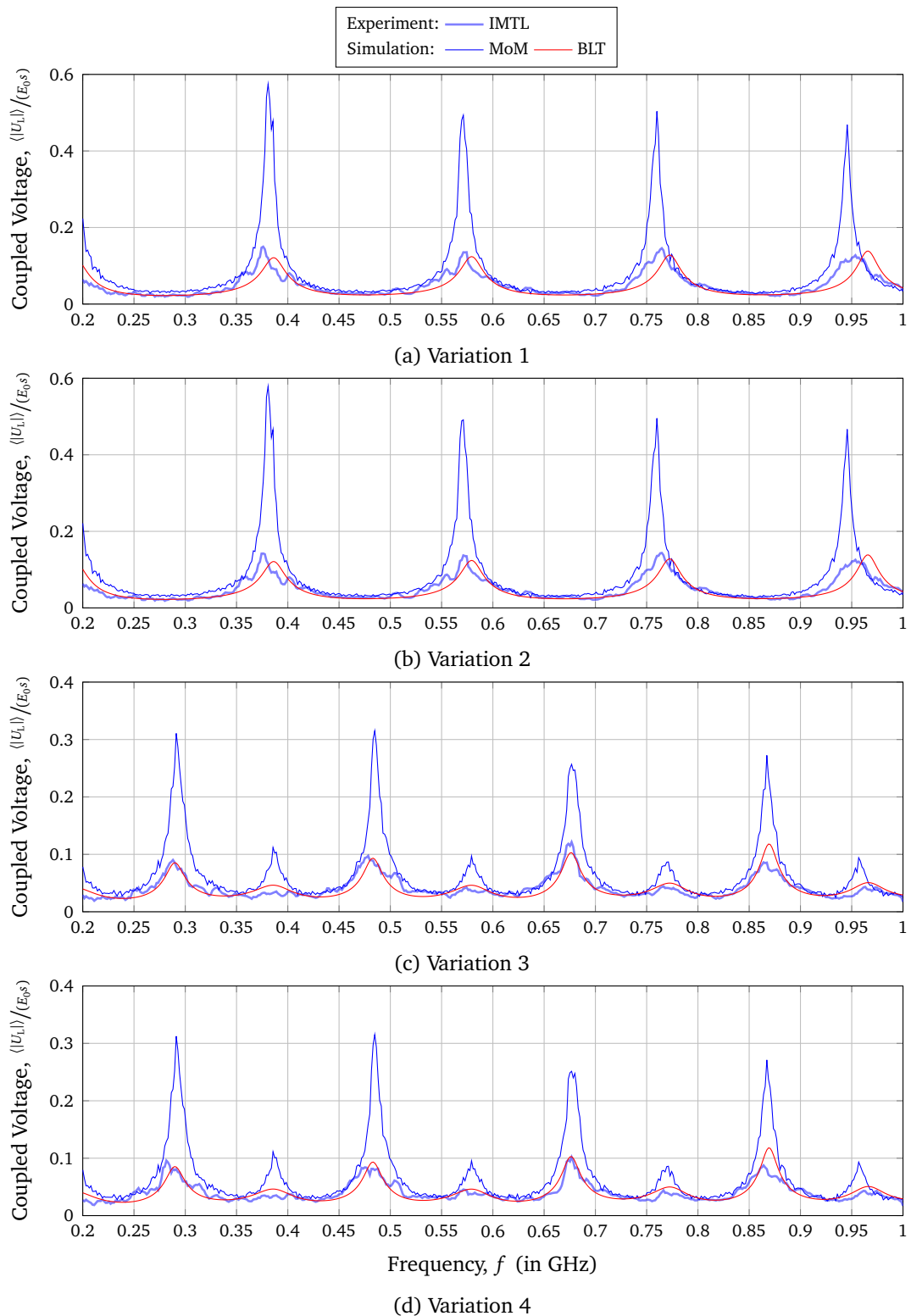


Figure 5.33: Average magnitude of the coupled voltage $\langle |U_{L,1}| \rangle$ at the beginning of the first line for the planar arrangement with different load resistances (Tab. 5.5)

Table 5.5: Variations of the terminating resistances at the end of the lines of the IMTL

Variation	Fig.	Scheme	$[Z_{L2}]$
1	5.33a	\equiv	$\begin{bmatrix} \infty & 0 \\ 0 & \infty \end{bmatrix}$
2	5.33b	\equiv	$\begin{bmatrix} 0 & 0 \\ 0 & 0 \end{bmatrix}$
3	5.33c	\equiv	$\begin{bmatrix} \infty & \infty \\ \infty & 0 \end{bmatrix}$
4	5.33d	\equiv	$\begin{bmatrix} 0 & \infty \\ \infty & \infty \end{bmatrix}$

5.5.3.4 Line Length

In the next test setup, the influence of the cable length was investigated. The resonant frequency strongly depends on the line length. For this reason, it plays the most important role from an immunity point of view. The longer the wire, the more transmission line resonances occur. Simulations in *CONCEPT-II* and using the BLT equation were performed with line lengths from 4 cm to 76 cm in steps of 2 cm.

In Fig. 5.34, a dependence of the coupled voltage on the line lengths is shown at 1000 MHz (Fig. 5.34a) and 400 MHz (Fig. 5.34b). In measurements, 19 different line lengths were investigated. The higher number of 36 line lengths in the simulation leads to softer curves. It can be seen how each frequency resonates along the line length. For higher frequencies more resonant frequencies occur. The measured line resonances correspond to the expected resonance frequencies of the multiconductor transmission line ($\frac{\lambda}{4}, \frac{3\lambda}{4}, \frac{5\lambda}{4}, \dots$):

1000 MHz: for 7.5 cm, 22.5 cm, 37.5 cm, 52.5 cm and 67.5 cm

400 MHz: for 18.7 cm and 56.1 cm

The results of the measurements agree very well with the simulations. The MoM simulation results show higher amplitudes for different line lengths compared to the measurements and the analytical simulation model.

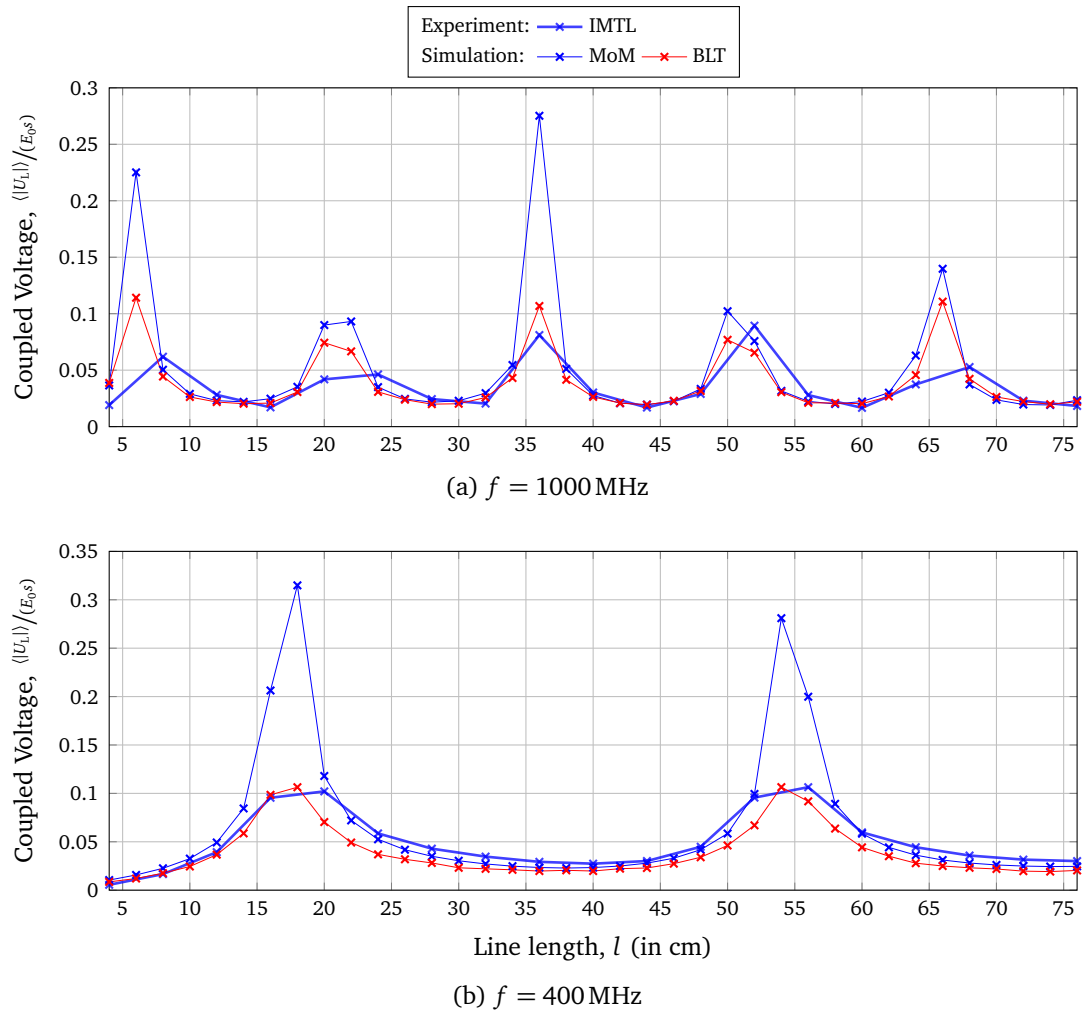


Figure 5.34: Average magnitude of the coupled voltage $\langle |U_{L1,1}| \rangle$ over the line length at the beginning of the first line for different frequencies

5.6 Comparison between the Multiconductor Structures

In this last section, the coupling to the multiconductor transmission line over ground and the isolated multiconductor transmission line were compared. For this purpose, Fig. 5.35 shows the coupled voltage to both structures. Here, the multiconductor transmission line over ground from Fig. 5.9a and the isolated multiconductor transmission line from Fig. 5.28 are compared. The multiconductor transmission line over ground consisted of two wires with the dimensions of $h_1 = h_2 = 3\text{ cm}$, $s = 2.5\text{ cm}$ and $l_1 = l_2 = 50\text{ cm}$. The isolated multiconductor transmission line consisted of two wires and a reference conductor in a planar arrangement. The distances between the lines and the reference conductor were $s = 3.2\text{ cm}$. All wires had a line length of $l_0 = l_1 = l_2 = 76\text{ cm}$.

In Fig. 5.35, the comparison of the measured coupled voltages of the two types of multiconductor transmission lines is shown. Both coupled voltages are normalized to the distance h or s . Resonances occur for the 50 cm long line at about 300 MHz, 600 MHz and 900 MHz for

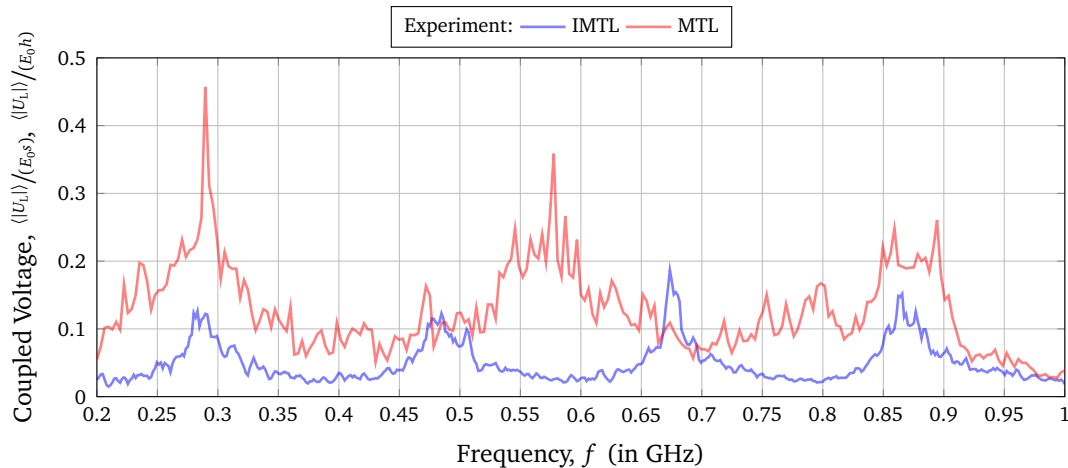


Figure 5.35: Comparison of the average magnitude of the measured coupled voltage of the isolated multiconductor transmission line (IMTL) and the multiconductor transmission line over ground (MTL)

the multiconductor line over ground. According to the line length of 72 cm of the isolated multiconductor line resonances occur at about 290 MHz, 490 MHz, 690 MHz and 890 MHz. Here, the coupled voltage to the multiconductor wire above the conductive ground plane is approximately twice as high as the voltage in the isolated multiconductor line. According to the comparison of the single and double wire case in 3.4.3, with the same transverse dimensions and load impedances $Z_{L,MTL} = Z_{L,IMTL}/2$ of the wires, the coupled voltage of an isolated multiconductor transmission line would have the same expected value of the amplitude at a resonance frequency compared with the case of a multiconductor transmission line over ground. In Fig. 5.35, it must be taken into account that the line terminations were not identical in both configurations.

5.7 Results of the Investigation of Multiconductor Transmission Lines

This chapter focused on the generalization of the theory from Section 3 of the Single conductor transmission line to the multiconductor transmission line system. This allows the investigation of the coupling of high-power microwaves and ultra-wideband pulses in multiconductor transmission lines as well as the coupling of these interferences into shielded cables.

In further investigations, for example, each individual wire of a braided shield can be represented as part of a multiconductor transmission line whose line parameters can be determined with the presented theory. Moreover, the solution for an isolated multiconductor transmission line from Section 5.5 can be extended by a dielectric surrounding of each line to examine a flat ribbon cable. With the help of the solutions from Section 5.2 for the multiconductor line above a ground plane it is possible to examine e. g. printed circuit boards or also shielded cables [KV18].

6 Summary and Outlook

In this chapter, the results of the present work are presented once again in a coherent way, in order to give an impression if and how the questions from Sec. 1.3 could be answered. In addition, an outlook for further work and possibilities for the application of the developed method is given.

6.1 Important Results

In this thesis, the stochastic electromagnetic field coupling to single and multiconductor transmission line structures is presented. The modeling of a single-wire transmission line is introduced in Chapter 3. For describing the transmission lines, an extension of classical transmission line theory was used, which led to complex and frequency dependent p. u. l. parameters as well as a characteristic impedance with equally dependency. The p. u. l. parameters are only depending on the dimensions of the wire and the frequency and not on the field excitation. This assumption is useful especially in case of the investigation of stochastic fields. In the end, parameters have been developed which can be transferred relatively easily to complex transmission line structures as they occur in reality. The described theory was validated against a full-wave simulation using the MoM. The high frequency modeling of the transmission lines leads to better results in comparison with the classical model. Moreover, the model was compared with measurements in a reverberation chamber. Furthermore, the modeling and the results were compared with those of a double wire line.

In order to investigate and take into account the influence of bends, in Chapter 4 a corresponding theory was developed. The analytical model was validated against the MoM and measurements in the reverberation chamber. Any kind of bending has an influence on the coupled voltage. The smaller the bend angle, the higher is the influence on the coupled voltage. Bend angles smaller than 30° cannot be neglected. Moreover, the curving of the lines and the radiation losses of bent and curved lines were studied as well as the simulation model was compared with some measurements of a transmission line network. In this context accurate results were also achieved.

Chapter 5 deals with the field-to-wire coupling to multiconductor transmission lines. Here, two types were investigated and compared with each other. First, the multiconductor transmission line over ground was investigated to model cables having a metallic structure as return conductor or high-voltage lines for power distribution. Then, an isolated multiconductor transmission line was analyzed to consider e. g. ribbon cables. Here, various parameter studies were carried out. For this purpose, e. g. the heights and distances or lengths of the conductors were varied.

During this thesis, an existing simulation model for a single line was enhanced by frequency dependent and complex transmission line parameters. Furthermore, the model was extended for various three-dimensional line structures and including the coupling between the wires as well as the effect of bends in the line. The simplicity of the model has been retained, which allows very expeditious parameter studies and investigations. Due to the extensive studies, the presented model could be verified for different transmission line structures. Additionally, their behavior in stochastic fields could be investigated.

6.2 Outlook for Future Works

The investigations within this thesis were limited exclusively to the frequency range. Because transmission lines in practice also have non-linear terminations and are excited by pulse fields, transient effects must also be taken into account. Even if approaches for measurements of the quality factor in the time domain already exist, there is still a need for research in the investigation of transient effects in comparison to the behavior in stationary state.

It has been shown that the simulated field by a superposition of many plane waves has the same properties as the field in an ideal reverberation chamber. For the time domain there is a lack of investigations under which conditions transient field generators provide good agreement with experimental data.

Bibliography

- [Abr74] ABRAMOWITZ, Milton: *Handbook of Mathematical Functions, With Formulas, Graphs, and Mathematical Tables*,. USA : Dover Publications, Inc., 1974. – ISBN 0486612724
- [APG80] AGRAWAL, Ashok K. ; PRICE, Harold J. ; GURBAXANI, Shyam H.: Transient Response of Multiconductor Transmission Lines Excited by a Nonuniform Electromagnetic Field. In: *IEEE Trans. Electromagn. Compat.* 22 (1980), Mai, Nr. 2, S. 119 – 129
- [CBK13] CHABANE, Sofiane ; BESNIER, Philippe ; KLINGLER, Marco: Extension of the transmission line theory application with modified enhanced per-unit-length parameters. In: *Progress In Electromagnetics Research, PIER* 32 (2013), September, S. 257–270. <http://dx.doi.org/10.2528/PIERM13072308>. – DOI 10.2528/PIERM13072308
- [CBK17] CHABANE, Sofiane ; BESNIER, Philippe ; KLINGLER, Marco: A Modified Enhanced Transmission Line Theory Applied to Multiconductor Transmission Lines. In: *IEEE Trans. Electromagn. Compat.* 59 (2017), April, Nr. 2, S. 518–528. <http://dx.doi.org/10.1109/TEM.C.2016.2611672>. – DOI 10.1109/TEM.C.2016.2611672. – ISSN 0018–9375
- [Col13] COLLIER, Richard: *Transmission Lines: Equivalent Circuits, Electromagnetic Theory, and Photons*. Cambridge : Cambridge University Press, 2013. – ISBN 9781139199018
- [Fra77] FRANKEL, Sidney: *Multiconductor Transmission Line Analysis*. Artech House, 1977 (Microwave Library). <https://books.google.de/books?id=FvKyAAAAIAAJ>. – ISBN 9780890060544
- [Gus18] GUSTRAU, Frank ; LEPPERT, Manuel (Hrsg.): *Angewandte Feldtheorie: Eine praxisnahe Einführung in die Theorie elektromagnetischer Felder*. 3. München : Carl Hanser Verlag, 2018. – ISBN 978–3–446–45671–6
- [Har93] HARRINGTON, Roger F. ; DUDLEY, Donald G. (Hrsg.): *Field Computation by Moment Methods*. 1. Piscataway, NJ, USA : IEEE Press, 1993 (IEEE Press Series

- on Electromagnetic Waves). – 229 S. – ISBN 0–7803–1014–4. – Originally published by R. E. Krieger Publishing Company Inc., Malabar, FL, USA, 1968
- [Hen15] HENKE, Heino: *Elektromagnetische Felder - Theorie und Anwendung*. 5. Berlin Heidelberg : Springer Vieweg, 2015. – 572 S. <http://dx.doi.org/10.1007/978-3-662-46918-7>. <http://dx.doi.org/10.1007/978-3-662-46918-7>. ISSN 0937–7433
- [Hil98] HILL, David A.: Plane Wave Integral Representation for Fields in Reverberation Chambers. In: *IEEE Trans. Electromagn. Compat.* 40 (1998), August, Nr. 3, S. 209 – 217. <http://dx.doi.org/10.1109/15.709418>. – DOI 10.1109/15.709418. – ISSN 0018–9375
- [Hil09] HILL, David A.: *Electromagnetic Fields in Cavities: Deterministic and Statistical Theories*. 1. Piscataway, NJ, USA : IEEE Press, 2009 (IEEE Press Series on Electromagnetic Wave Theory). – 280 S. – ISBN 0–470–46590–5
- [Int03] INTERNATIONAL ELECTROTECHNICAL COMMISSION (Hrsg.): *IEC 61000-4-21, Testing and measurement techniques – Reverberation chamber test methods*. ; International Electrotechnical Commission, 2003
- [Int11] INTERNATIONAL ELECTROTECHNICAL COMMISSION (Hrsg.): *IEC 61000-4-21, Testing and measurement techniques – Reverberation chamber test methods*. 2. ; International Electrotechnical Commission, Januar 2011
- [Jac99] JACKSON, John D.: *Classical Electrodynamics*. 3. John Wiley & Sons, 1999. – ISBN 978–0471–30932–1
- [JPD10] JUNQUA, I. ; PARMANTIER, J. ; DEGAUQUE, P.: Field-to-Wire Coupling in an Electrically Large Cavity: A Semianalytic Solution. In: *IEEE Transactions on Electromagnetic Compatibility* 52 (2010), Nov, Nr. 4, S. 1034–1040. <http://dx.doi.org/10.1109/TEM.2010.2057433>. – DOI 10.1109/TEM.2010.2057433. – ISSN 0018–9375
- [Kin55] KING, Ronold Wyeth P.: *Transmission-Line Theory*. New York : McGraw-Hill Book Company, 1955
- [KMR08] K., Küpfmüller ; MATHIS, W. ; REIBIGER, A.: *Theoretische Elektrotechnik*. Berlin : Springer-Verlag Berlin Heidelberg, 2008. – 791 S. <http://dx.doi.org/10.1007/978-3-540-78590-3>. <http://dx.doi.org/10.1007/978-3-540-78590-3>. ISSN 0937–7433

- [KT49] KING, R. ; TOMIYASU, K.: Terminal Impedance and Generalized Two-Wire-Line Theory. In: *Proceedings of the IRE* 37 (1949), Oct, Nr. 10, S. 1134–1139. <http://dx.doi.org/10.1109/JRPROC.1949.233610>. – DOI 10.1109/JRPROC.1949.233610. – ISSN 0096–8390
- [KV18] KASPER, Johanna ; VICK, Ralf: Modellierung der Einkopplung statistischer Felder in geschirmte Mehrfachleitungen. In: *emv – Internationale Fachmesse und Kongress für Elektromagnetische Verträglichkeit*. Düsseldorf, Februar 2018
- [Lan10] LANGLEY, R. S.: A Reciprocity Approach for Computing the Response of Wiring Systems to Diffuse Electromagnetic Fields. In: *IEEE Transactions on Electromagnetic Compatibility* 52 (2010), Nov, Nr. 4, S. 1041–1055. <http://dx.doi.org/10.1109/TEMC.2010.2068051>. – DOI 10.1109/TEMC.2010.2068051. – ISSN 0018–9375
- [LMRT16] LUGRIN, Gaspard ; MORA, Nicolas ; RACHIDI, Farhad ; TKACHENKO, Sergey V.: Electromagnetic field coupling to transmission lines: A model for the risers. In: *Asia-Pacific International Symposium on Electromagnetic Compatibility (APEMC)* Bd. 01. Shenzhen, China, Mai 2016. – ISBN 978–1–4673–9494–9, S. 174–176
- [Mag12] MAGDOWSKI, Mathias: *Vergleich der Einkopplung deterministischer und statistischer elektromagnetischer Felder in Leitungen*. 1. Magdeburg : Nitsch, Jürgen and Styczynski, Zbigniew Antoni, 2012 (Res Electricae Magdeburgenses, Magdeburger Forum zur Elektrotechnik 46). – ISBN 978–3–940961–75–4
- [MT96] MITRA, Atindra K. ; TROST, Thomas F.: Power transfer characteristics of a microwave reverberation chamber. In: *IEEE Trans. Electromagn. Compat.* 38 (1996), Mai, Nr. 2, S. 197–200. <http://dx.doi.org/10.1109/15.494624>. – DOI 10.1109/15.494624. – ISSN 0018–9375
- [MTV11] MAGDOWSKI, Mathias ; TKACHENKO, Sergey V. ; VICK, Ralf: Coupling of Stochastic Electromagnetic Fields to a Transmission Line in a Reverberation Chamber. In: *IEEE Trans. Electromagn. Compat.* 53 (2011), Mai, Nr. 2, S. 308 – 317. <http://dx.doi.org/10.1109/TEMC.2010.2097267>. – DOI 10.1109/TEMC.2010.2097267. – ISSN 0018–9375
- [MV12] MAGDOWSKI, Mathias ; VICK, Ralf: Closed-Form Formulas for the Stochastic Electromagnetic Field Coupling to a Transmission Line With Arbitrary Loads. In: *IEEE Trans. Electromagn. Compat.* 54 (2012), Oktober, Nr. 5, S. 1147 – 1152. <http://dx.doi.org/10.1109/TEMC.2012.2193130>. – DOI 10.1109/TEMC.2012.2193130. – ISSN 0018–9375

- [MV15] MAGDOWSKI, Mathias ; VICK, Ralf: Numerical Simulation of the Stochastic Electromagnetic Field Coupling to Transmission Line Networks. In: *Proceedings of the Joint IEEE International Symposium on Electromagnetic Compatibility and EMC Europe*. Dresden,, August 2015. – ISBN 978–1–4799–6615–8, S. 818–823. – IEEE Catalog Number: CFP15EMC-USB
- [NT04] NITSCH, Jürgen B. ; TKACHENKO, Sergey V: Complex-valued transmission-line parameters and their relation to the radiation resistance. In: *IEEE Trans. Electromagn. Compat.* 46 (2004), August, Nr. 3, S. 477–487. <http://dx.doi.org/10.1109/TEMC.2004.831905>. – DOI 10.1109/TEMC.2004.831905. – ISSN 0018–9375
- [Orf08] ORFANIDIS, Sophocles J.: *Electromagnetic Waves and Antennas*. 2008. – ISBN 978–0–9793713–2–5
- [Pau08] PAUL, Clayton R.: *Analysis of Multiconductor Transmission Lines*. 2. Hoboken, New Jersey, USA : John Wiley & Sons, 2008 (IEEE Press). – ISBN 978–0–470–13154–1
- [PBM86] PRUDNIKOV, A.P ; BRYCHKOV, Yu.A. ; MARICHEV, O.I.: *Integrals and Series*. New York : CRC Press, 1986 (Vol. 1: Elementary Functions). – ISBN 978–2881240973
- [Per95] PEREZ, Reinaldo (Hrsg.): *Handbook of Electromagnetic Compatibility*. 1. London : Academic Press, 1995. – ISBN 0–12–550710–0
- [PXP06] PARK, Sang W. ; XIAO, Fengchao ; PARK, Dong C. ; KAMI, Yoshio: Analysis of Coupling Between Two Bent Transmission Lines by a Circuit-Concept Approach. In: *IEEE Electromagnetic Compatibility Magazine* (2006), aug. <http://dx.doi.org/10.1109/CEEM.2006.258059>. – DOI 10.1109/CEEM.2006.258059
- [RT08] RACHIDI, Farhad (Hrsg.) ; TKACHENKO, Sergey V. (Hrsg.): *Electromagnetic Field Interaction With Transmission Lines – From Classical Theory to HF Radiation Effects*. 1. Ashurst, Southampton, UK : WIT Press, 2008. – ISBN 978–1–84564–063–7
- [Ser17] SERRA, Ramiro: Reverberation chambers through the magnifying glass: an overview and classification of performance indicators. 6 (2017), Juli, Nr. 2, S. 76–88. <http://dx.doi.org/10.1109/MEMC.0.7990003>. – DOI 10.1109/MEMC.0.7990003. – ISSN 2162–2264
- [Tec] TECHNICAL UNIVERSITY HAMBURG-HARBURG: *CONCEPT-II, Version 12.0*. <http://www.tet.tu-harburg.de/concept/?lang=en>
- [TIK96] TESCHE, Frederick M. ; IANOZ, Michel ; KARLSSON, Torbjörn: *EMC Analysis Methods and Computational Models*. 1. New York : Wiley-Interscience, 1996. – ISBN 0–471–15573–X

- [Tom50] TOMIYASU, Kiyō: The Effect of a Bend and Other Discontinuities on a Two-Wire Transmission Line. In: *Proceedings of the IRE* 38 (1950), Juni, Nr. 6, S. 679–682. <http://dx.doi.org/10.1109/JRPROC.1950.233114>. – DOI 10.1109/JRPROC.1950.233114. – ISSN 0096–8390
- [Uni77] UNITED STATES DEPARTMENT OF DEFENSE (Hrsg.): *MIL-STD-1377, Effectiveness of cable, connector, and weapon enclosure shielding and filters in precluding hazards of electromagnetic radiation to ordnance*. Arlington County, Virginia, USA: United States Department of Defense, August 1977
- [Wat44] WATSON, G. A.: *Treatise on the Theory of Bessel Functions*. 2. Cambridge University Press, 1944 (Cambridge Mathematical Library). – ISBN 978–0521483919
- [Wik20] WIKIPEDIA, DIE FREIE ENZYKLOPÄDIE: *The (large) Electromagnetic Reverberation Chamber at the Otto-von-Guericke-University Magdeburg, Magdeburg, Germany*. https://de.wikipedia.org/wiki/Modenverwirbelungskammer#/media/Datei:Magdeburg-reverberation_chamber.jpg. Version: 2020

A Calculating the Coupled Current from the Scattering Parameters

The coupled current can be calculated using a four-port VNA

$$\frac{I}{H_0 h} = S_{31} \cdot \frac{\lambda}{h} \sqrt{\frac{\mu c_0}{8\pi Z_{\text{VNA}} \langle |S_{21}|^2 \rangle}} \quad (\text{SCL over ground}) \quad (\text{A.1})$$

B Comparison of the Solutions of the Integrals of the Field-to-Wire Coupling Equations

The current in a transmission line in y -direction is approximated with

$$I(y) = I_0 \left[\frac{-e^{-jk_1 l} + e^{-jkl}}{e^{jkl} + e^{-jkl}} e^{-jky} - \frac{e^{-jk_1 l} + e^{-jkl}}{e^{jkl} + e^{-jkl}} e^{-jky} + e^{-jk_1 y} \right]. \quad (\text{B.1})$$

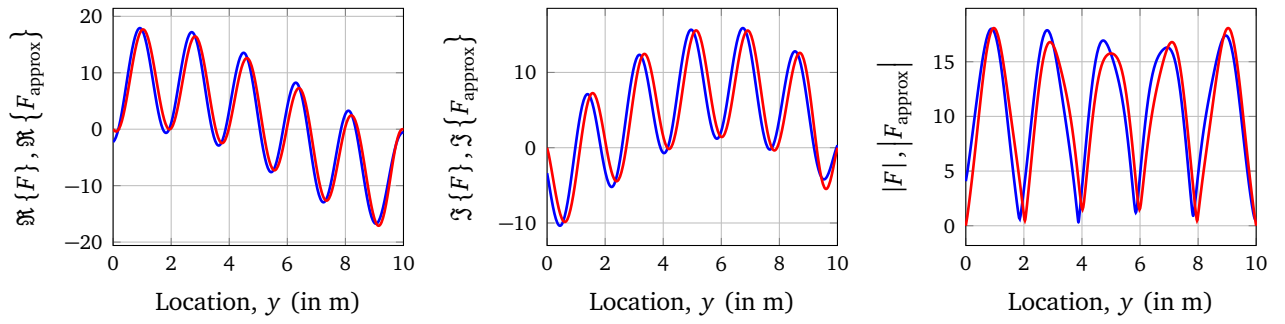
Now, the integral from the field-to-wire coupling Eqs. 2.21 shall be calculated. The integral is proportional to the y -component of the vector potential on the boundary of the wire and also (for the straight wire it is also proportional to the scalar potential on the boundary of the wire)

$$F(y) = \int_0^l I(y') g(y - y') dy. \quad (\text{B.2})$$

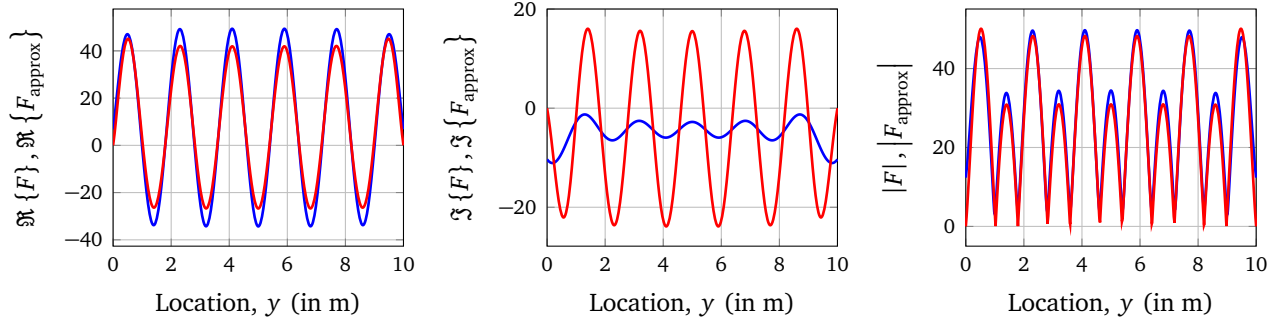
$$F_{\text{approx}}(y) = I(y) \cdot \int_0^l g(y - y') dy. \quad (\text{B.3})$$

The investigated wire had a line length of $l = 10$ m, a height of $h = 0.5$ m and a wire radius of $a = 1$ cm. Now, several k_1 shall be considered for $k = 3.5 \text{ m}^{-1}$. In Fig. B.1, the solution of the exact and the approximated function $F(y)$ and $F_{\text{approx}}(y)$ for their real, imaginary and absolute value are shown. It can be seen that for a small k_1 the solutions fit very well, especially in the absolute value.

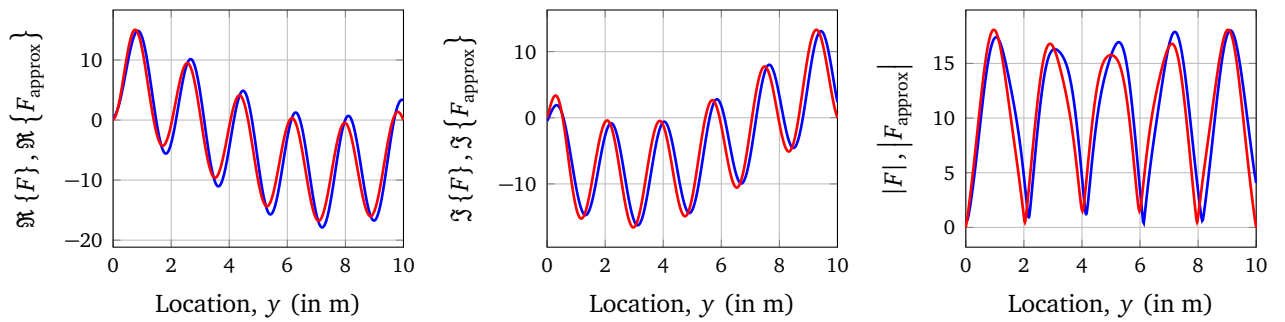
It can be concluded that for the consideration of statistical fields, where k_1 is assumed to be normally distributed, this approximation is valid.



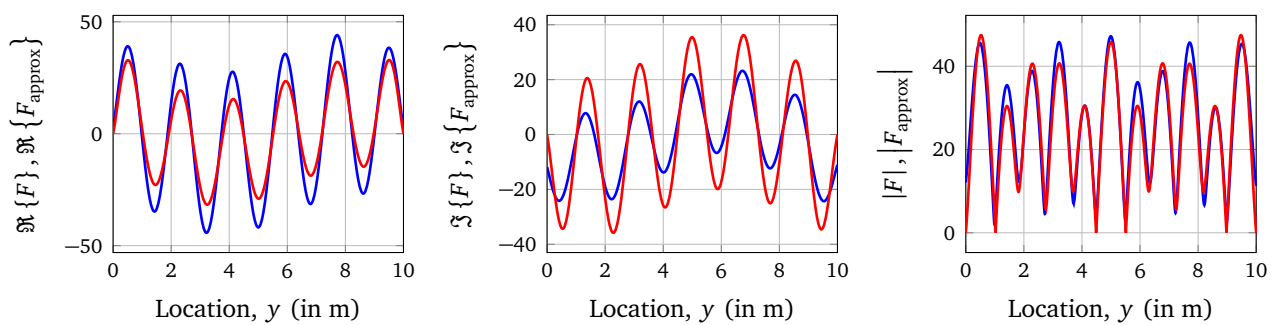
(a) $k_1 = -0.1 \cdot k$



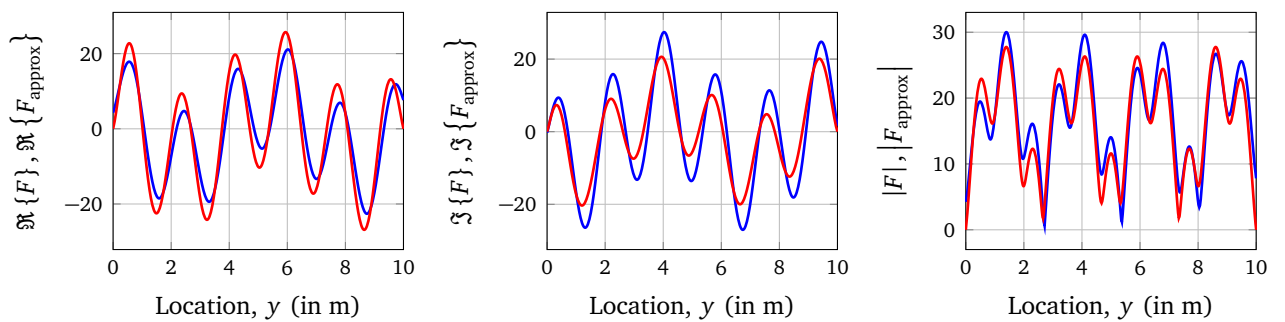
(b) $k_1 = 0 \cdot k$



(c) $k_1 = 0.1 \cdot k$



(d) $k_1 = 0.2 \cdot k$



(e) $k_1 = 0.3 \cdot k$

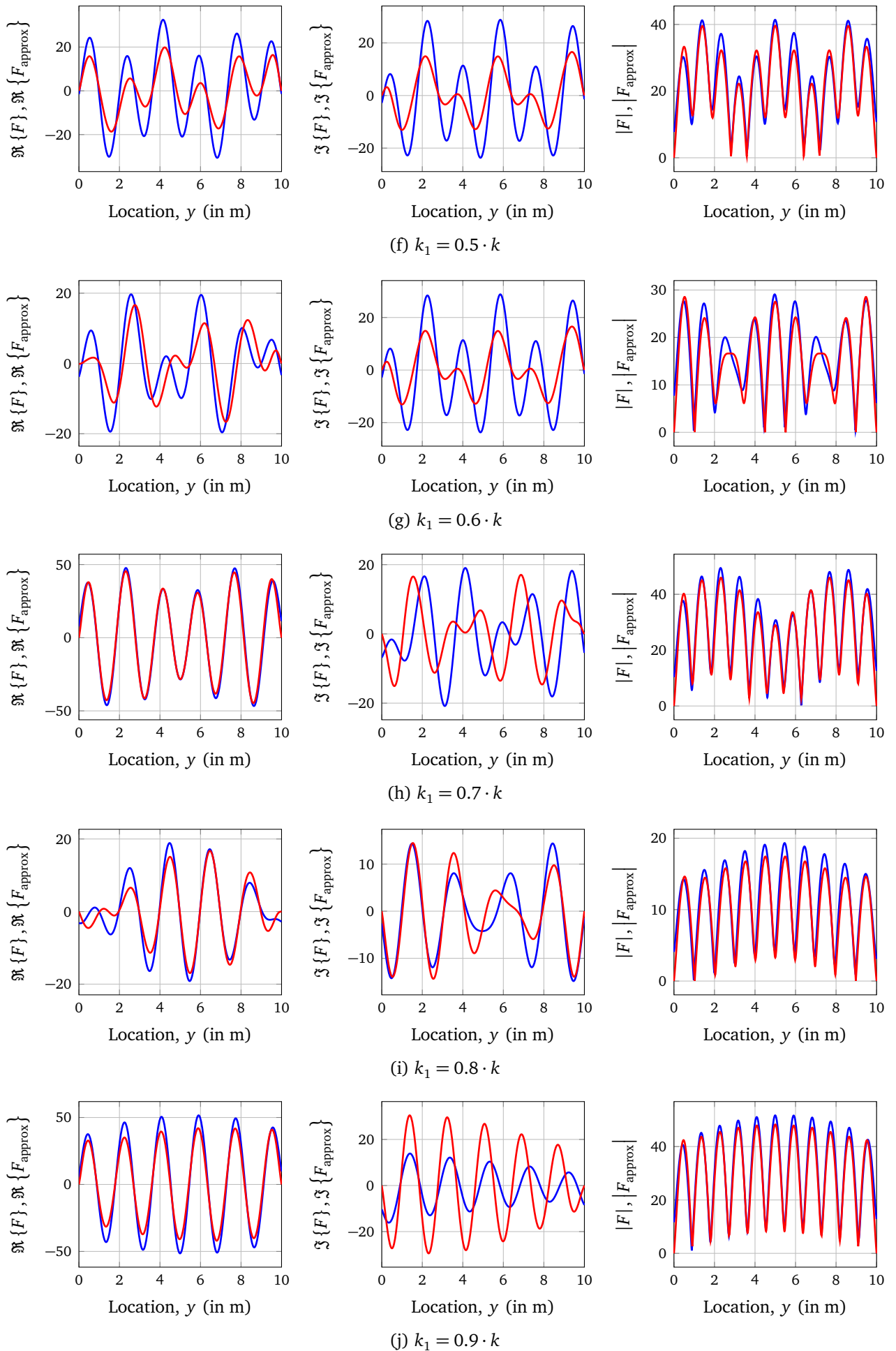


Figure B.1: Comparison of the solution of the exact and approximated function F and F_{approx}

C Simulation Model of the Curved Transmission Line in *CONCEPT-II*

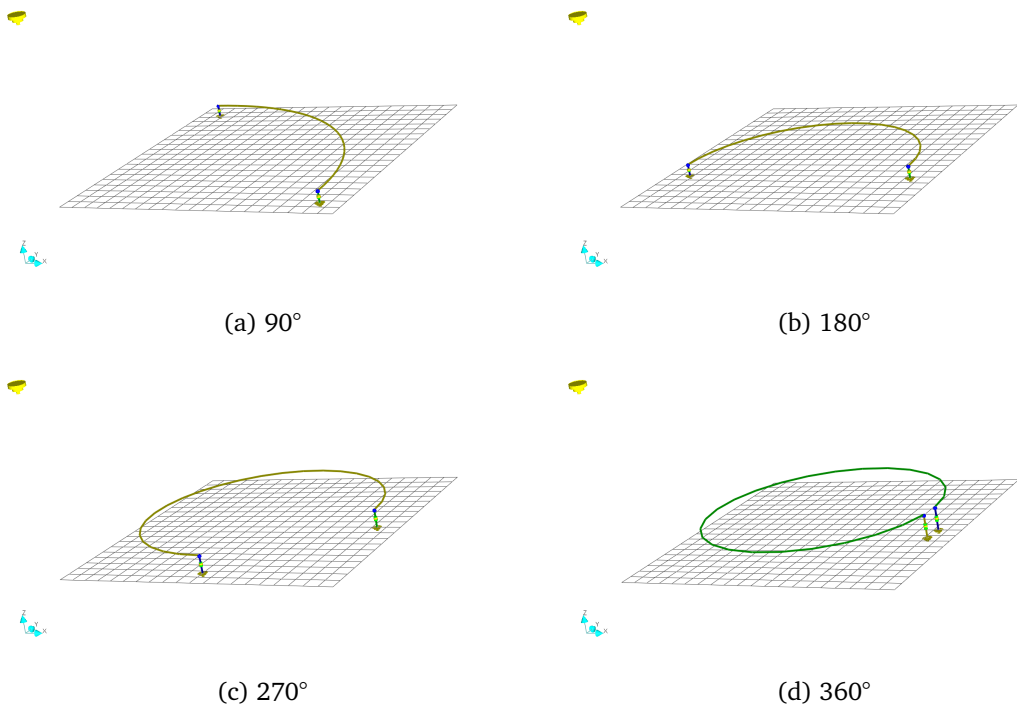


Figure C.1: Screenshots of the simulation model of the curved transmission line in *CONCEPT-II*

D Vector Potential for the Double Line with a Bend

In Fig. 4.5, a conductor with the radius a_1 is shown with a bent at an angle θ . The reference conductor with a radius a_0 is parallel to the bent line at a distance s . The coordinates w and u have their origins at the bent and are directed away from it. The distances that are used in the double-wire case are [Tom50]

$$R_{00} = \sqrt{a_0^2 + (w - w')^2}, \quad (\text{D.1a})$$

$$R_{11} = \sqrt{a_1^2 + (w - w')^2}, \quad (\text{D.1b})$$

$$R_{01} = R_{10} = \sqrt{s^2 + (w - w')^2}. \quad (\text{D.1c})$$

For the coupling between wire 1 and 2 follow the distances

$$R_{12} = \sqrt{(w + u' \cos \theta)^2 + (u' \sin \theta)^2 + a_1^2}, \quad (\text{D.2a})$$

$$R_{012} = \sqrt{(w + u' \cos \theta)^2 + (u' \sin \theta)^2 + s^2}. \quad (\text{D.2b})$$

In case of $\theta = 0^\circ$, R_{11} and R_{10} correspond to the double-wire case. With the distances the solution of the vector potential is

$$A_x(x) = \frac{\mu}{4\pi} \int_0^{l_1} I_{x1}(w') g_1(w, w') dw' + \frac{\mu}{4\pi} \int_0^{l_2} I_{x2}(u') g_{12}(u, u') du', \quad (\text{D.3a})$$

$$A_y(y) = \frac{\mu}{4\pi} \int_0^{l_2} I_{y2}(u') g_{12}(u, u') du'. \quad (\text{D.3b})$$

Here, g_1 and g_{12} are defined as

$$g_1(w, w') = \frac{e^{-jkR_{10}}}{R_{10}} + \frac{e^{-jkR_{01}}}{R_{01}} - \frac{e^{-jkR_{00}}}{R_{00}} - \frac{e^{-jkR_{11}}}{R_{11}} \quad (\text{D.4})$$

and

$$g_{12}(u, u') = \frac{e^{-jkR_{12}}}{R_{12}} - \frac{e^{-jkR_{012}}}{R_{012}}. \quad (\text{D.5})$$

The condition for the currents at the junction is equal to Eq. (4.4)

$$I_{x1}(w' \mapsto 0) = I_{u2}(u' \mapsto 0). \quad (\text{D.6})$$

If $I_{u1}(u')$ is the total axial current at u' in the termination, then the current on wire 2 can be expressed by angular relation between the wires

$$I_{x2}(u') = I_{u2}(u') \cdot \cos(\theta), \quad (\text{D.7a})$$

$$I_{y2}(u') = I_{u2}(u') \cdot \sin(\theta), \quad (\text{D.7b})$$

From the relations of Eq. (D.7) and under the condition, that the current is locally constant, the current can be put in front of the integral

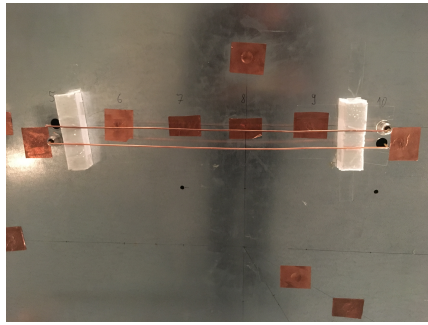
$$A_x(x) = \frac{\mu}{4\pi} I_{x1} \int_0^{l_1} g_1(w, w') dw' + \frac{\mu}{4\pi} \cos(\theta) \cdot I_{x1} \int_0^{l_2} g_{12}(u, u') du', \quad (\text{D.8a})$$

$$A_y(y) = \frac{\mu}{4\pi} \sin(\theta) \cdot I_{x1} \int_0^{l_2} g_{12}(u, u') du'. \quad (\text{D.8b})$$

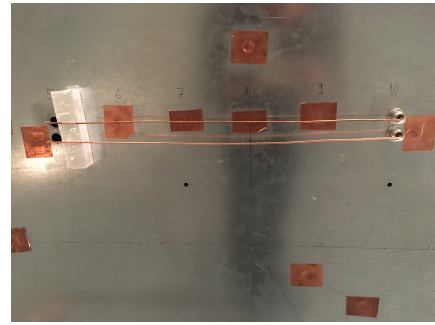
E Measurement Setup of Different Terminations of the Multiconductor Transmission Line over Ground

Table E.1: Terminating resistances of the multiconductor transmission line while the load impedance $Z_{L1,1}$ is always $50\ \Omega$

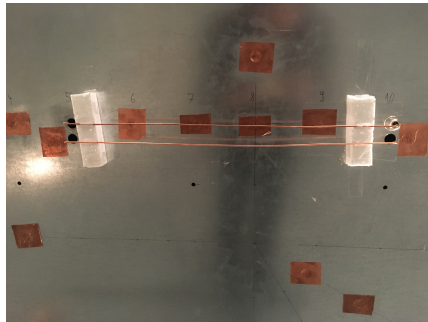
$Z_{L2,1}$	$Z_{L1,2}$	$Z_{L2,2}$	Figure
$50\ \Omega$	$50\ \Omega$	∞	E.1e
	∞	$50\ \Omega$	E.1d
	∞	∞	E.1f
∞	$50\ \Omega$	$50\ \Omega$	E.1g
	$50\ \Omega$	∞	E.1b
	∞	$50\ \Omega$	E.1a
∞	∞	∞	E.1c



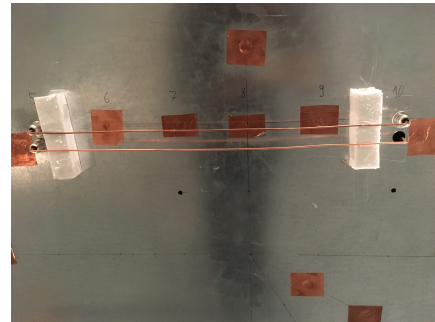
(a)



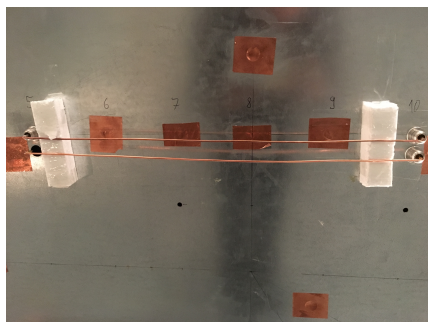
(b)



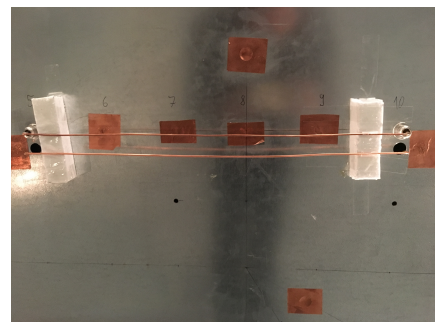
(c)



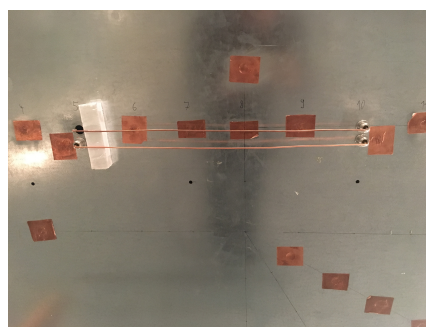
(d)



(e)



(f)



(g)

Figure E.1: Photographs of the different configurations of the terminations of the two-wire MTL over ground in the reverberation chamber

F MATLAB Program Setting for MoM Results at 0 Hz

For the MoM, simulations at 0 Hz are not possible, therefore the value is replaced in *MATLAB* as shown in Fig. F.1.

```
% Werte bei der Frequenz Null ersetzen -> Zeilenvektor(1,F)
I(f==0)=0;
I(nozeros_in_f)=I_mom;
```

Figure F.1: Replacing the simulated values at 0 Hz with zero in *MATLAB*

Acknowledgement

Doing this PhD was a truly life-changing experience for me, and it would not have been possible without the support and advice I received from many people.

Firstly, I would like to express my sincere gratitude to my advisor Prof. Ralf Vick who, with his trust in me, made it possible for me to work very independently and on my own responsibility. He gave me the opportunity to present my research results at conferences around the world. A second thank goes to Dr. Mathias Magdowski, who was also an important source of ideas for this work. His professional expertise led to a lively exchange and we were able to submit numerous publications and supervise student works in this field. I would like to thank Prof. Enders for taking over the external reviewer. Special thanks go to my colleagues of the chair of electromagnetic compatibility for their insightful comments and encouragement, but also for the hard question which incited me to widen my research from various perspectives. I would also like to acknowledge Anke Fröbel. I am gratefully indebted to her for her very valuable comments on this thesis and her constant support and motivation.

Finally, I would also like to thank my partner Max for his loving support and understanding, as well as my family and friends and especially my closest friends Lisa, Janice and Karoline for their constant encouragement throughout my years of study and through the process of researching and writing this thesis. This accomplishment would not have been possible without them. Thank you.

Curriculum Vitae

Johanna Kasper
Otto-von-Guericke Straße 79
39104 Magdeburg



Education

- 2012 – 2015 Main study period of mechatronics at the OvGU, Magdeburg, Germany, completion with a master thesis (grade 1,6)
- 2009 – 2012 Basic study period of mechatronics at the OvGU, Magdeburg, Germany, completion with an bachelor degree (grade 1,8)
- 2001 – 2009 Grammar school at the Norbertus Gymnasium in Magdeburg, Germany, 5. to 12. class, intensive courses in mathematics and physics, completion with a general qualification for university entrance (Abitur) with the grade 1,2
- 1990 – 1994 Primary school at the Grundschule in Samswegen, Germany, 1. to 4. class

Work Experience

- Juni – Aug. 2009 Basic internship at the Fraunhofer Institute for Factory Operation and Automation (IFF), Sandtorstr. 22, 39106 Magdeburg, Germany
- April – Juli 2012 Research assistant at the Chair for Microsystems Technology, Institute for Micro and Sensor System (IMOS) at the OvGU, Magdeburg, Germany
- Sept. – Dez. 2012 Advanced internship at the Volkswagen AG, Technology Centre Electric Traction (TZE), Am Krainhop 5, 38550 Isenbüttel, Germany
- since May 2015 Scientific co-worker at the Chair for Electromagnetic Compatibility, Institute for Medical Engineering at the OvGU, Magdeburg, Germany

Membership

- Member of the Electromagnetic Compatibility (EMC) Society within the Institute of Electrical and Electronics Engineers (IEEE)
- Young Professional Coordinator of the IEEE German EMC Chapter
- Study advisor of the study course Mechatronics at the OvGU



- MAFO-01** ORTHS, A.: *Multikriterielle, optimale Planung von Verteilungsnetzen im liberalisierten Energiemarkt unter Verwendung von spieltheoretischen Verfahren*, 2003. ISBN 3-929757-57-5.
- MAFO-02** PURMANN, M.: *Optimierung des Betriebsverhaltens von PEM-Brennstoffzellen unter Berücksichtigung von elektrischem und Gesamtwirkungsgrad bei unterschiedlichen Lastanforderungen und Betriebsparametern*, 2004. ISBN 3-929757-63-X.
- MAFO-03** AL-HAMID, M.: *Extraktion von höheren Moden in TEM-Wellenleitern*, 2004. ISBN 3-929757-64-8.
- MAFO-04** HAASE, H., J. NITSCH, and T. STEINMETZ: *Transmission-Line Super Theory – A new Approach to an Effective Calculation of Electromagnetic Interference*, 2004. ISBN 3-929757-67-2.
- MAFO-05** BACHRY, A.: *Power Quality Studies in Distribution Systems Involving Spectral Decomposition*, 2004. ISBN 3-929757-68-0.
- MAFO-06** STYCZYNSKI, Z. A.: *Power Network and Renewables – A Scientific Report*, 2004. ISBN 3-929757-69-9.
- MAFO-07** BLUME, E.: *Numerische Analyse der Kopplung linearer Antennen innerhalb eines Resonators*, 2004. ISBN 3-929757-71-0.
- MAFO-08** HANDSCHIN, E. and Z. A. STYCZYNSKI: *Power System Application of the Modern Battery Storage*, 2004. ISBN 3-929757-75-3.
- MAFO-09** HAASE, H.: *Full-Wave Field Interactions of Nonuniform Transmission Lines*, 2005. ISBN 3-929757-78-8.
- MAFO-10** NITSCH, D.: *Die Wirkung eingekoppelter ultrabreitbandiger elektromagnetischer Impulse auf komplexe elektronische Systeme*, 2005. ISBN 3-929757-79-6.
- MAFO-11** HADZI-KOSTOVA, B.: *Protection Concepts in Distribution Networks with Decentralized Energy Resources*, 2005. ISBN 3-929757-84-2.
- MAFO-12** STEINMETZ, T.: *Ungleichförmige und zufällig geführte Mehrfachleitungen in komplexen technischen Systemen*, 2006. Nummerierung geändert, ISBN 3-929757-98-2.
- MAFO-13** STYCZYNSKI, Z. and J. HAUBROCK: *Influence of Distributed and Renewable Generation on Power System Security – Proceedings of the CRIS Workshop 2006*, 2006. ISBN 3-929757-99-0.
- MAFO-14** HEIDECK, G.: *Ein autonomes Brennstoffzellensystem: Optimierungsansätze*, 2006. ISBN 3-929757-94-X.
- MAFO-15** STYCZYNSKI, Z. und H.-D. MUSIKOWSKI: *Dresdener Kreis Elektroenergieversorgung 7*, 2006. ISBN 3-929757-85-0.
- MAFO-16** GRONWALD, F.: *Antenna Theory in Resonating Systems derived from Fundamental Electromagnetism*, 2007. ISBN 3-929757-93-1.
- MAFO-17** KRAUTHÄUSER, H.G.: *Grundlagen und Anwendungen von Modenverwirbelungskammern*, 2007. ISBN 978-3-929757-43-9.

- MAFO-18** DZIENIS, C.: *Ersatzmodelle nichtlinearer Lasten in elektrischen Verteilungsnetzen*, 2007. ISBN 978-3-929757-07-1.
- MAFO-19** STYCZYNSKI, Z. and J. HAUBROCK: *Renewable and Dispersed Power Generation in Power Systems*, 2007. ISBN 978-3-929757-44-6.
- MAFO-20** HAUBROCK, J.: *Parametrierung elektrischer Äquivalentschaltbilder von PEM-Brennstoffzellen*, 2008. ISBN 978-3-940961-02-0.
- MAFO-21** ANGELOV, A. N.: *Rechnergestütztes Lernen im Bereich der Regenerativen Energien (Ausgewählte Aspekte)*, 2008. ISBN 978-3-940961-03-7.
- MAFO-22** KOMARNICKI, P.: *Anwendung hochgenauer, synchroner Messungen zur Verbesserung des Betriebs von Verteilungsnetzen*, 2008. ISBN 978-3-940961-04-4.
- MAFO-23** ROGGATZ, C.: *Trainingssimulator für die Führung von elektrischen Systemen mit dezentralen Energieeinspeisungen – Trainingsszenarien und Umsetzung*, 2008. ISBN 978-3-940961-05-1.
- MAFO-24** RUDION, K.: *Aggregated Modelling of Wind Farms*, 2008. ISBN 978-3-940961-14-3.
- MAFO-25** GANJAVI, M. R.: *Protection System Coordination Using Expert System*, 2008. ISBN 978-3-940961-15-0.
- MAFO-26** BOFINGER, S.: *Energieversorgungsnetze mit einem hohen Anteil an photovoltaischer Solarenergie: Standortbestimmung, Solarstromprognose, Netzintegration*, 2008. ISBN 978-3-940961-25-9.
- MAFO-27** STYCZYNSKI, Z. and P. KOMARNICKI: *Distributed and Renewable Power Generation*, 2008. ISBN 978-3-940961-26-6.
- MAFO-28** KOCHETOV, S. V.: *Time- and Frequency-Domain Modeling of Passive Interconnection Structures in Field and Circuit Analysis*, 2008. ISBN 978-3-940961-27-3.
- MAFO-29** MAGDOWSKI, M.: *Entwicklung und Validierung eines Werkzeugs zur Berechnung der elektromagnetischen Einkopplung von stochastischen Feldern in Leitungsstrukturen*, 2008. ISBN 978-3-940961-28-0.
- MAFO-30** SONNEMANN, F.: *Elektromagnetische Effekte an elektrischen Zündmitteln (EED) mit angeschlossener Zündkreiselektronik (ZKE) bei impulsförmiger, breitbandiger Bestrahlung*, 2009. ISBN 978-3-940961-32-7.
- MAFO-31** SMIEJA, T.: *Multikriterielle Planung interregionaler Elektrizitätsnetze im liberalisierten Energiemarkt*, 2009. ISBN 978-3-940961-35-8.
- MAFO-32** HEYDE, C. O.: *Dynamic Voltage Security Assessment for On-Line Control Room Application*, 2010. ISBN 978-3-940961-40-2.
- MAFO-33** STYCZYNSKI, Z. A. and N. I. VOROPAI (EDITORS): *Renewable Energy Systems Fundamentals, Technologies, Techniques and Economics*, 2010. ISBN 978-3-940961-42-6.
- MAFO-34** Styczynski, Z. A. и N. I. Voropai (Editors): *Renewable Energy Systems Fundamentals, Technologies, Techniques and Economics (Russian Version)*, 2010. ISBN 978-3-940961-44-0.
- MAFO-35** STYCZYNSKI, Z. A. and A. LINDEMANN (EDITORS): *Integration of Renewable Energies into the Grid / Proceedings of the Power & Energy Student Summit 2010*, 2010. ISBN 978-3-940961-47-1.

- MAFO-36** STYCZYNSKI, Z. A. und H.-D. MUSIKOWSKI (EDITORS): *Dresdener Kreis Elektroenergieversorgung 11*, 2010. ISBN 978-3-940961-51-8.
- MAFO-37** GURBIEL, M. A.: *Definition and Testing of a Digital Interface of a Power Substation*, 2011. ISBN 978-3-940961-54-9.
- MAFO-38** LOMBARDI, P.: *Multi Criteria Optimization of an Autonomous Virtual Power Plant*, 2011. ISBN 978-3-940961-55-6.
- MAFO-39** POWALKO, M.: *Beobachtbarkeit eines elektrischen Verteilungsnetzes – Ein Beitrag zum Smart Grid*, 2011. ISBN 978-3-940961-62-4.
- MAFO-40** STYCZYNSKI, Z. A., K. RUDION, and C. NGUYEN-MAU (EDITORIAL BOARD): *Power System Dynamic Security Assessment*, 2011. ISBN 978-3-940961-61-7.
- MAFO-41** KÄBISCH, M.: *Optimale Dimensionierung und Betriebsführung einer brennstoffzellenbasierten Auxiliary Power Unit im Fahrzeug*, 2011. ISBN 978-3-940961-67-9.
- MAFO-42** STYCZYNSKI, Z. A. und N. I. VOROPAI (EDITORS): *Special Issue Grant 220 Russian Federation SSmart Grid for Efficient Energy Power System for the Future”, Proceedings Volume I*, 2012. ISBN 978-3-940961-74-7.
- MAFO-43** STYCZYNSKI, Z. A., P. KOMARNICKI und A. NAUMANN (EDITORS): *Abschlussbericht Harz.ErneuerbareEnergien-mobility*, 2012. ISBN 978-3-940961-71-6.
- MAFO-44** HEUER, M.: *Diagnosetool für stationär betriebene PEM-Brennstoffzellensysteme*, 2012. ISBN 978-3-940961-77-8.
- MAFO-45** STÖTZER, M.: *Demand Side Integration in elektrischen Verteilnetzen – Potenzialanalyse und Bewertung*, 2012. ISBN 978-3-940961-78-5.
- MAFO-46** MAGDOWSKI, M.: *Vergleich der Einkopplung deterministischer und statistischer elektromagnetischer Felder in Leitungen*, 2012. ISBN 978-3-940961-75-4.
- MAFO-47** NAUMANN, A.: *Leitwarte im Smart Grid*, 2012. ISBN 978-3-940961-81-5.
- MAFO-48** RUDION, K.: *Offshore Power System Planning – Selected Aspects*, 2012. ISBN 978-3-940961-82-2.
- MAFO-49** NGUYEN-MAU, C.: *Electric Power System Stability Enhancement by Voltage Source Converter based High Voltage Direct Current Technology*, 2012. ISBN 978-3-940961-84-6.
- MAFO-50** GUO, H.: *Measurement-Based Load Modeling for Smart Grid Planning*, 2012. ISBN 978-3-940961-86-0.
- MAFO-51** STYCZYNSKI, Z. A.: *Proceedings No. 2 in the Scope of Mega Grant Baikal*, 2013. ISBN 978-3-940961-95-2.
- MAFO-52** STYCZYNSKI, Z. A.: *Proceedings No. 3 in the Scope of Mega Grant Baikal*, 2013. ISBN 978-3-940961-98-3.
- MAFO-53** WENGE, C.: *Optimaler Betrieb von mobilen Speichern im Smart Grid. -Mobilitätsleitwarte-*, 2013. ISBN 978-3-944722-01-6.
- MAFO-54** RÖHRIG, C.: *Smart Distribution Planung unter Berücksichtigung von residualen Lasten*, 2014. ISBN 978-3-944722-06-1.

- MAFO-55** MIDDELSTÄDT, F.: *Research of SEM Poles of Complex Wire Structures*, 2014. ISBN 978-3-944722-07-8.
- MAFO-56** STYCZYNSKI, Z. A. (EDITOR): *Power Network and Renewables – A Scientific Report – 15 Years Research*, 2014. ISBN 978-3-944722-08-5.
- MAFO-57** SOLONINA, N. N., V. S. STEPANOV, and K. V. SUSLOV: *Information technology in intelligent power networks*, 2014. ISBN 978-3-944722-13-9.
- MAFO-58** KREBS, R.: *Fundamentals of Power System Protection*, 2014. ISBN 978-3-944722-15-3.
- MAFO-59** MOSKALENKO, N.: *Optimal Dynamic Energy Management System in Smart Homes*, 2014. ISBN 978-3-944722-16-0.
- MAFO-60** HAUER, I.: *Optimale Last- und Erzeugungsanpassung bei kritischen Netzzuständen – Algorithmen und deren Bewertung*, 2014. ISBN 978-3-944722-18-4.
- MAFO-61** RICHTER, M.: *Dresdner Kreis Elektroenergieversorgung 15, Begleitband zum Workshop 2014*, 2014. ISBN 978-3-944722-21-4.
- MAFO-62** STYCZYNSKI, Z. A., A. RICHTER und P. KÜHNE: *Second ELECON Workshop – Begleitband zum Workshop 2014*, 2014. ISBN 978-3-944722-23-8.
- MAFO-63** BERNSTEIN, P.: *Modellgestützte optimale Betriebsführung von PEM-Brennstoffzellen für autonome Anlagen*, 2015. ISBN 978-3-944722-24-5.
- MAFO-64** RABE, S.: *Betrieb einer Zweipunkt-Offshore-HGÜ-Verbindung – Modelluntersuchungen*, 2015. ISBN 978-3-944722-31-3.
- MAFO-65** ARENDARSKI, B.: *Reliability Assessment of Smart Grids*, 2015. ISBN 978-3-944722-32-0.
- MAFO-66** PAN, X.: *Numerisches EMV-Simulationsverfahren zur Berechnung der Störaussendung elektrischer Antriebssysteme in Hybridfahrzeugen*, 2016. ISBN 978-3-944722-34-4.
- MAFO-67** RICHTER, M.: *PMU-basierte Zustandsabschätzung in Smart Distribution*, 2016. ISBN 978-3-944722-43-6.
- MAFO-68** BIELCHEV, I.: *Adaptiver Distanzschutz im Standard IEC 61850*, 2016. ISBN 978-3-944722-45-0.
- MAFO-69** HASSAN, A.: *Modeling of Single and Double-Shielded Cables for EMC Applications*, 2016. ISBN 978-3-944722-41-2.
- MAFO-70** LIU, X.: *Control of Voltage Source Converter Based High Voltage Direct Current Transmission Systems for Grid Code Compliance*, 2016. ISBN 978-3-944722-46-7.
- MAFO-71** KAISER, M.: *Fusion of Interventional Ultrasound & X-ray*, 2016. ISBN 978-3-944722-51-1.
- MAFO-72** GRIEGER, F.: *Ein Beitrag zur Bestimmung der Zuverlässigkeit von Leistungshalbleiterbauelementen unter Berücksichtigung der Anwendung*, 2016. ISBN 978-3-944722-52-8.
- MAFO-73** LI, M.: *Towards a Robust Electromagnetic Tracking System for Use in Medical Applications*, 2018. ISBN 978-3-944722-66-5.

- MAFO-74** KLABUNDE, C., J. DANCKER, N. GAST, T. SCHRÖTER, F. SCHULZ, J. ROSSBERG und A. RICHTER: *Statusbericht der Otto-von-Guericke-Universität Magdeburg zum Verbundprojekt: Intelligentes Multi-Energie-System (SmartMES)*, 2018. ISBN 978-3-944722-69-6.
- MAFO-75** SCHRÖTER, T.: *19. Dresdner Kreis Elektroenergieversorgung, Begleitband zum Workshop 2018 in Magdeburg*, 2018. ISBN 978-3-944722-79-5.
- MAFO-76** KLABUNDE, C., J. DANCKER, N. GAST, T. SCHRÖTER, F. SCHULZ und J. ROSSBERG: *Intelligentes Multi-Energie-System (SmartMES) – Statusbericht der Otto-von-Guericke-Universität Magdeburg zum Verbundprojekt, 2. Statusseminar 04. April 2019 in Magdeburg*, 2019. ISBN 987-3-944722-80-1.
- MAFO-77** HELM, S., J. DANCKER, M. FRITSCH und T. SCHRÖTER: *Power and Energy Student Summit 2019, 09.–11. Juli, 2019*. ISBN 978-3-944722-84-9.
- MAFO-78** CHYCHYKINA, I.: *Comparison of Different Redispatch Optimization Strategies*, 2019. ISBN 978-3-944722-89-4.
- MAFO-79** BALISCHEWSKI, S.: *Multifunktionaler Einsatz von Batteriespeichern in elektrischen Verteilnetzen*, 2020. ISBN 978-3-944722-92-4.
- MAFO-80** PETZOLD, J.: *Analytische Beschreibung der Kopplung elektromagnetischer Felder durch Aperturen in Resonatoren*, 2020. ISBN 978-3-944722-91-7.
- MAFO-81** MIDDELSTÄDT, L.: *Transiente Effekte in leistungselektronischen Schaltungen mit schnell-schaltenden Leistungshalbleitern unter besonderer Berücksichtigung der elektromagnetischen Verträglichkeit*, 2020. ISBN 978-3-944722-95-5.
- MAFO-82** LIU, Y.: *Contribution to Improve the EMI Performance of Electrical Drive Systems in Vehicles With Special Consideration of Power Semiconductor Modules*, 2021. ISBN 978-3-948749-01-9.
- MAFO-83** GERLACH, A.: *Regelung von direktangetriebenen elektrischen Maschinen für Verbrennungsmotoren*, 2021. ISBN 978-3-948749-03-3.
- MAFO-84** ZHANG, Y.: *Analysis and Control of Resonances in HVDC Connected DFIG-Based Offshore Wind Farms*, 2021. ISBN 978-3-948749-05-7.
- MAFO-85** PANNICKE, E.: *Empfangsspulen für bildgeführte Eingriffe mittels Magnetresonanztomographie*, 2021. ISBN 978-3-948749-12-5.
-